

Republic of Iraq
Ministry of Higher Education & Scientific Research
University of Kerbala
College of Science
Department of Chemistry



***Synthesis of Mesoporous Silica-based materials
derivatised from Rice Husk and their Analytical
Applications***

A Thesis

Submitted to the college of Science, Kerbala University as a Partial
Fulfillment of the Requirements for the Degree of Doctor of Philosophy of
Science in Chemistry

By

Raghad Saad Hatem Al-Bustan

B.Sc. University of Kerbala (2005)

M.Sc. University of Kerbala (2012)

Supervised by

**Prof. Dr.
Alaa Frak Hussain**

**Prof. Dr.
Hayder Hamied Mihsen**

2024 AD

1446 AH



بِسْمِ اللّٰهِ الرَّحْمٰنِ الرَّحِیْمِ

(يَرْفَعِ اللَّهُ الَّذِينَ آمَنُوا مِنْكُمْ وَالَّذِينَ
أُوتُوا الْعِلْمَ دَرَجَاتٍ وَاللَّهُ بِمَا تَعْمَلُونَ خَبِيرٌ)،

صدق الله العلي العظيم

سورة المجادلة: الآية 11

الاهداء

الى من أرسى أسس ألتعلم والتعلم خاتم الانبياء ونبي الرحمة (ص) وآل
بيته الطيبين الأطهار (عليهم السلام) .
الى اساتذتي المشرفين عرفانا بالجميل
الى والدي ووالدتي حفظهما الله
الى أخوتي وأخواتي واهلي جميعا مودةً واخلاصاً
الى زوجي الغالي وفاءً وحباً
الى من هم قطعة مني منتظر وحيدر ومهدي

رغد

Acknowledgments

Thank **Allah** almighty for His guidance and His grace which strengthens me to complete my thesis successfully.

I would like to sincerely thank my academic supervisors, **Prof. Dr. Alaa frak Hussain and Prof. Dr. Hydar Hamied Mihsen** who gave me the opportunity to start this research, and whose inspiration and guidance made such a valuable experience possible. They have stood by me and encouraged me throughout my research, providing support when my morale was failing. Many thanks for their support and guidance throughout the time of my research.

I am especially grateful to the **Dean of College of Science** and the **Head of Chemistry Department** for their kind assistance.

I would like to thank my **parents** for their support, encouragement and understanding. Thanks to my **brother, sisters** and **my colleagues** for being there for me in the time when I needed support.

Finally, I thank my **dear husband** for his patience and flexibility, and our lovely **Kids** for being the sunshine of my life

Raghad Saad Hatem
2024

Supervisor Certification

We certify that preparation of this thesis entitled “**Synthesis of Mesoporous Silica-based materials derivatised from Rice Husk and their Analytical Applications**” was made under our supervision of the department of chemistry, College of science, University of Karbala by ***Raghad Saad Hatem*** in partial fulfillment of the requirements for the degree of ***Doctor of Philosophy of science in Chemistry*** .



Signature:

Name: ***Dr. Alaa Frak Hussain***

Title: Professor

Date: / / 2024

Signature:



Name: ***Dr. Hydar Hamied Mihsen***

Title: Professor

Date: / / 2024

Report of the Head of the Chemistry Department

According to the recommendation presented by the Chairman of the Postgraduate Studies Committee, I forward this thesis **“Synthesis of Mesoporous Silica-based materials derivatised from Rice Husk and their Analytical Applications”** for examination.

Signature:



Assist. Prof. Dr. Thaer M.M.

Head of Chemistry Department

Address: University of Kerbala, College of Science, Department of Chemistry

Date: 6 / 8 /2024



Kerbala University
Science College



Asst. Prof. Dr. Thaer M. M. Al-Rammahi
Head of Chemistry Department

Linguistic Certification

This is to certify that I have read the thesis entitled ,**“Synthesis of Mesoporous Silica-based materials derivatised from Rice Husk and their Analytical Applications”** and corrected the grammatical mistake I found. The thesis is, therefore, qualified for debate.

Signature:

Name: *Dr.*

Title:

Date: / /2024

Scientific Certification

This is to certify that we have read the thesis entitled, “**Synthesis of Mesoporous Silica-based materials derivatised from Rice Husk and their Analytical Applications**”, and corrected the scientific mistakes we found. The thesis is, therefore, qualified for debate.

Signature:

Name: *Dr.*

Title:

Date: / /2024

Signature:


Name: *Dr.*

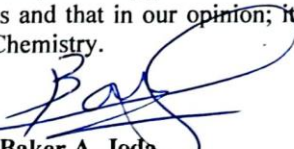
Title:


Date: / /2024


Committee Certificate


We, the examining committee, certify that we have read this thesis "Synthesis of Mesoporous Silica-based materials derivatised from Rice Husk and their Analytical Applications" and examined the student (Raghad Saad Hatem Al-Bustan) in its contents and that in our opinion; it is adequate as a thesis for the degree of Doctor of Philosophy of science in Chemistry.


Signature: 
Name: **Dr. Munner Abdul-Ali Abbas**
Address : University of Kerbala/ College of Education
of Pure Science
Title: Professor
Date: / /2024
(Chairman)


Signature: 
Name: **Dr. Baker A. Joda**
Address: University of Kerbala/ College
of Science
Title: Professor
Date: / /2024
(Member)

Signature: 
Name: **Dr. Tariq Hussein Magheer**
Address: University of Babylon/College
of medicine
Title: Professor
Date: / /2024
(Member)

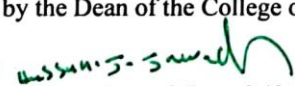
Signature: 
Name: **Dr. Hassn F. Alesary**
Address: University of Kerbala/ College
of Science
Title: Assistant Professor
Date: / /2024
(Member)

Signature: 
Name: **Dr. Ahmed Al-Yasari**
Address: University of Kerbala/ College
of Science
Title: Assistant Professor
Date: / /2024
(Member)

Signature: 
Name: **Dr. Alaa Frak Hussain**
Address: University of Kerbala/ College
of Science
Title: Professor
Date: / /2024
(Member/Supervisor)

Signature: 
Name: **Dr. Hydar Hamied Mihsen**
Address: University of Kerbala/ College
of Science
Title: Professor:
Date: / /2024
(Member/Supervisor)

Approved by the Dean of the College of Science

Signature: 
Name: **Dr. Hassan Jameel Jawad Al-fatlawy**
Title: Professor
Dean of the College of Science/University of Kerbala
Date: / /2024

Abstract

Rice husk (RH) is regarded as one of the most common agricultural residues worldwide. RH can itself be transformed to sodium silicate. Mobil Composition of Matter No. 41 (MCM-41) is prepared from sodium silicate. This thesis includes three steps, the first of which involves extraction of silica from RH, generation of RH-SiO₂, MCM-41 and functionalized compounds from the extracted silica; The second and third steps involve characterization of the synthesized compounds can be successfully achieved via the use of various techniques and then some analytical applications.

MCM-41 was functionalized with 3-aminopropyltriethoxysilane (APTES) to obtain MCM-41@APTES. In the next step, 5-bromosalicylaldehyde (BSAL) was refluxed with MCM-41@APTES in toluene to obtain the Schiff base-functionalized mesoporous silica material, MCM-41@APTES-BSAL. Additionally, MCM-41 was functionalized with N-[3-(trimethoxysilyl)propyl]ethylenediamine (NTPE) to obtain MCM-41@NTPE. In the following step, 5-bromosalicylaldehyde (BSAL) was refluxed with MCM-41@NTPE in toluene to obtain a Schiff-base functionalized mesoporous silica material (MCM-41@NTPE-BSAL).

The amount of carbon, hydrogen and nitrogen present in compounds were improved through elemental analysis. The FT-IR spectra of prepared compounds shows several distinct peaks related to compounds. The XRD and TEM investigation demonstrated that MCM-41 and functionalized compounds with an extremely ordered hexagonal arrangement was generated. The N₂ adsorption-desorption analysis revealed that the average pore diameter, total pore volume, and specific surface area. Thermogravimetric analysis (TGA/DSC) of RH-SiO₂ and MCM-41 revealed two mass reduction steps while for functionalized compounds, revealed three mass reduction steps. The surface topographies for RH-SiO₂ and MCM-41 were demonstrated via AFM analysis which shows the presence of blocks of different shapes in RH-SiO₂. For MCM-41, it is clear from result that the roughness factor is low. The increase in the AFM parameter for MCM-41@APTES compare with MCM-41. The average roughness of MCM-41@APTES-BSAL was decreased upon functionalization of MCM-41@APTES with 5-Bromosalicylaldehyde (BSAL). The increase

in the AFM parameter for MCM-41@NTPE compared with MCM-41, While for MCM-41@NTPE-BSAL the results demonstrated that the functionalization of MCM-41@NTPE led to a decreased in the surface roughness material upon functionalization. FESEM images shows that RH-SiO₂ is composed of amorphous silica, while for MCM-41 and functionalized compounds, it is clear from the images that the particles are smooth with spherical agglomerations. According to EDX analysis, the existence of elements in the solid ligands was proven.

Mesoporous materials (organic-inorganic materials) derived from rice husk as low-cost adsorbents and applied them in the removal of metal ions (Co (II) and Cu (II)) from their aqueous solutions after prepared column from solid ligands and attempt to activate the column. Removal experiments were performed after optimize the concentration of Co(II) and Cu(II) ions, pH, exposure time, and mass of prepared compounds. The amount of Co (II) in pharmaceuticals was determined using the prepared compounds. Investigation Langmuir and Freundlich models showed that the data was best fitted with the Freundlich adsorption isotherm model in multilayer fashion.

List of contents

No.	Title	Page No.
	Abstract	I
	List of contents.	III
	List of symbols and abbreviations.	VIII
	List of Tables.	IX
	List of Schemes.	X
	List of Figures.	XI
	List of Pictures.	XV
	Chapter One :Introduction	
1	Introduction	1
1.1	Definition and classification of porous materials	2
1.2	Mesoporous materials	3
1.3	Mesoporous nano silica nanoparticles	4
1.4	MSNs features	5
1.5	M41S family	5
1.6	Methods of synthesizing mesoporous materials	6
1.6.1	Sol- gel process	6
1.6.2	Template assisted technique	7
1.6.3	Liquid crystal template approach(LCTA)	8
1.6.4	Microwave assisted technique	9
1.6.5	Chemical etching technique	9
1.7	Mechanism for mesoporous materials mechanism	10
1.8	Functionalization	11
1.8.1	Grafting methods	12
1.8.2	Co-condensation methods	13
1.9	Functionalization of MCM-41 with organic amine	15
1.10	Applications of mesoporous silica	16
1.11	Surfactants	17
1.12	Chemistry of surfactant/silicate solutions	17
1.13	Structural characterization of the M41S mesoporous materials	18
1.14	Rice husk (RH)	19
1.15	Application of rice husk	20
1.16	Adsorbent	21
1.17	Properties of rice husk and rice husk ash	22

1.18	Silica	22
1.19	Pollutions	24
1.20	Cobalt	26
1.21	Copper	26
1.22	Adsorption of metals on the surface of functionalized mesoporous	27
1.23	Extraction	29
1.24	Classification of extraction	29
1.25	Solid phase extraction (SPE)	30
1.26	Schiff base	32
1.27	Application of Schiff base	33
1.28	Some of the complexes of Schiff base producing from functional silica	34
1.29	The aim of thesis	41
Chapter Two: Experimental part		
2	Experimental part	42
2.1	Instruments	42
2.2	Chemicals	43
2.3	Preparations of materials	44
2.3.1	Preparation of RH-SiO ₂ and sodium silicate	44
2.3.2	Preparation of MCM-41	47
2.3.3	The functionalization of MCM-41	49
2.3.3.1	Synthesis of 3-aminopropyltriethoxysilane functionalized mesoporous silica (MCM-41@APTES).	49
2.3.3.2	Synthesis of 5-bromosalicylaldehyde functionalized mesoporous silica (MCM-41@APTES-BSAL).	49
2.3.3.3	Synthesis of N-[3-(Trimethoxysilyl)propyl]ethylenediamine functionalized mesoporous silica(MCM-41@NTPE).	50
2.3.3.4	Synthesis of 5-bromosalicylaldehyde functionalized mesoporous silica (MCM-41@NTPE-BSAL).	50
2.3.4	Preparation of stock solution of Co (II) ion.	51
2.3.5	Preparation of stock solution of copper (II) ion.	51
2.3.6	(2% W/V) solution of ascorbic acid.	52
2.3.7	(50% W/V) solution of ammonium thiocyanate	52
2.3.8	(0.5 M) of Hydrochloric acid solution	52
2.3.9	Sodium hydroxide solution	52
2.3.10	(5%) (EDTA) Ethylenediaminetetraaceice acide solution.	52
2.3.11	Characterization studies.	52
2.3.11.1	UV-Visible measurements for aqueous solutions of Co(II) and	52

	Cu(II)	
2.3.11.2	Elemental analysis CHNS	52
2.3.11.3	Study of FT-IR(spectra furrier transforms infrared spectrophotometry)	53
2.3.11.4	Study of X-ray diffraction analysis (XRD).	53
2.3.11.5	BET surface area analyzer(N ₂ adsorption-desorption)	53
2.3.11.6	Thermal analysis(TGA/DSC)	53
2.3.11.7	AFM analysis	54
2.3.11.8	Study of field emission scanning electron microscopic(FESEM-EDX) transmission electron microcopy (TEM)	54
2.4	Calibration curve of Co (II) and Cu(II) ions for determination	55
2.5	Removal ions experiments	55
2.6	Optimum conditions	56
2.6.1	Effect of shaking time	56
2.6.2	Effect of pH	56
2.6.3	Effect of metal ion concentration	56
2.6.4	Effect of mass of the ligand.	57
2.7	Column separation experiment	57
2.8	Determination of Co(II) ion in vitamin B12	58
2.9	Adsorption equilibrium isotherms	58
	Chapter Three: Result and discussion(Characterization)	
3	The characterization of RH-SiO ₂ ,MCM-41 and its derivatives (MCM-41@APTES, MCM-41@APTES-BSAL, MCM-41@NTPE and MCM-41@NTPE-BSAL)	61
3.1	The characterization of RH-SiO ₂ and MCM-41	61
3.1.1	Fourier –transform infrared spectroscopic analysis (FT-IR)	61
3.1.2	X-ray powder diffraction(XRD) for RH-SiO ₂ and MCM-41	62
3.1.3	Nitrogen adsorption desorption analysis.	64
3.1.4	Thermogravimetric analysis (TGA)	66
3.1.5	Atomic force microscopy(AFM)	68
3.1.6	Field emission scanning electron microscopy-energy dispersive X-ray (FESEM and EDX).	70
3.1.7	Transmission electron microscopy (TEM).	73
3.2	The characterization of MCM-41@APTES.	75
3.2.1	Elemental analysis.	76
3.2.2	Fourier –transform infrared spectroscopic analysis (FT-IR)	76
3.2.3	X-ray powder diffraction(XRD) for MCM-41@APTES	77
3.2.4	Nitrogen adsorption- desorption analysis.	79

3.2.5	Thermogravimetric analysis (TGA).	80
3.2.6	Atomic force microscopy (AFM).	81
3.2.7	Field emission scanning electron microscopy-energy dispersive X-ray (FESEM and EDX).	82
3.2.8	Transmission electron microscopy (TEM).	84
3.3	The characterization of MCM-41@APTES-BSAL.	85
3.3.1	Elemental analysis.	86
3.3.2	Fourier –transform infrared spectroscopic analysis (FT-IR)	86
3.3.3	X-ray Powder diffraction(XRD) for MCM-41@APTES-BSAL	87
3.3.4	Nitrogen adsorption-desorption analysis.	88
3.3.5	Thermogravimetric analysis (TGA)	90
3.3.6	Atomic force microscopy(AFM)	91
3.3.7	Field emission scanning electron microscopy-energy dispersive X-ray (FESEM and EDX)	92
3.3.8	Transmission electron microscopy(TEM)	94
3.4	The characterization of MCM-41@NTPE	95
3.4.1	Elemental analysis	95
3.4.2	Fourier –transform infrared spectroscopic analysis (FT-IR)	96
3.4.3	X-ray powder diffraction(XRD) for MCM-41@APTES-BSAL	97
3.4.4	Nitrogen adsorption desorption analysis.	98
3.4.5	Thermogravimetric analysis (TGA)	100
3.4.6	Atomic force microscopy(AFM).	101
3.4.7	Field emission scanning electron microscopy-energy dispersive X-ray (FESEM and EDX).	102
3.4.8	Transmission electron microscopy (TEM).	104
3.5	The characterization of MCM-41@NTPE-BSAL.	105
3.5.1	Elemental analysis.	106
3.5.2	Fourier –transform infrared spectroscopic analysis (FT-IR)	106
3.5.3	X-ray powder diffraction(XRD) for MCM-41@NTPE-BSAL	107
3.5.4	Nitrogen adsorption desorption analysis.	108
3.5.5	Thermogravimetric analysis (TGA).	111
3.5.6	Atomic force microscopy (AFM).	111
3.5.7	Field emission scanning electron microscopy-energy dispersive X-ray (FESEM and EDX).	112
3.5.8	Transmission electron microscopy (TEM).	114
Chapter Four: Result and discussion(Applications)		
4	Removal of metal ions from aqueous solution.	116
4.1	Study of UV-visible spectra of divalent ions (Cobalt and Copper)	116

4.2	Calibration curve of ions (Co(II) and Cu(II))	118
4.3	Removal tests	119
4.3.1	Removal ions experiments	119
4.3.1.1	Removal ions by RH-SiO ₂ and MCM-41	119
4.3.1.1.1	Effect of exposure time	119
4.3.1.1.2	Effect of pH	120
4.3.1.1.3	Effect of concentration of Co (II) and Cu (II) ions	123
4.3.1.1.4	Effect of mass of RH-SiO ₂ and MCM-41	126
4.3.1.2	Removal of metal ions by MCM-41@APTES and MCM-41@APTES-BSAL.	128
4.3.1.2.1	Effect of exposure time	128
4.3.1.2.2	Effect of pH	130
4.3.1.2.3	Effect of concentration of Co (II) and Cu (II) ions.	132
4.3.1.2.4	Effect of mass of the (MCM-41@APTES and MCM-41@APTES-BSAL).	134
4.3.1.3	Removal of metal ions by MCM-41@NTPE and MCM-41@NTPE-BSAL.	137
4.3.1.3.1	Effect of exposure time.	137
4.3.1.3.2	Effect of pH.	138
4.3.1.3.3	Effect of concentration of Co (II) and Cu (II) Ions.	141
4.3.1.3.4	Effect of mass of MCM-41@NTPE and MCM-41@NTPE-BSAL.	143
4.4	Column separation experiment.	146
4.5	Column recovery experience.	150
4.6	Determination of Co(II) ion in vitamin B12	150
4.7	Adsorption equilibrium isotherms	151
4.7.1	Langmuir isotherm model	151
4.7.2	Freundlich isotherm model	152
4.8	Conclusions	154
4.9	Future studies	156
	References	157

List of symbols and abbreviations.

Symbol	Meaning
AFM	Atomic Force Microscopy
APTES	(3-Aminopropyl)triethoxysilane
BDH	British Drug Houses
BET	Brunauer-Emmet-Teller
BSAL	5-Bromosalicylaldehyde
cm	Centimeter
CMC	Critical Micelles Concentration
CTAB	Cetyltrimethylammonium bromide
DSC	Differential Scanning Calorimetry
EDX	Energy Dispersive X-ray
FESEM	Field Emission Scanning Electron Microscopy-
FT-IR	Fourier –Transform infrared
g	Gram
hr.	Hour
H2	Hysteresis loop type 2
H3	Hysteresis loop type 3
HMS	Hollow Mesoporous Silica
IUPAC	International Union of Pure and Applied Chemistry
m	Meter
MCM-41	Mobil Composition of Matter No. 41
MCM-41@APTES	MCM-41 immobilized with APTES
MCM-41@APTES-BSAL	MCM-41@APTES immobilized with BSAL
MCM-41@NTPE	MCM-41 immobilized with NTPE
MCM-41@NTPE-BSAL	MCM-41@NTPE immobilized with BSAL
M	Molarity
MSNs	Mesoporous nano particals
nm	Nanometer
NTPE	<i>N</i> -[3-(trimethoxysilyl)propyl]ethylenediamine
pH	Acidic function
SBA	Santa Barbara Amorphou
SiO₂	Silicon dioxide
Sz	ergs.cm ⁻² .S ⁻¹

TEM	Transmission Electron Microscopy
UV-vis	Ultraviolet–visible spectroscopy
XRD	X-ray Diffraction
2D	Two dimension
3D	Three dimension
λ_{max}.	Lambda maximum

List of Tables

No.	Title	Page No.
1.1	Applications of mesoporous silica.	16
1.2	Summary of some studies involved adsorption capacities of heavy metal using rice husk (RH) as adsorbent	23
1.3	The most important parameter and its characterization of these type of SPE	31
2.1	Instrument and the place of measurement.	42
2.2	Solvents used	43
2.3	Organic and inorganic materials used	43
2.4	Equations of removal percentage, adsorption capacity, adsorption isotherm, kinetic, and mathematical modeling.	59
3.1	BET analysis for RH-SiO ₂ and MCM-41.	64
3.2	AFM parameters of the RH-SiO ₂ and MCM-41.	69
3.3	Difference between FESEM and TEM	70
3.4	The average values obtained from EDX analysis for RH-SiO ₂ and MCM-41	72
3.5	The percentage of elements present in MCM-41@APTES that can be found through elemental analysis.	76
3.6	BET analysis for MCM-41@APTES and starting materials.	79
3.7	AFM parameters for MCM-41@APTES.	82
3.8	The average values obtained from EDX analysis for MCM-41@APTES.	83
3.9	The percentage of elements present in MCM-41@APTES-BSAL that can be found through elemental analysis.	86
3.10	BET analysis for MCM-41@APTES-BSAL and starting materials.	89
3.11	AFM parameters of the MCM-41@APTES-BSAL and starting materials.	92
3.12	The average values obtained from EDX analysis for MCM-	93

	41@APTES-BSAL.	
3.13	The percentage of elements present in MCM-41@NTPE that can be found through elemental analysis.	96
3.14	BET analysis for MCM-41@NTPE-BSAL and starting materials.	99
3.15	AFM parameters of the MCM-41@NTPE and starting materials.	102
3.16	The average values obtained from EDX analysis for MCM-41@NTPE.	103
3.17	The percentage of elements present in MCM-41@NTPE-BSAL that can be found through elemental analysis.	106
3.18	BET analysis for MCM-41@NTPE-BSAL and starting materials.	110
3.19	AFM parameters of the MCM-41@NTPE-BSAL and starting materials	112
3.20	The average values obtained from EDX analysis for MCM-41@NTPE-BSAL.	113
4.1	Different concentration (20,50,100,500 and1000)ppm	147
4.2	Removal % after activation	150
4.3	Results of determination of Co(II) ions in Vit.B12	150
4.4	The value of separation factor	152
4.5	Langmuir parameters for Co(II) ions adsorption	152
4.6	Langmuir parameters for Cu(II) ions adsorption	152
4.7	Freundlich parameter for Co(II)ions adsorption	153
4.8	Freundlich parameter for Cu(II)ions adsorption	153

List of Schemes

No.	Title	Page No.
1.1	Representative event of the development story for hybrid and porous materials.	1
1.2	Important MSNs features(Reproduced)	5
1.3	Methods of synthesizing mesoporous materials(Reproduced)	6
1.4	Schematic diagram of applications of derived rice husk.	21
1.5	Methods of extraction of silica from SiO ₂	23
1.6	Extraction based on phase type(Reproduced)	29
1.7	Advance extraction techniques (Reproduced)	30
1.8	The Schiff base formation.	32
1.9	Typical Schiff base, their metal complexes and bioactivities	33
1.10	Immobilization of I, II and III onto modified silica gel	34

1.11	Assembly of SPEA within the SBA-15	34
1.12	a) silica gel surface modification by using organo-silan to silica gel-O ₂ -(EtO)Si-L1H) b) Mn(II) immobilization on functionalized silica gel surface to produce compound 2	35
1.13	Synthesis of Fe ₂ O ₄ @SiO ₂ @KIT-6-NH ₂ @Schiff base complex	36
1.14	Synthesis of the catalyst	37
1.15	Synthesis of the functionalized MSNs.	38
1.16	Preparation of the silica gel-immobilized zwitter ionic Schiff base adsorbent SG-H ₂ L ² (SG-H ₂ L ¹ inset for reference)	38
1.17	Synthesis of copper complex with Schiff base ligand derived from 2-furylmethylketone, 2-furadyhde and 2-hydroxyacetophenone	39
1.18	Synthesis of LMSN-NH ₂ -CC	40
1.19	HSPTMS formation reaction	40
2.1	The synthesis steps of RH-SiO ₂ and MCM-41.	47
2.2	The synthesis steps of MCM-41@APTES	49
2.3	The synthesis steps of MCM-41@APTES-BSAL.	50
2.4	The synthesis steps of MCM-41@NTPE	50
2.5	The synthesis steps of MCM-41@NTPE-BSAL.	51
2.7	The method of preparation.	60

List of Figures

No.	Title	Page No.
1.1	Pore shapes for porous materials.	2
1.2	Pore size for different kinds of porous material.	2
1.3	Representation of MSNs channels and TEM micrograph	5
1.4	Soft template method(endoplate)and hard template method (exotemplate)	8
1.5	Proposed procedures for synthesizing MCM-41.	9
1.6	Chemical etching process.	10
1.7	Mechanism for mesoporous materials synthesis.	11
1.8	Grafting method for functionalization of mesoporous silicates.	12
1.9	Functionalization of mesoporous silicates by Co-condensation method silicates.	14
1.10	Sequences phase of surfactant /water system.	17
3.1	FTIR spectra for RH-SiO ₂ and MCM-41.	62

3.2	XRD spectra (low angle) of RH-SiO ₂ and MCM-41.	63
3.3	XRD spectra (high angle) of RH-SiO ₂ and MCM-41.	63
3.4	N ₂ adsorption–desorption isotherms for RH-SiO ₂ and MCM-41	65
3.5	Pore size distributions for RH-SiO ₂ and MCM-41.	66
3.6	TGA/DSC plot of RH-SiO ₂ .	67
3.7	TGA/DSC plot of MCM-41.	68
3.8	AFM 2D (on the left) and 3D (on the right) micrographs of RH-SiO ₂ and MCM-41.	69
3.9	FESEM analysis for RH-SiO ₂ and MCM-41 at scales of 500 nm and 1000 nm.	71
3.10	EDX analysis for RH-SiO ₂ .	72
3.11	EDX analysis for MCM-41.	73
3.12	TEM images for RH-SiO ₂ at scales of 50 nm and 100 nm	74
3.13	TEM images for MCM-41 at scales of 50 nm and 100 nm	75
3.14	FTIR spectra for MCM-41@APTES and starting material.	77
3.15	XRD spectra (low angle) of MCM-41@APTES and starting material.	78
3.16	XRD spectrum (high angle) of MCM-41@APTES.	78
3.17	N ₂ adsorption–desorption isotherms for MCM-41@APTES	80
3.18	Pore size distributions for MCM-41@APTES.	80
3.19	TGA/DSC plot of MCM-41@APTES.	81
3.20	AFM 2D (on the left) and 3D (on the right) micrographs of MCM-41@APTES.	82
3.21	FESEM analysis for MCM-41@APTES at scales of 500 nm and 1000 nm.	83
3.22	EDX analysis for MCM-41@APTES.	84
3.23	TEM images for MCM-41@APTES at different scale	85
3.24	FTIR spectra for MCM-41@APTES-BSAL and starting materials.	87
3.25	XRD spectra (low angle) of MCM-41@APTES-BSAL and starting materials.	88
3.26	XRD spectrum (high angle) of MCM-41@APTES-BSAL.	88
3.27	N ₂ adsorption–desorption isotherms for MCM-41@APTES-BSAL	89
3.28	Pore size distributions for MCM-41@APTES-BSAL.	90
3.29	TGA/DSC plot of MCM-41@APTES-BSAL.	91
3.30	AFM 2D (on the left) and 3D (on the right) micrographs of MCM-41@APTES-BSAL.	92
3.31	FESEM analysis for MCM-41@APTES-BSAL at scales of 500 nm and 1000 nm.	93
3.32	EDX analysis for MCM-41@APTES-BSAL.	94

3.33	TEM images for MCM-41@APTES-BSAL at different scales.	95
3.34	FTIR spectra for MCM-41@NTPE and starting material. .	97
3.35	XRD spectra (low angle) of MCM-41@NTPE and starting material.	98
3.36	XRD spectrum (high angle) of MCM-41@NTPE	98
3.37	N ₂ adsorption–desorption isotherms for MCM-41@NTPE	100
3.38	Pore size distributions for MCM-41@NTPE.	100
3.39	TGA/DSC plot of MCM-41@NTPE.	101
3.40	AFM 2D (on the left) and 3D (on the right) micrographs of MCM-41@NTPE.	102
3.41	FESEM analysis for MCM-41@NTPE at scales of 500 nm and 1000 nm.	103
3.42	EDX analysis for MCM-41@NTPE.	104
3.43	TEM images for MCM-41@NTPE at different scale	105
3.44	FTIR spectra for MCM-41@NTPE-BSAL and starting materials.	107
3.45	XRD spectra (low angle) of MCM-41@NTPE-BSAL and starting material.	108
3.46	XRD spectrum (high angle) of MCM-41@NTPE-BSAL.	108
3.47	N ₂ adsorption–desorption isotherms for MCM-41@NTPE-BSAL	109
3.48	Pore size distributions for MCM-41@NTPE-BSAL.	110
3.49	TGA/DSC plot of MCM-41@NTPE-BSAL.	111
3.50	AFM 2D (on the left) and 3D (on the right) micrographs of MCM-41@NTPE-BSAL.	112
3.51	FESEM analysis for MCM-41@NTPE-BSAL at scales of 500 nm and 1000 nm.	113
3.52	EDX analysis for MCM-41@NTPE-BSAL.	114
3.53	TEM images for MCM-41@NTPE-BSAL at different scale	115
4.1	Uv-vissible of Co (II) ions	117
4.2	Uv-vissible of Cu(II) ions	117
4.3	Calibration curve of Co (II) ion.	118
4.4	Calibration curve of Cu (II) ion.	118
4.5	The removal of Cu (II) and Co (II) ions by the RH-SiO ₂ ligand as a function of time.	120
4.6	The removal of Cu (II) and Co (II) ions by the MCM-41 ligand as a function of time	120
4.7	The removal of Co (II) ions by RH-SiO ₂ at various pHs.	122
4.8	The removal of Co (II) ions by MCM-41 at various pHs.	122
4.9	The removal of Cu (II) ions by RH-SiO ₂ at various pHs.	123
4.10	The removal of Cu (II) ions by MCM-41 at various pHs.	123

4.11	The removal of Co (II) ions by RH-SiO ₂ using various initial concentration	124
4.12	The removal of Co (II) ions by MCM-41 using various initial concentration	125
4.13	The removal of Cu (II) ions by RH-SiO ₂ using various initial concentration.	125
4.14	The removal of Cu (II) ions by MCM-41 using various initial concentration.	126
4.15	The removal of Co (II) ions by various mass of RH-SiO ₂ .	127
4.16	The removal of Co (II) ions by various mass of MCM-41.	127
4.17	The removal of Cu (II) ions by various mass of RH-SiO ₂ .	128
4.18	The removal of Cu (II) ions by various mass of MCM-41.	128
4.19	The removal of Cu (II) and Co (II) ions by the MCM-41 @ APTES ligand versus time.	129
4.20	The removal of Cu (II) and Co (II) ions by the MCM-41 @ APTES-BSAL ligand versus time	129
4.21	The removal of Co (II) ions by MCM-41 @ APTES with various pHs.	130
4.22	The removal of Co (II) ions by MCM-41 @ APTES-BSAL with various pHs.	131
4.23	The removal of Cu (II) ions by MCM-41 @ APTES with various pHs.	131
4.24	The removal of Cu (II) ions by MCM-41 @ APTES-BSAL with various pHs.	132
4.25	The removal of Co (II) ions by MCM-41 @ APTES with various initial concentration	133
4.26	The removal of Co (II) ions by MCM-41 @ APTES-BSAL with various initial concentration	133
4.27	The removal of Cu (II) ions by MCM-41 @ APTES with various initial concentration.	134
4.28	The removal of Cu (II) ions by MCM-41 @ APTES-BSAL with various initial concentration.	134
4.29	The removal of Co (II) ions by MCM-41 @ APTES with various mass.	135
4.30	The removal of Co (II) ions by MCM-41 @ APTES-BSAL with various mass.	136
4.31	The removal of Cu (II) ions by MCM-41 @ APTES with various mass.	136
4.32	The removal of Cu (II) ions by MCM-41 @ APTES-BSAL with various mass	137
4.33	The removal of Cu (II) and Co (II) ions by the MCM-41 @ NTPE ligand as a function of time.	138
4.34	The removal of Cu (II) and Co (II) ions by the MCM-41 @ NTPE-	138

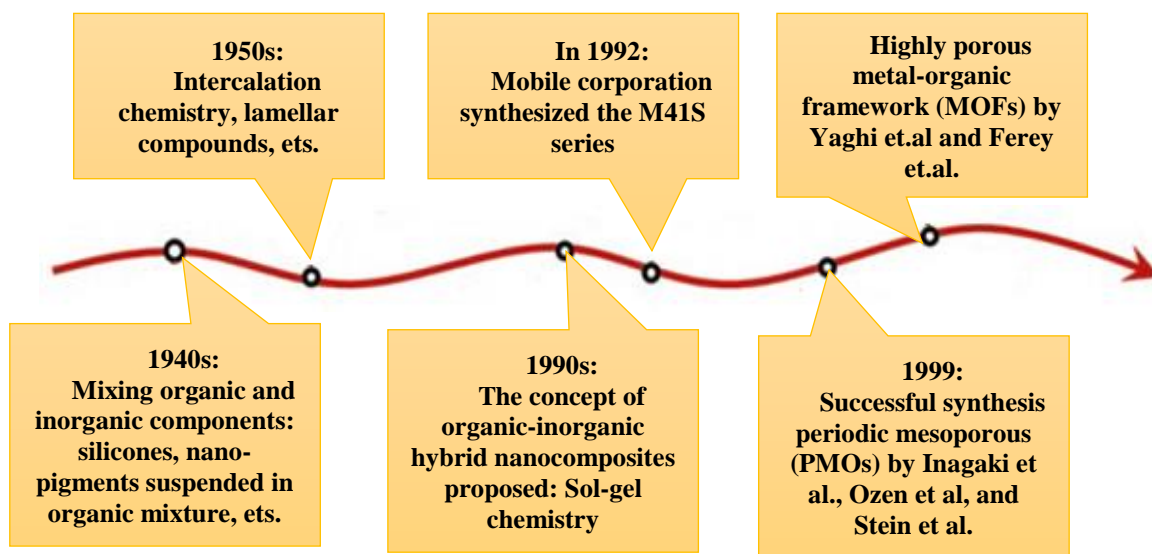
	BSAL ligand as a function of time.	
4.35	The removal of Co (II) ions by MCM-41@NTPE at various pHs..	139
4.36	The removal of Co (II) ions by MCM-41@NTPE-BSAL at various pHs.	140
4.37	The removal of Cu (II) ions by MCM-41@NTPE at various pHs.	140
4.38	The removal of Cu (II) ions by MCM-41@NTPE-BSAL at various pHs.	141
4.39	The removal of Co (II) ions by MCM-41@NTPE using various initial concentration	142
4.40	The removal of Co (II) ions by MCM-41@NTPE-BSAL using various initial concentration	142
4.41	The removal of Cu (II) ions by MCM-41@NTPE using various initial concentration.	143
4.42	The removal of Cu (II) ions by MCM-41@NTPE-BSAL using various initial concentration.	143
4.43	The removal of Co (II) ions by MCM-41@NTPE with various mass .	144
4.44	The removal of Co (II) ions by MCM-41@NTPE-BSAL with various mass	145
4.45	The removal of Cu (II) ions by MCM-41@NTPE with various mass .	145
4.46	The removal of Cu (II) ions by MCM-41@NTPE-BSAL with various mass	146

List of Picture

No.	Title	Page No.
2.1	Dried RH	44
2.2	RH + Nitric acid	45
2.3	Dried RH after acidity	45
2.4	RH+NaOH	46
2.5	Sodium silicate	46
2.6	RH-SiO ₂	47
2.7	Preparation of MCM-41	48
2.8	Separation column	58

1. Introduction

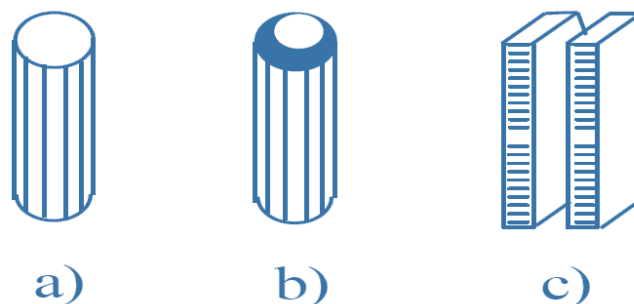
Science and technology are developed quickly, science is very important in helping society and human move forward. Every time a new material is created, it helps society to do more and move forward. Metal, inorganic nonmetallic and polymer materials are widely used in national economic, modern science and technology. There are different kinds of materials; one significant type is called porous materials with well-defined mesoporous in their matrix. These materials have a small porous. They are considered very special. Their unique characteristics, exceptional physical / chemical properties and wide range of uses are always being studied and explored by scientists in the field of materials science. According to the classification reported from International Union of Pure and Applied Chemistry (IUPAC), there are three kinds of porous materials. Microporous materials have tiny pore, smaller than 2 nm. Mesoporous materials have pore that ranging from 2-50 nm. Macroporous materials have the biggest pore, larger than 50nm[1–3]. The event of the development story for hybrid and porous materials represented in scheme (1.1).



Scheme (1.1): Representative event of the development story for hybrid and porous materials[4].

1.1 Definition and classification of porous materials

The word porous is referred to describe the materials that contain pores, which are small holes or channels that differ in size and shape. Natural or synthetic porous materials have many advantages for human activities. Their pore structure is usually created during or subsequent formation process and includes separate or interconnected pores that can have different shapes and forms. The pore range in width from very tiny (0.3 nm) to slightly bigger (10 μm) are being currently investigated to their ability to select molecules. The geometry of pore size can be explained using three pore basic models as illustrated in Figs. (1.1) and (1.2) [5, 6].



- Pores which have circular cross section, called cylindrical pores.
- Pores which have narrow neck and wide body, called ink bottle pores.
- Pore with parallel plates, called slit shaped pores.

Figure (1.1): Pore shapes for porous materials.

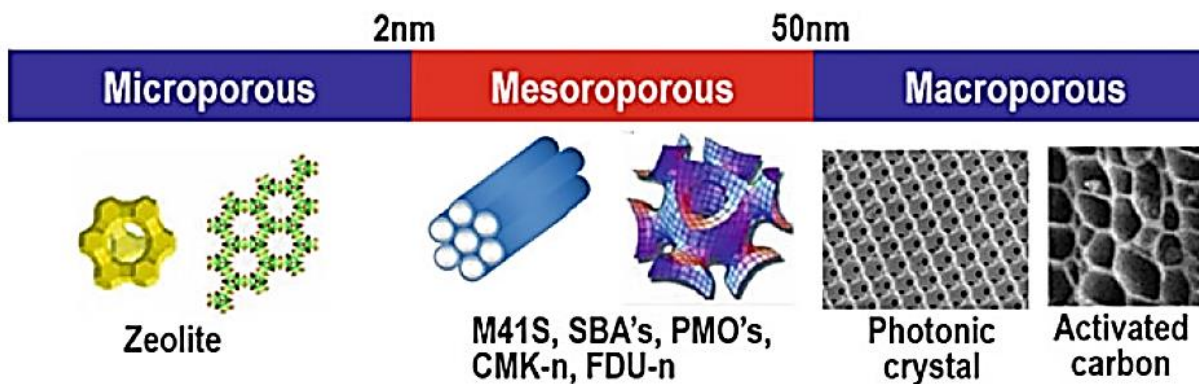


Figure (1.2): Pore size for different kinds of porous material [7].

1.2 Mesoporous materials

The first discovery of mesoporous materials announced in 1990s[8]. During this period, the solid porous industry was searching for materials with higher pores compared to zeolites. It was in 1992 when Mobil Oil Corporation successfully produced Mobil Composition of Matter(MCM) by combining a silica precursor with an amphiphilic surfactant. The major benefit of these novel substances compared to zeolites was that their porous dimensions could be easily adjusted within the range of 2-10 nm. These MCM substances, alternatively referred to as MSNs, offer a highly adaptable manufacturing method, allowing for precise adjustment of their dimensions and porosity by adjusting various factors, such as the surfactant type, pH, and temperature.

Typically, materials with mesoporous structure produced using micelle – templating method, then proceeds with one of the two ways: by using anionic routs or by using an electrostatically stimulated collaborative assembly pathway. In both cases surfactants, which have no charge, were used to help in formation of the mesoporous materials[7].

There are two main categories of mesoporous materials:

- 1- Groups based on mesoporous silicon materials.
- 2- Groups based on non-silicon mesoporous materials.

Silicon-based mesoporous materials are often called mesoporous silicate and can be divided into two types: one is made from pure silicates and the second type is made of modified silicates. Pure silicate materials are hexagonal in shaped porous silica which called SBA, MCM and HMS. On the other hand, non-silicate porous materials are made up of metal oxide and metal sulfide as transitions (WS_2 , MoS_2 , FeS_2 , CoS_2 , NiS_2 , etc.) and nonmetallic oxide (like mesoporous carbon phosphate and sulfate)[9, 10].

There is other sort of porous materials besides silicon- based that can have tiny pore like coordinate solid, carbon and heteropolyanion salts. Ordered porous carbon is fascinating substance due to its distinct characteristics such as water-repellent quality of its surface, chemical non reactivity, excellent durability and thermal stability. These characterizations make it useful for making tubes, membrane and special kinds of fibers.

Carbon with porous structures can be made by using silicate as template in a process called Nano casting. The non-silicate mesoporous substances are very important to use as catalysts because of their unique transition state. In general, this sort of mesoporous is considered unstable. The tiny pore in this type of porous materials can be compressed during the process of production. In addition to that the production and calcination processes are difficult. For that, Scientists focusing in silica mesoporous materials due to these difficulties. Divers approaches have been applied to enhance mesoporous silica materials, resulting in expansion of the framework utilized. Hybrid materials produced from combining organic and inorganic components proves to be an effective method to obtaining valuable materials due to the facilitation of collaboration and the integration of diver's functionalization in the design of these materials [11, 12].

Mesoporous silica is employed in diverse applications such as adsorbent surfaces [13]molecular sieves and filters[14], in separation processes[15], participating as catalysts in chemical reactions [16]and the process of drug delivery due to its stability, permeability, high specific area, and flexibility[17].

1.3 Mesoporous nano silica nanoparticles

Ever since its detection in 1991, mesoporous silicon-based nanoparticles (MSNs) have been extensively utilized in the fields of catalysis and biomedicine owing to their exceptional physicochemical properties, biocompatibility, chemical stability, mechanical resistance and considerable adaptability in synthesis[18]. Nanocomposites derived from biomass have many applications in the biomedical fields, chemical industries, energy applications, and the removal of environmental pollutants[19–23]. MSNs are composed of a silica framework filled with porous cavities ranging in size from 2 to 50 nanometers. This unique characteristic provides MSNs with two distinct surfaces: the outer external surface and the internal porous surface (Figure(1.3)) [8].

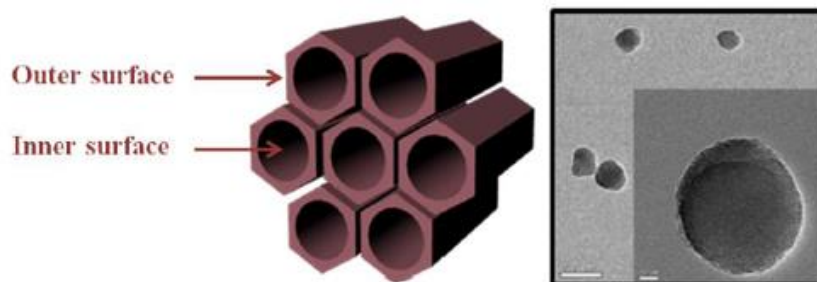
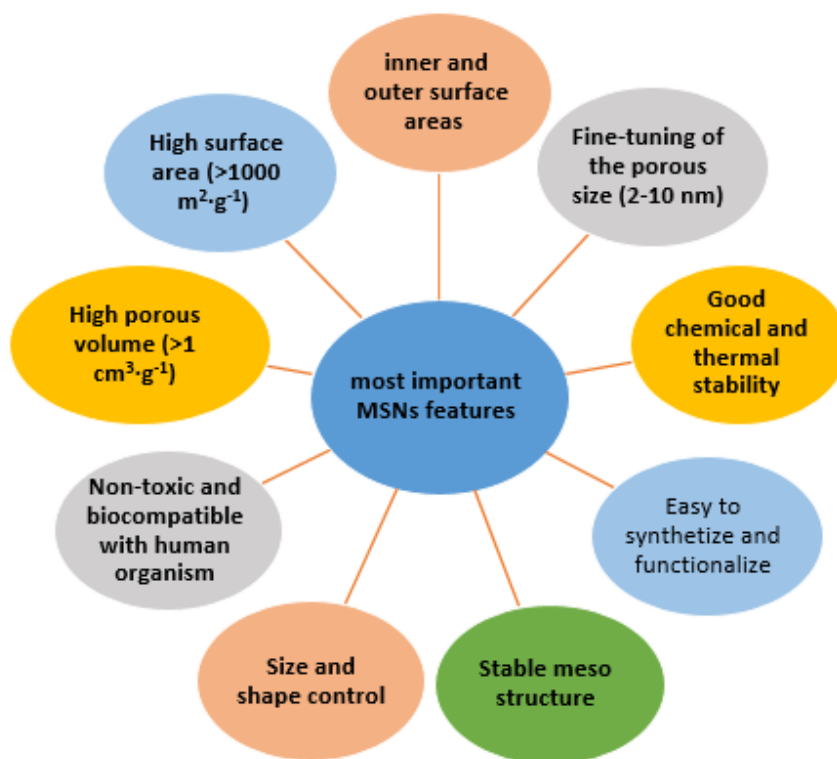


Figure (1.3): Representation of MSNs channels and TEM micrograph

1.4 MSNs features

Some of the most important MSNs features are explained in scheme (1.2)[24].



Scheme (1.2): important MSNs features(Reproduced).

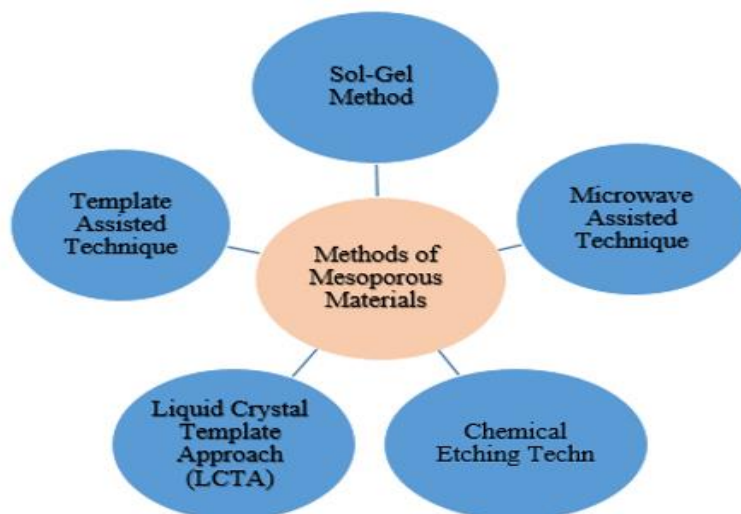
1.5 M41S family

The Family of M41S includes three different types of mesoporous called MCM-50, MCM-48, and MCM-41. Silicon and Directing agent are commonly used in the synthesizing these materials. The differences between these materials are determined by the agent and silicon ratio. According to Vartuli and colleagues[25] , MCM-50 is

generated when the ratio is between 1.2:2, MCM-48 when the ratio is 1:15 and MCM-40 when the ratio is less than 1. Silica and directing agent play important role in the production of materials from the M41S family. The template serves as a director for the chemical during the synthesis. Surfactants are chemicals with chain of carbon atoms that have hydrophilic in one end and hydrophobic end in the other end. Cetyltrimethylammonium bromide (CTAB) is regarded as the famous surfactant that used for synthesizing mesoporous materials. However, other substances, that have the same properties of CTAB, are used instead [26, 27].

1.6 Methods of synthesizing mesoporous materials

Different techniques were utilized to produce mesoporous materials such as process of sol gel, template assisted, microwave assisted and chemical etching techniques as illustrated in scheme (1.3) [28].



Scheme (1.3): Methods of synthesizing mesoporous materials (Reproduced)

1.6.1. Sol-gel process

The process of sol-gel is a method applied in materials science and ceramic engineering that includes wet chemicals. This method can be named also the chemical solution deposition method. This method is stated by producing a formation a mixture called sol which forms inorganic structure. Next step, sol is converted into a gel, leading to the formation of continuous liquid framework. The starting materials used in to form

these collides generally includes a metalloid or metal component surrounded by various reactive ligands. The original substance is transformed into oxide that can easily mix with water or weak acid and create gel. When the fluid is taken out of the sol, it is called a gel. The change forms liquid to gel determined the shape and size of particles. When the gel is calcinated, it changes to the oxide. Chemical reaction in the sol-gel system involved hydrolysis followed by the synthesis of metal alkoxides. The results in the formation of different type of oxides with different stoichiometry[29, 30].

Recently, this method is widely used to product of mesoporous substances with varying shapes. When synthesizing porous materials using the sol-gel method, different templates can be used such as small organic molecules, copolymers and cationic surfactants[31].

1.6.2. Template assisted technique

This method is a popular affordable method to synthesize ordered mesoporous materials. In this process, template is used to make mesoporous materials. There are two main routes to apply this method: hard matter templates (exotemplate) Fig. (1.4), which use solid template, which replaced the surfactants by porous solid or by using soft matter (endotemplate), In endotemplate, ordered mesoporous materials are created using agent to activate the surface which called a surface active agent. The vacant area constituting the exotemplate framework is packed with an inorganic material undergoes alteration under suitable conditions. When the filled exotemplate is removed, it replicated the pore system of the template as a negative image. This means that a substance with large surface will obtain [32].

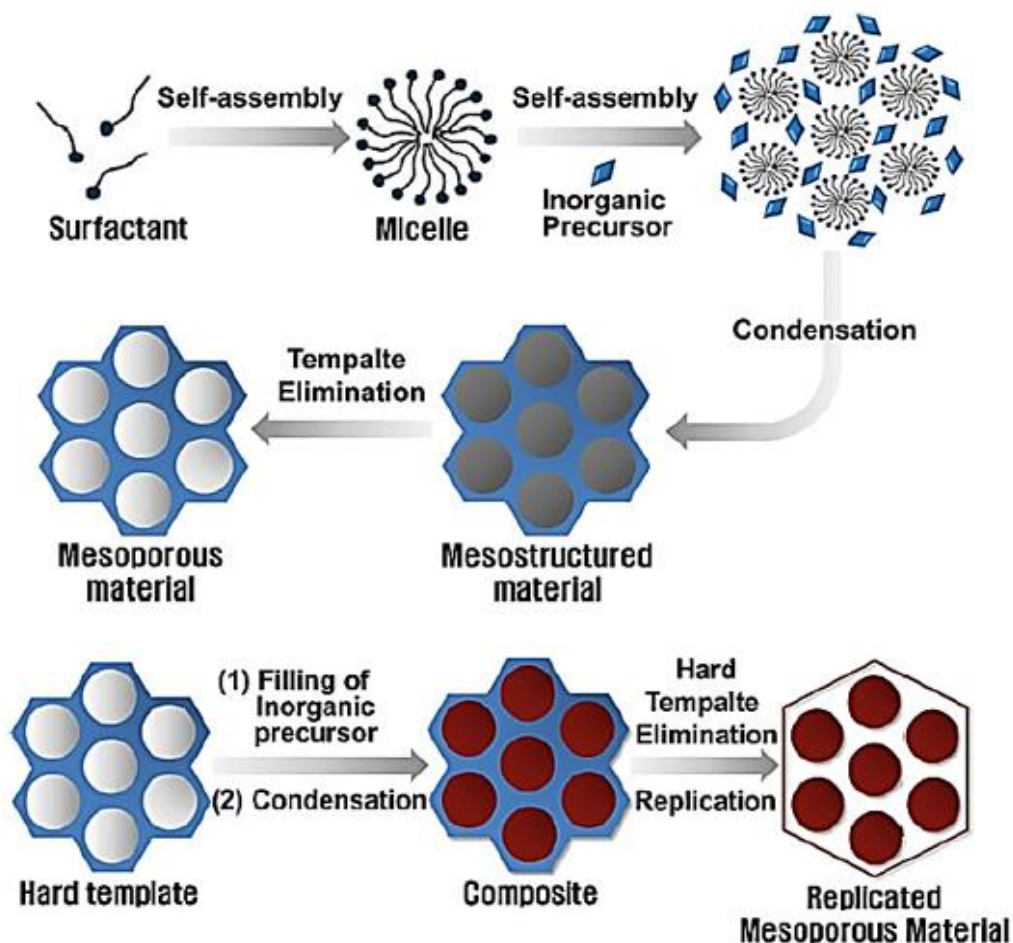


Figure (1.4):Soft template method(endoplate)and hard template method (exotemplate)

[28]

1.6.3. Liquid crystal template approach (LCTA)

This technique involves using of special template called surfactant instead of using solid template to create the shape of silica material, for that it can be under the type of soft matter template technique [33].

This technique is first used in 1991 to synthesis of MCM-41(Fig.(1.5)) and there were two methods explained to obtain the mesoporous materials.Firstly, a substance called surfactant creates hexagonal structure before adding the silica materials. Secondly, the silica framework is precipitated by surrounding the template, which leads to formation of mesoporous structure. The surfactant is removed throughout calcination and mesoporous structure is produced [28, 34].

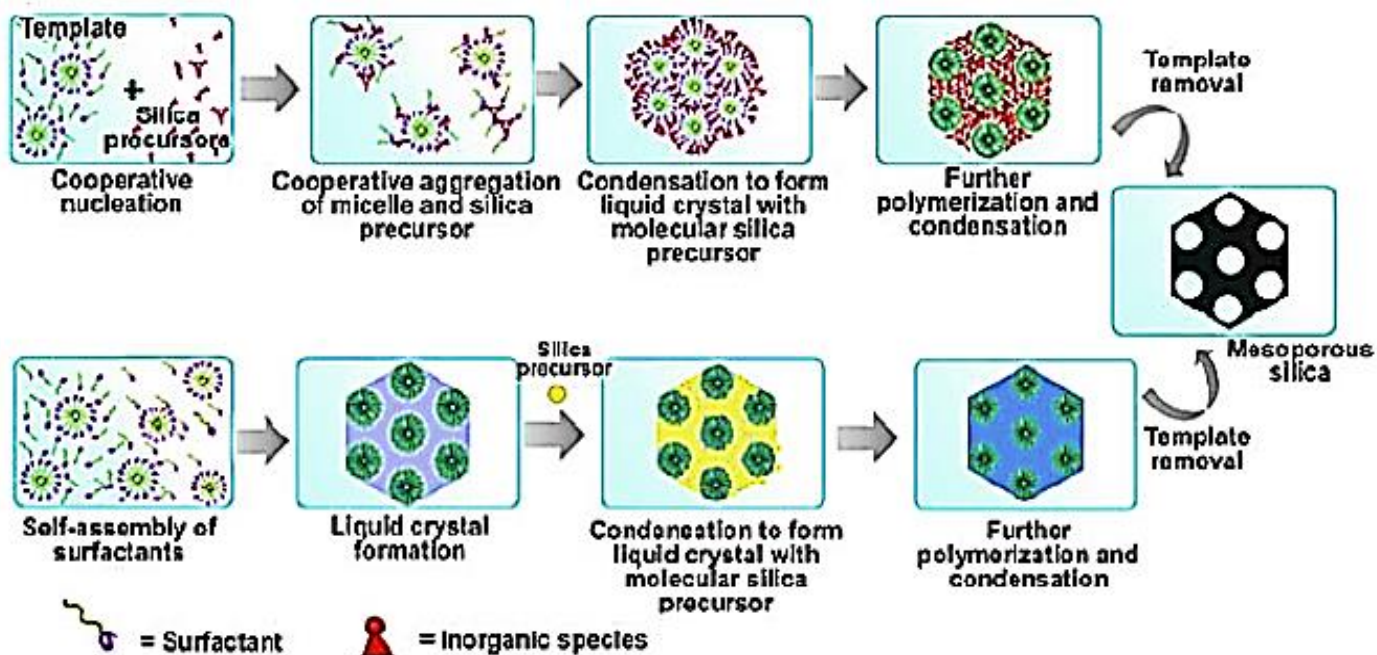


Figure (1.5): Proposed procedures for synthesizing MCM-41 [35]

1.6.4. Microwave assisted technique

This method has been applied for synthesizing mesoporous structure. It has been reported that MCM-41 can be made by using microwave and a substance called cetyltrimethylammonium bromide (CTAB) as template. Scientist discovered that by using microwave to heat the substance, they can synthesize highly ordered mesoporous materials due to the ability of microwave to heat up a small area very strongly. That may be due the possibility of microwave to make the container hotter than what the thermometer measures [36, 37].

1.6.5. Chemical etching technique

This method involved formation of mesoporous materials depending on the difference between the core and surface layer of silica core / mesoporous silica structure to create empty hollows which can be a carrier for high loading capacity. This method can be applied to produce various hollow nanoparticles having nanostructures like Fe_2O_3 , Fe_3O_4

and Au nanoparticles represented as a core and mesoporous silica represented as a shell[38].

Typically, in the presence of chemical etching, a homogenous templating method called “selective etching based on structural differences” is used to create a porous structure and generate core / shell structure. By selecting the suitable etching agent the interior of an object can be etched without significantly affecting its exterior. This generates hollow structure like in Fig. (1.6).

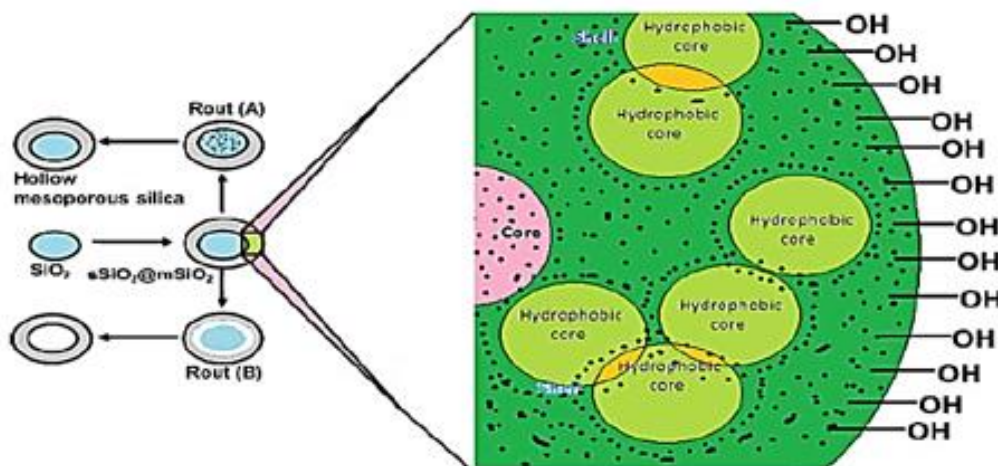
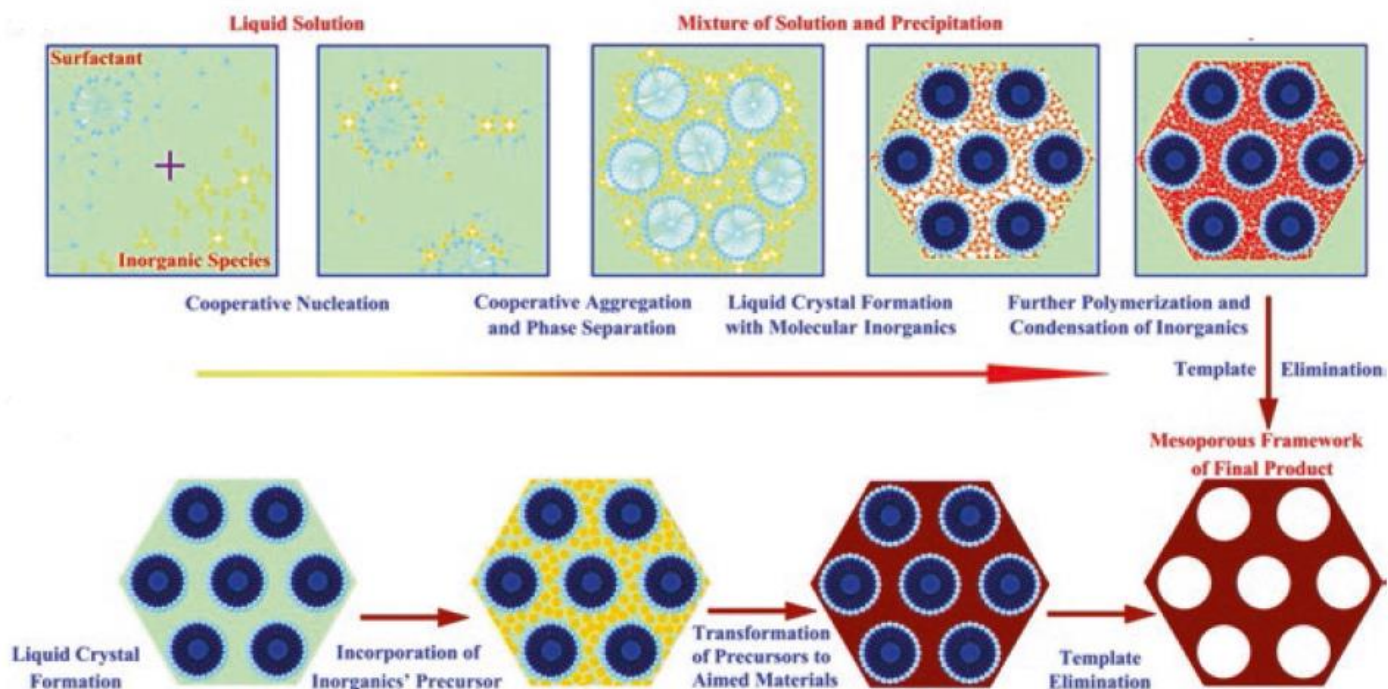


Figure (1.6): Chemical etching process[28]

1.7 Mechanism for mesoporous materials

Template is often needed to produce well defined mesoporous materials. Soft and hard template methods are regarded as the famous techniques to obtain mesoporous materials (Fig.(1.7)) [8, 39].

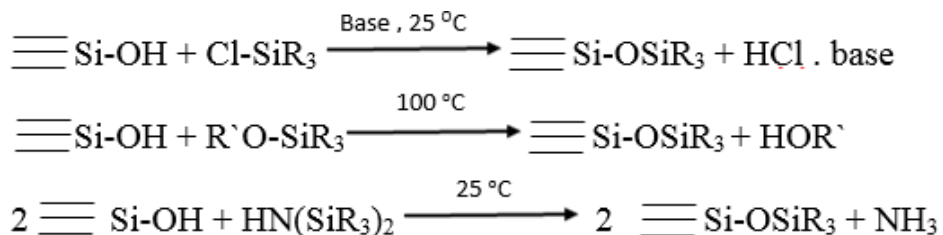


Figure(1.7) : Mechanism for mesoporous materials synthesis [40]

1.8 Functionalization

A lot of research has been made on the performance of mesoporous materials to improve their application by functionalized with various group. Modifying the outer layer of mesoporous is very interesting because it can make the surface basic or acidic [41, 42], binding to biomolecules selectively[43], production of photocatalytic activity[44], altering the optical properties[45], modulation of in vivo bio distribution [46] and modified surface hydrophobicity [47].Two main methods are used to alter the mesoporous materials: direct method (also called co-condensation method) and post synthesis method (also known as grafting method) [48].Functionalization procedure throughout the synthesis involves the corporation of a coating agent into the surface groups of a porous materials, producing liquid medium free of water [49].Various agents can be used to modify the surface such as disilazanes[50], trialkoxysilanes[49] and chlorosilanes [51].The grafting method results in reduction of amount and size of pores. Additionally, there are not many silanol groups available, further that only a small

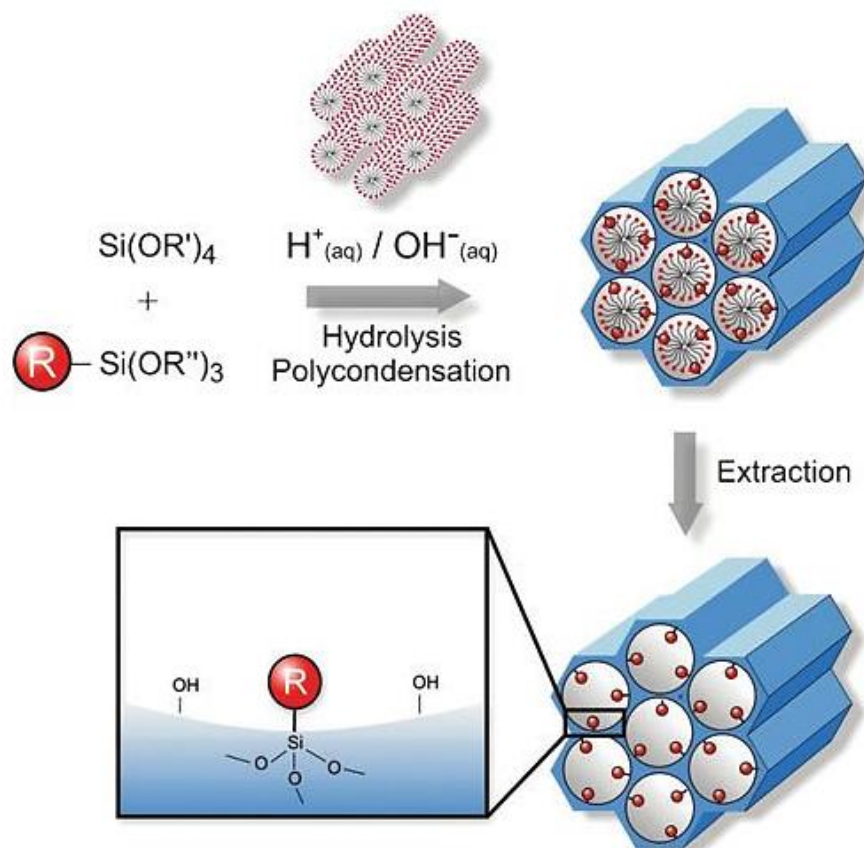
Surface modification with organic groups through grafting are typically conducted using silylation, which is achieved through one of the three methods below.



Silylation takes place on silanol ($=\text{Si}(\text{OH})_2$) and unbound ($\equiv \text{Si-OH}$) groups, but silanol groups connected by hydrogen bonds are more difficult to modify due to their formation of hydrophilic networks with each other[62].The inherent structure of the mesoporous support remains intact following the process of grafting.It is well-established that mesoporous silicates possess two distinct surfaces, namely the interior surface within the mesopores and the exterior surface. In the aforementioned grafting procedure, the external surface is more easily accessible and undergoes functionalization to a greater extent than the internal surface within the mesoporous. The functional group on the outer surface is also more reachable in following responses, resulting in decreased selectivity in operations that gain advantages from pore restriction.To reduce the involvement of the outer surface in the reaction and to enhance the selectivity, it is possible to deactivate these surfaces first, prior to functionalizing the internal silanol units.Managed double functionalization has been accomplished by two distinct site-specific grafting techniques (Fig.(1.8)) [61].

1.8.2. Co-condensation methods

The co-condensation method(fig.(1.9)) is different technique to change the surface properties of porous silicates using process called sol-gel, which involved functionalization between trialkoxysilanes and one or more organoalhoxysilanes that have Si-C bonds [61].



Figure(1.9) : Functionalization of mesoporous silicates by Co-condensation method silicates [61].

In contrast to the post-grafting technique, where the arrangement of functional groups frequently become inhomogeneous, co-condensation ensures a homogeneous distribution of organic groups throughout the entire inner pore surfaces, without any issues of pore-blockage or shrinkage reported. Despite the fact that large organoalkoxysilane precursors frequently disturb the initial textural characteristics of the systems, several novel techniques have been devised to effectively to decorate the surface wall while keeping the mesoporous structure [63, 64]. Another advantage of co-condensation method over the past synthesis method (grafting method) is the ability to regulate the particle shape of the mesoporous silicate [65] which is intimately connected to the biomineralization process observed in nature, such as the intricate shapes of diatoms [66].

1.9 Functionalization of MCM-41 with organic amine

The basic properties of MCM-41 can be improved by adding groups that have basic property to silica framework. Microporous and mesoporous materials, involved solid base catalysis, have been understudied compared to acid catalysis. Organic functional groups being immobilized on the internal surface of porous silicate regarded as conventional procedure to develop different catalytic system by obtaining special kinds of surface with molecular sieves. The specific properties of these nano composites, such as mechanical properties, thermal, surface hydrophobicity and hydrothermal, are determined by the nature and content of the organic group. The consistency of the organic group interior the pore channel influences the surface properties and make it reactive and available for further modifications. One way to achieve the basicity in silica-MCM-41 molecular sieve is to disperse them with alkali metal oxide[67].

However, this method can damage the structure of the molecular sieve due to the high pH used in the impregnation process and to overcome this problem, the MCM-41 surface modified with organic compound especially amines using the implementation method. This method involved removing the cationic surfactant present in the pore by calcination process before functionalization [68]. Aminopropyltriethoxysilan organic amine (APTES) impregnation method often results in an effective surface coating (inhomogeneous) due to the agglomeration of the introduced particles along with the interior site of the mesoporous and on the surface. This is because the APTES molecules are likely to interact with the silanol groups on the surface of the mesoporous pore than with that inside the pore. In co-condensation process, on the other hand, results in more homogenous distribution of organic moieties throughout the mesoporous pore. MCM-41 samples modified by APTES gave enhanced catalytic activity towards different catalyzed bases organic reaction such as Henry reaction, Michael and Knoevenagel condensations and many other reactions [63].

1.10 Applications of mesoporous silica

Table (1.1): Applications of mesoporous silica.

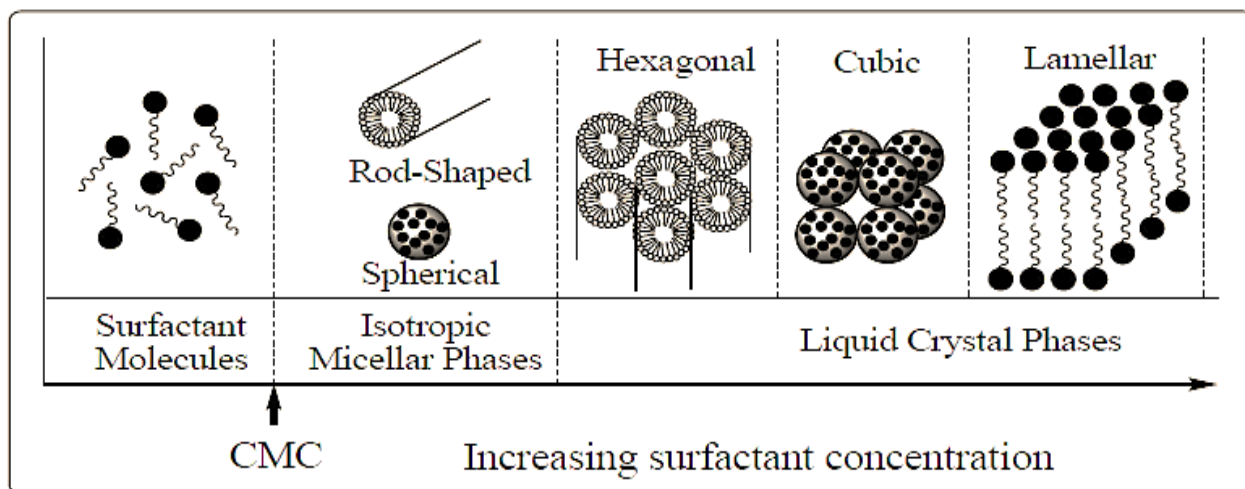
Field	Type	Applications	Ref.
Adsorption	Adsorption of Biomolecules	Amino acid, vitamins, biochemical, DNA and protein separations	[35, 69]
	Ions removal	Co ²⁺ , As ²⁺ , Cu ²⁺ , Ni ²⁺ , Li ²⁺ , Fe ³⁺ , Fe ²⁺ , Cr ³⁺ , F ⁻ , As ⁺ , SO ₄ ²⁻ , Mo ⁶⁺ , SeO ₄ ²⁻ , CrO ₄ ²⁻ , ReO ₄ ²⁻ and water purification	[70, 71]
	Adsorption of gas	CO ₂ and H ₂ gas adsorption and storage	[72, 73]
	Adsorption of pollutant	Microcystins, chloroacetic acid (mono-, di and tri), naphthalene and toluene.	[74, 75]
	Adsorption and desorption	Dyes, DNA, 5-C-phosphate-G-3, and drugs in the cell of human.	[76, 77]
Catalysis	Oxidation – Reduction	Oxidation process such as (Glucose to gluconic acid, cyclohexene to adipic acid and olefin). Reduction process such as (nitro compounds, carbonyl groups, allylic) , amination, combustion of methan and hydrosilylation.	[35, 78]
	Acid – base	Production of biofuel , esterification, preparation of Xanthene, base catalyzed Knoevenagel condensation and Friedel- craft benzylation	[79, 80]
	Named reaction	Mannich reaction, C-C and C-S cross coupling and Biginelli condensation reaction.	[81, 82]
Optics	Optical	UV and chemo sensors .	[83, 84]
Sensing	Ion sensing	Electro-chemical and optical sensing such as NH ₂ , Sb ³⁺ , Fe ³⁺ , Cr ³⁺ , Bi ³⁺ , Cu ²⁺ , C ₆ H ₅ O ₇ ³⁻ , RCOO ⁻ and others	[85, 86]
	Bio sensing	Detection and sensing of protein , glucose and others	[87, 88]
	pH sensing	pH sensor for special medium	[89]
	Monitoring of humidity	Relative humidity	[90, 91]
	Gas sensing	Nitroenergetic compounds, NO ₂ , O ₂ , P-cresol, 1.3.5- trinitro, 2.4.6- trinitrotoluene and p-nitrophenol	[92, 93]

1.11 Surfactants[94]

Surfactants are molecules that tend to adsorb on the surface and interface. They have two chemical components, part of the molecule is hydrophobic and the other is hydrophilic. This amphiphilic property for surfactant will reduce the free energy when adsorbed on the surface. Fundamentally, there are three forms of surfactant; some are dissolved in water as a single molecule while others are found at the boundary between water and air. Some can also be found at the boundary between water and a solid surface. Once the saturation of all interfacing, the complete surfactant remaining within the water is on the shape of cluster called micelles. When the primary micelles shaped, that are called Critical Micelles Concentration (CMC). The CMC influenced is by the chemical structure of each compound. Generally, longer in the hydrophobic tail leads to lower the CMC, this may be due to the tendency of hydrocarbon tail to join together, resulting in lower energy and more stable system.

1.12 Chemistry of surfactant/silicate solutions

The structured mesoporous materials Fig. (1.10) is influenced by the unique and reactive nature of surfactant molecules. As the amount of the surfactant increased, their shape and arrangement change[94].



Figure(1.10): Sequences phase of surfactant /water system[94]

Typically, the surfactant at lower concentration act as monomolecules , but in the presence of higher surfactant concentration, molecules aggregate together to form micelles, in a point called critical micelles concentration (CMC), reducing the entropy of the system [95, 96].The micelle`s core, primarily composed of liquid hydrocarbon, has more freedom for movement leading to increase in entropy. The capacity of surfactant to reduce surface or interfacial tension is believed to be directly related to the critical micelles concentration. Hexagonal structures start to form with progressing in the concentration process which leads finally to the creation of hexagonal phases[97].The next step involves aggregation of adjusting parallel cylinder and generate the layered structure .Sometimes, the cubic phase may appear before the lamellar phase[98].

The manner in which the surfactant solution transforms depends on how concentrated it and the characteristics of the surfactant, includes the size of the carbon chain that repels water, the head group that attracts water, and the counter ion in the case of surfactants with an electrical charge. Furthermore, it is influenced by environmental factors such as ionic strength, temperature, acidity or alkalinity, the type of solvent used, and other substances added to the solution, such as organic compounds.It`s very important to note that generating of cylindrical micelles and hexagonal phases increased with increasing in the amount of surfactant and alkalinity and decreasing in temperature and the level of silicate polymerization [99, 100].

1.13 Structural characterization of the M41S mesoporous materials

Mesoporous materials are analyzed in different physicochemical investigations, such as UV-Visible, FTIR, TEM, SEM, XRD, TGA, EDX and N₂ adsorption – desorption. The images of SEM and TEM provides information regarding both the morphology of mesoporous array and the dispersion pattern of the functionalization agent on the surface. Chang in the crystal structure can be observed through XRD analysis during the synthetic condition[101]. The information provided from N₂ adsorption –

desorption helps to understand the texture of materials such as the size of its pore, the volume and surface area which is typically determined using BET models [102].

1.14 Rice husk (RH)

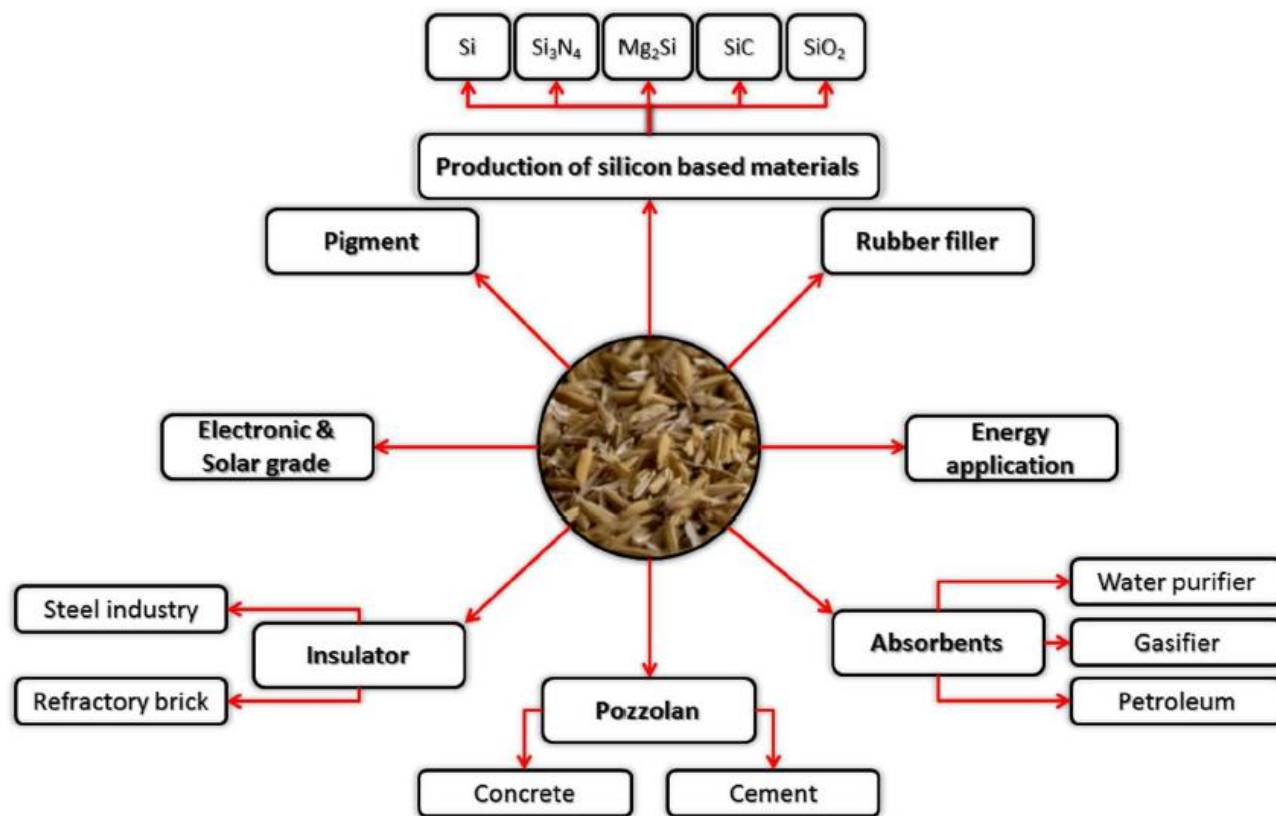
Rice husk (RH) is an agricultural leftover readily accessible: in fact, it constitutes one-fifth of the yearly global rice harvest. The annual worldwide paddy production has been approximated at 510 million tons for 2018, which means over 150 million tons of RH production, according to the information published by Food and Agriculture Organization (FAO) of the United Nations in Rice Market Monitor[103, 104] ,Although RH has already been utilized in various areas (specifically, as organic fertilizer, as material for animal farming, as absorbent and construction material, or pest control agent[105], it is still commonly viewed as a useless by-product of rice milling and thus frequently incinerated in the open air or discarded on unproductive land. Moreover, it is widely recognized that RH can also be utilized as a sustainable fuel in co-generating facilities, taking into account its elevated heating value (4012 Kcal/kg)[106]. In fact, when burned, approximately 20-25% by weight of rice husk ash (RHA) is generated, which consists of over 90% silica and small amounts of other metal oxides [107, 108].

Among the different biomasses, with plentiful and sustainable energy sources, rice husk is not just a promising energy source, but also a valuable byproduct [109]. In recent years, there have been numerous factors linked to rice husk not being utilized efficiently, such as (1) farmers and industry personnel lacking awareness of its potential, (2) socio-economic issues, (3) technology implementation,(4) insufficient attention to environmental matters, and so on. The solution for this problem related to the use of this solid waste must be tackled in terms of both quality and quantity. In recent year, the main attention focused on using rice husk to reduce the cost of industrial processing. However, the tough outer layer of rice husk, high contents of silica, low density and the ability to resist the bacterial decomposition, make it serious pollution problem that can harm the environment and human [110]. Because of this, many complaint and concern have been recorded; furthermore, rice husks burning can cause cancer and bio accumulative

consequences. Moreover, a large amount of greenhouse can be released throughout using RH for production of electricity [111]. Rice husks made up of organic compounds and about 20% inorganic components. The main elements in rice husk includes Nitrogen (11.06%), (37.07%) carbon, (9.01%) silicon, (8.80%) hydrogen and (35.03%) oxygen. In addition to that, rice husk contains (34.4%) cellulose in its composition, (18.85%) ash, (19.2%) lignin and (24.3%) hemicellulose and (3.25%) other substances. Rice husks consist of organic compounds and 20% of inorganic matter [112].

1.15 Application of rice husk

Pakistan, India, Sri Lanka, Bangladesh, Australia, Indonesia, Thailand and USA were the first countries to use the rice husks between 1970-1985. This initiative was supported by the governments and other organizations. Rice husks are considered valuable material in comparison to the other field residue due to the high amount of silica (87-79%), high porosity and a large surface area. Schematic diagram of applications of derived rice husk Scheme(1.4) [113].



Scheme (1.4): Schematic diagram of applications of derived rice husk.

1.16 Adsorbent

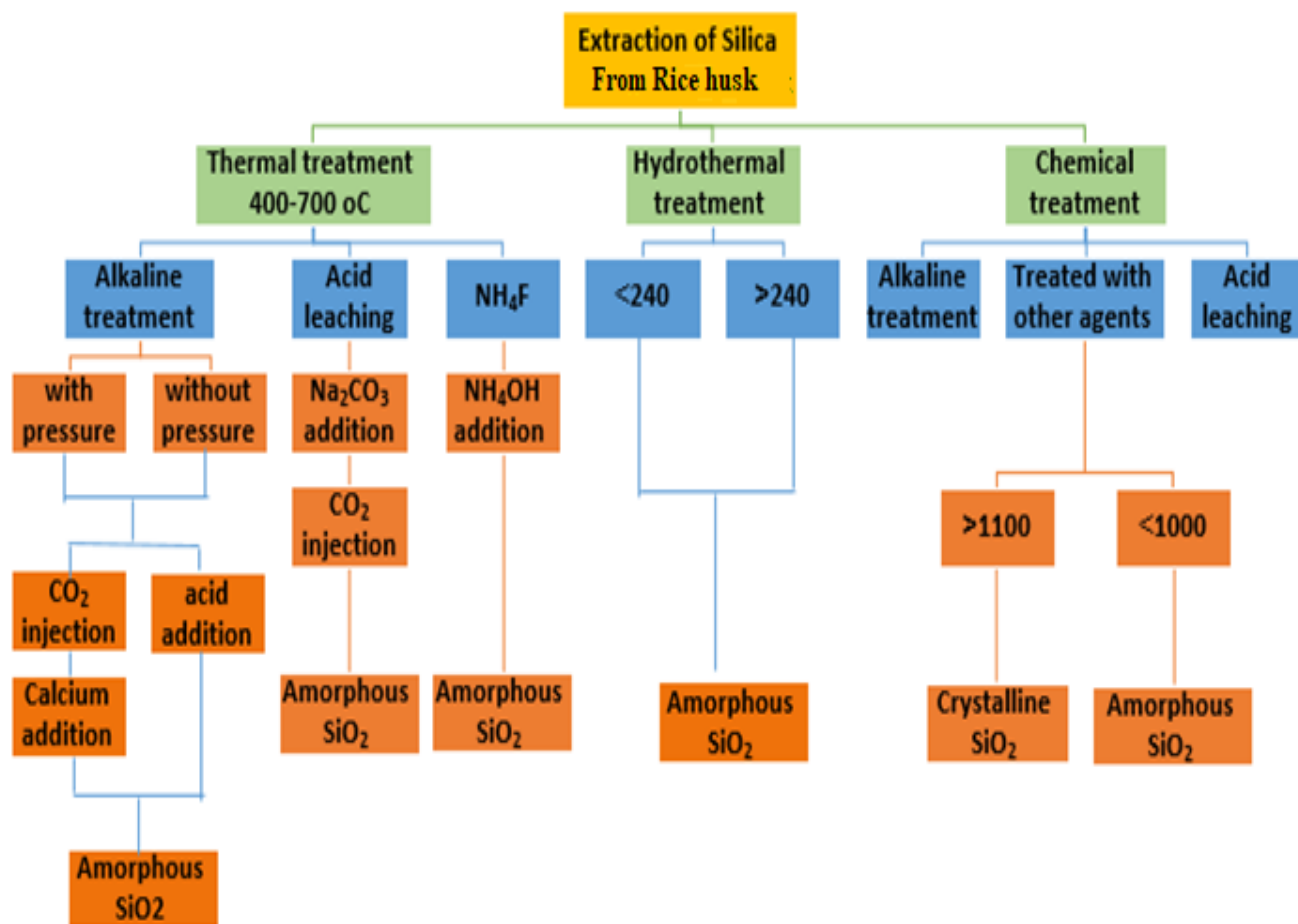
Serious problems due to the presence of heavy metal in aqueous system were observed and this problem causing many diseases such as hair loss, chronic, liver cirrhosis, cancer and renal failure. In addition to the toxicity and stability of heavy metals, it has the tendency to accumulate in environment. In the previous period, removal of heavy metal by using activated carbon as adsorbent has been limited because of the high cost and low efficacy in regeneration of activated carbon after exhausted, for that, the approach was to use alternative low cost process such as rice husk ash, lignite, wood, bagasse fly ash and peat as adsorbents to treat the effluents. The rice husk has been focused on being cheap and includes high percentage of silica[114, 115].

1.17 Properties of rice husk and rice husk ash

In general, rice husk has a granular composition which is insoluble in water with high mechanical strength and chemical stability, for that, it is regarded as a better absorbance in treatments process of wastes from water. (RHA) has high content of MgO, H₂O, Al₂O₃, SiO₂, Fe₂O₃, CaO, K₂O and Na₂O. RHA has fluctuating chemical composition, which changes related to the variety of paddy, fertilizer, soil chemistry, proportion of irrigated area, and geographical conditions [116, 117].

1.18 Silica

Silica (SiO₂) regarded as fundamental materials for many technological applications due to its unique properties such as thixotropic, filler composite compounds and thermal insulator [118]. Silica has become of great importance in many industries including cosmetic, cement, glass, medicine, purging margarine and pharmaceutical sector [119–121]. In addition to that, silica serves as precursor to produce various organic and inorganic materials which can be used as catalyst and also utilized in optical and electronic coating materials [122]. Rice (*Oryza sativa*) is a plant that contains high quantity of silica [123] for that, this plant is regarded as important cheap source for amorphous silica [124]. The importance of silica lie in its amorphous form in contrast of crystalline form, which is inactive and cannot be subjected in chemical reactions [125]. The starting ingredient to produce silica materials is sodium silicate that is usually obtained from melting quartz rock in presence of sodium carbonate at a temperature of 1300°C. However, this process has taken up long time and cost-effective [126]. One of noteworthy applications of amorphous silica is synthesis of mesoporous silica compounds [127, 128]. Method of extraction of silica from SiO₂ illustrated in Scheme (1.5) and the summary of some studies involved adsorption capacities of heavy metal using rice husk (RH) as adsorbent in Table (1.2).



Scheme (1.5): Method of extraction of silica from SiO₂[129].

Table(1.2): Summary of some studies involved adsorption capacities of heavy metal using rice husk (RH) as adsorbent.

Type of adsorbent	Metal	Capacity of adsorption (mg/g)	Ref.
Activated RH	Arsenic (II)	1.220	[130]
RH	Cadmium (II)	4.000	[131]
RH	Cadmium (II)	8.820	[132]
RH	Cadmium (II)	16.700	[133]
Activated RH	Cadmium (II)	45.600	[134]
RH treated with HNO ₃	Cadmium (II)	11.300	[132]
RH	Zinc (II)	0.750	[135]
RH	Zinc (II)	29.690	[136]

RH	Zinc (II)	19.617	[137]
RH	Copper (II)	0.200	[138]
RH	Copper (II)	29.000	[139]
RH treated with HNO ₃	Copper (II)	9.360	[140]
RH activated	Copper (II)	112.43	[141]
RH with tartaric acid	Copper (II)	29.000	[139]
RH	Mercury (II)	66.660	[142]
RH	Nickel (II)	8.860	[143]
RH	Nickel (II)	5.520	[143]
RH	Lead (II)	11.40	[144]
RH	Lead (II)	5.690	[145]
RH with tartaric acid	Lead (II)	10.8	[139]

1.19 Pollution

Pollution of water can be caused by different types of pollutants. These pollutants can be divided into various groups such as radioactive isotopes, natural pollutants and inorganic fertilizers. Natural pollutants can be decomposed by organisms unlike the heavy metals which cannot [146, 147].

Heavy metals can cause serious problems for the environment especially when found in surface water or groundwater. Generally, heavy metals are well-known pollutants that are present in many kinds of waste materials such as electronics, dyes, mining processes, chemicals, pharmaceuticals and many others. Because heavy metals are environmentally difficult to decompose, it's important to remove them from the polluted stream to meet increasingly stringent standards for environmental quality. The elimination of heavy metals can be accomplished through various methods. Conventional methods involved adsorption, precipitation, coagulation, membrane processes, ion exchange, extraction, electrochemical processes and others. Among these methods, adsorption is currently regarded as more appropriate for the treatment of wastewater due to its effectiveness and simplicity. Some commonly utilized adsorbents for heavy metal adsorption include zeolites [146, 148], biomaterials [149], activated carbon [150], and clay materials [151] which are characterized by the porosity of these adsorbents. Since

industrial wastewater is the primary source of heavy metal contamination in water, it is crucial to remove these pollutants before releasing wastewater into the environment in order to protect public health and manage pollution. Heavy metal has recently removed from polluted solution using a various technique, including evaporation, chemical treatments, coagulation and flocculation, ion exchange, regeneration, membrane separation, flotation and biological purification[152–154]. Adsorption technique, in addition to ion exchange, received a lot of interest to remove heavy metal in low concentration as its low-cost, simple and effective methods[155, 156]. These two methods have been applied to a wide range of media for removing cobalt ion and other heavy metal, including coal dust [157] coir pith [158] Black carrot residue [159] Lemon peel [160] sunflower shell[161] Wood ash [162] *Trichoderma reesei* [163] Cashew nut shell [164] *Spirulina platensis*[165] Chitosan, sugar beet factory line, egg and humate potassium [166] Rice shell, wheat shell, oil palm leaf powder, sawdust, lentil shell, rubber tree leaf and modified polyethylenimine[167], Adsorption on the surface of porous adsorbents like mesoporous is an ecologically friendly method for removing organic and inorganic contaminants, including heavy metal from polluted water and wastewater[168, 169].

Progressing in the field of materials science has taken significant interest in the synthesizing of new adsorbents which are effective in water treatments. The concept of combining two or more substances into bigger one has demonstrated to be an exceeding effective approach in materials science to produce new materials with new effective properties. This specific focus has been driven to discovery of various adsorbents, including mesoporous silica adsorbents [170, 171]. Ordered mesoporous silica (OMS) is producing an expanding interest in the chemistry of water treatment because of distinctive characterization. This characteristic includes chemical inertness, cost-effective production costs, expansive pore size, abundant collection of surface utilitarian functional groups that are tailored for exceptional selectivity towards specific pollutants, high specific surface area and good thermal stability[70, 172].

1.20 Cobalt

Cobalt is a crucial trace element for living things because it's one of the components of cyanocobalamin and vitamin B12 [173]. Cobalt contamination of water can lead to serious problem due to the toxic nature and adverse effect of cobalt on human health, including asthma, heart failure, liver damage, mutation in living cell, thyroid damage and allergies. In addition to that, exposure to cobalt radiation can lead to neurotoxic logical symptoms such as headaches as well as an increase risk of cancer, furthermore, ionizing radiation is also released by cobalt isotopes [174].

Pure cobalt is a bright, hard metal that is steely –grey in color odorless. The permissible range of cobalt in drinking water according to Environmental Protection Agency (EPA) is 0.0020 to 0.107 $\mu\text{g}/\text{mL}$. Conversely, the water used for farming has a cobalt content of 0.05 to 1.00 $\mu\text{g}/\text{mL}$, meaning that everyone is exposed to cobalt through food, drink and air [174].

1.21 Copper

Copper is one of the transition element that is metallic in nature. Its atomic weight is 29 and its atomic weight is $63.53 \text{ gm}\cdot\text{mol}^{-1}$ with $(1s^2 2s^2 2p^6 3s^2 3p^6 3d^{10} 4s^1)$ electronic configuration [175]. In crystalline metallic copper, like other metals, the single electron in the outer shell (4S) plays important role in for many of materials significant physical characteristics, like, chemical stability, electrical conductivity and reddish color, in general, the 4S electron dose not attach to any one atoms, instead, it joins the electron cloud that dominate the crystal lattice [176, 177]. Copper is used in many field, such as, feed additives containing to prevent illnesses and encourage growth in animal [178], electronic and engineering applications [179]. Copper is crucial trace elements that serve as variety of physiological purposes in living organisms. As a result, the handling of heavy metal pollution in the environment including copper contamination, has received special attention in recent years [180]. Excessive adsorption and consumption on this element can be harmful to health and can cause certain illnesses, as a result, it's important

to regulate the amount of this element in the environment. The reasons of this element presence in water sample are due to the extensive usage of copper in industrial and agriculture process. Because the largest amount of copper ion allowed in tap water is 1.3 mg L^{-1} , it's crucial to monitor the concentration in order to prevent the it from building up in liver and kidney[181].

1.22 Adsorption of metals on the surface of functionalized mesoporous

Heavy metals enter the water system through different industrial processes such as fertilization, purification and pesticides displays a critical threat to the environments [182]. Due to the high toxicity and high ability to accumulate heavy metal can be harmful for human and other life form of organism. Anyway, the trace amount of elements essential nutrients is required for human body, but consuming to much lead to adviser health effect like kidney failure, liver damage and irritation of the central nervous system[154, 183].

Thus, the elimination of excessive heavy metals from industrial wastewater prior to discharge is crucial concern for the safety of both human health and the environment. Numerous conventional methods have been employed to remove these positively charge ions from water system, including flotation, ion exchange, coagulation-flocculation, reverse osmosis, chemical precipitation and ultra-filtration. However, these approaches do have their limitations including limited effectiveness, the need for specialized conditions, and creation harmful sludge[184].As a results, there is a pressing requirements for more feasible and environmentally sustainable technology. Adsorption is currently recognized as one of the most efficient, cost-effective and discerning technique used for treatment and analysis of water[185].Activated carbon has been widely used to clean polluted water[186] due to its extremely large surface area, chemical stability and long lasting nature. However, its arbitrary ore structure limits the access of pollutant to the adsorption sites thereby, reducing the effectiveness of removal. Additionally, the cost of activated charcoal continues to rise [185]which promoted

numerous scientists to concentrate on creating more affordable by product. These byproducts of agriculture materials can adsorb metallic ions without any modifications. Nevertheless, chemical and physical alteration has been recently documented to enhance the adsorption capability[187]. Some of the analysts have utilized bacteria, fungi, algae and yeast to adsorb the heavy metals from water[188].

Another strategy involved the utilization of organic materials and by product for the development of innovate adsorbents. Neutral red mud[189], coal ashes[190], zeolites[191], clay and soil components [192]and chitosan [193] possess numerous benefits like being a boundary available and cost effective. Furthermore, they can undergo chemical modifications to enhance their binding ability. However, these sorbents show various disadvantages due to the limitation in adsorption capacity, heterogeneous composition, irregular distribution of pore size and limited selectivity for materials. Consequently, it's vital to make a novel sorbent that fulfills the specific criteria, such as

- 1- Produce fast kinetics by designed optimized pore size and geometry.
- 2- Improvement of adsorption capability by modifying the surface properties and making the adsorption site more accessible.
- 3- Selectivity of specific materials can be improved in presence of other ions like Na^+ and Ca^{2+} .
- 4- Take in the consideration the cost of the equipment used to determine the effectiveness of adsorbents.
- 5- Long term stability of materials during sorption process and ability to recover its capacity.

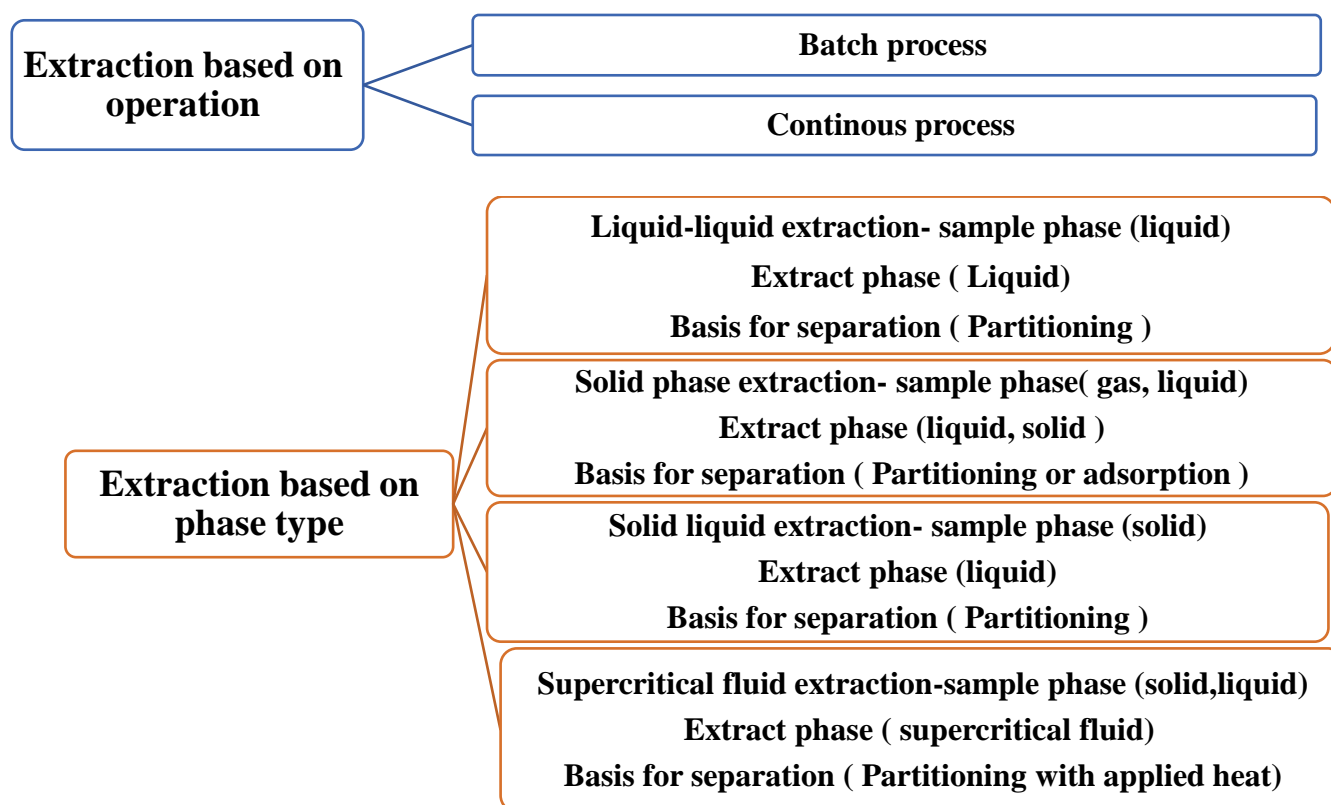
Mesoporous silica like SBA-15, HMS, MCM-41 and MCM -48 considers very excellent materials for these type of uses due to the large surface area, limited pore size, and controlled pore dimension [194] In addition to that , desired properties of materials can be enhanced by applying appropriate functional group to the surface[195].

1.23 Extraction

Extraction is a technique used to separate the desire analyte from gas, liquid and solid samples. Liquid–liquid extraction (LLE) and solid-phase extraction (SPE) were regarded as the conventional method used to extract the analyte since 1990s. The LLE extraction required large amount of solvent and time consuming to reach the equilibrium due to the mass transfer of analyte while SPE required lesser amount of solvent and faster than LLE, in addition to that this technique need skills about condition, cleaning, eluting and loading [196].

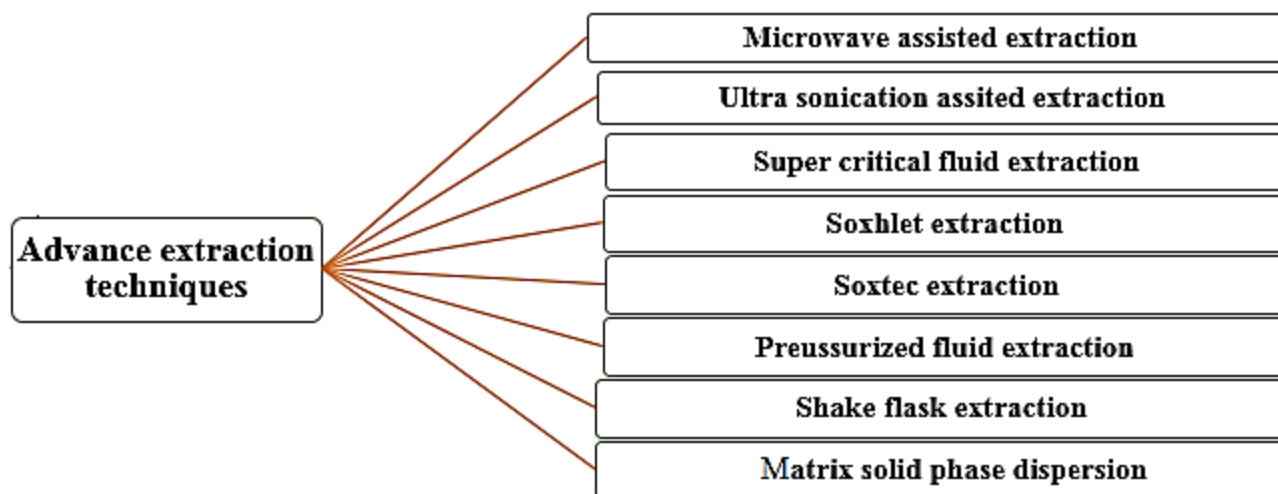
1.24 Classification of extraction

Generally, extraction can be divided into two categories, operation and phase type as in the schematic diagram (1.6) [197].



Scheme (1.6): Extraction based on phase type(Repreoduced)

Extraction processes were developed to overcome the consuming of time and the use of high amount of solvent by applying special type of extraction with different techniques as illustrated in schematic diagram (1.7) [196, 198].



Scheme (1.7): Advance extraction techniques(Repreoduced)

1.25 Solid phase extraction (SPE)

Starting in the 1950s, the primary experimental uses of SPE were for the analysis of organic residue in water sample. Many of articles in scholarly journals have been published in recent years explaining SPE as a water analytical technique and method for determining organic substances [199, 200].Solid phase extraction (SPE) was considered an effective method to extract the analyte. This method overcomes a gap being from sample collection in addition to that, in most cases there is no need for further preparation steps such as pH adjustment and dilution[196, 199].According to the miscellaneous properties of solid phase extraction method, different procedures and adsorbents can be used [201].

The analyte adsorbed on the surface of adsorbent by covalent bond. This bond formed due to the different interaction such as dipole – dipole and Van der Waals intermolecular force. Adsorption process includes uptaking the analyte from the adsorbent and then using suitable process to remove this analyte from the medium[202].SPE is a flexible method that utilizes flow- through equilibrium to purify, separate and concentrate the analyte from a sample solution of matrix. A variety of SPE extraction methods includes solid phase micro extraction (SPME), in tube SPME (IT-

SPME), cartridge, multi well SPE, disks and pipette tips SPE are developed with convenience of use and affordability in mind.

Generally, the most important parameter and its characterization of these type of SPE can be summarize in the Table (1.3) [127].

Table (1. 3): The most important parameter and its characterization of this type of SPE

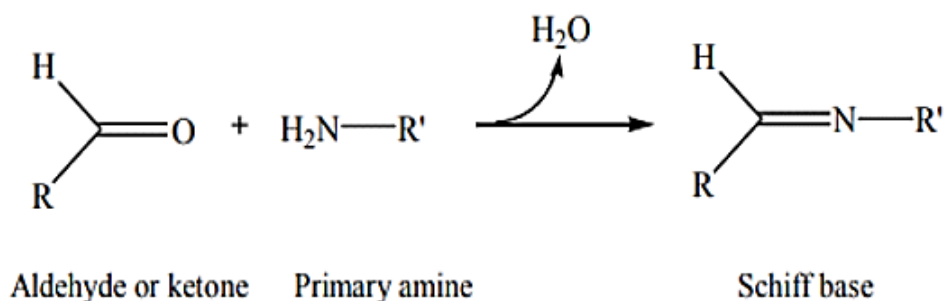
Parameter	Cartridge	PT-SPE Pipette-tips SPE	Disk	Multi well SPE	SPME solid-phase microextraction	IT SPME in-tube solid-phase microextraction
Weight of sorbent	4-30 mg	4-400 µg	4-200 mg	3-200 mg	-	-
Applicable volume	50-500 mL	0.5-1.0 mL	0.5-1.0 L	0.65-2.0 mL	-	-
Application	Wide variety of sample matrices	Biological samples	Substantial samples	Biological samples	Environmental and biomedical samples	Environmental and biomedical samples
Benefits	Easy to assemble in the laboratory, wide range of uses, low cost, Possibility of storage of analytes , enriched on solid sorbent	Simplicity and short extraction time, high sensitivity and recovery factors, a small quantity of elution volume, conditioning steps are not required, amenable to automation by available tools.	Operation with a smaller elution volume, Greater cross-section area, fast flow rate, smaller void time, ignored the filtration of the extract, slighter extraction period of substitutional samples	Rapid preparation of a large number of samples, less labor and time consuming, les solvent waste, fast flow rate, amenable to automation.	Green extraction, rapid extraction, miniaturized technique, low analysis cost, friendly eco.	miniaturized technique, large sample size, compatible with analytical instruments.
Limitation	Partially small cross section, sluggish flow rate, un available	Restricted flow rate and plugging , a large amount of plastic waste.	Decrease in break flow through volume, small samples will	Due to open bed configuration, the technique is not suitable	Low adsorption capacity, limited effectiveness.	A large amount of volume needed

	vented volume, plugging, channeling, costly with a large number of samples		be lost, Costly.	for volatile analytes.		
--	----------------------------------------------------------------------------	--	------------------	------------------------	--	--

1.26 Schiff base

The Schiff base reaction was discovered by German Chemist Hugo Schiff in 1864 which refers to the reaction between ketone or aldehyde with compound contains amino group producing imine group. Schiff base ligands are easily synthesized and form complexes with practically any metal ion. Furthermore, there complexes with metal ion had greater antibacterial activity than Schiff base ligand[203].

The bond generated by reacting with aldehyde is known as azomethine or aldimine, whereas, the bond generated by reacting with ketone known as imine or ketamine. Imine is regarded as a precursor for many reaction such as indoles[204], betalactam[205], pyrimidine derivative, Scheme(1.8)[206].



Where: R and R' are alkyl or alkyl substituents

Scheme(1.8): The Schiff base formation.

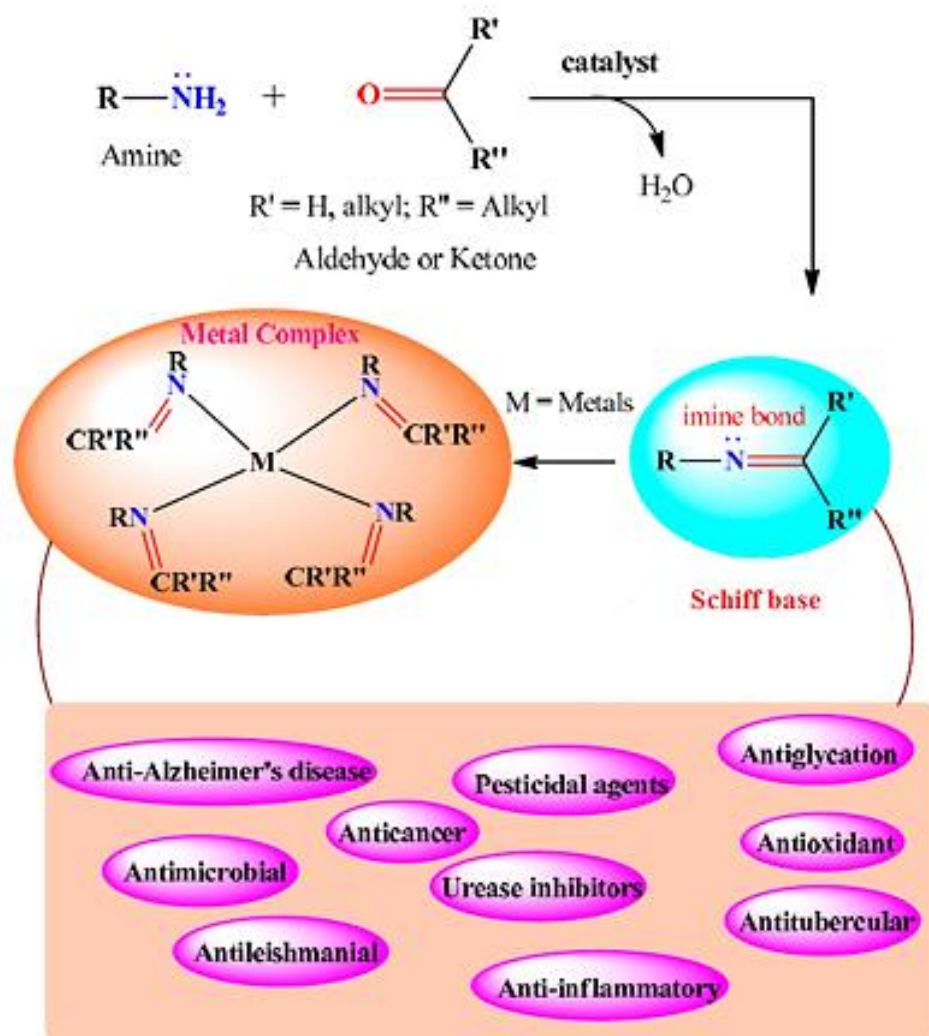
Schiff base ligand is interested family of ligand due to their many effective beneficial properties such as modification by adding donor groups. The numerous advantages of imine encourage the scientists in the field of catalysis, bioinorganic,

encapsulation, analytical chemistry, separation and transport science to synthesize metal complexes[207].

1.27 Application of Schiff base

Schiff base has many biological and analytical applications due to presence of ion pair electrons in sp^2 orbital belongs to nitrogen atom in azomethine group [208, 209].

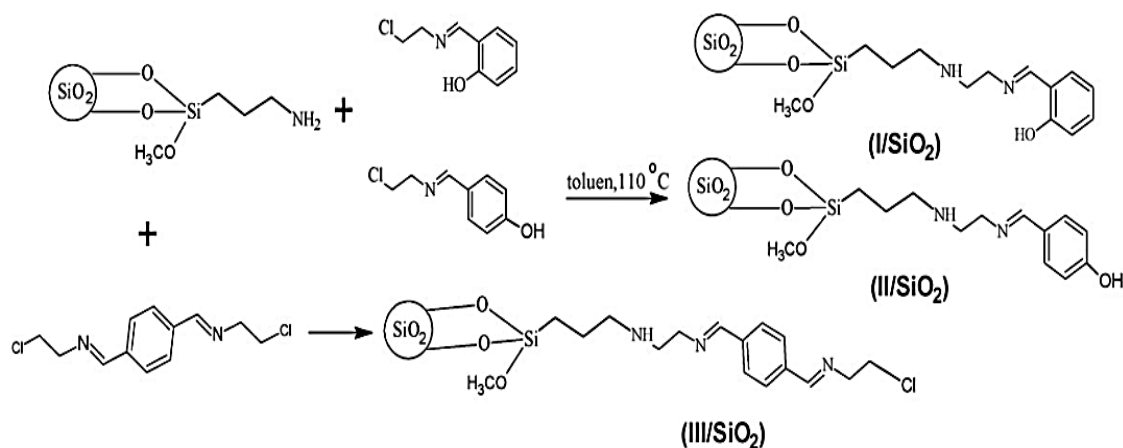
Schiff base is regarded as important agent used as antioxidant [210]. Schiff base which includes hydroxyl group in their structure can inhibit the negative effect of free radical from antioxidant [211]. Typical Schiff base, their metal complexes and bioactivities were shown in Scheme (1.9).



Scheme(1.9):Typical Schiff base, their metal complexes and bioactivities[212] .

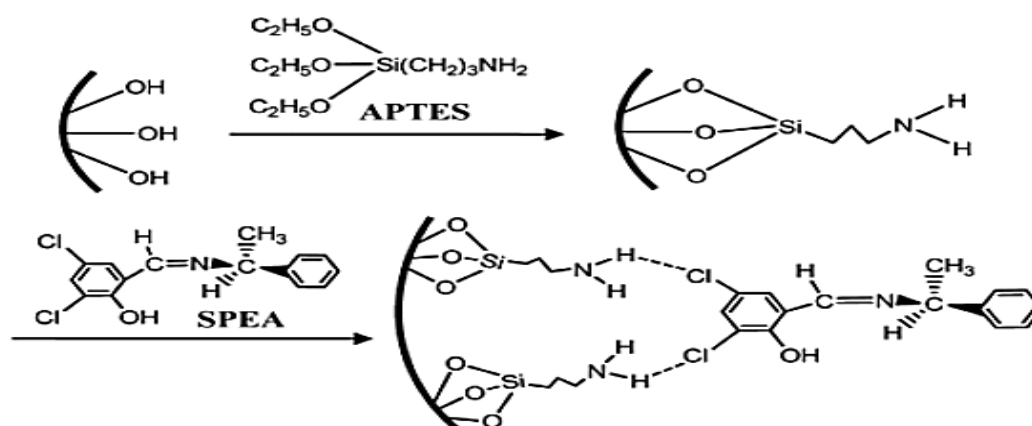
1.28 Some of the complexes of Schiff base producing from functional silica.

After silanizing silica gel by (3-aminopropyl)trimethoxysilane (APTS) using appropriate method, the Schiff base derivatives *N,N'*-[1,4-phenyldimethylidene]bis(2-chloroethanamine) (E)-2-[(2-chloroethylimino)methyl]phenol and (E)-4-[(chloroethylimino)methyl]phenol were added to the gel in appropriate amounts (Scheme(1.10)).



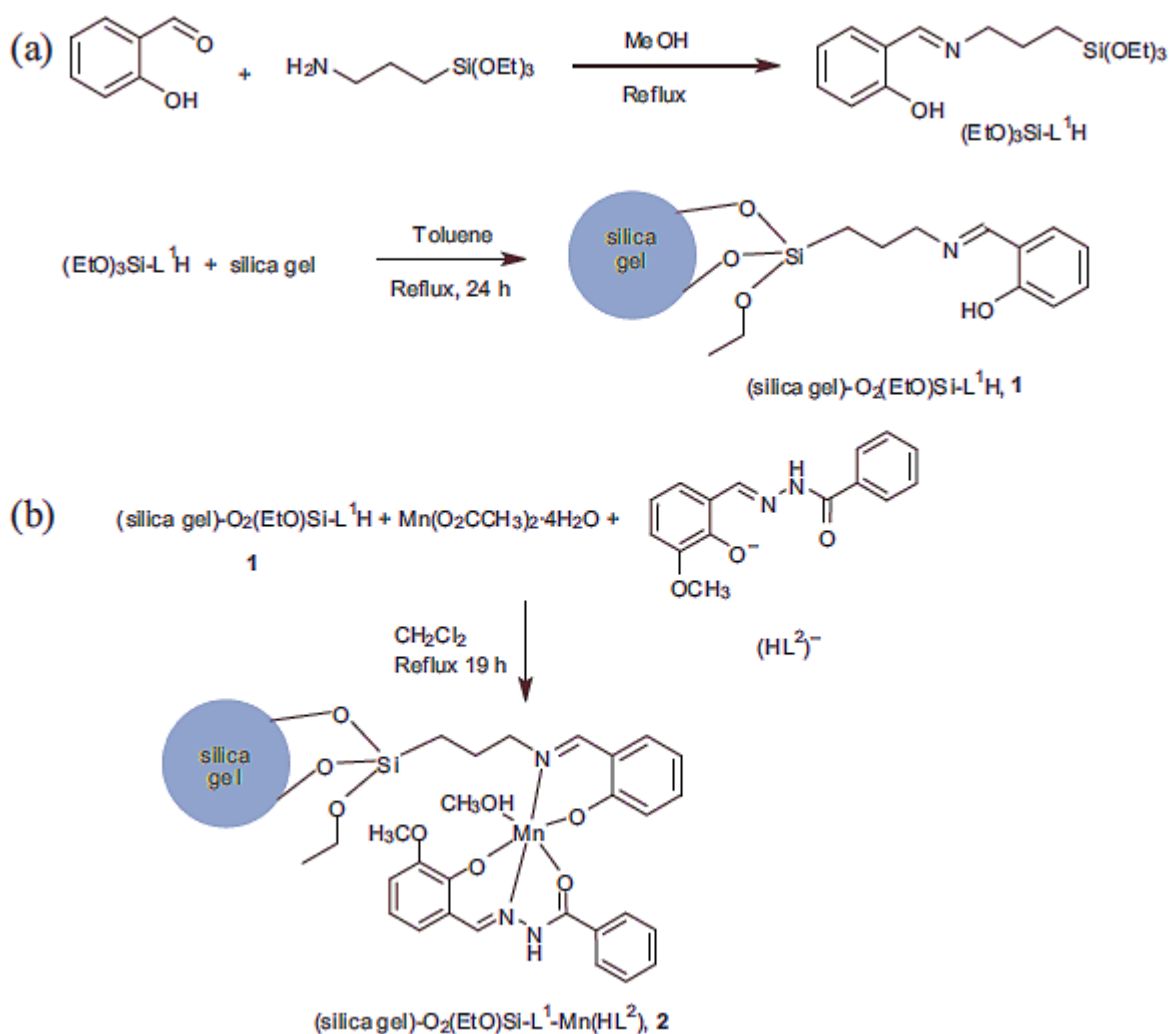
Scheme(1.10):Immobilization of I, II and III onto modified silica gel.[213]

2- *N*-3,5-dichlorosalicylidene-(*S*)-*R*-phenylethylamine (SPEA), a multiresponse molecule salicylidene Schiff base, was completely encapsulated into the channel of the amino- functionalized mesoporous molecular sieve SBA-15 via the hydrogen bond assembly Scheme(1.11).



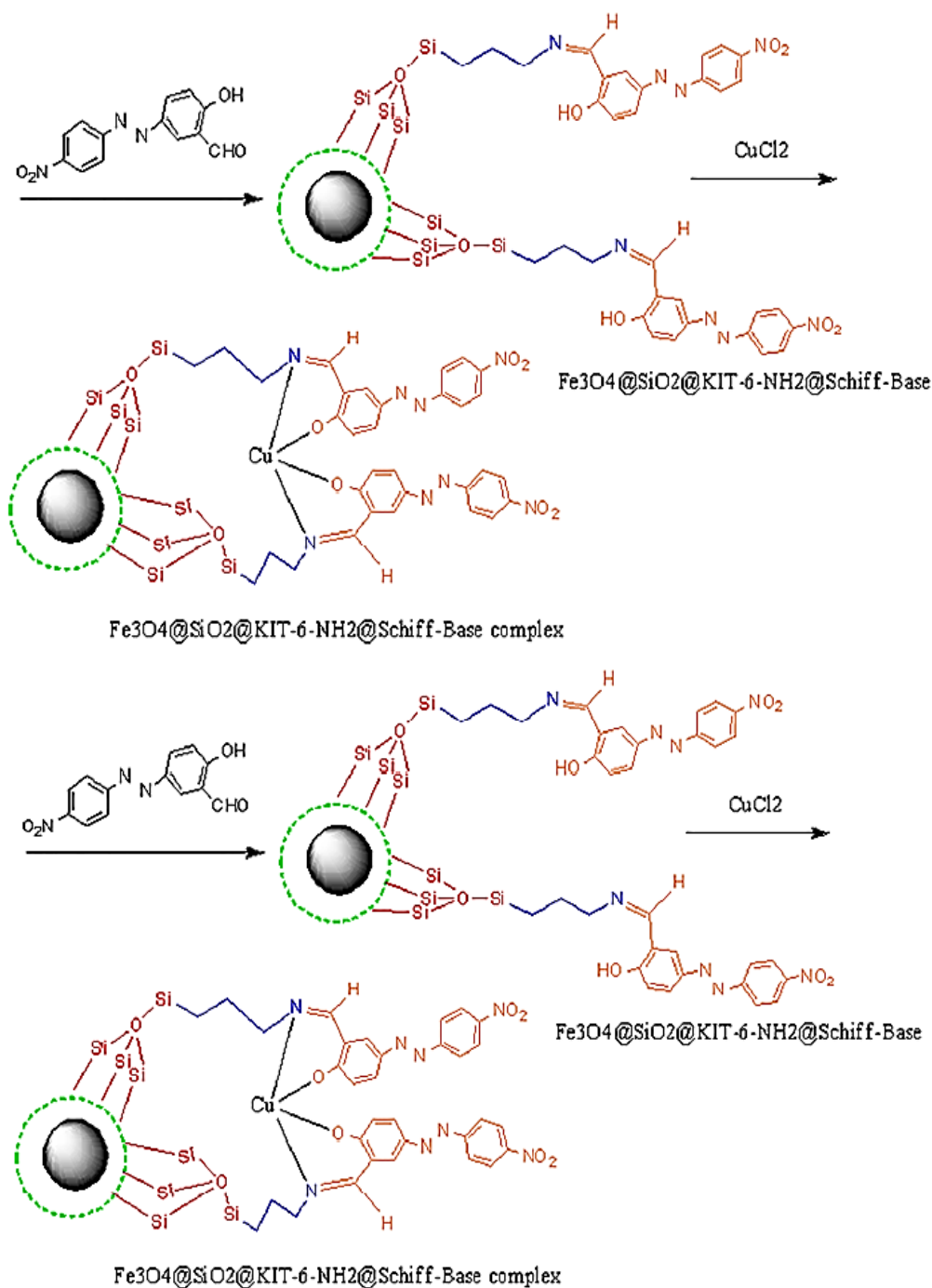
Scheme(1.11):Assembly of SPEA within the SBA-15[214]

3- By immobilizing manganese complex on an inorganic support, effective and highly selective catalyst were synthesized, producing silica gel-O₂-(ETO)-Si-L¹-Mn(HL²)[(L¹)=modified salicyladiminato and H₂L²=N⁻-(2-hydroxy-3-methoxybenzylidene)benzohydrazide)]. The surface of functionalized silica has been stabilized with Mn by N,O-coordination to the covalently Si-O bound modified salicylaldiminiato Schiff base ligand (Scheme (1.12))[215].



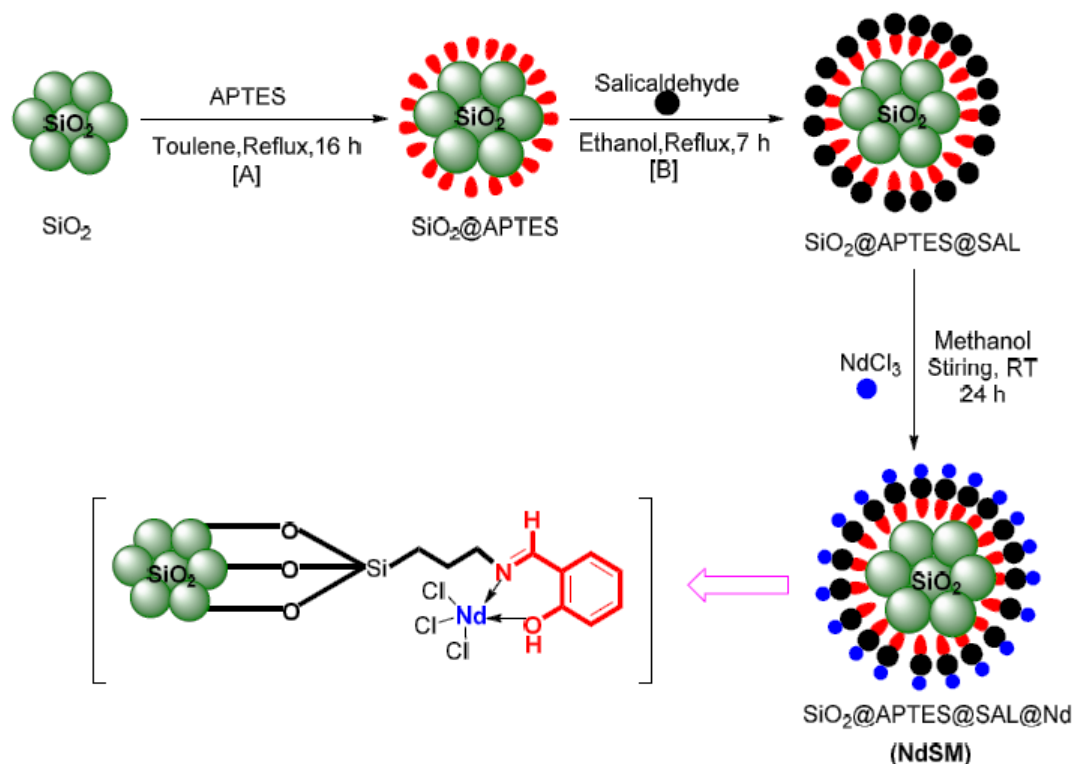
Scheme (1.12): a) silica gel surface modification by using organo-silanane to silica gel-O₂-(EtO)Si-L¹H
 b) Mn(II) immobilization on functionalized silica gel surface to produce compound 2

- 4- A new magnetic interphase nanoparticle, amino –functionalized silica mesoporous magnetic nanoparticles supporting copper/Schiff base combination were synthesized (Scheme (1.13))[216].



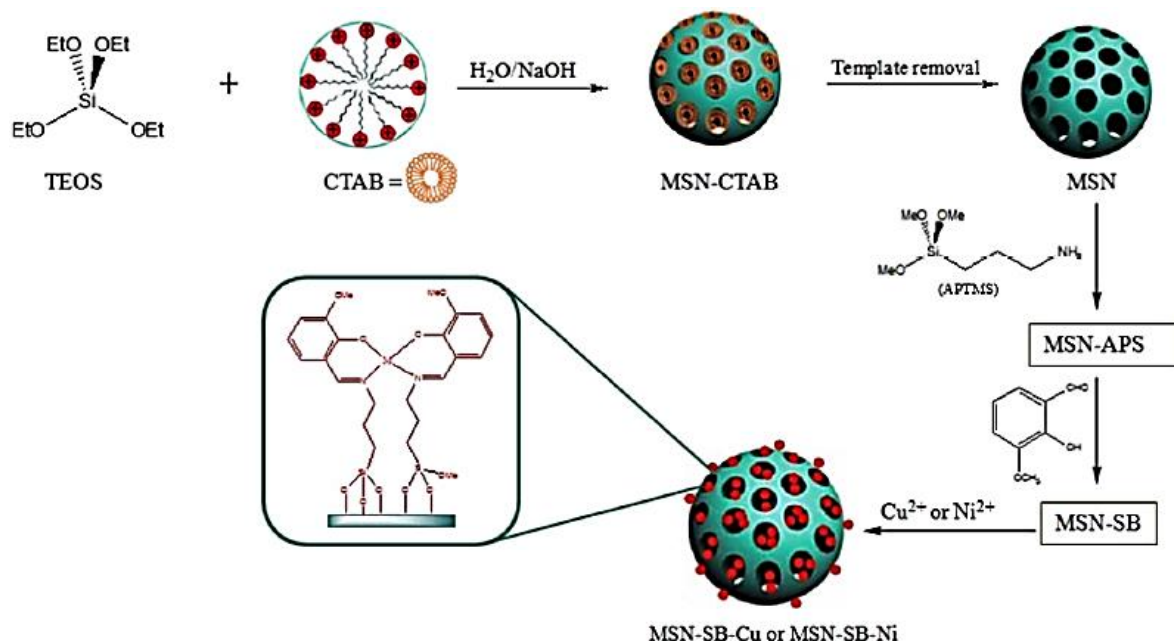
Scheme(1.13):Synthesis of $\text{Fe}_2\text{O}_4@SiO_2@KIT-6-NH_2@Schiff$ base complex.

5- NdCl_3 was absorbed on the mesoporous SiO_2 to synthesize the new Nd-Salen schiff base complex immobilized mesoporous silica (Scheme (1.14))[217].



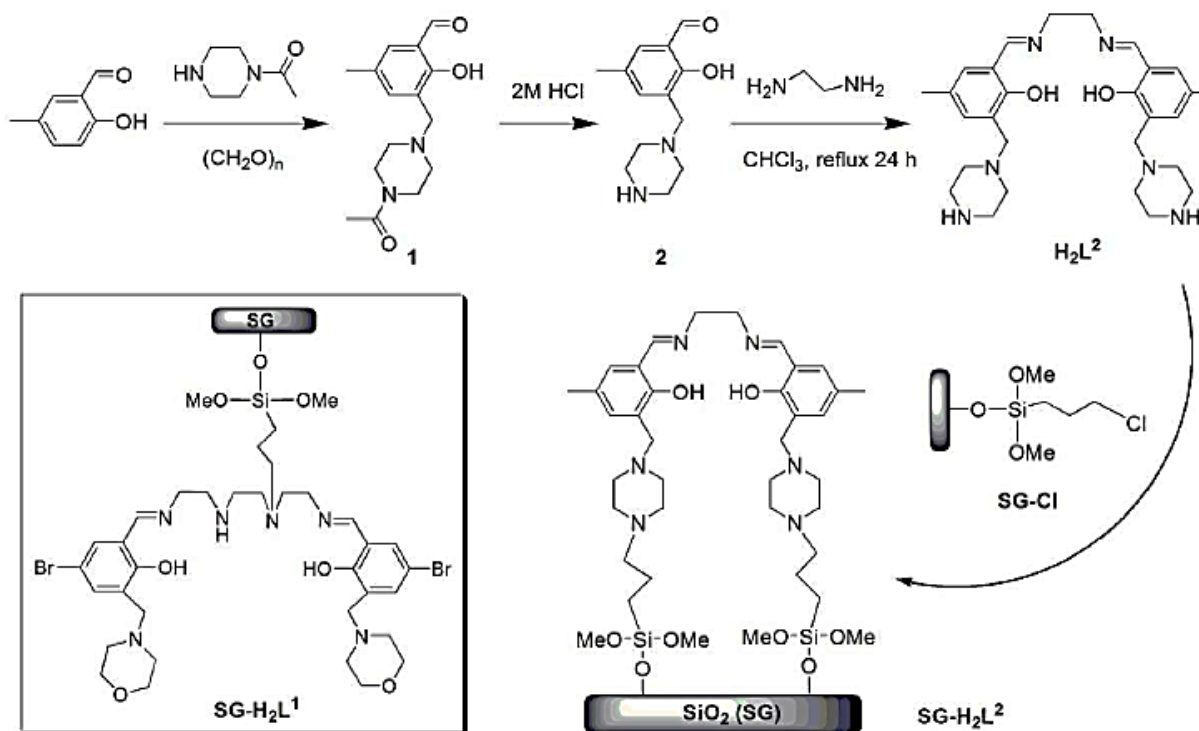
Scheme (1.14): The synthesis of the catalyst.

6-Aminoptopyltriethoxysilane was used to functionalize the sol-gel process utilized to produce mesoporous silica nanoparticles, or MSNs. The formation of Schiff base grafted silica nanoparticles involved the condensation of amino – functionalized MSMs and 2 – hydroxyl-3-methoxybenzaldehyde. Copper and nickel salts were subsequently applied to the latter material independently to produce Cu(II) and Ni(II) complex anchored mesoporous composite Scheme (1.15)[218].



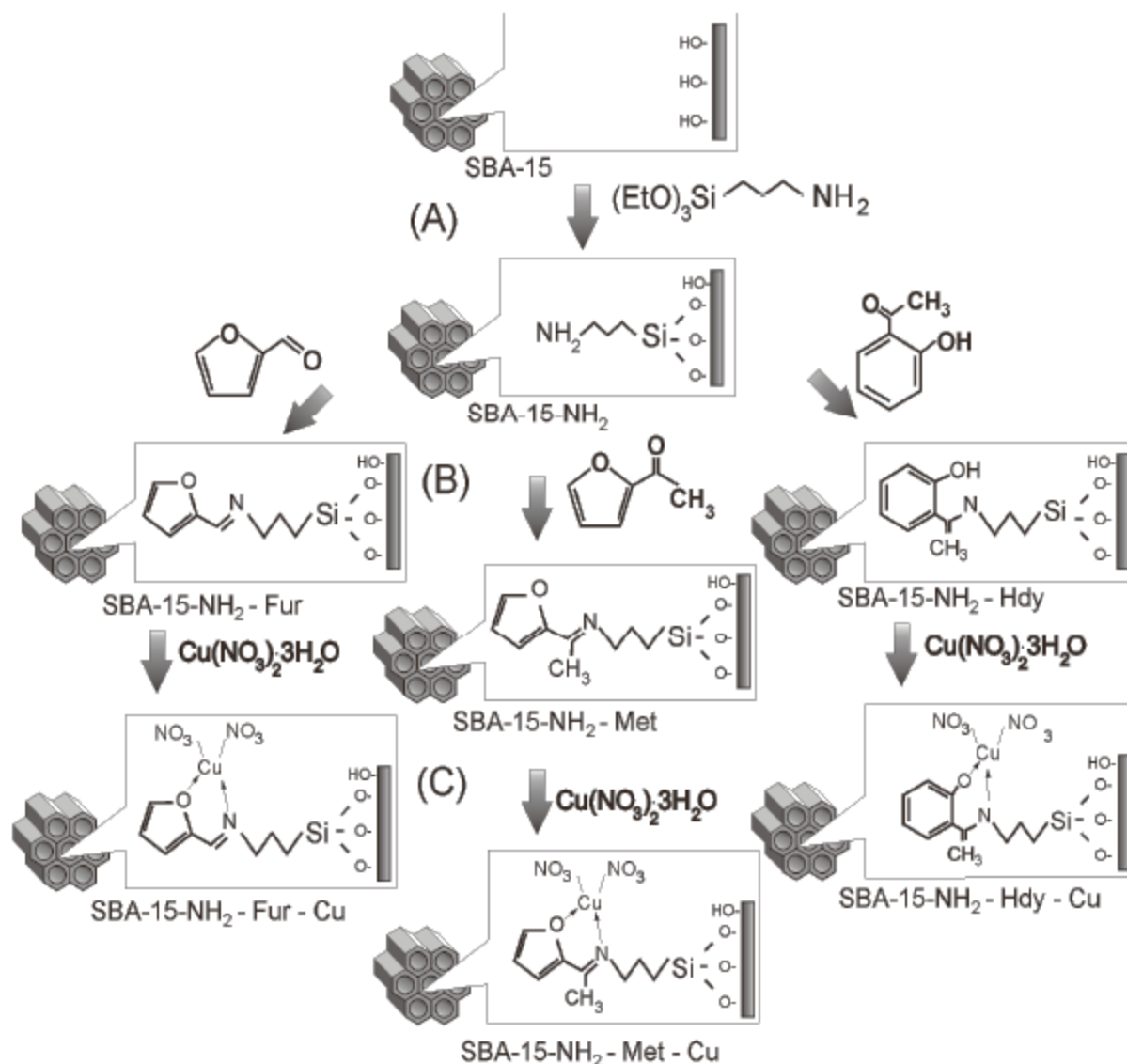
Scheme (1.15): Synthesis of the functionalized MSNs.

7-The silica gel adsorbent SG-H₂L² was modified with a ditopic zwitterionic Schiff base. From the aqueous solution of metal salts, Sg-H₂L², may absorb accompanying anions as well as metal ion concurrently (Scheme (1.16))[219].



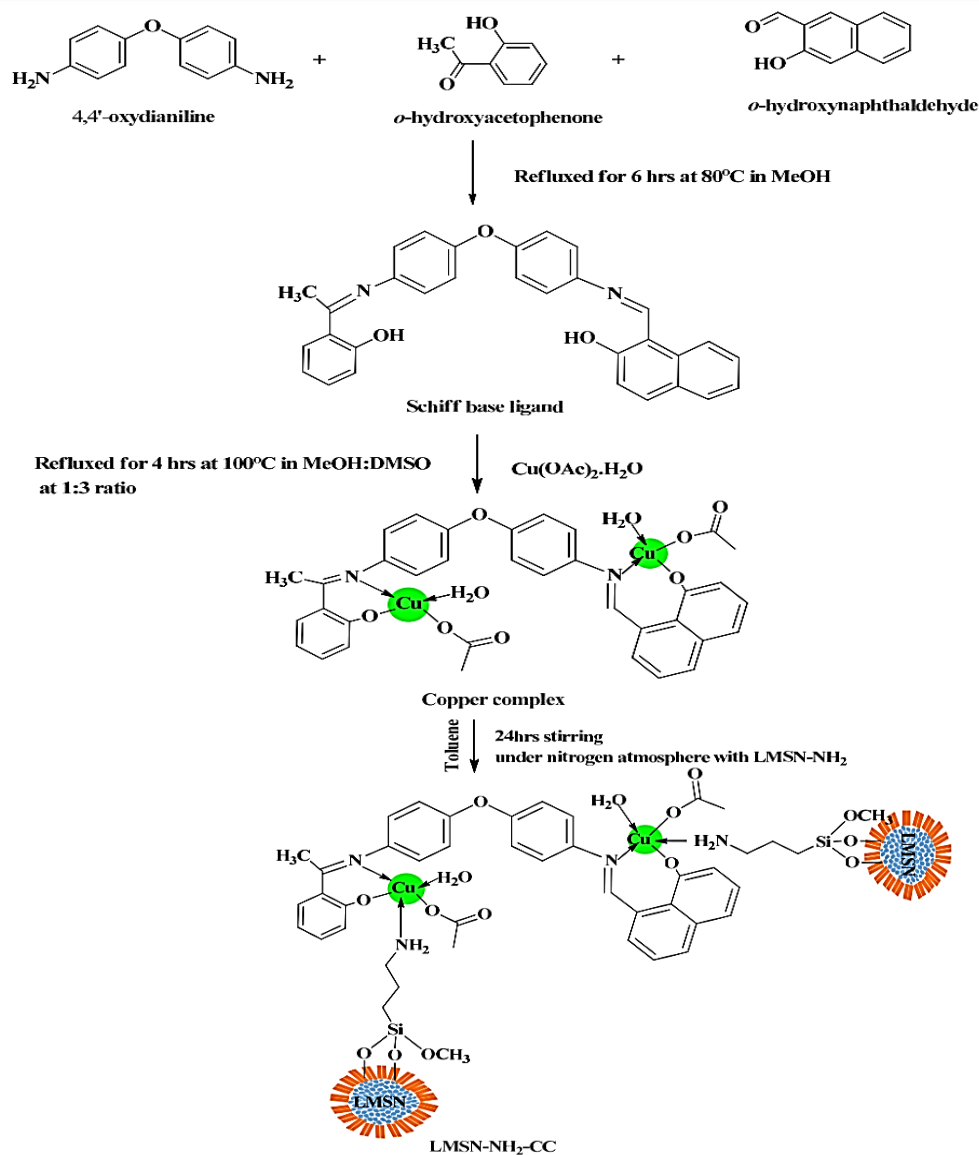
Scheme (1.16): Preparation of the silica gel-immobilized zwitterionic Schiff base adsorbent SG-H₂L² (SG-H₂L¹ inset for reference)

8- SAB-15-NH₂, MCM-48-NH₂ functionalized supports have been used to synthesize an in sites of new copper and manganese complex with Schiff base ligand produced from 2-furylmethylketone, 2-furadyhde and 2-hydroxyacetophenone (Scheme (1.17))[220].



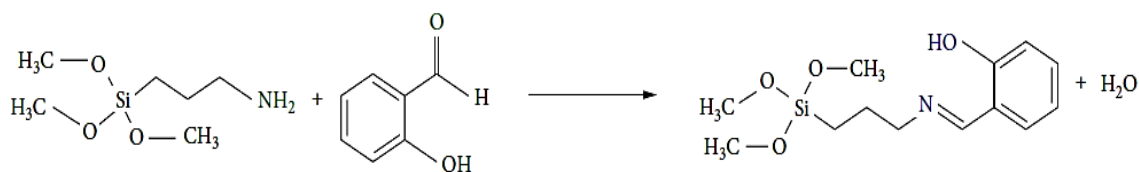
Scheme (1.17): Synthesis of copper complex with Schiff base ligand derived from 2-furylmethylketone, 2-furadyhde and 2-hydroxyacetophenone

9- Synthesis and functionalization of Lychee-like mesoporous silica nanoparticles using 3-aminopropyltrimethoxysilane and a new type of copper complex (Scheme (1.18))[221].



Scheme (1.18): Synthesis of LMSN-NH₂-CC

10- A schiff base organically modified silica aerogel was synthesized as a new adsorbent by including a salen ionophore into the silica based network. This allowed for the selective removal of Ni(II) from wastewater containing other metal ions (Scheme (1.19))[222].



Scheme (1.19): HSPTMS formation reaction.

1.29 The aim of thesis

- 1- Preparing porous material (MCM-41) which derived from rice husk, then functionalize of MCM-41 material with some organic molecules to prepare solid ligands (MCM-41@APTES, MCM-41@APTES-BSAL, MCM-41@NTPE and MCM-41@NTPE-BSAL). Characterization have been made by using suitable physical measurements, such as: Elemental analysis (CHNS), Fourier-transform infrared spectroscopy (FT-IR), X-ray diffraction (XRD), the N₂ adsorption-desorption isotherms, Thermogravimetric analysis (TGA/DSC), Field emission scanning electron microscopy (FESEM), Atomic force microscope (AFM), Energy dispersive spectroscopy (EDX) and Transmission electron microscopy (TEM).
- 2- Extraction of Co(II) and Cu(II) ions from their aqueous solutions used prepared compounds and optimizes the chemical parameters such as pH, the concentration of the ions, time of reaction and amount of prepared compounds.
- 3- Attempting to make a glass column and using it in removal and determined of Co(II) and Cu(II) ions by using (MCM-41, MCM-41@APTES, MCM-41@APTES-BSAL, MCM-41@NTPE and MCM-41@NTPE-BSAL) as adsorbent and trying to reuse this column after activation.
- 4- Using the new prepared compounds to determine cobalt ion in parametrically compounds (Vit. B12) and study some of adsorption isotherm.

2. Experimental part

2.1 Instruments

Table (2.1) shows the instruments used, manufacturing company and the place of measurement.

Table (2.1): Instrument, manufacturing company and the place of measurement

Instruments	Manufacturing company	Place of measurement
Shaker	Gemmy industrial Orbit VRN-480, England	University of Kerbala-College of Science-Iraq
Digital balance	Sartorius BS-210, Germany	University of Kerbala-College of Science-Iraq
Muffle furnace	Carbolite /1100 C	University of Kerbala-College of Science-Iraq
Centrifuge	Model EBA-720	University of Kerbala-College of Science-Iraq
Hot plate magnetic stirrer	LMS1003, Labtech, Techco, LTD	University of Kerbala-College of Science-Iraq
UV-Visible spectrophotometer	Shimadzu double beam 1800	University of Kerbala-College of Science-Iraq
Single beam visible spectrophotometer	Sp-300, Japan	University of Kerbala-College of Science-Iraq
pH-Meter	Hanna, Italy	University of Kerbala-College of Science-Iraq
Fourier transform infrared spectroscopy(FTIR)	8400, Shimadzo, Japan	University of Kerbala-College of Science-Iraq
XRD(X-Ray diffraction)	Shimadzu X-ray Diffractometer	Beam Gostar Taban Lab-Iran
BET(surface area analysis)	BEL BELSORP MINI II	Beam Gostar Taban Lab-Iran
Atomic force microscopy (AFM)	Scanning Probe Microscope-AA3000	Beam Gostar Taban Lab-Iran
Field emission scanning electron microscopy–energy dispersive X–ray (FESEM/EDX)	FESEM MIRA III Thermo Fisher ,carizeiss	Beam Gostar Taban Lab-Iran
CHNS (CHNS elemental analyzer)	Eager 300 for EA1112	Beam Gostar Taban Lab-Iran

TEM(Transmission electron microscopy)	Philips CM12	Beam Gostar Taban Lab-Iran
Thermogravimetric – differential thermal(TGA/DSC)	Universal V4.5A TA Instruments	Beam Gostar Taban Lab-Iran

2.2 Chemicals

The chemicals materials (solvents, organic and inorganic materials) that were used in this thesis are presented in Tables (2.2) and (2.3).

Table (2.2): Solvents used

No.	Chemicals	Formula	Purity %	The producing company
1	Absolute ethanol	C ₂ H ₅ OH	> 99	Fluka
2	Toluene	C ₇ H ₈	99	Fluka
3	Nitric acid	HNO ₃	65	BDH
4	Acetic acid	CH ₃ COOH	99.5	BDH
5	Hydrochloric acid	HCl	37.0	Thomas Baker

Table (2.3): Organic and inorganic materials used

NO	Chemicals	Formula	Purity %	Company
1	Sodium hydroxide	NaOH	99.0	Merck
2	Cobalt(II)chloride hexahydrate	CoCl ₂ .6H ₂ O	97	BDH, England
3	Copper(II)chloride dihydrate	CuCl ₂ .2H ₂ O	96	BDH, England
4	Ascorbic acid solution	C ₆ H ₈ O ₆	99.5	Carlo Erba
5	Ammonium Thiocyanate	NH ₄ SCN	99	BDH
6	Ethylenediaminetetraaceice acide(EDTA)	C ₁₀ H ₁₆ N ₂ O ₈	99	BDH
7	Cetyltrimethylammonium bromide	[(C ₁₆ H ₃₃)N(CH ₃) ₃]Br	>98	Sigma-Aldrich
8	(3-Aminopropyl)triethoxysilane	H ₂ N(CH ₂) ₃ Si(OC ₂ H ₅) ₃	99	Sigma-Aldrich,
9	N-[3-Trimethoxysilyl]propyl] ethylenediamine	C ₈ H ₂₂ N ₂ O ₃ Si	>98	Sigma-Aldrich
10	5-Bromosalicylaldehyde	BrC ₆ H ₃ -2-(OH)CHO	99	Sigma-Aldrich

2.3 Preparations of materials:

2.3.1 Preparation of RH-SiO₂ and sodium silicate

First, the rice husk (RH) was washed with water to remove solid particles, mud and soil, then allowed to dry, as shown in Picture (2.1). A 30.0 g of dried RH was added into a plastic container and treated with 500 mL and 1.0 M nitric acid for 24 hrs. Picture (2.2) acid. RH was then rinsed with deionized water to remove the acid until to be neutral (pH=6-7) before drying in oven at 110 °C overnight, Picture (2.3).



Picture (2.1): Dried RH



Picture (2.2): RH + Nitric acid



Picture(2.3): Dried RH after acidity

RH was stirred in 200 mL of 1.0 M NaOH for 24 hrs. at room temperature Picture (2.4). The mixture was filtered to obtain a dark filtrate (sodium silicate) Picture (2.5) which was kept in a covered plastic container.



Picture (2.4): RH + NaOH



Picture (2.5): Sodium silicate

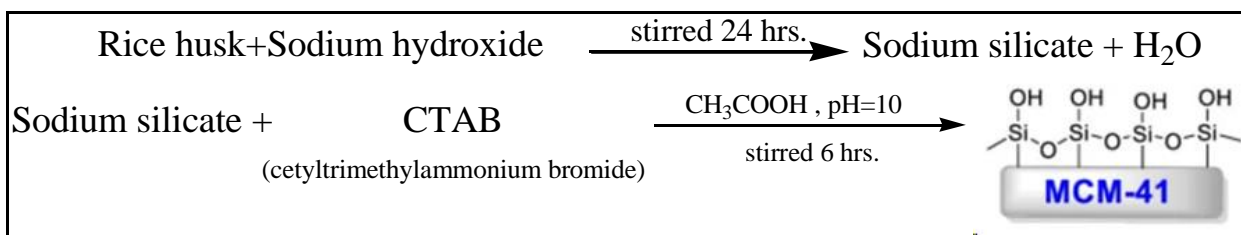
The prepared sodium silicate was titrated slowly with 3.0 M HNO_3 until it reached $\text{pH}=5$. The yellowish gel obtained was kept in covered container for 2 days. The gel was recovered by centrifuge at 4000 rpm followed by washing with deionized water and later with acetone. It was dried in an oven at $110\text{ }^\circ\text{C}$ for 24 hrs. then allowed to cool in a desiccator. Finally, the product was grounded in to fine powder and labeled as RH- SiO_2 Picture (2.6).



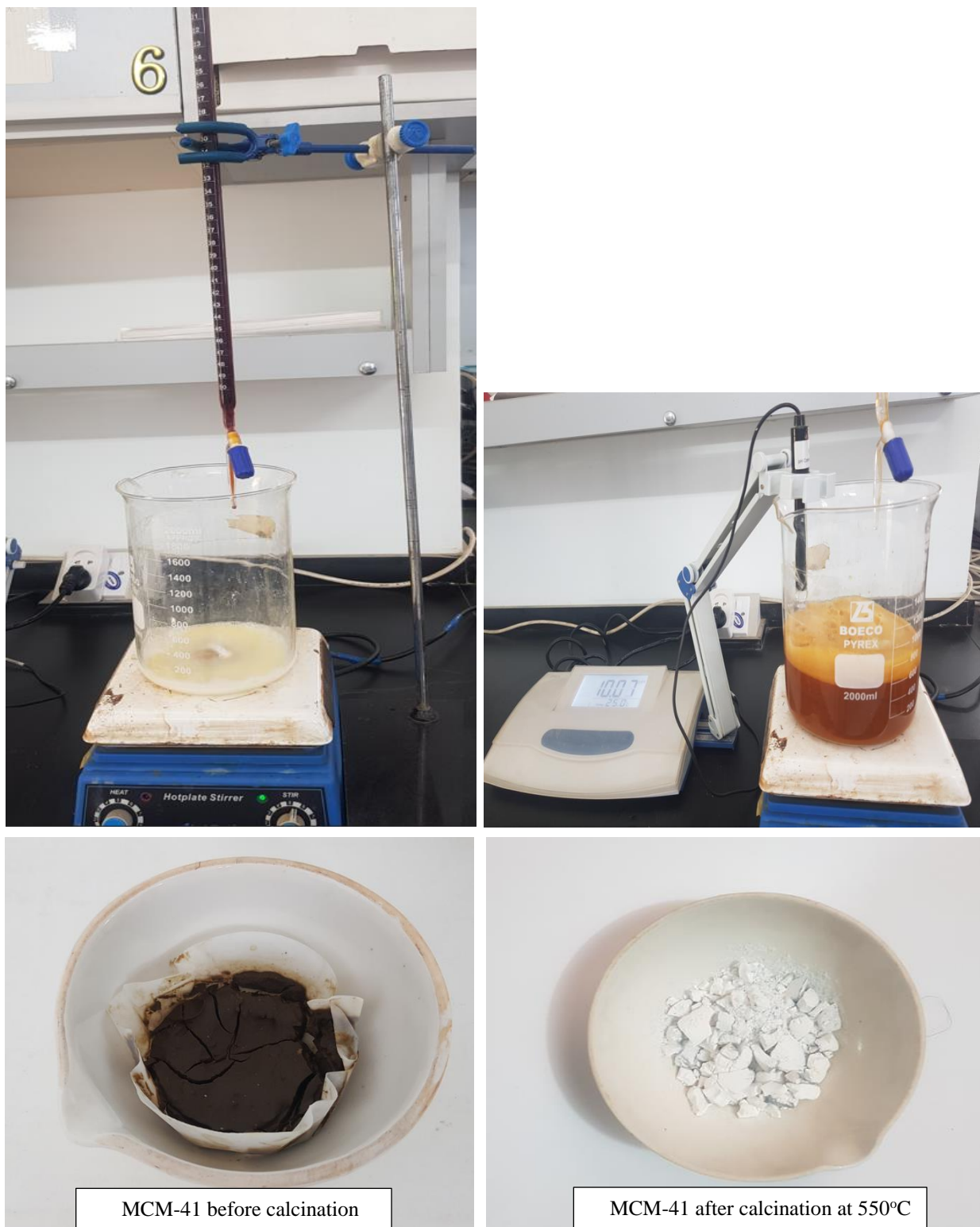
Picture (2.6): RH-SiO₂

2.3.2 Preparation of MCM-41

A surfactant solution has been prepared by mixing 2.0 g of CTAB (cetyltrimethylammonium bromide) with 25 mL of deionized water (Liquid crystal template approach) (LCTA) [33]. Sodium silicate solution was prepared using the procedures detailed in [223, 224]. The cleaned RH was stirred with 200 mL of 2.0 M NaOH for 24 hrs. at room temperature. The mixture was filtered to obtain a dark filtrate (sodium silicate) which was kept in a covered plastic container. Sodium silicate was added dropwise under vigorous stirring at room temperature to the surfactant solution, adjusting the solution to pH 10 using CH₃COOH acid (2 M), then stirring the solutions at ambient temperature for six hours followed by ageing at a temperature of 100°C for 72 hrs. The final mixture was filtered and rinsed with deionized water prior to drying at 50°C for 24 hrs.. The materials were subjected to calcination at (550±3) °C for 5 hrs. to eliminate the surfactant as shown in Scheme (2.1) and Picture (2.7).



Scheme (2.1): The synthesis steps of MCM-41.

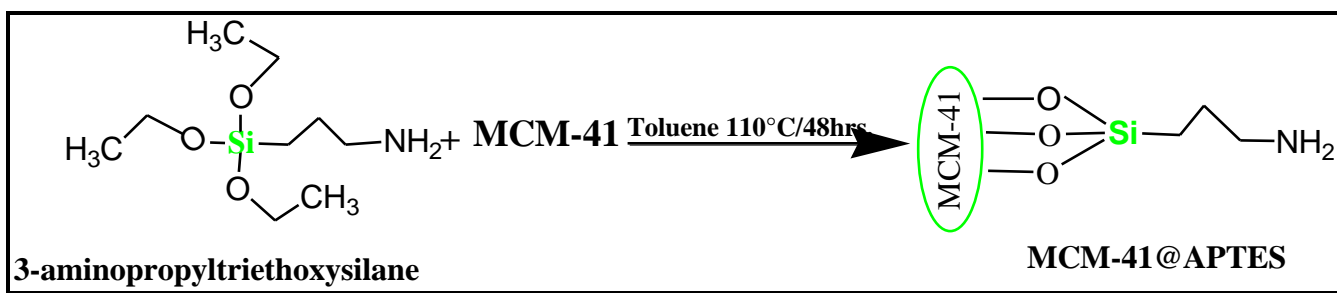


Picture (2.7): Preparation of MCM-41

2.3.3 The functionalization of MCM-41

2.3.3.1 Synthesis of 3-aminopropyltriethoxysilane functionalized mesoporous silica(MCM-41@APTES)

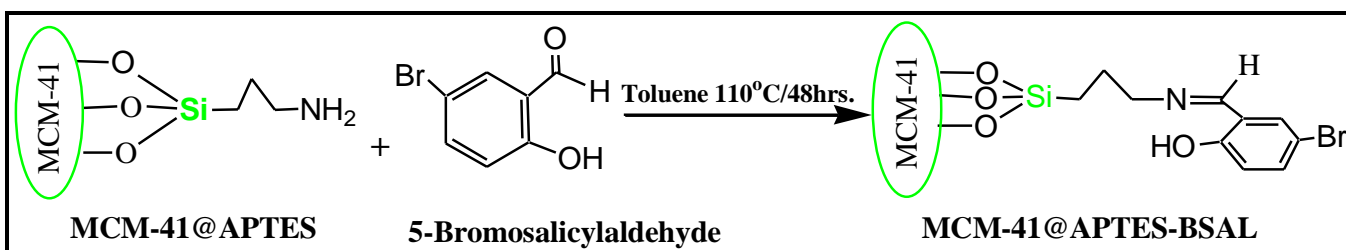
Desired amount of MCM-41 was dried at 110°C in an oven for three hours to remove physisorbed moisture. 1.0 mL of 3-aminopropyltriethoxysilane was added to the dried MCM-41(1.0g) followed by addition of 30 mL toluene. Next, refluxed the mixture for 24 hrs. with stirring, then filtered. Toluene and then ethanol were used for washing the product, then dried at 70°C for 48 hrs. Finally, 1.200 g of powder was collected and labelled as MCM-41@APTES. Summary of this methodology was represented in Scheme (2.2).



Scheme (2.2): The synthesis steps of MCM-41 @APTES .

2.3.3.2 Synthesis of 5-bromosalicylaldehyde functionalized mesoporous silica (MCM- 41@APTES-BSAL)

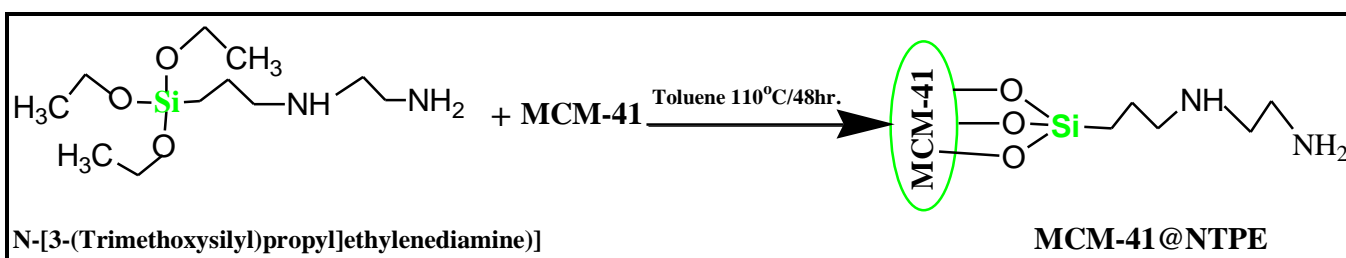
A mixture of 2.0 g of 5-Bromosalicylaldehyde(BSAL) and 1.0 g of MCM-41@APTES was mixed with 30 mL of toluene to prepare MCM-41@APTES-BSAL. The mixture was refluxed at 110°C for 48 hrs. The product was filtered, rinsed with toluene and then ethanol and left to dry at 100°C for 24 hrs. The final product collected as powder and labelled as MCM-41@APTES-BSAL. Summary of this methodology was represented in Scheme (2.3).



Scheme (2.3): The synthesis steps of MCM-41@APTES-BSAL.

2.3.3.3 Synthesis of N-[3-(Trimethoxysilyl)propyl]ethylenediamine functionalized mesoporous silica(MCM-41@NTPE).

One gram of MCM-41, after dried amount of MCM-41 at 110°C in an oven for three hours to remove physisorbed moisture, was added to 1.0 mL of N-[3-(Trimethoxysilyl)propyl]ethylenediamine(NTPE) followed by addition of 30 mL toluene and refluxed the mixture for 48 hrs. at 110°C . The resulting solution containing the solid was filtered and washed with toluene and ethanol. Finally, powder was collected and labeled as MCM-41@NTPE. The overall preparation steps have been shown in Scheme (2.4).

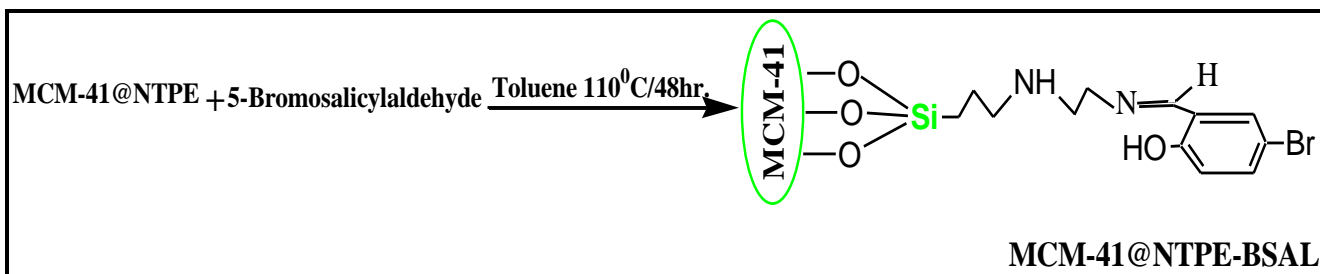


Scheme (2.4): The synthesis steps of MCM-41@NTPE.

2.3.3.4 Synthesis of 5-bromosalicylaldehyde functionalized mesoporous silica (MCM-41@NTPE-BSAL)

To prepare MCM-41@NTPE-BSAL, a mixture of 2 g of 5-Bromosalicylaldehyde (BSAL) and 1.0 g of MCM-41@NTPE was mixed with 30 mL of toluene. The mixture was refluxed at 110°C for 48 hrs. The product was separated using a filter, rinsed with

toluene and then ethanol and left to dry at 100°C for 24 hrs, and then crushed until became a very fine powder that was labelled as MCM-41@NTPE-BSAL. The overall preparation steps have been shown in Scheme (2.5).



Scheme (2.5): The synthesis steps of MCM-41@NTPE-BSAL.

2.3.4 Preparation of stock solution of Co (II) ion

The stock solution of (1mg/mL) Co (II) ions was prepared by dissolving (0.415g) of $\text{CoCl}_2 \cdot 6\text{H}_2\text{O}$ in deionized water and completed the volume to 100mL in a volumetric flask. Dilute cobalt ion solutions were prepared by dilutes the stock solution with the necessary volume of water.

A 0.1 M of Co (II) solution was prepared by dissolving (1.224g) of $\text{CoCl}_2 \cdot 6\text{H}_2\text{O}$ in deionized water and then completed the volume to 50 mL with deionized water in a volumetric flask. Dilute cobalt ion solutions were prepared by dilutes this standard solution with the necessary volume of water.

2.3.5 Preparation of stock solution of copper (II) ion

A (1mg/mL) of Cu(II) solution was prepared by dissolving (0.279g) of $\text{CuCl}_2 \cdot 2\text{H}_2\text{O}$ in deionized water and completed the volume to 100mL in a volumetric flask. Dilute copper ion solutions were prepared by dilutes the stock solution with the necessary volume of water.

A 0.1 M of Cu (II) solution was prepared by dissolving (0.888g) of $\text{CuCl}_2 \cdot 2\text{H}_2\text{O}$ in deionized water and then completed the volume to 50 mL with deionized water in a volumetric flask. Dilute copper ion solutions were prepared by dilute this standard solution with the necessary volume of water.

2.3.6 (2% W/V) solution of ascorbic acid

(2.00g) of ($C_6H_8O_6$) was dissolved in deionized water and the volume was completed to (100 mL) in a volumetric flask.

2.3.7 (50% W/V) solution of ammonium thiocyanate

(50.00g) of NH_4SCN was dissolved in deionized water and the volume was completed to (100 mL) in a volumetric flask.

2.3.8 (0.5 M) of hydrochloric acid solution

(4.180 mL) concentrated hydrochloric acid (37%, $1.18g/cm^3$) was diluted in 100 mL volumetric flask with deionized water. Dilute Hydrochloric acid solutions were prepared by diluting this stock solution with the necessary amount of deionized water.

2.3.9 Sodium hydroxide solution(0.1M)

NaOH solution (0.1M) was prepared of by dissolving 0.400 g NaOH in 100 mL deionized water.

2.3.10 (5%) (EDTA) ethylenediaminetetraaceice acide solution

EDTA solution (5%) was prepared by dissolving 5.000 g of disodium salt of ethylenediaminetetraaceice acide in 100mLof deionized water.

2.3.11 Characterization studies

2.3.11.1 UV-Visible measurements for aqueous solutions of Co (II) and Cu (II)

UV-Visible spectra of Co (II) and Cu (II) aqueous solutions were examined to find λ_{max} .The spectra acquired shows that λ_{max} of Co (II) and Cu (II) are 620 and 730 nm, respectively.

2.3.11.2 Elemental analysis CHNS

The percentage of carbon, hydrogen, nitrogen and sulfur analysis was determined by elemental analysis. This analysis is carried out at a high temperature (about $1000^\circ C$) in an oxygen-rich environment and is based on the classical Pregl – Dumas method [225].

2.3.11.3 Study of FT-IR (spectra furrier transforms infrared spectrophotometry)

Furrier transforms infrared spectrophotometry FTIR was used to identifying the functional groups in the structure of compounds. Grind about 1 mg of compound with KBr in agate- grinding mill, a piston was used to compress the sample, thin layer was formed, the wavelength ranges (400-4000) cm^{-1} [226].

FT- IR spectra recorded for the compounds: -

1. Infrared spectrum of RH- SiO_2 .
2. Infrared spectrum of MCM-41.
3. Infrared spectrum of MCM-41 @ APTES.
4. Infrared spectrum of The MCM-41 @ APTES-BSAL.
5. Infrared spectrum of The MCM-41 @ NTPE.
6. Infrared spectrum of The MCM-41 @ NTPE-BSAL.

2.3.11.4 Study of X-ray diffraction analysis (XRD)

The amorphous or crystalline structure of prepared compounds has been detected by using XRD analysis. The compact disc containing about 1mg of powder put inside the device for analysis. The diffraction angle was scanned in the 2θ range (5-90) for 2 hrs. at a rate of $6.0^\circ \text{ min}^{-1}$ [227].

2.3.11.5 BET surface area analyzer(N_2 adsorption-desorption)

The brunauer – Emmett-Teller (BET) methods were used to calculated the surface area and the pore size by passing nitrogen gas on 1.0 g of compounds after empty the oven from pressure at equal temperature [228].

2.3.11.6 Thermal analysis(TGA/DSC)

Thermogravimetric analysis (TGA/DSC) is a technique by which physicochemical properties (moisture, crystalline water, and or volatile components) of a substrate and or surface reaction products can be probed as a function of temperature, whilst the substrate is subjected to a controlled heating rate. The mass of the sample in a controlled

atmosphere is recorded continuously as a function of temperature or time during the heating process. The amount and the rate of weight loss at elevated temperatures are related to the chemical structure and composition of the given samples. In general, higher temperature is required to decompose more stable materials. The heating is from (30-900) °C at a heating rate of 20 °C min⁻¹[229].

2.3.11.7 AFM analysis

AFM technique was employed to investigate the topography of the prepared compounds surface. The samples were suspended in absolute ethanol or in distilled water. One droplet of the suspension was placed on a small glass slide and allowed to dryness at room temperature before being examined by AFM[230].

2.3.11.8 Study of field emission scanning electron microscopic (FESEM-EDX) and transmission electron microscopy (TEM)

In electron microscopy, a narrow beam of high energy electron is directed at a specimen. Images are formed either by electrons passing through a thin sample via transmission electron microscopy(TEM), or by secondary emission from the surface of a thick sample using so called scanning electron microscopy.Both FESEM and TEM are commonly used to study the size, shape and chemical composition of nano- materials. Electron beams generated in electron microscopes have a much shorter wavelength than light and therefore provide high resolutions image(~ 1.0 nm).Electron microscopy also provides further information about the chemical composition and crystallography of the material under study. Scanning electron microscopic is used to study the morphology and distribution of samples at different magnification [232 ,231]. Also EDX(Energy-dispersive X-ray spectroscopy) detector, which is attachment to electron microscopy instrument (Scanning electron microscopy), was used to determine the chemical composition of compounds[233].

2.4 Calibration curve of Co (II) and Cu(II) ions

The calibration curve of Co (II) and Cu (II) were performed by measuring the absorption of known metal concentration for series of solutions for Co (II) and Cu (II), respectively, against blank as a reference. Calibration curves were prepared for Co(II) and Cu(III), separately, according to colorimetric method [234].

To measure the absorption of standard solutions of Co (II), the processes are as follows: (5 mL) of solutions containing different concentration of ions, ranged from (50-1000 μg) for Co (II) were taken, to each solution (0.5mL) of (0.5M) hydrochloric acid solution, 2mL of Ammonium thiocyanate (50% w/v), (1mL) of ascorbic acid solution was added followed by addition of (1.5 mL) acetone. The absorbance was measured at ($\lambda_{\text{max}}=620\text{nm}$) against a reagent blank solution, using (1cm) cell. The relationship between the absorbance and concentration was constructed to the calibration curve.

To a series of 10mL volumetric flasks transfer aliquots of the standard copper (II) solution, add 0.4 mL of (5%) EDTA solution, the necessary drops of hydrochloric acid or sodium hydroxide solutions was added to obtain pH range from (7.5-8), and dilute to the mark with deionized water. The absorbance measured at ($\lambda_{\text{max}}= 730 \text{ nm}$) against a reagent blank solution. Using cell absorption (1cm) after that the relationship between the absorption and concentration was plotted for the calibration curve.

2.5 Removal ions experiments

The prepared solid materials were tested with many metal ions because of their properties as adsorbent and mesoporous materials and the choice fell on cobalt and copper ions, which were characterized by a high ability to be removed by the porous material MCM-41.

A (0.1gm) of ligand (MCM-41) and its derivatives were shaken with 50 mL, 0.05M of an aqueous solution of (Co(II) and Cu(II)) metal ions, respectively. Measurement of the metal ion concentration was carried out by allowing the insoluble

complex to settle down then appropriate volume of the supernatant was withdrawn using a micropipette to study the removal ions by using spectrophotometer.

2.6 Optimum conditions

The removal experiments were performed to evaluate the effect of variable parameters on the removal efficiency of the MCM-41 and the functionalization compounds as a metal ions adsorbent. The removal percentage of the metal ions by different types of MCM-41 and the functionalization compounds were calculated from the following equations[235]:

$$\%E = (C_o - C_e / C_o) \times 100$$

C_o : the initial metal concentration(mg.L^{-1})

C_e : final(at equilibrium) metal ion concentration(mg.L^{-1})

2.6.1 Effect of shaking time

The effect of the reaction time on the metal ion uptakes over MCM-41 and its derivatives were explored. The response was performed with 0.1 g ligands and shaken for 72 hrs. with an aqueous solution of divalent metal ions. The absorption was calculated at different time for 72 hrs..

2.6.2 Effect of pH

The effect of pH was studied by taking four different pH (2,4,6,8) and (2,4,5,6) respectively for Co(II) and Cu(II) ions with 0.1 g ligands MCM-41 and its derivatives. The absorption was calculated at different time for 72 hrs..

2.6.3 Effect of metal ion concentration

The effect of metal ion concentration was studied using three different concentration (0.02 M, 0.05 M, 0.08 M and 0.1M) for each metal ion with 0.1 g ligands MCM41 and its derivatives. The absorption was calculated at different time for 72 hrs..

2.6.4 Effect of mass of the ligand

The effect of mass of the ligand was investigated using three different mass (100, 150, and 200 mg) of ligands (MCM-41) and its derivatives. The absorption was calculated at different time for 72 hrs..

2.7 Innovator column separation experiment

A 500 mm long glass column with 25 mm diameter was homemade manufactured that contain an inlet to enter the solution and outlet to exit the solution after adsorption process is complete. The adsorbent material is placed on a glass clip inside the column as shown in Picture (2.6).

A glass column was washed and dried, and then an amount of the prepared ligand was packed in the column, respectively. After each use the column was washed with deionized water. Before any sample injection, the column was conditioned by passage of 50 cm³ of the appropriate eluent (ions solution). The pH of the eluent was controlled using NH₄OH (0.1 M)/HCL (0.1 M), and the amount of metal ion (removal) in each fraction was collected and determined using spectrophotometer.



Picture (2.8): Separation column

2.8 Determination of Co(II) ion in vitamin B12

An ampule of vit.B12 having 1000 $\mu\text{g}/4\text{mL}$ of cyanocobalamine($43.471\mu\text{g}(\text{Co}(\text{II}))/4\text{mL}$) was used. The ampule was thoroughly shaken before used, and then poured in beaker then 8 mL of $\text{HNO}_3(1:1)$ has been added and the mixture heated until it become dry. Next, 8 mL of $\text{HCl}(1:1)$ were add to the beaker and heated again until near dried. The specimen was collected and subsequently mixed with deionized water, transferred to 10 mL volumetric flask and completed with deionized water[236].

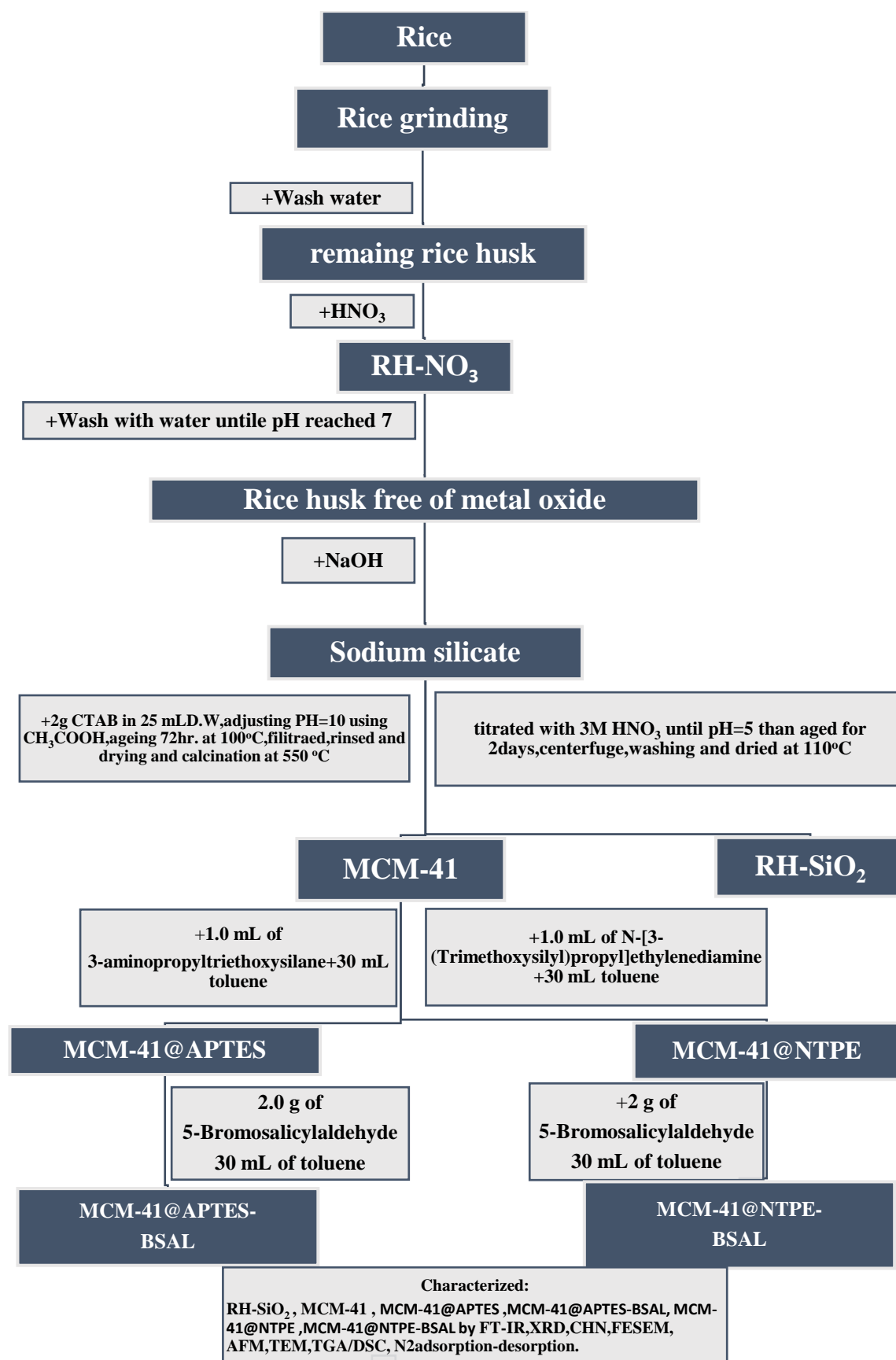
2.9 Adsorption equilibrium isotherms

Using the Langmuir and Frundlich isotherm models Table(2.4) to predict the best adjustment to equilibrium data at different temperatures[237][238].The adsorption isotherm for prepared compounds with different concentration of $\text{Co}(\text{II})$ and $\text{Cu}(\text{II})$ ions

were used, adjusting the acidity at optimum condition, using spectrophotometric method to determination the C_e based on calibration curve.

Table(2.4): Equations of removal percentage, adsorption capacity, adsorption isotherms and mathematical modeling.

	Mathematical expression	Parameters
Removal percentage	$(C_0 - C_e / C_0) \times 100$	C_0 :The initial concentration of the adsorption solution (mg.L ⁻¹) C_e :The equilibrium concentration of the adsorption solution(mg.L ⁻¹)
Adsorption capacity[239]	$Q_e = \frac{V(C_0 - C_e)}{m}$	Q_e : Adsorption capacity(mg/g) C_e :The equilibrium concentration of the adsorption solution(mg.L ⁻¹) C_0 :The initial concentration of the adsorption solution (mg.L ⁻¹) V :Total volume of the adsorption solution(L) m :Weight of the adsorbent (g)
Isotherm models	Mathematical expression	Parameters
Langmuir [240]	$Q_e = \frac{abC_e}{1 + bC_e}$	a :Maximum amount adsorbend (mg ⁻¹ .g ⁻¹) b :Is the langmuir isotherm constant(L.g ⁻¹)
Freundlich[241]	$\text{Log } Q_e = \text{Log } K_f + \frac{1}{n} \text{Log } C_e$	K_f : Adsorption capacity n : Adsorption intensity



Scheme (2.7): Method of preparation.

3.The characterization of RH-SiO₂,MCM-41 and its derivatives(MCM-41@APTES, MCM-41@APTES-BSAL, MCM-41@NTPE and MCM-41@NTPE-BSAL).

3.1 The characterization of RH-SiO₂ and MCM-41

Sodium silicate from RH was used to prepared RH-SiO₂ and MCM-41.The structures of RH-SiO₂ and MCM-41 were characterized using various techniques.

3.1.1 Fourier –transform infrared spectroscopic analysis (FT-IR):

FT-IR (Fourier transform infrared spectroscopy) was utilized to identify the different organic and inorganic groups present in prepared materials. The findings from this method are shown in figures below.

Different types of chemicals groups in RH-SiO₂ were identified by using FT-IR spectra. Fig.(3.1) shows a group of distinct bands at 3499 cm⁻¹ and a weak sharp band at 1631 cm⁻¹, due to hydroxyl group located on the silica surface and coordinated water[242] .

The FT-IR spectrum of prepared compound MCM-41,as shown in Fig.(3.1) shows vibrations of the hydroxyl (-O-H) group of silanol (Si-OH) and absorbed water molecules give a characteristic wide adsorption band in the rang (3730-2980) cm⁻¹[243, 244].Trapped molecules of water give a peak at 1640 cm⁻¹ [245].It was observed that the asymmetric and symmetric stretching vibration of Si-O-Si group gives a band in the (1345-875) and (875-736) cm⁻¹ ,respectively.The band at (1099 , 795 and 462) cm⁻¹ which hands over to siloxane to the expansion shaking of Si-O-Si bond.[246].While peaks in the range of (516-416) cm⁻¹ is related to the bending vibrations of Si-O-Si structure[247].The FT-IR spectra did not clearly demonstrate the distinction between RH-SiO₂ and MCM-41.

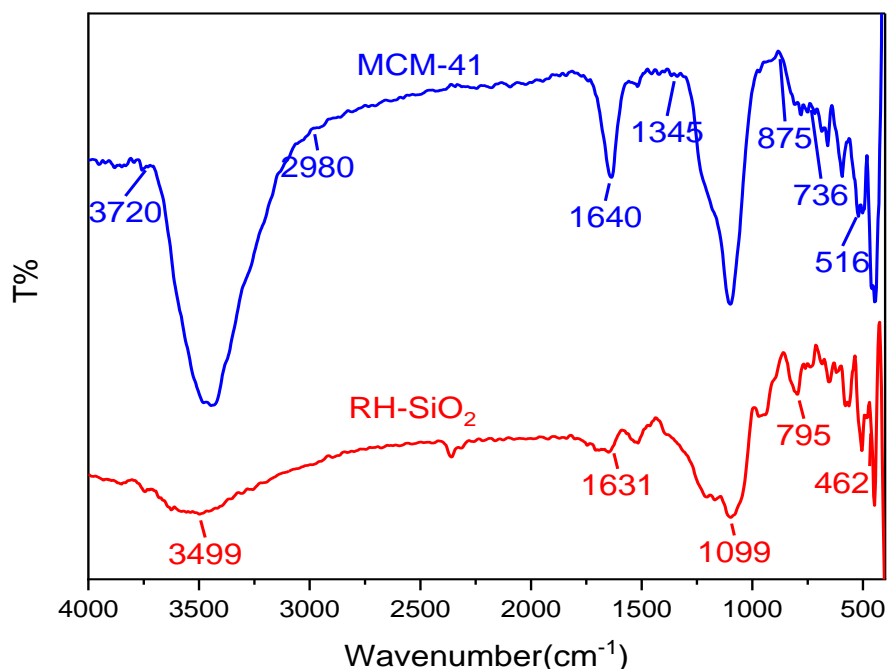


Figure (3.1): FTIR spectra for RH-SiO₂ and MCM-41.

3.1.2 X-ray powder diffraction (XRD)

The X-ray diffraction (XRD) analysis was carried out for the synthesized materials, RH-SiO₂ and MCM-41. The results of the XRD analysis at low and high angles are presented in Figs.(3.2) and (3.3), respectively. For low-angle XRD pattern Fig.(3.2), RH-SiO₂ doesn't give any distinguish peaks, while the appearance of peaks at 2.17 (100), 4.25 (200) and 5 (210) demonstrate to the hexagonal structure of mesoporous silica, as present in MCM-41 [248]. Further confirmation can be seen in the associated TEM image in section(3.1.7).The high-angle XRD pattern in Fig.(3.3) shows a wide peak between (15°–30°) from 2 θ due to the amorphous structures of the RH-SiO₂ and MCM-41 [249, 250].

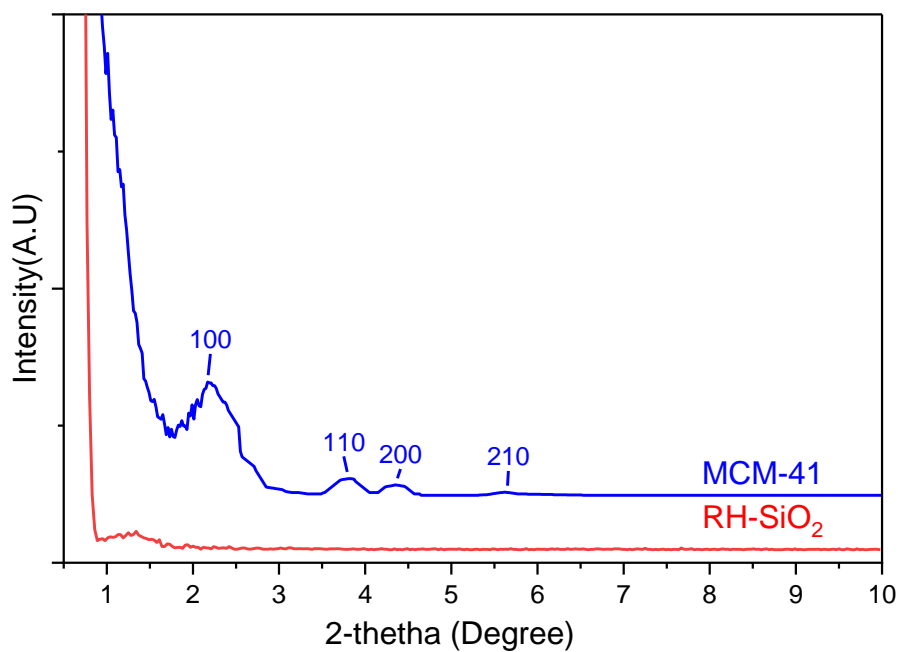


Figure (3.2): XRD spectra (low angle) of RH-SiO₂ and MCM-41.

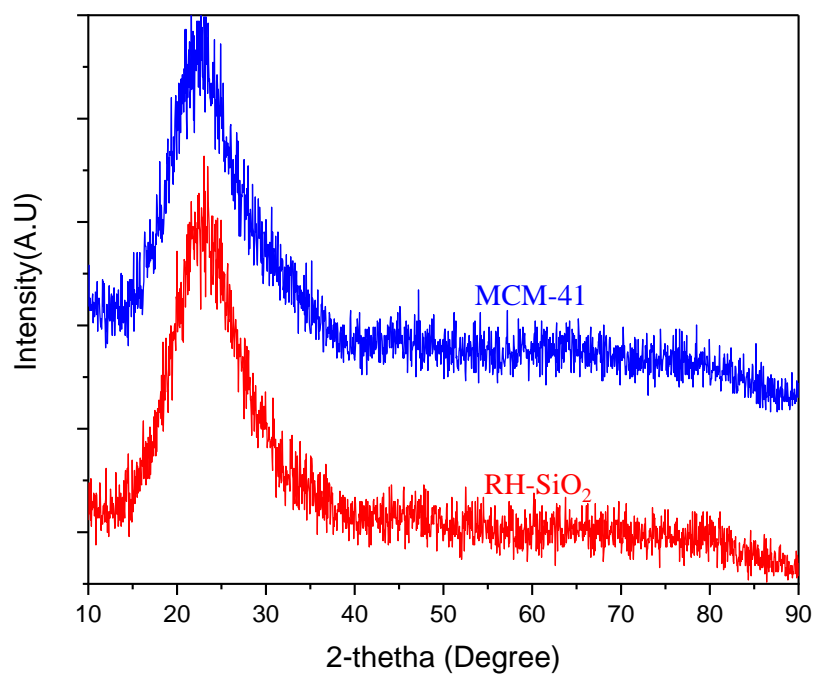


Figure (3.3): XRD spectra (high angle) of RH-SiO₂ and MCM-41.

3.1.3 Nitrogen adsorption-desorption analysis

The BET (Brunauer-Emmet-Teller) method is the most frequently used procedure to determine the surface area of a porous material[102].The method has evolved from the Langmuir theory[251].

The specific surface area and the pore size distribution can be demonstrated via N₂ adsorption–desorption analysis. From the results represented in Fig. (3.4), the specific surface areas, the total pore volumes and the average pore diameters for RH-SiO₂ and MCM-41, were illustrated in Table (3.1). The data obtained for all parameters was increased in comparison to RH-SiO₂, which can be attributed to the existence of a hexagonal mesoporous arrangement in MCM-41. A hysteresis loop was detected for both RH-SiO₂ and MCM-41 within the range from $0.4 < P/P_0 < 1$, associated with capillary condensation as per the IUPAC classification. The isotherm in RH-SiO₂ was type IV(mono and multilayer adsorption with capillary condensation), and the hysteresis loop(associated with the pore shape) was of type H2(It looks like round bottom flask)[252, 253].The MCM-41 sample exhibited a type IV isotherm with an H3 hysteresis loop(the ring is observed with clusters of sheet-like molecules leading to the cleft pores), Fig.(3.5) below shows the pore size distributions of RH-SiO₂ and MCM-41 which is characteristic of mesoporous solids[254].

Table (3.1): BET analysis for RH-SiO₂ and MCM-41.

Compounds	BET surface area (m ² .g ⁻¹)	Total pore volume (cm ³ .g ⁻¹)	Average pore diameter (nm)
RH-SiO ₂	390.12	0.33	3.47
MCM-41	548.92	0.94	6.85

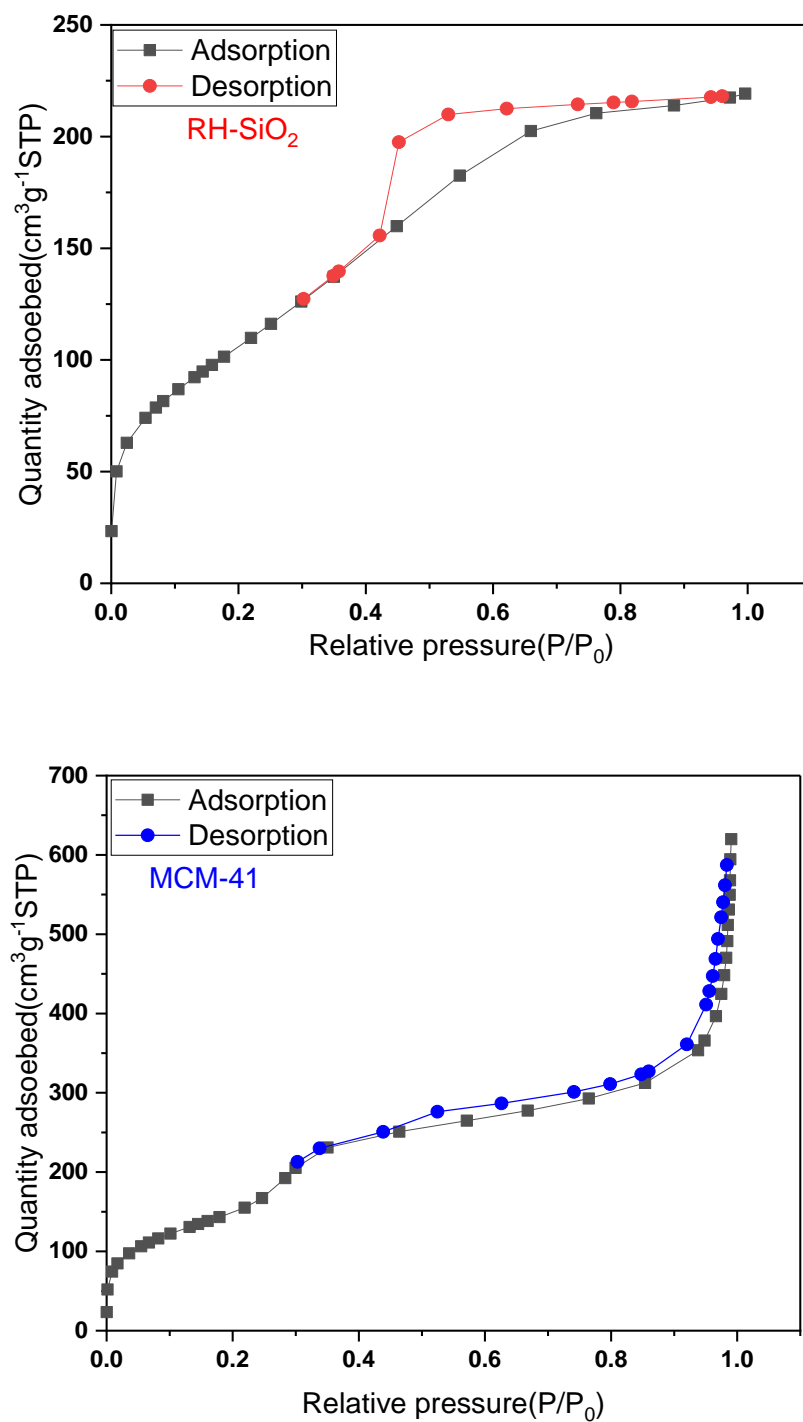


Figure (3.4): N_2 adsorption–desorption isotherms for RH-SiO₂ and MCM-41

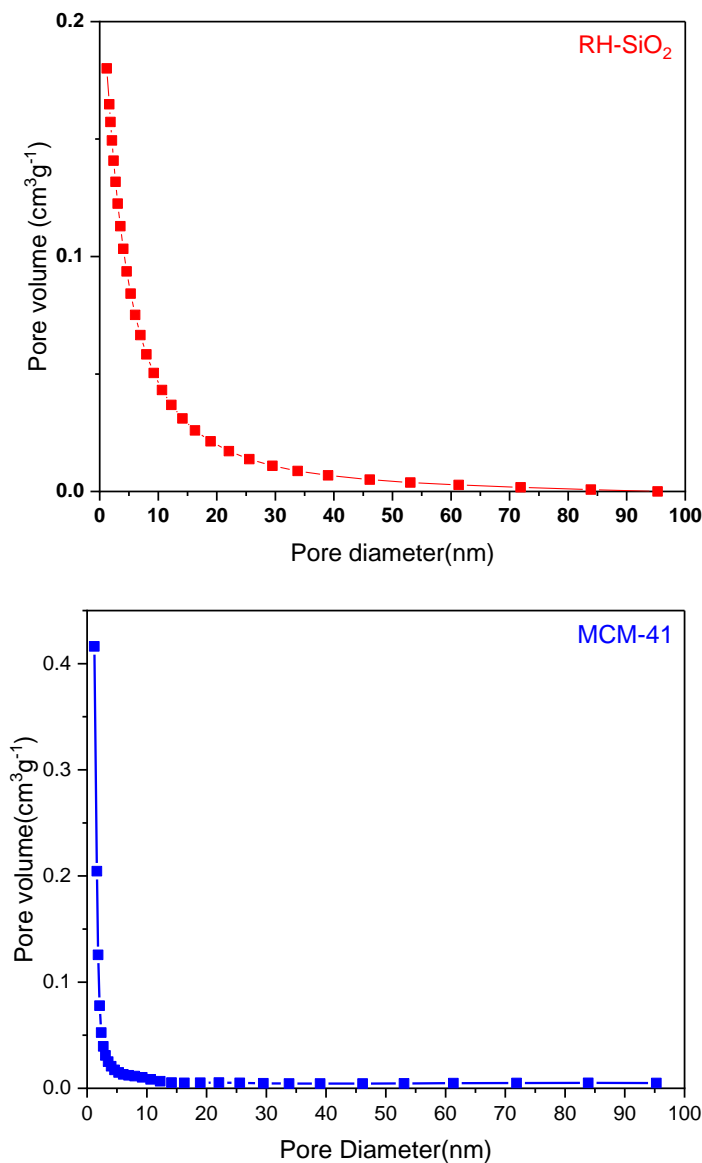


Figure (3.5): Pore size distributions for RH-SiO₂ and MCM-41

3.1.4 Thermogravimetric analysis (TGA/DSC):

Thermogravimetric analysis (TGA) is a technique that measures the mass loss of materials as a function of increasing temperature. The content of organic functional groups present in the mesoporous silica structure was determined using TGA technique. In a furnace, the sample is heated at a constant rate until it reaches temperature of 900 °C. A constant gas flow (inert gas or synthetic air) is applied in order to remove the desorbed

or combusted components from the compounds. The weight loss of the compounds is measured using a sensitive thermo balance while is being heated process, gives information on the amount of the organic functional groups as well as the temperature stability of the examined compounds[255].

The thermal stabilities of RH-SiO₂ and MCM-41 were investigated via the TGA/DSC analysis. Fig. (3.6) explained that there was loosing of 40.81% RH-SiO₂ weight due to the exothermic losing of 15% water molecules at 100°C. In the second step the exothermic decomposition due to modification in silica matrix leads to lose 25.8% of RH-SiO₂ weight.

The TGA result, Fig (3.7), exhibited two-stage mass production at approximately 15-900 °C for MCM-41. The initial step at 100 °C involved the exothermic elimination of water(15%) adsorbed due to physical/chemical processes on the silica surface, whilst the second(300-900) °C exothermic step involved the breakdown of Si-OH groups in the silica structure and their transformation into Si-O-Si siloxane groups(82.67%). The TGA spectrum showed that the compound has a good thermal stability [256, 257].

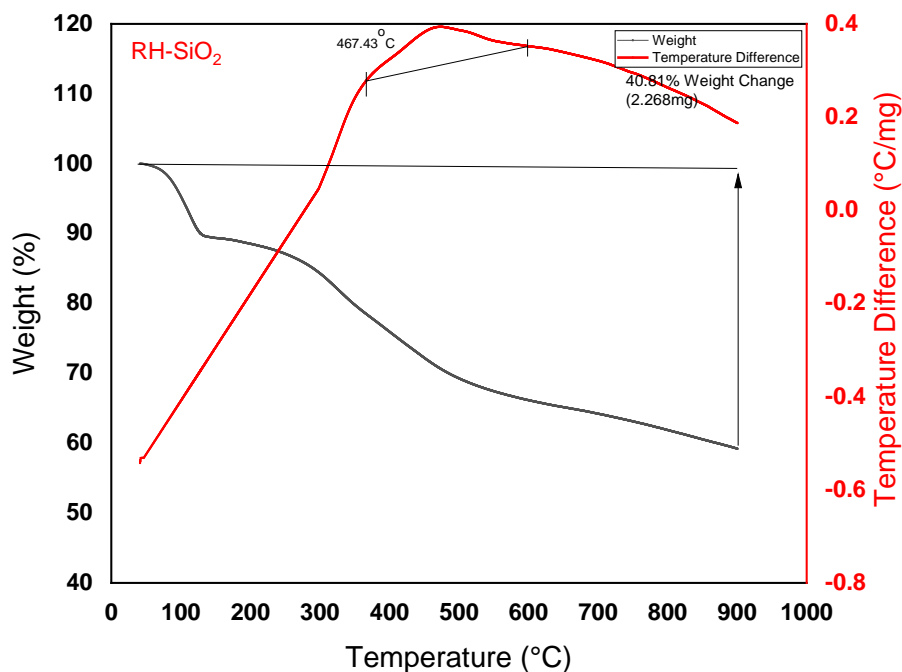


Figure (3.6): TGA/DSC plot of RH-SiO₂.

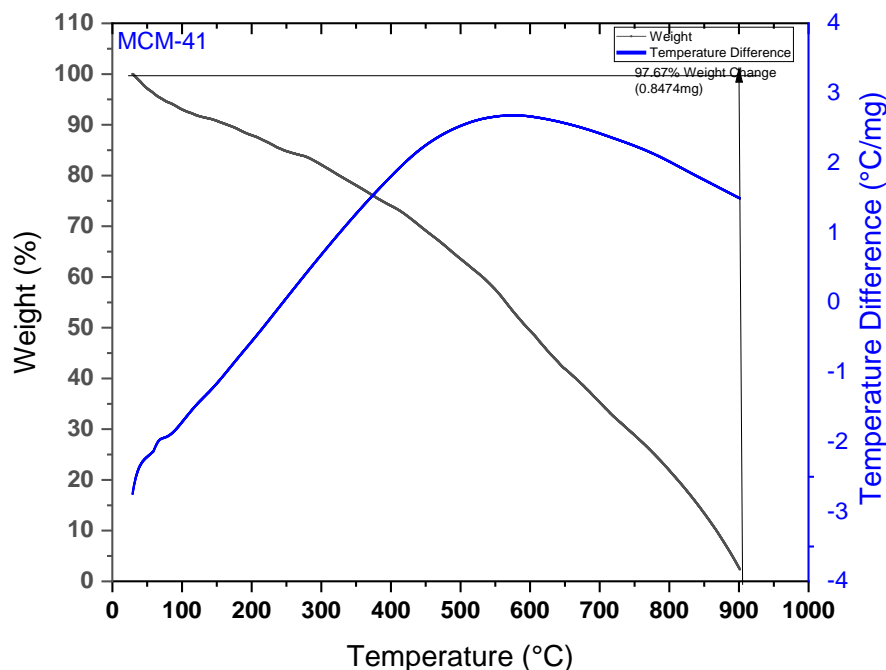


Figure (3.7): TGA/DSC plot of MCM-41.

3.1.5 Atomic force microscopy (AFM)

This type of microscope is used to measure the electron force between the tip at the end of a cantilever and the atoms at the surface of a specimen. The main advantages of an AFM over other related techniques are its high spatial resolution and ultra-low forces exerted at the surface. AFM makes it possible to image non-conducting materials, a requirement for the study of the polymer/silica interfaces[230]. Fundamental issues regarding interracial bonding and structure may be addressed by examining the fracture surface characterizations of topographic and morphological changes of the residual polymer and/or fiber surface as a result of a fracture process can lead to the understanding of adhesion and failure mode at a polymer/silica fiber interface. AFM is ideal to permits examination of surface topography at scales rang from micrometers to nanometers [230].The AFM has some benefits over other techniques. It can provide high spatial resolution (as high as 0.1 nm for the vertical resolution, and 1.0 nm for the lateral resolution)and ultra-low forces exerted at the surface (typically ranging from (10^{-6}) to (10^{-11}) N) [258].

The surface topographies for RH-SiO₂ and MCM-41 were demonstrated via AFM analysis, as shown in Fig. (3.8). It was found that the two-dimensional images of the RH-SiO₂ and MCM-41 topographies was unclear, while the three-dimensional images showed high and low topographies indicative of the surface roughness of the silica surface[256].The images for RH-SiO₂ show the presence of blocks of different shapes which due to agglomeration of nanoparticles[259].Table(3.2) shows the parameters obtained from AFM for the surfaces of the prepared compounds, RH-SiO₂ and MCM-41.

It is clear from this table that the roughness factor is low for the MCM-41, so its topography is smooth and clear in all electron microscopes, i.e., SEM, TEM, and AFM[260].

Table (3.2): AFM parameters of the RH-SiO₂ and MCM-41

Sample	Average roughness (Ra)	Root square roughness (Rms)	Average height (Sz)
RH-SiO ₂	0.8964 nm	1.10 nm	6.94 nm
MCM-41	0.702 nm	0.896 nm	7.90 nm

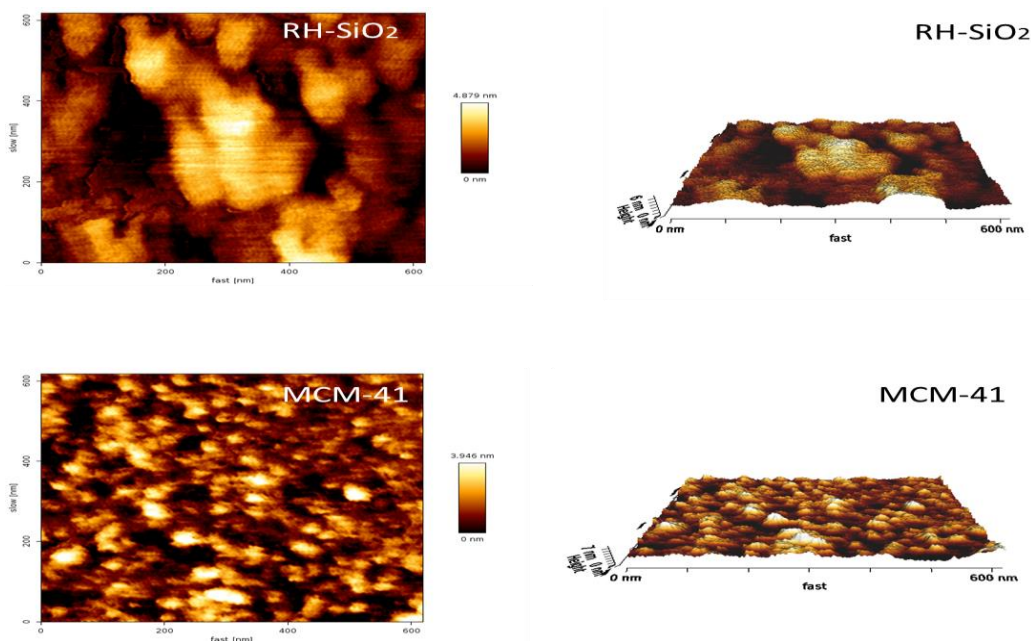


Figure (3.8): AFM 2D (on the left) and 3D (on the right) micrographs of RH-SiO₂ and MCM-41.

3.1.6 Field emission scanning electron microscopy-energy dispersive X-ray (FESEM and EDX)

FESEM and TEM were used to monitor the size and morphology of compounds prepared [261, 262]. Both techniques are similar because they both use electron microscopy. Both of these techniques were used to examine subatomic particles and composition of samples. These instruments make images have high resolution and highly magnified. But there are also some differences between FESEM and TEM, which are listed in a Table (3.3).

Table(3.3): Difference between FESEM and TEM[231][263].

	FESEM	TEM
Electron	Using scattered electrons	Using transmitted electrons
Image	The image produce after the microscope collects and counts the scattered collects electrons.	Electrons are straightforwardly pointed towards the sample.
Focus	Only on the samples surface.	On the surface of the samples and either inside or outside of the surface
Dimensional	Give image 3D	Give image 2D
Magnification	We can provide a maximum magnification level of two million.	We have the capability to magnify up to a level of 50 million.

FESEM images for RH-SiO₂ and MCM-41 are shown in Fig. (3.9). The images show that RH-SiO₂ is composed of amorphous silica, while for MCM-41 it is clear from the images that the particles are smooth with spherical agglomerations [264].

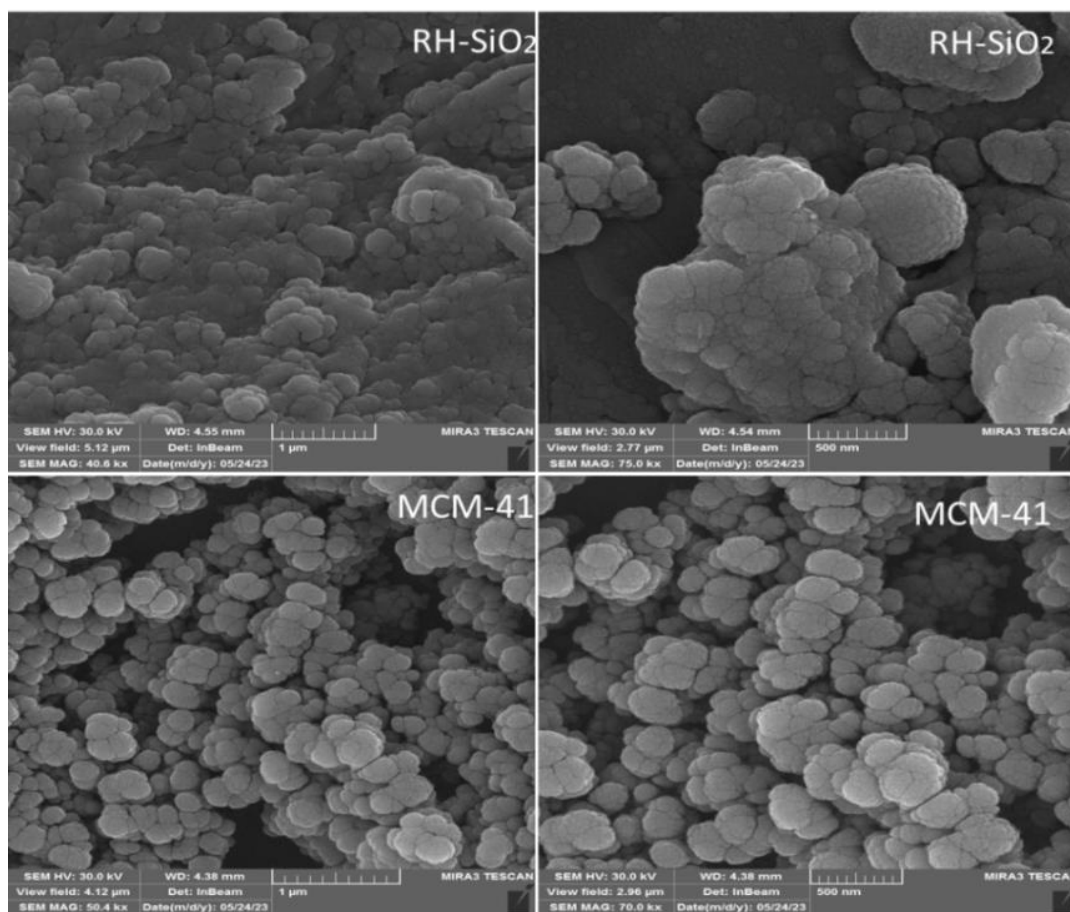


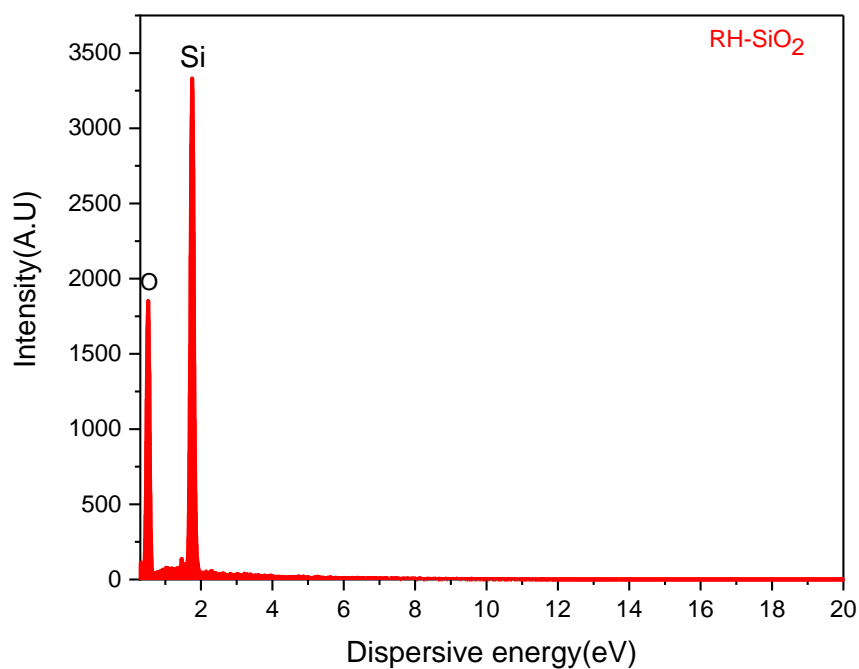
Figure (3.9): FESEM analysis for RH-SiO₂ and MCM-41 at scales of 500 nm and 1000 nm.

An elemental analysis method related to scanning electron microscopy called energy dispersive X-ray (EDX) spectroscopy relies on the generation of distinctive X-rays that indicate the presence of elements in the samples. EDX microanalysis is widely used in several biomedical fields by scientists and physicians. The most prevalent element in these samples, according to the EDX chemical analysis, is silicon (Si). The uneven surface of this material can facilitate metal adsorption because of its shape [233].

According to EDX analysis, the existence of silicon and oxygen in the solid ligand are demonstrated in Figs. (3.10), (3.11) and Tables (3.4); which indicates that MCM-41 and RH-SiO₂ had been successfully prepared.

Table (3.4):The average values obtained from EDX analysis for RH-SiO₂ and MCM-41

	Elements	Average mass (%)
RH-SiO₂	Si	42.62
	O	57.38
MCM-41	Si	36.09
	O	63.91

**Figure (3.10):** EDX analysis for RH-SiO₂.

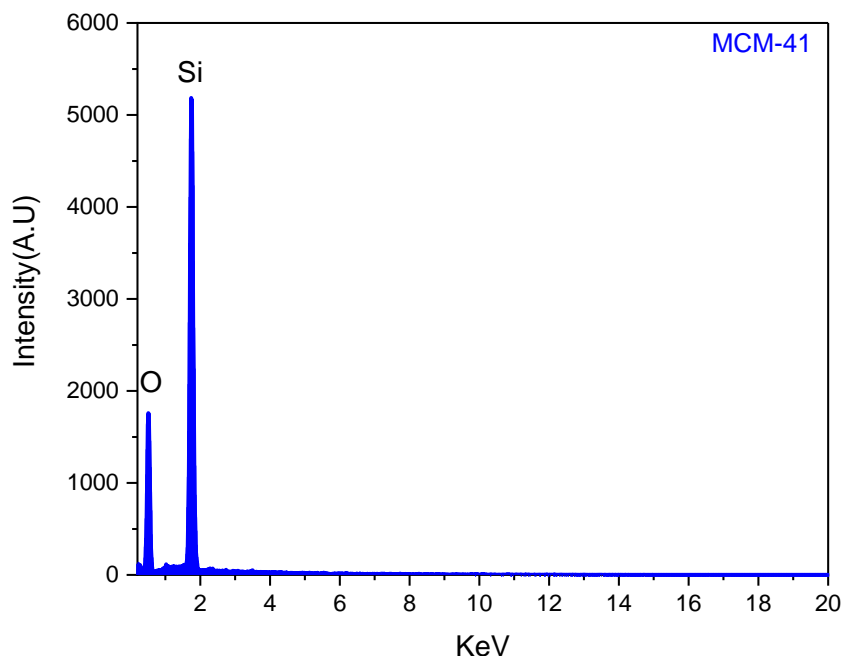


Figure (3.11): EDX analysis for MCM-41.

3.1.7 Transmission electron microscopy (TEM)

TEM analysis was conducted to acquire further information regarding the structural characteristics of the two substances (RH-SiO₂ and MCM-41). It is clear from the image in Figs. (3.12) and (3.13) that some of the particles of RH-SiO₂ are spherical whilst others have longitudinal slits, with irregularly agglomerated aggregates which indicates the particles shape is amorphous[265]. In contrast, the TEM images for MCM-41, indicate its hexagonal honeycomb structure [266, 267].The average diameter is between (2-50) nm, which corresponds to the average diameter of mesoporous materials [264].

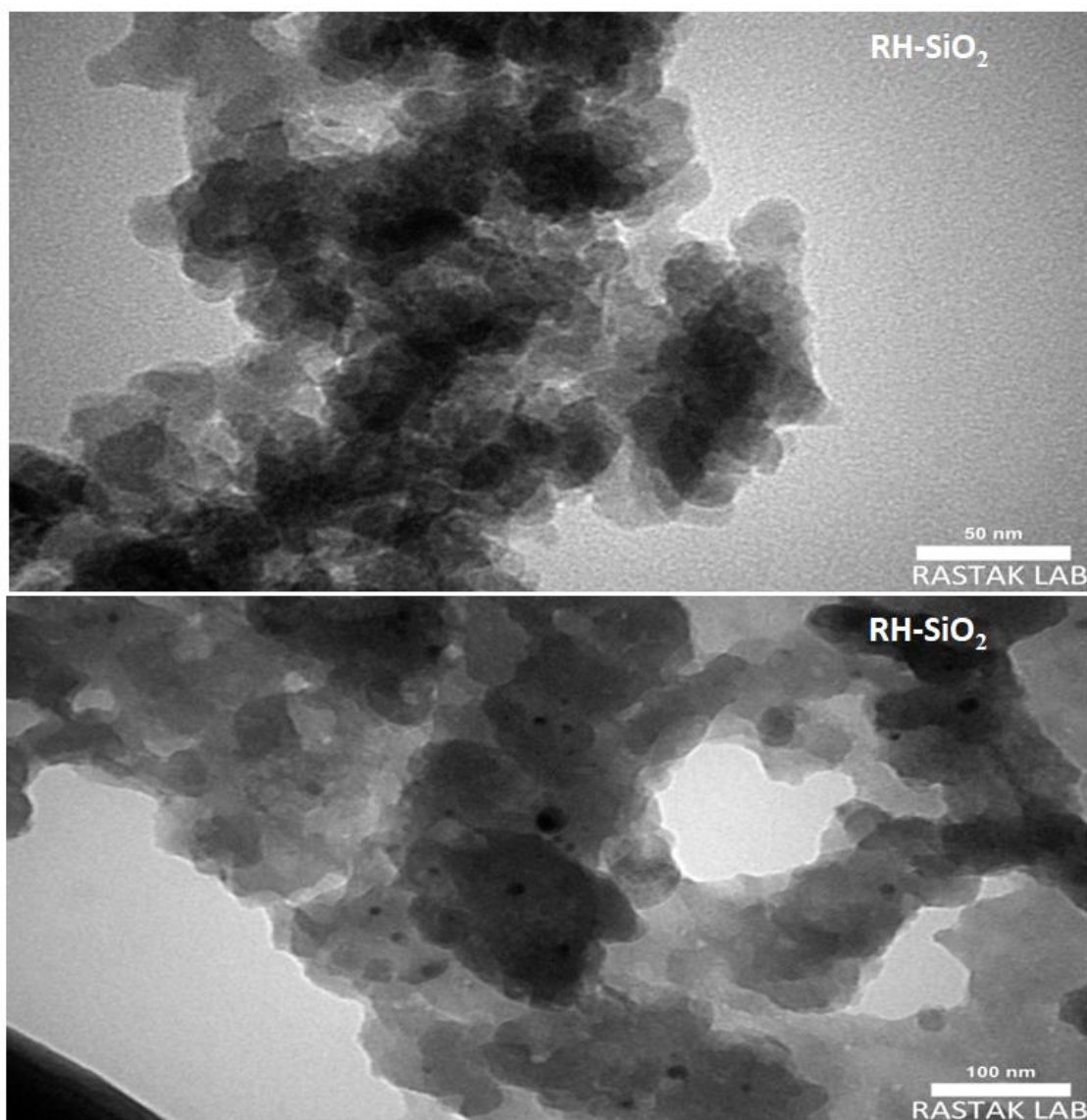


Figure (3.12): TEM images for RH-SiO₂ at scales of 50 nm and 100 nm.

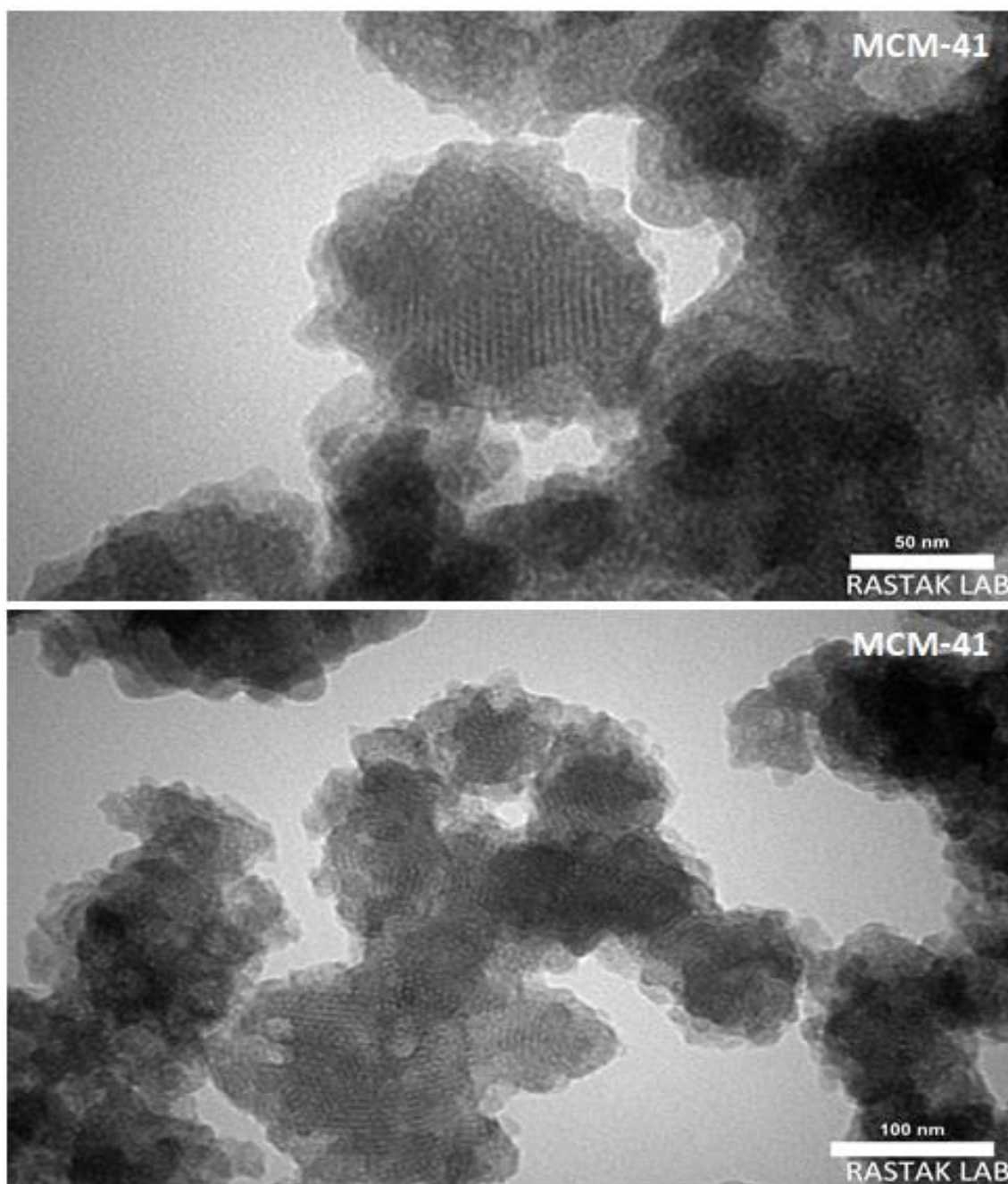


Figure (3.13): TEM images for MCM-41 at scales of 50 nm and 100 nm.

3.2 The characterization of MCM-41@APTES

There are no active sites on the surface of silica without an additional or modification, consequently, their utilization is restricted to specific methods, thereby necessary modification to their outer covering as per requirements. In order to maximize the unique capabilities of mesoporous materials such as sensing, ion exchange, adsorption and

catalysis, it is necessary to introduce reactive organic functional groups. The primary challenge is to incorporate organic components into silicate walls or trap them within channels to synthesize inorganic-organic hybrid materials. Inorganic-organic hybrid materials are a class of materials that combine the properties of both inorganic and organic materials. This makes them highly versatile and useful for a variety of application [268, 269].

The synthesis of MCM-41@APTES was maintained via immobilization of (3-Aminopropyl)triethoxysilane onto MCM-41 through heterogeneous reaction. The reaction mixture was refluxed in toluene for 24 hrs., producing the products. The structure of MCM-41@APTES was characterized using various techniques.

3.2.1 Elemental analysis

The elemental analysis result of MCM-41@APTES was tabulated in Table (3.5). The elemental analysis of MCM-41@APTES reveals the existence of nitrogen was found to be 0.8 %. While MCM-41 do not contain this element. The result confirmed the appearance of carbon in the analysis of MCM-41@APTES. These results clearly indicate that the (3-Aminopropyl)triethoxysilane was successfully immobilized onto MCM-41 [270].

Table 3.5: The percentage of elements present in MCM-41@APTES that can be found through elemental analysis.

sample	Elemental analysis %			
	C	H	N	S
MCM-41@APTES	7.45	4.32	0.80	-----

3.2.2 Fourier–transform infrared spectroscopic analysis (FT-IR)

Fig.(3.14) shows the FT-IR analysis of the MCM-41@APTES that prepared in this study. The spectra show how MCM-41 change when (3-Aminopropyl)triethoxysilane is added.

The FT-IR spectra of MCM-41@APTES Fig. (3.14) showed a number of absorption bands for silanol groups (Si-OH), which was greatly reduced compared with MCM-41; this indicates successful anchoring of (3-aminopropyl)triethoxysilane. The wide peak at 3000-3200 cm^{-1} can be attributed to free NH_2 . The bending vibration of N-H (primary amine) appears at 1520 cm^{-1} , while the peak at $\sim 1390\text{cm}^{-1}$ can be attributed to the combination of the stretching of the C-N group in primary amine. Distinct bands at 1090, 935 and 445 cm^{-1} can be attributed to the symmetric and ant symmetric stretching modes of Si-O-Si [254].

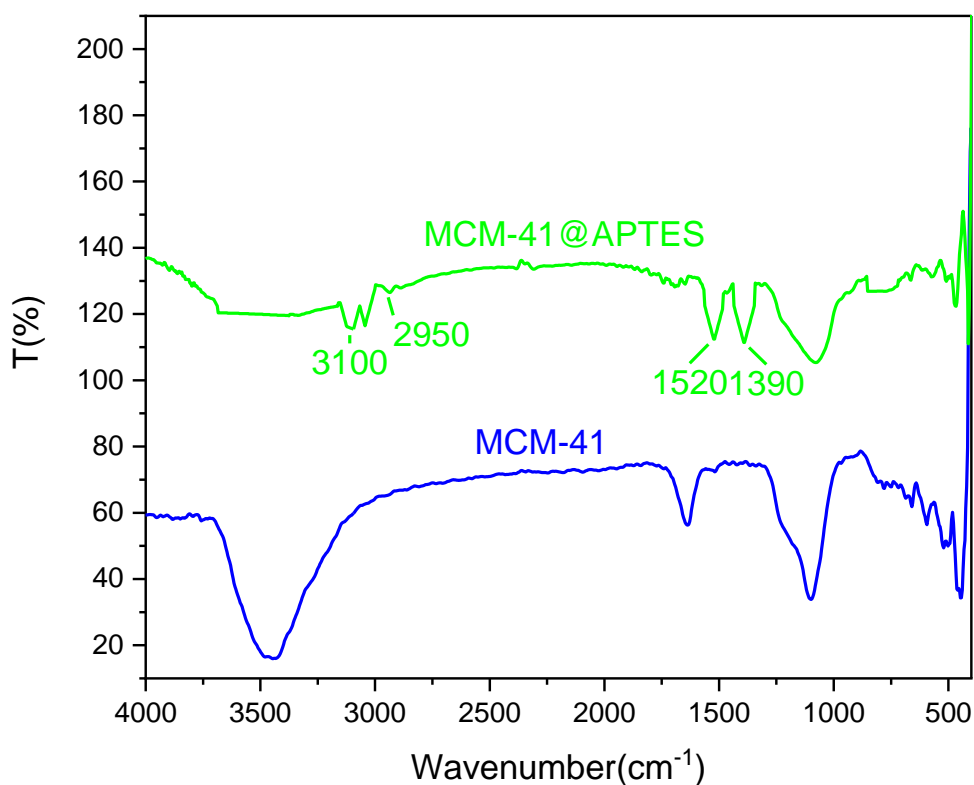


Figure (3.14): FTIR spectra for MCM-41@APTES and starting material.

3.2.3 X-ray powder diffraction (XRD)

Fig. (3.15) illustrates the XRD analysis of low angle for MCM-41@APTES. The peak at around 2.17(100) appeared due to the hexagonal structure of mesoporous present in MCM-41@APTES. This can be confirmed due to TEM images in Fig.(3.23). Filling the honeycomb structure of mesoporous may be led to lower peak intensity of MCM-

41@APTES compared to MCM-41 peak[271]. The high angle XRD pattern Fig.(3.16) showed the absence of distinct peaks in the X-ray diffraction pattern indicates the amorphous nature of the samples, with only a wide diffraction peak visible around 22 degrees[249, 272].

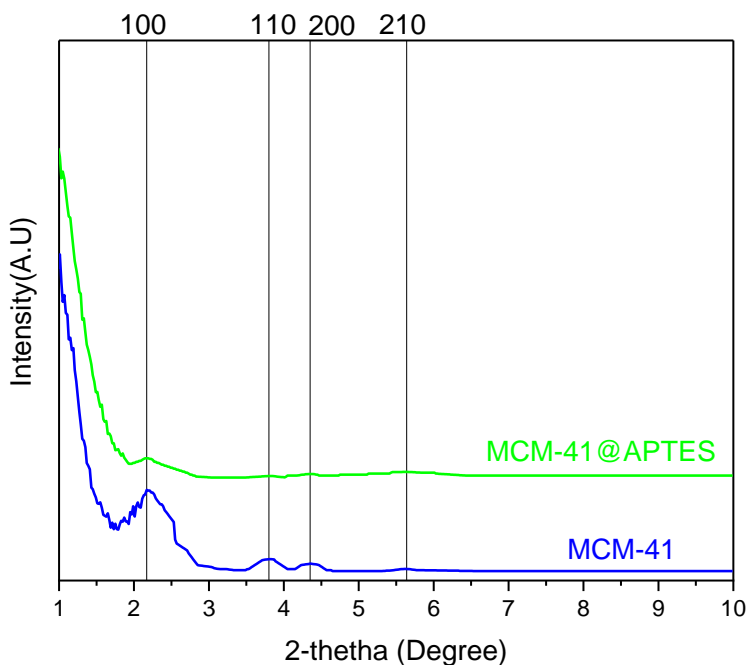


Figure (3.15): XRD spectra (Low angle) for MCM-41@APTES and starting material.

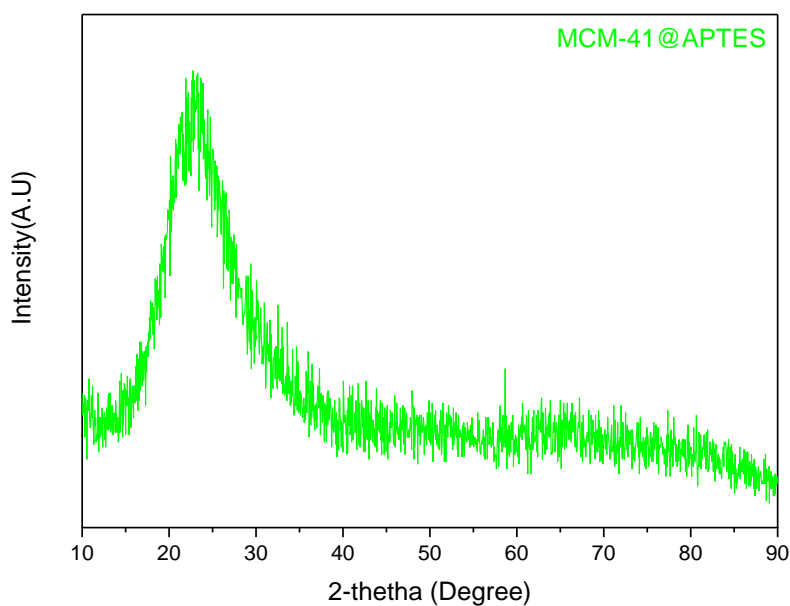


Figure (3.16): XRD spectrum (High angle) for MCM-41@APTES.

3.2.4 Nitrogen adsorption-desorption analysis

The nitrogen adsorption isotherms for MCM-41@APTES is shown in Fig. (3.17). The hysteresis loop was detected in MCM-41@APTES within the range from $0.4 < P/P_0 < 1$, associated with capillary condensation as per in the IUPAC classification. The sample MCM-41@APTES exhibited type IV isotherm with H3 hysteresis loop, which is characteristic for mesoporous solids[254]. The BET analysis revealed that the specific surface area, the total pore volume and average pore diameter were illustrated in Table (3.6). According to the BET plots, MCM-41@APTES porosities changed but they still had a narrow pore width distribution, which is typical for MCM-41 derivative materials[273]. The pore volumes and surface areas of MCM-41@APTES decreased significantly compared to MCM-41. This suggests that the hexagonal pores at the surface are being blocked by large ligand molecules when immobilizing (3-Aminopropyl)triethoxysilane onto MCM-41, The average pore size between (2 and 10 nm) within the range of mesoporous compounds as shown in Fig.(3.18) [271].

Table (3.6): BET analysis for MCM-41@APTES and starting materials.

Compounds	BET surface area ($\text{m}^2.\text{g}^{-1}$)	Total pore volume ($\text{cm}^3.\text{g}^{-1}$)	Average pore diameter (nm)
RH-SiO ₂	390.12	0.33	3.47
MCM-41	548.92	0.94	6.85
MCM-41@APTES	155.19	0.29	7.53

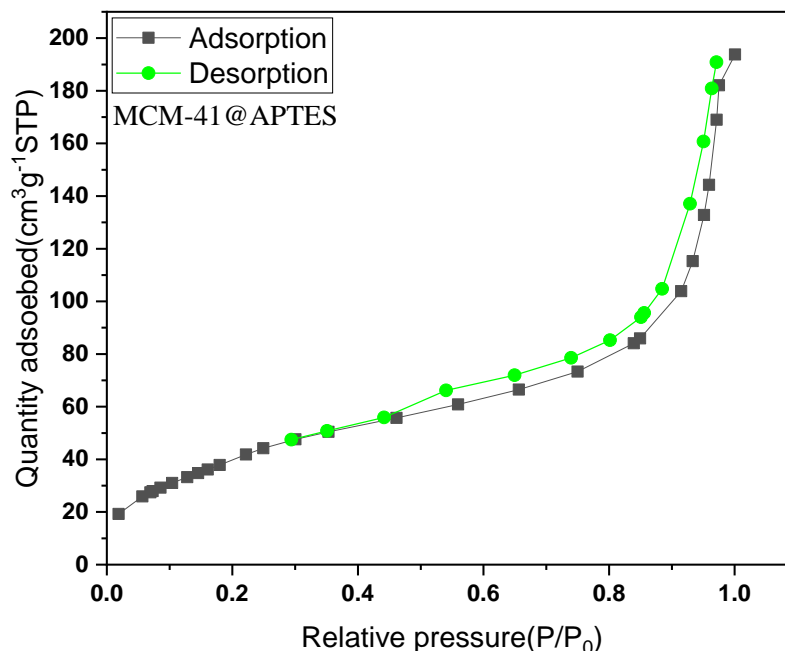


Figure (3.17): N_2 adsorption–desorption isotherms of MCM-41@APTES

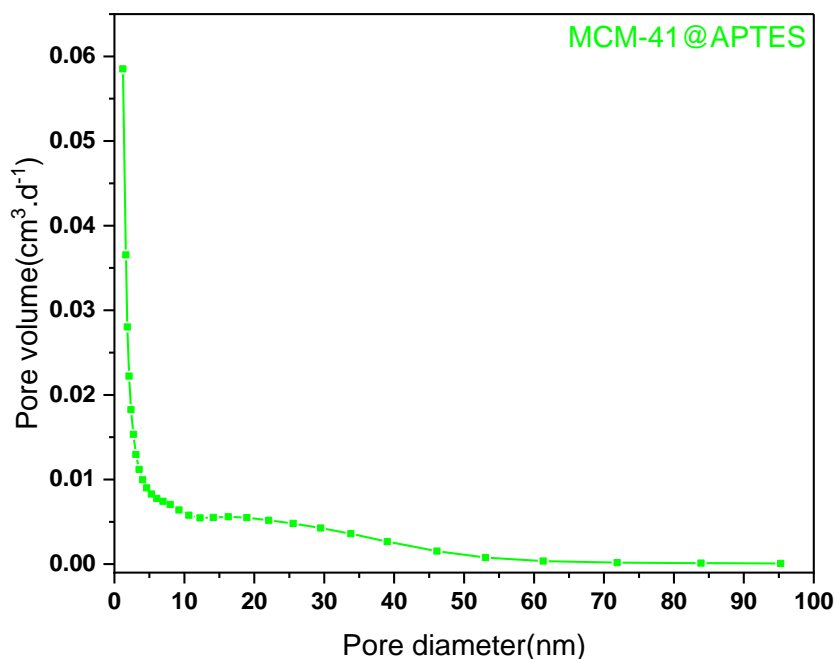


Figure (3.18): Pore size distribution of MCM-41@APTES.

3.2.5 Thermogravimetric analysis (TGA/DSC):

The thermogravimetric analysis of the TGA/DSC ranged from 15 to 900°C. Fig. (3.19) refers to the TGA of the MCM-41@APTES which showed a three stage of decomposition. The initial step (100°C) was a mass exothermic loss(10%) of is attributed

to the absorbed water on the silica surface. The second mass exothermic loss(300-450°C) to decomposition of organic moiety(18%) for MCM-41@APTES a third exothermic step(500-900°C)(35%) involved breakdown of Si-OH groups in the silica structure and transforming them into Si-O-Si siloxane group[256, 274]. The results show that the synthesis procedure was successful and that a high-stability material was produced.

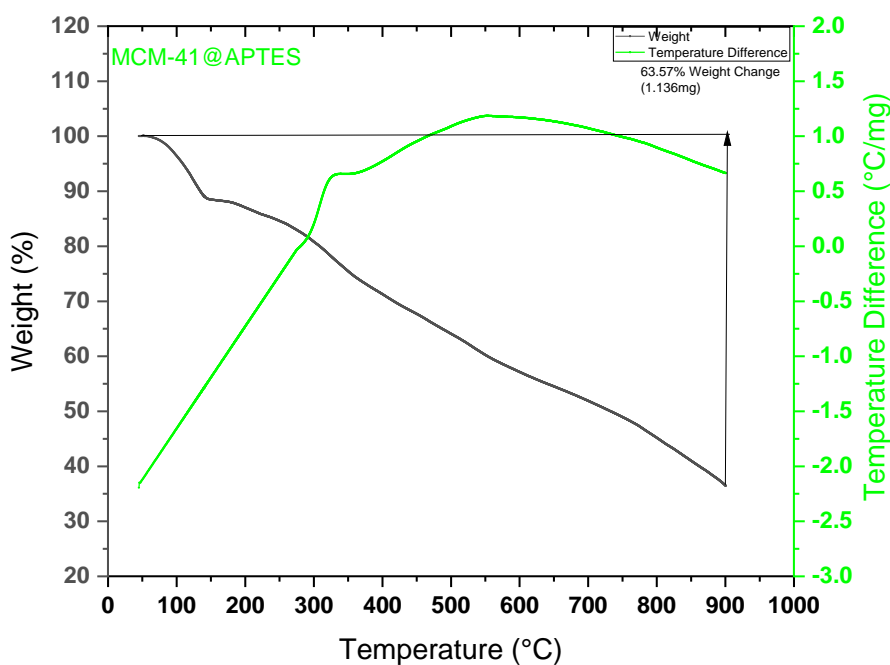


Figure (3.19): TGA/DSC plot of MCM-41@APTES.

3.2.6 Atomic force microscopy (AFM)

The surface topographies of MCM-41@APTES have been determined through the AFM analyses shown in Fig.(3.20).It was found that two-dimensional images of MCM-41@APTES topographies was unclear with blocks due to increase the rate of agglomeration of the materials. While the three-dimensional image showed the high and low topography responsible for the surface roughness of the silica surface[247].The parameters obtained from AFM for the surface of the prepared compounds, MCM-41@APTES is illustrated in Table(3.7), which indicates that the roughness factor for MCM-41@APTES, indicating the relatively roughness topography. The increase in the

AFM parameter for MCM-41@APTS compare with MCM-41 is due to the increase in the rate of agglomeration of particle [259].

Table (3.7): AFM parameters for MCM-41@APTES.

Sample	Average roughness (Ra)	Root square roughness (Rms)	Average height (Sz)
MCM-41	0.702 nm	0.896 nm	7.900 nm
MCM-41@APTES	1.161 nm	1.585 nm	12.090 nm

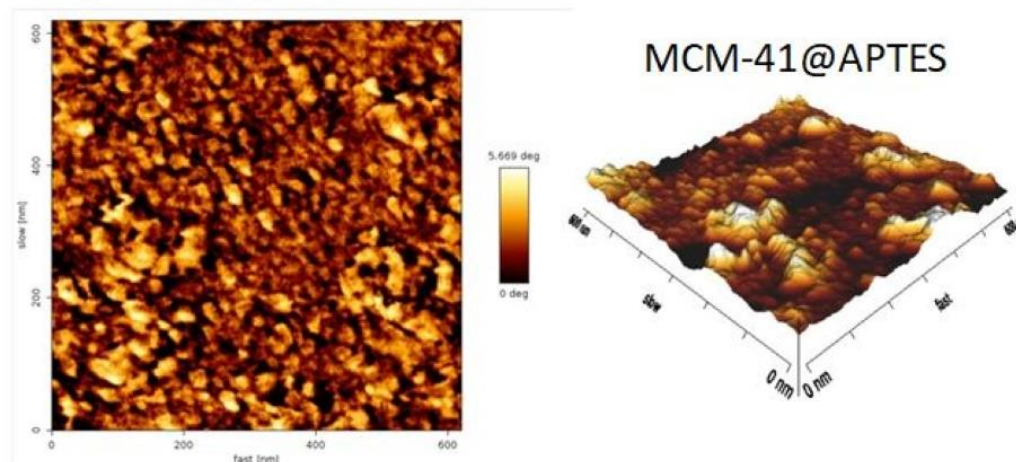


Figure (3.20): AFM 2D (on the left) and 3D (on the right) micrographs of MCM-41@APTES.

3.2.7 Field emission scanning electron microscopy-energy dispersive X-ray (FESEM and EDX)

Images of FESEM related to MCM-41@APTES showed in Fig.(3.21). From the images that the particles are smooth with spherical agglomeration [264].

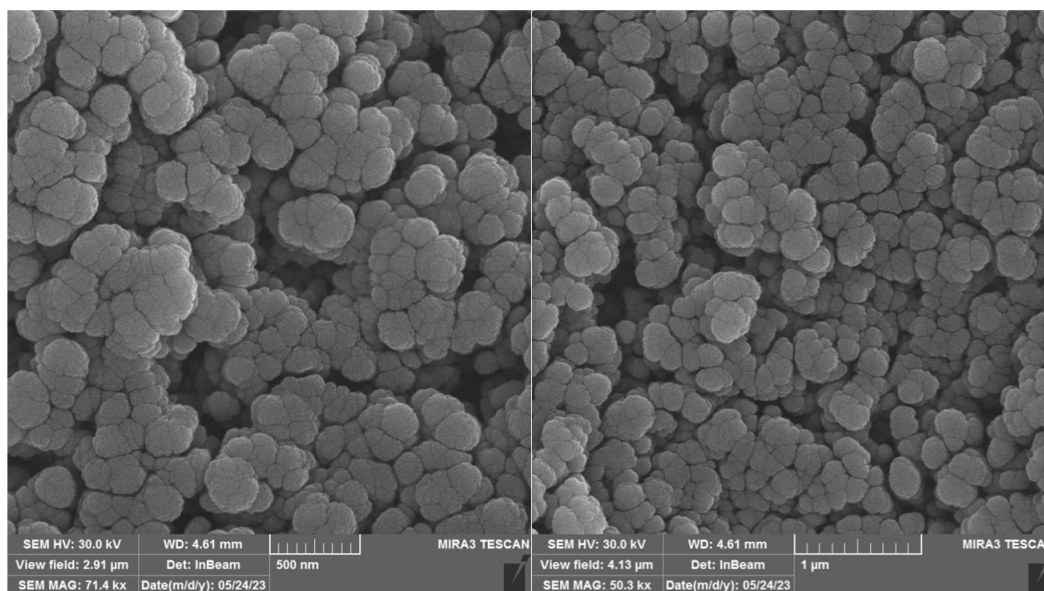


Figure (3.21): FESEM analysis for MCM-41@APTES at scales of 500 nm and 1000 nm.

According to EDX analysis, existence of silicon and oxygen in addition to nitrogen and carbon in the solid ligand (MCM-41@APTES) were a proved as shown in Fig.(3.22).It can be further concluded that the MCM-41 was incorporated on the (3-Aminopropyl)triethoxysilane. Table (3.8) shows the average values obtained from the EDX analysis of MCM-41@APTES.

Table (3.8): The average values obtained from EDX analysis for MCM-41@APTES.

Elements	Average mass (%)
Si	9.83
O	42.09
N	8.80
C	39.27

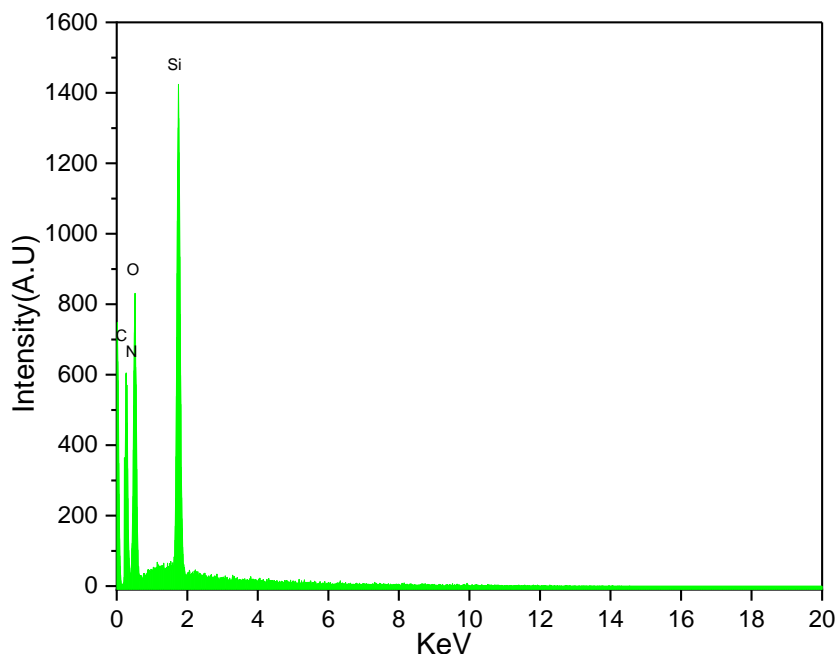


Figure (3.22): EDX analysis for MCM-41@APTES.

3.2.8 Transmission electron microscopy(TEM)

TEM analysis was conducted to acquire further information regarding the structural characteristic of MCM-41@APTES. The TEM images proved the hexagonal honeycomb structure as shown in Fig.(3.23) [266, 271]. The honeycomb structure of the MCM-41@APTES not clearly preserved after functionalization of MCM-41 with 3-aminopropyltriethoxysilane, because immobilization of large organic compounds on the MCM-41 causing the surface is occupied with the ligand and blocking the pores. The compounds exhibited ordered porous structure consistent with previous work on MCM-41[248]. The average diameter of particals between (20-50) nm was corresponding to the average diameter of mesoporous materials[264] .

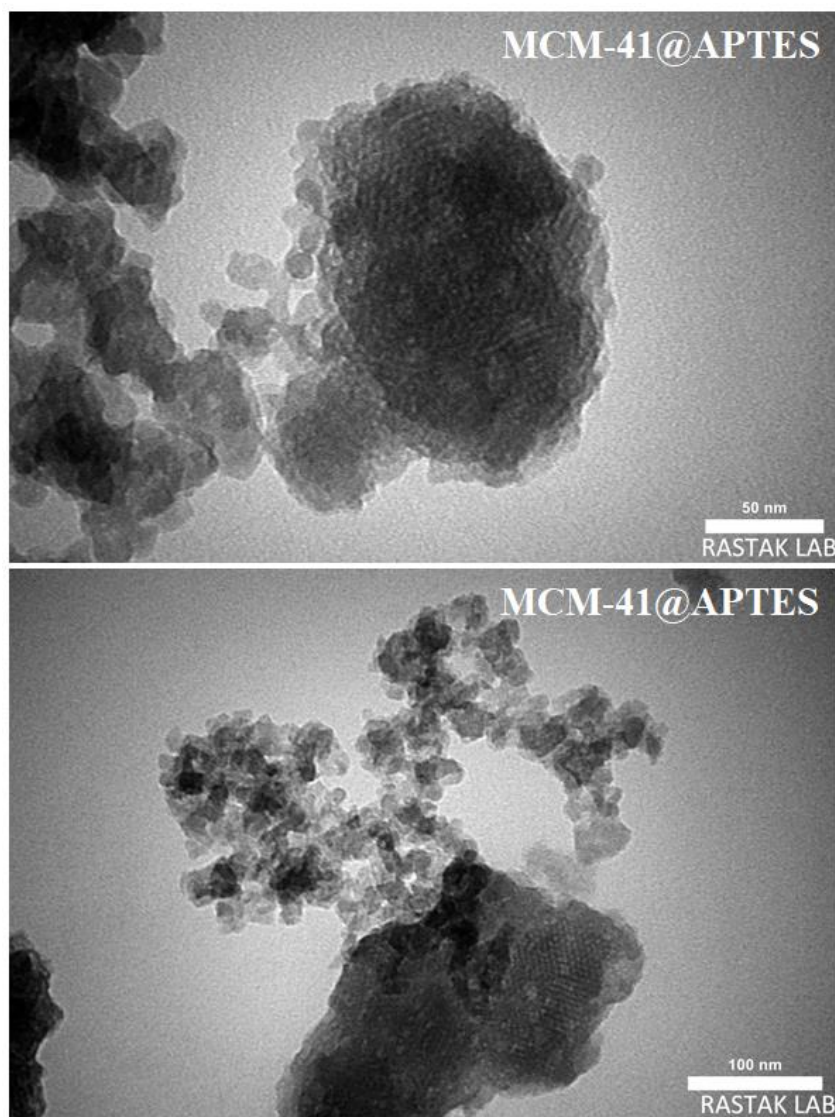


Figure (3.23): TEM images for MCM-41 @ APTES at different scale.

3.3 The characterization of MCM-41 @ APTES-BSAL

Heterogeneous reaction was used to immobilize 5-Bromosalicylaldehyde onto MCM-41 @ APTES. The reaction was refluxed in toluene for 24 hrs., yielding the product. The structures of MCM-41 @ APTES-BSAL were characterized using various techniques.

3.3.1 Elemental analysis

The elemental analysis (Table 3.9) of MCM-41@APTES-BSAL showed that the percentages of carbon and hydrogen were 11.28 and 8.1 respectively which were greater than those of MCM-41@APTES. Based on these findings, it can be concluding that the 5-Bromosalicylaldehyde was indeed incorporated into MCM-41@APTES.

Table (3.9): The percentage of elements present in MCM-41@APTES-BSAL and starting materials that can be found through elemental analysis.

Sample	Elemental analysis %			
	C	H	N	S
MCM-41@APTES	7.45	4.32	0.80	-----
MCM-41@APTES-BSAL	11.28	8.10	3.30	-----

3.3.2 Fourier –transform infrared spectroscopic analysis (FT-IR):

FTIR spectrum of MCM-41@APTES-BSAL is illustrated in Fig.(3.24). The hydroxyl vibration band can be seen to have shifted to around 3400 cm^{-1} . The stretching vibration of C-H aliphatic and aromatic groups is responsible for low intensity bands at ~ 3000 and 2500 cm^{-1} , respectively [245]. Schiff base ligand formation could be inferred due to the presence of the $\text{C}=\text{N}^{\bullet}$ group, which overlaps with H_2O bending and the double bond at 1640 cm^{-1} [275]. This provides substantial evidence that the reaction between MCM-41@APTES and 5-bromosalicylaldehyde produced C–O, whose vibrational band appears at around $1000\text{--}1300\text{ cm}^{-1}$ [271].

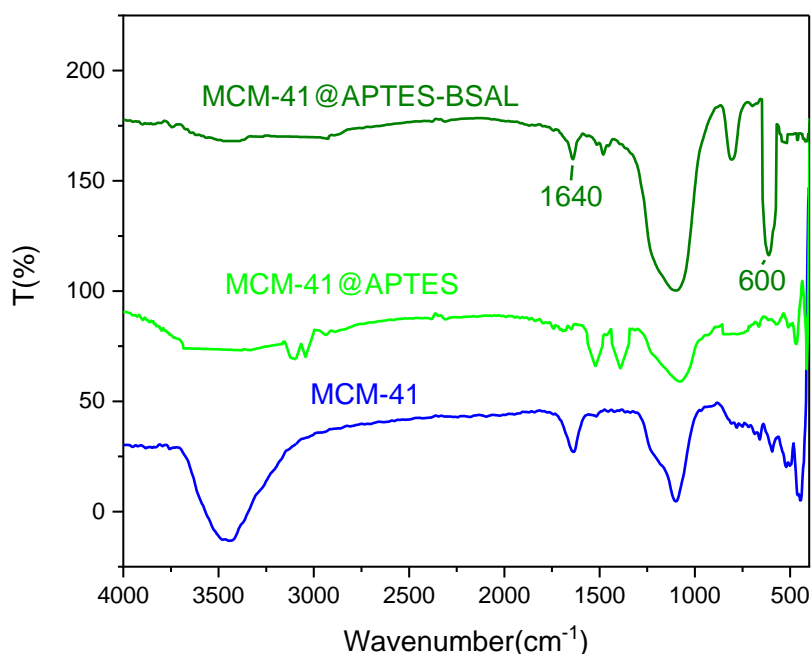


Figure (3.24): FTIR spectra for MCM-41@APTES-BSAL and starting materials.

3.3.3 X-ray powder diffraction (XRD):

XRD analysis at low and high angle for MCM-41@APTES-BSAL are presented in Figs.(3.25) and(3.26), respectively. The weak peak at around $2.17(100)$ is appeared due to the hexagonal structure of mesoporous present in MCM-41@APTES-BSAL. This can be confirmed due to TEM images in Fig.(3.33). Filling the honeycomb structure of mesoporous may be led to lower peak intensity of MCM-41@APTES-BSAL compared to MCM-41@APTES and MCM-41 peaks[271].The high angle XRD pattern (Fig.(3.25)) showed a broad peak at 22° from 2 theta due to the amorphous structure of the MCM-41@APTES-BSAL[249].

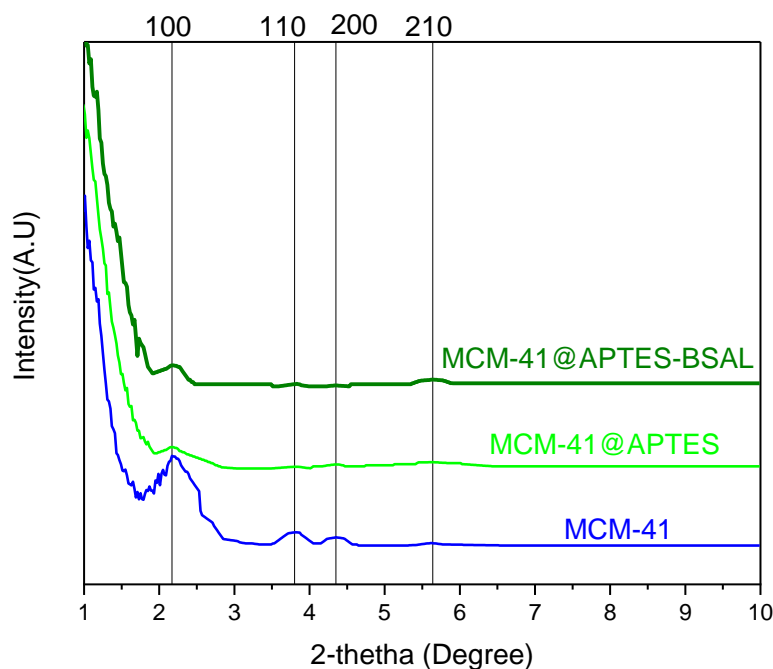


Figure (3.25): spectra (Low angle) for MCM-41@APTES-BSAL and starting materials.

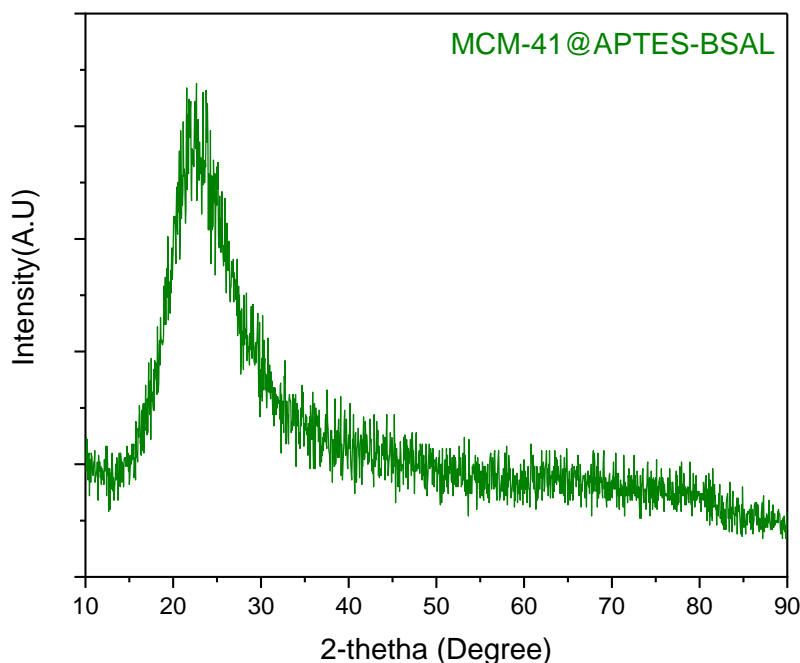


Figure (3.26): XRD spectrum (High angle) for MCM-41@APTES-BSAL.

3.3.4 Nitrogen adsorption-desorption analysis:

The specific surface area and the pore size distribution can be demonstrated via N_2 adsorption-desorption analysis. From the results represented in Fig.(3.27) and Table(3.10), the specific surface area, the total pore volume and average pore diameter

illustrated in Table (3.10). According to BET plots, the samples porosity changed, but they still had a narrow pore width distribution, which is typical for MCM-41 derivative materials[273].The hysteresis loop was detected for MCM-41@APTES-BSAL within the range from $0.4 < P/P_0 < 1$, associated with capillary condensation as per in the IUPAC classification. For Mesoporous solid, type IV is the dominant isotherm with H3 hysteresis loop. The sample exhibited type IV isotherm with H3 hysteresis loop, which is characteristic for mesoporous solids [254].

Table (3.10): BET analysis for MCM-41@APTES-BSAL and starting materials.

Compounds	BET surface area ($\text{m}^2\cdot\text{g}^{-1}$)	Total pore volume ($\text{cm}^3\cdot\text{g}^{-1}$)	Average pore diameter (nm)
RH-SiO ₂	390.12	0.33	3.47
MCM-41	548.92	0.94	6.85
MCM-41@APTES	155.19	0.292	7.53
MCM-41@APTES-BSAL	17.491	0.055	12.654

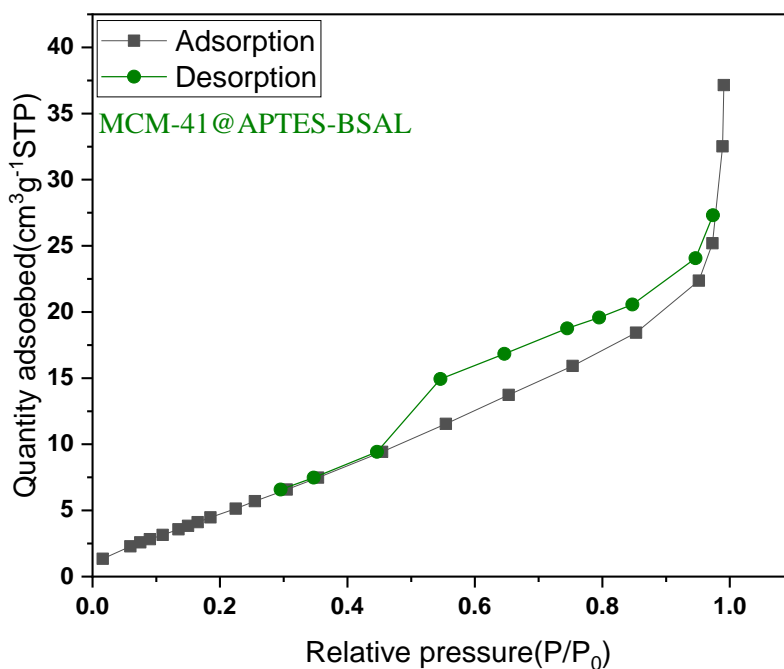


Figure (3.27): N₂ adsorption–desorption isotherms of MCM-41@APTES-BSAL.

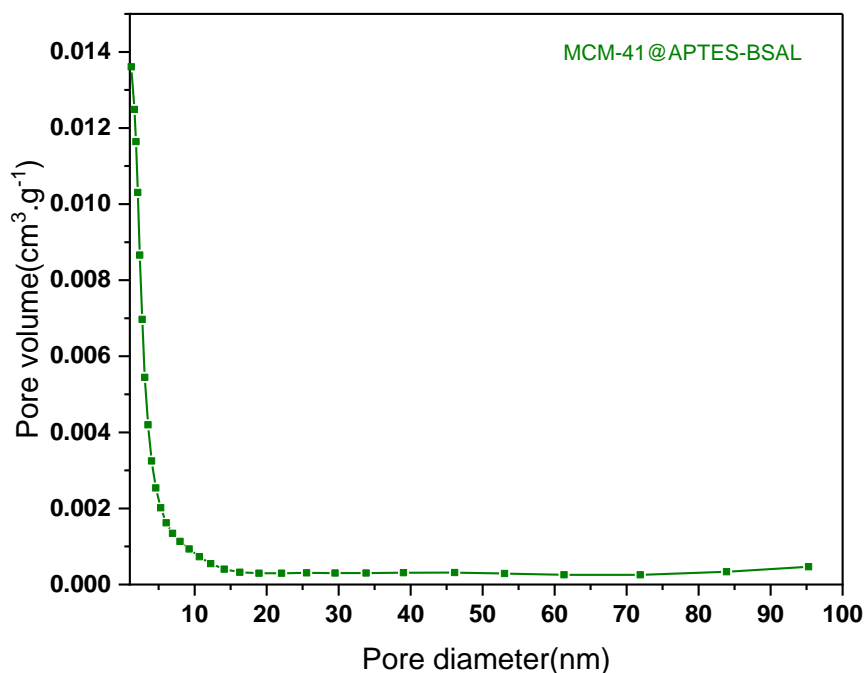


Figure (3.28): Pore size distribution of MCM-41@APTES-BSAL.

The pore volume and surface area of MCM-41@APTES-BSAL decreased significantly compared to MCM-41 and MCM-41@APTES. This means that the hexagonal pores in the surface are being blocked by large molecules of ligand [276]. Fig. (3.28) shows the average pore size between (2 and 10 nm) within the range of mesoporous compounds [271].

3.3.5 Thermogravimetric analysis (TGA/DSC):

The TGA/DSC analysis was done between 15 and 900°C. Fig. (3.29) displays the TGA/DTA of MCM-41@APTES-BSAL, which demonstrates three distinct stages of decomposition. The first step (100°C) showed an exothermic loss of weight (10%) is attributed to water absorbed on the silica surface. The second mass an endothermic loss (150-300°C) (15%) is attributed to the decomposition of organic moiety for MCM-41@APTES-BSAL. The third mass an exothermic loss (500-900) (14%) is attributed to the decomposition of silanol groups and also to the remaining decomposition of the remaining organic part [256, 274]. The results show that a high-stability material was produced.

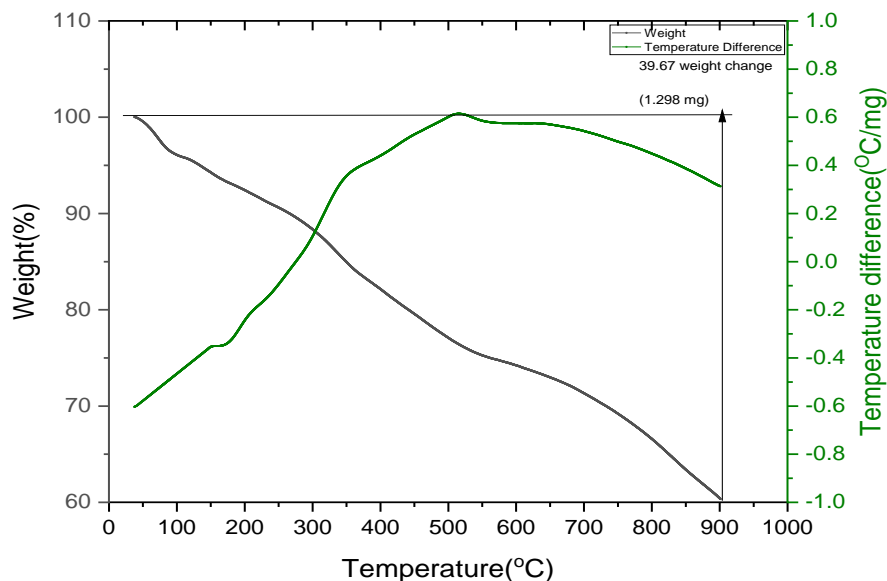


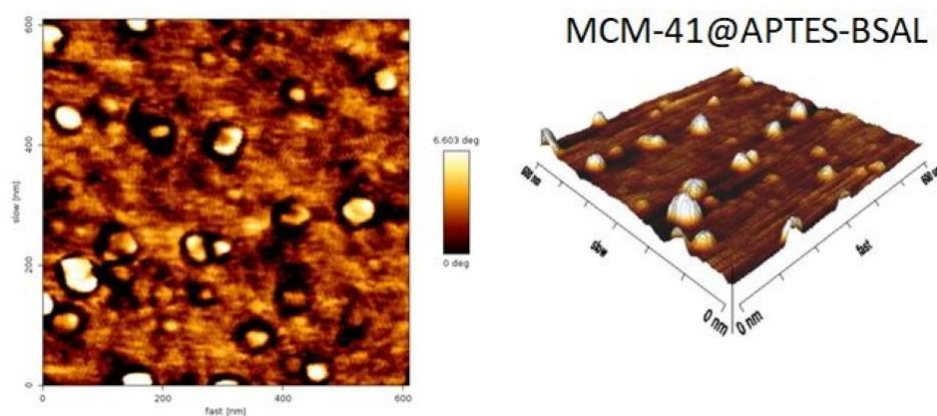
Figure (3.29): TGA-DSC plot of MCM-41@APTES-BSAL.

3.3.6 Atomic force microscopy (AFM)

AFM technique used to investigate the topography of the ligand surface of MCM-41@APTES-BSAL. Fig(3.30) has shown the atomic force microscopy (AFM) images and granularity normal distribution of the MCM-41@APTES-BSAL. The results showed that average roughness of MCM-41@APTES-BSAL decreased upon functionalization of MCM-41@APTES with 5-Bromosalicylaldehyde from 1.161 nm to 0.429nm. This may be attributed to the successful modification of the surface of the ligand from MCM-41@APTES to MCM-41@APTES-BSAL, increase the bonding between 5-Bromosalicylaldehyde with MCM-41@APTES, which leads to a decrease in the surface roughness and the disappearance of nanoparticle clusters[277]. Moreover, AFM findings root square roughness (Rms) and an average height (S_z) in Table (3.11).

Table (3.11): AFM parameters for MCM-41@APTES-BSAL and starting materials.

Sample	Average roughness (Ra)	Root square roughness (Rms)	Average height (Sz)
MCM-41	0.702 nm	0.896 nm	7.9 nm
MCM-41@APTES	1.161 nm	1.585 nm	12.09 nm
MCM-41@APTES-BSAL	0.4294 nm	0.7608 nm	9.201 nm

**Figure (3.30):** AFM 2D (on the left) and 3D (on the right) micrographs of MCM-41@APTES-BSAL.

3.3.7 Field emission scanning electron microscopy-energy dispersive X-ray (FESEM and EDX).

The surface characteristic of MCM-41@APTES-BSAL was examined by using FESEM analysis. The findings are shown in Fig.(3.31). This study found that the particles smooth with spherical agglomeration, and is in agreement with the shape and size of MCM-41 [278].

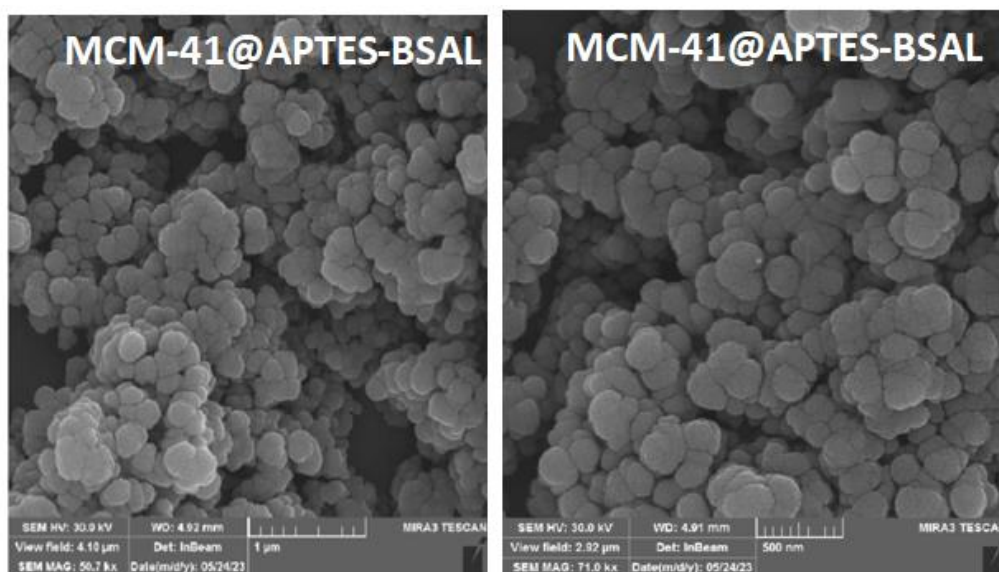


Figure (3.31): FESEM analysis for MCM-41@APTES-BSAL at scales of 500 nm and 1000 nm.

EDX analysis of MCM-41@APTES-BSAL showed in Fig. (3.32) explained that the compounds contained carbon, nitrogen, bromine, in addition to oxygen and silicon elements in the complex, from which it can further concludes that the 5-bromosalicylaldehyde was incorporated on the MCM-41@APTES. Table (3.12) shows the average values obtained from the EDX analysis of MCM-41@APTES-BSAL.

Table (3.12): The average values obtained from EDX analysis for MCM-41@APTES-BSAL.

Elements	Average mass (%)
Si	21.88
O	50.43
Br	3.65
N	7.32
C	16.72

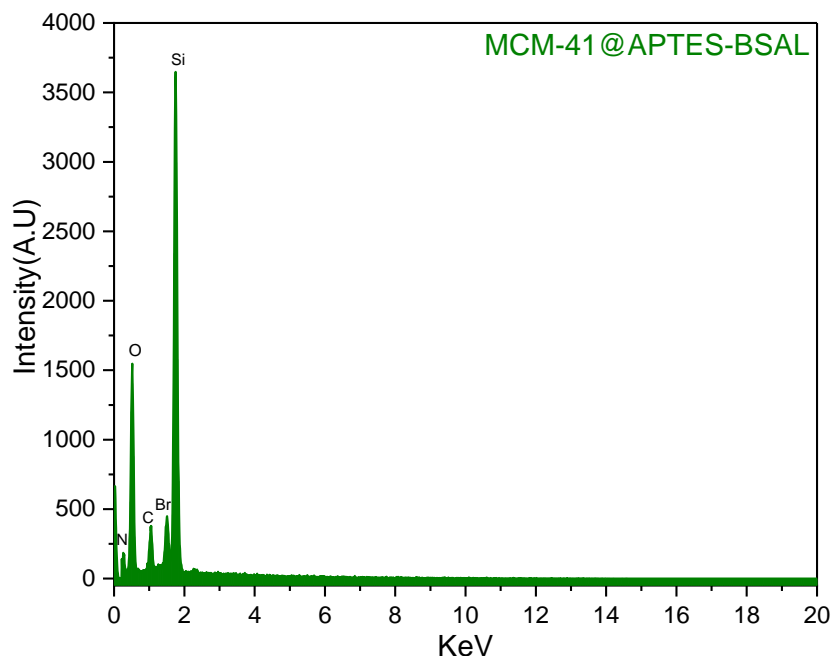


Figure (3.32): EDX analysis for MCM-41@APTES-BSAL.

3.3.8 Transmission electron microscopy(TEM)

The hexagonal honeycomb structure of MCM-41@APTES-BSAL can be not clearly observed in the Fig.(3.33) after functionalization MCM-41@APTES with 5-bromosalicylaldehyde, because immobilization of large organic compounds on the MCM-41@APTES causing the surface occupied with the ligand and blocking the pores. Furthermore, the samples showed ordered porous structure, which is consistent with previous research done on MCM-41[248]. The average diameter between (20-50)nm was corresponding to the average diameter of mesoporous materials [264].

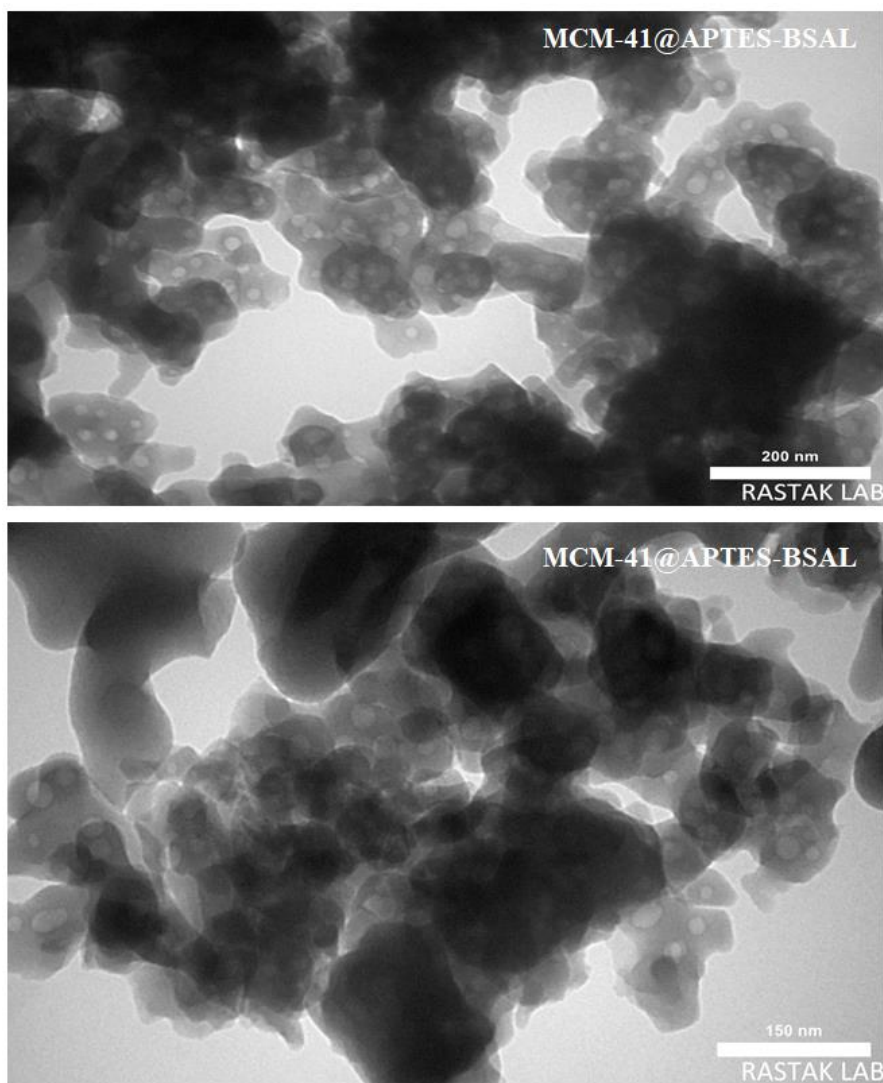


Figure (3.33): TEM images for MCM-41 @ APTES-BSAL at different scales.

3.4 The characterization of MCM-41 @ NTPE

MCM-41@NTPE was synthesized through a heterogeneous reaction between N-[3-(Trimethoxysilyl)propyl]ethylenediamine and MCM-41 in toluene as a solvent for 24 hrs. The structures of MCM-41@NTPE were characterized using various techniques.

3.4.1 Elemental analysis

The elemental analysis (Table 3.13) shows that MCM-41@NTPE contains 1.4% of nitrogen. In contrast, both RH-SiO₂ and MCM-41 do not contain this element. These findings clearly demonstrate that N-[3-(Trimethoxysilyl)propyl]ethylenediamine was incorporated into the MCM-41 to form MCM-41@NTPE.

Table (3.13): The percentage of elements present in MCM-41@NTPE that can be found through elemental analysis.

sample	Elemental analysis %			
	C	H	N	S
MCM-41@NTPE	9.72	4.95	1.40	-----

3.4.2 Fourier–transform infrared spectroscopic analysis (FT-IR)

FT-IR spectrum of the compound MCM-41@NTPE Fig. (3.34) showed a number of absorption bands silanol groups (Si-OH) was reduced compared with MCM-41. This indicates successful anchoring of N-[3-(Trimethoxysilyl)propyl]ethylenediamine [279]. The weak peak at (3000-3200 cm^{-1}) corresponds to the free NH_2 . The peaks around 3300 cm^{-1} are attributed to the symmetric and asymmetric stretching of N-H bond of the primary amine, while the peak at 3340 and 1655 cm^{-1} are attributed to the stretching and bending of N-H bond in the secondary amine. The bending vibration of N-H (primary amine) is appeared at 1520 cm^{-1} , while the strong peak at 1380 cm^{-1} signifies the combination of stretching C-N group in primary amine [280]. FT-IR spectrum also exhibits bands at 445, 935 and 1090 cm^{-1} , characteristic of symmetric and anti-symmetric stretching of Si-O-Si peaks [281].

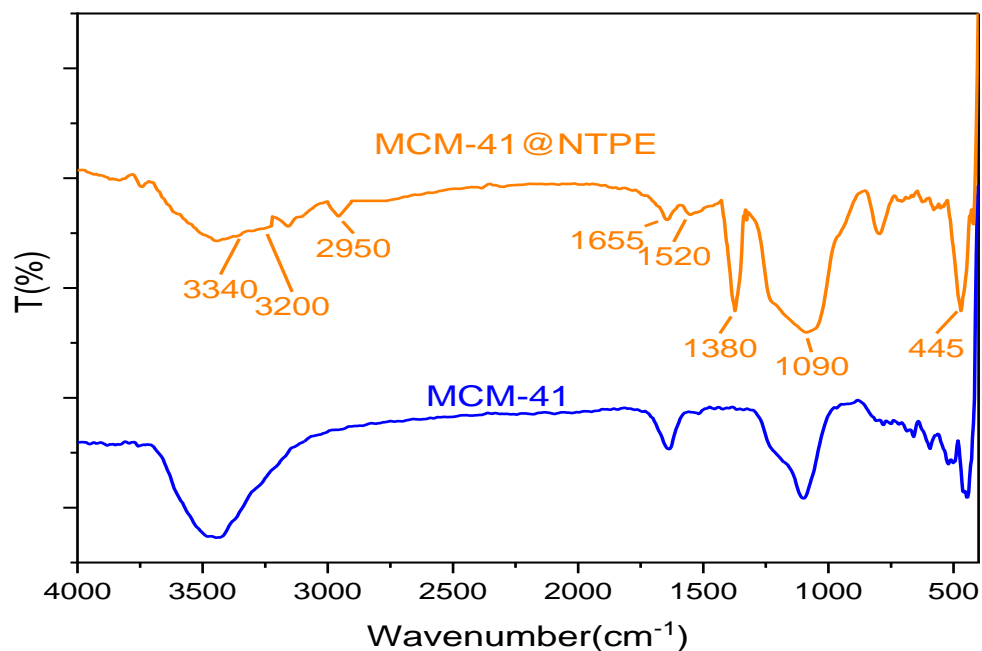


Figure (3.34): FTIR spectra for MCM-41@NTPE and starting material.

3.4.3 X-ray powder diffraction(XRD)

XRD analysis for MCM-41@NTPE at low-angle are presented in Fig.(3.35).The peak at approximately 2.17° (100) is attributed to the presence of a hexagonal mesoporous structure[282],which is characteristic of MCM-41@NTPE.This can be seen in TEM images in Fig.(3.43). The intensity of the peaks for MCM-41@NTPE however, were low compared to MCM-41, which might be because of the filling of the mesoporous honeycomb structure of MCM-41[271].The high angle XRD pattern Fig.(3.36)demonstrated the presence of broad diffused peak with peak intensity at $22-23^\circ$ (2θ), even though the lack of distinct peaks. This result, consistent with the strong broad peak of amorphous silica proposes the amorphous nature of the functionalized silica analyzed as shown in Fig.(3.36)[283].

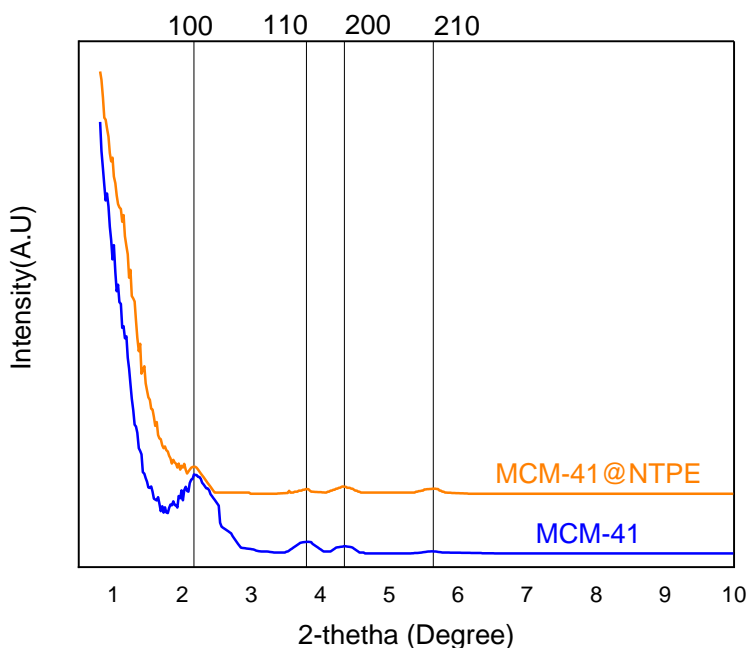


Figure (3.35): XRD spectra (low angle) of MCM-41@NTPE and starting material.

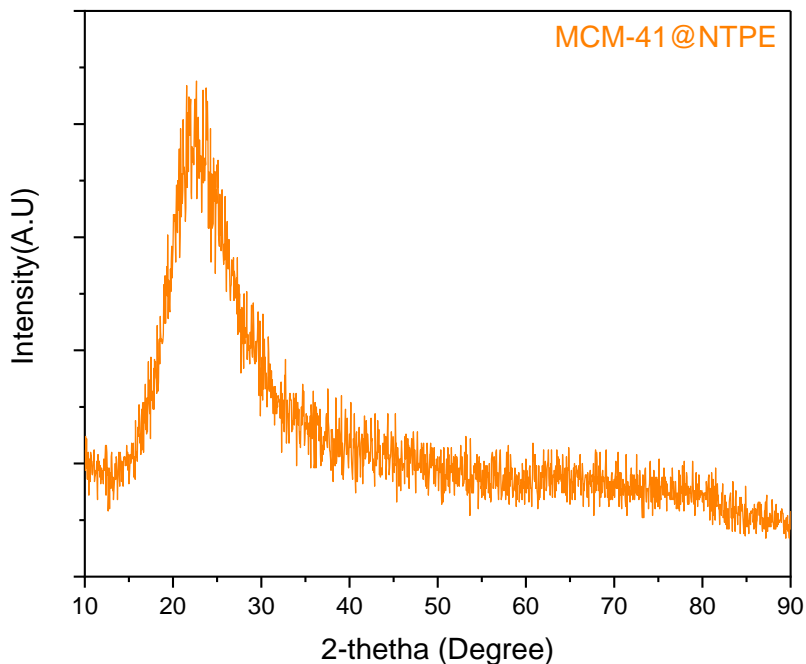


Figure (3.36): XRD spectrum (high angle) of MCM-41@NTPE.

3.4.4 Nitrogen adsorption-desorption analysis:

One of the main characterization issues for mesoporous silica is identifying the pore network based on physical adsorption–desorption analysis. Type IV isotherms with H3

hysteresis loop were identified for MCM-41@NTPE (Fig. (3.37)), in accordance with the IUPAC definition, which were associated with the presence of mesoporous (Fig. (3.38))[284]. The initial segment of the adsorption isotherm ($P/P_0 < 0.2$) was attributed to the monolayer and multilayer occurrences. The second segment, at higher P/P_0 , exhibited an upward deviation correlated to the continuous filling of mesoporous by capillary condensation [285]. The BET specific surface area, the average pore volume and average pore diameter for MCM-41@NTPE were illustrated in Table (3.14).

Table (3.14): BET analysis for MCM-41@NTPE and starting materials.

Compounds	BET surface area ($\text{m}^2\cdot\text{g}^{-1}$)	Total pore volume ($\text{cm}^3\cdot\text{g}^{-1}$)	Average pore size (nm)
RH-SiO₂	390.12	0.33	3.47
MCM-41	548.92	0.94	6.85
MCM-41@NTPE	8.873	0.094	42.468

The pore volumes and surface areas of MCM-41@NTPE decreased significantly compared to MCM-41. This suggests that the hexagonal pores at the surface are being blocked by large ligand molecules when immobilizing N-[3-(Trimethoxysilyl)propyl]ethylenediamine onto MCM-41. The average pore size between (3 and 10 nm) within the range of mesoporous compounds [271] is shown in Fig.(3.38).

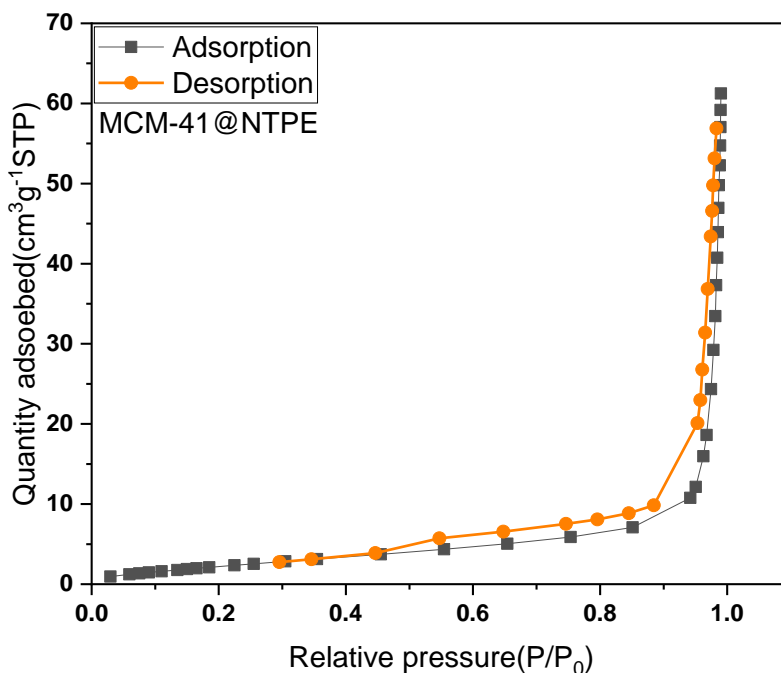


Figure (3.37): N_2 adsorption–desorption isotherms of MCM-41@NTPE

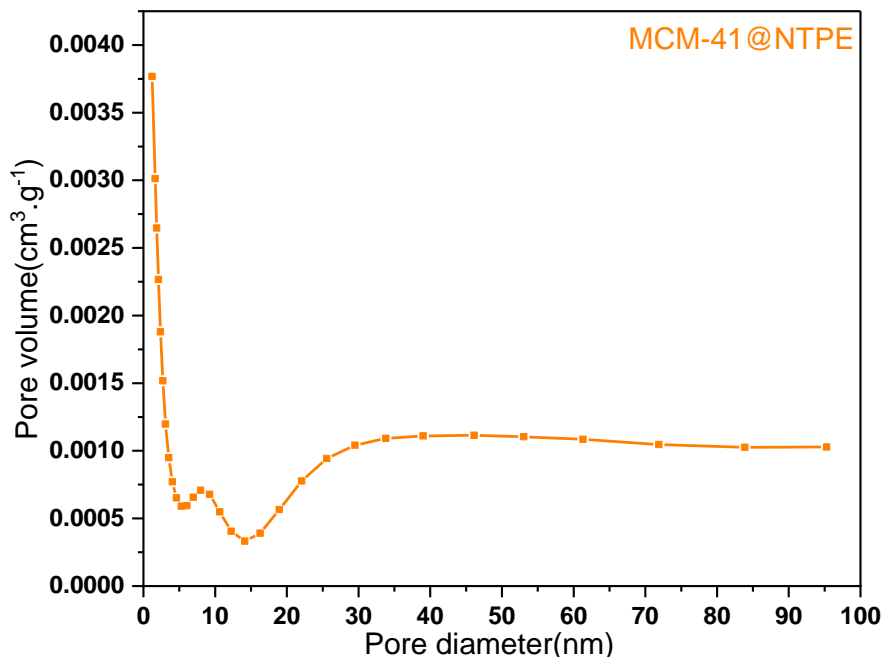


Figure (3.38): Pore size distribution of MCM-41@NTPE.

3.4.5 Thermogravimetric analysis (TGA/DSC):

The thermal stability of the functionalized silica was applied by using TGA/DSC analysis, the obtained results are illustrated in Fig. (3.39). The findings show that the functionalized silica exhibited three characteristic stages of weight loss.

At first (100°C), there was weight loss (10%) was attributed to water molecules that were adsorbed to the silica's surface was evaporation. The second weight loss(250-350°C)(15%) could be due to decomposition of organic moiety for MCM-41@NTPE and the third step(400-900°C)(33%) involving breakdown of Si-OH groups in the silica structure and transforming them into Si-O-Si siloxane group. The results show that the synthesis procedure was successful and that a high-stability material was produced[286].

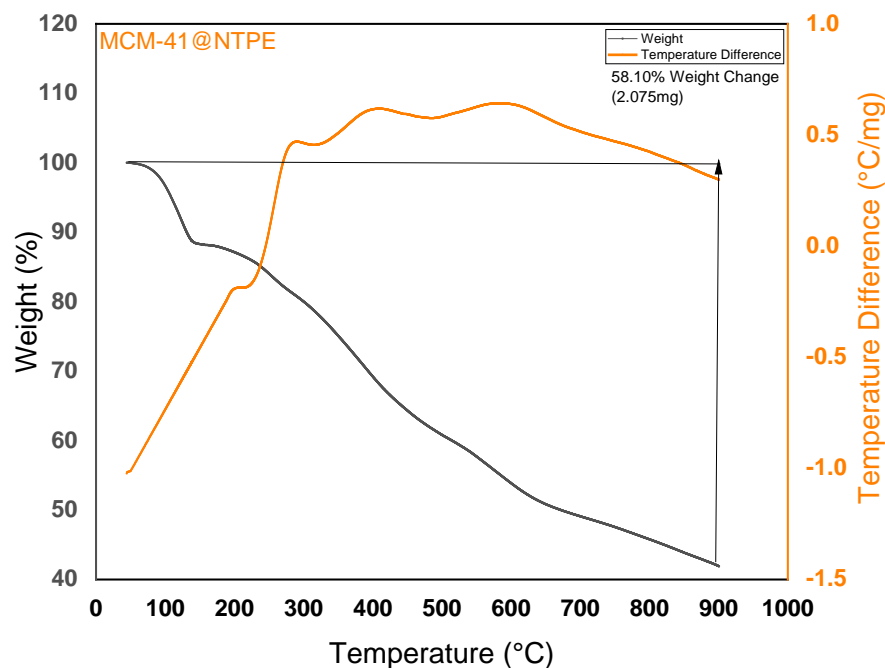


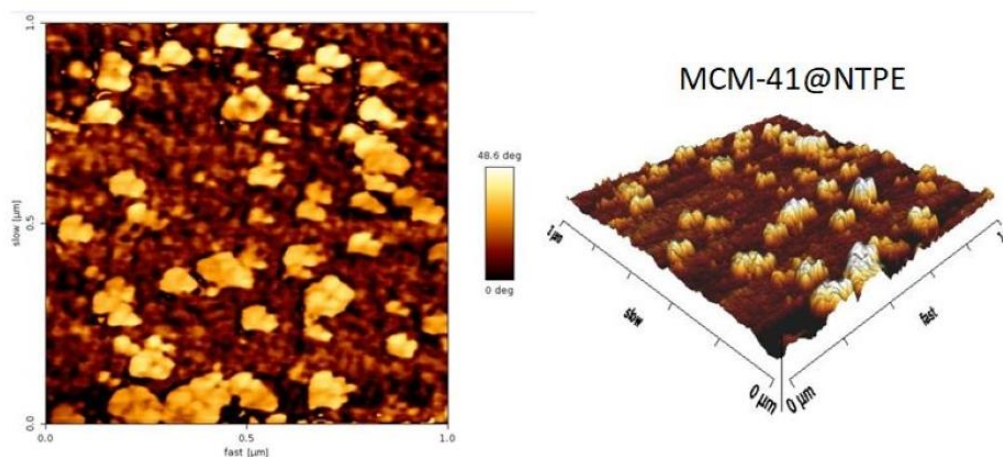
Figure (3.39): TGA/DSC plot of MCM-41@NTPE.

3.4.6 Atomic force microscopy(AFM):

The surface topographies of MCM-41@NTPE have been demonstrated via the AFM analysis as shown in Fig. (3.40). It was found that the two-dimensional images of the MCM-41@NTPE topographies were not clear, while three-dimensional images showed a high and a low topography responsible for the surface roughness of the silica [46]. Table(3.15) shows the parameters obtained from AFM for the surfaces of the prepared MCM-41@NTPE. The increase in the AFM parameter for MCM-41@NTPE is compared with MCM-41 due to the increase in the rate of agglomeration of partial [259].

Table (3.15): AFM parameters for MCM-41@NTPE and starting material.

Sample	Average roughness (Ra)	Root square roughness (Rms)	Average height (Sz)
MCM-41	0.702 nm	0.896 nm	7.900 nm
MCM-41@NTPE	1.161 nm	1.585 nm	12.090 nm

**Figure (3.40):** AFM 2D (on left) and 3D (on right) micrographs of MCM-41 @NTPE.

3.4.7 Field emission scanning electron microscopy-energy dispersive X-ray (FESEM and EDX)

FESEM images of MCM-41@NTPE are shown in Fig. (3.41). It is clear from these images that the particles are smooth with a spherical agglomeration. The average diameter ranges between (20-100) nm, which corresponds to the average diameter of mesoporous and macroporous materials [264].

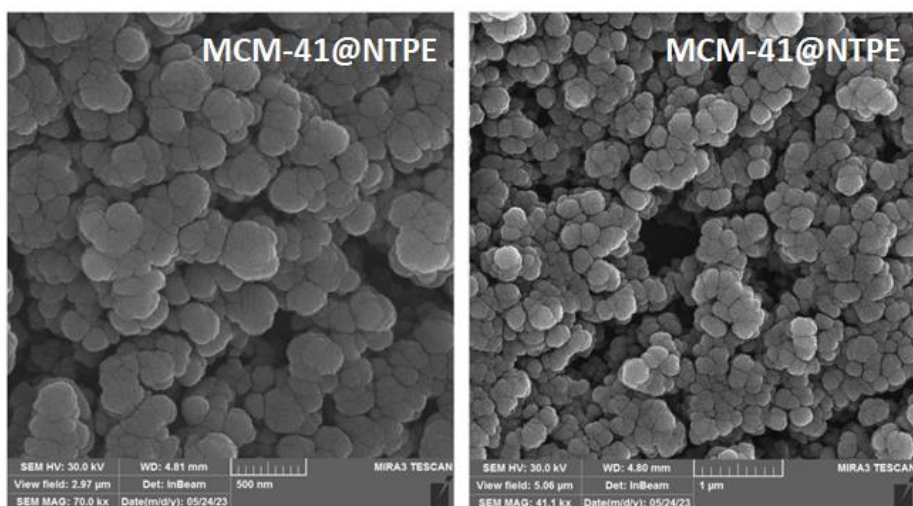


Figure (3.41): FESEM analysis of MCM-41@NTPE at scales of 500 nm and 1000 nm.

According to EDX analysis, the presence of silicon and oxygen, in addition to nitrogen and carbon were demonstrated in the solid ligand (MCM-41@NTPE), as shown in Fig.(3.42). From this, it can be further concluded that the MCM-41 was incorporated on the *N*-[3-(trimethoxysilyl)propyl]ethylenediamine. The average value of the chemical composition obtained from EDX analysis is shown in Table(3.16) .

Table(3.16) :The average values obtained from EDX analysis for MCM-41@NTPE.

Elements	Average mass (%)
Si	15.98
O	41.22
N	15.81
C	26.95

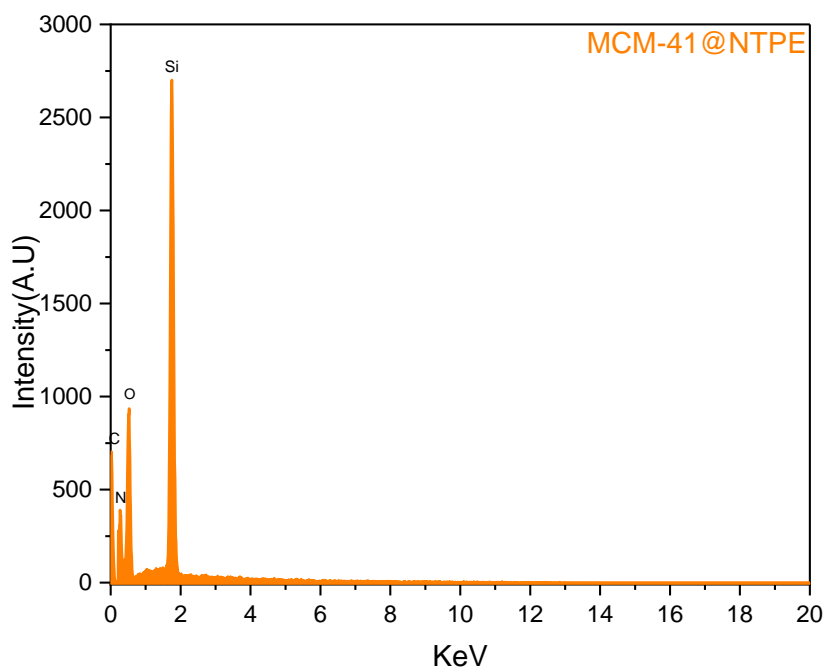


Figure (3.42): EDX analysis of MCM-41@NTPE.

3.4.8 Transmission electron microscopy(TEM)

TEM images of MCM-41@NTPE is shown in fig. (3.43). It can be seen that the hexagonal honeycomb structure of the MCM-41@NTPE. The TEM images showed the multifarious layers of the accumulated ordered pores in the structures of MCM-41@NTPE[266].

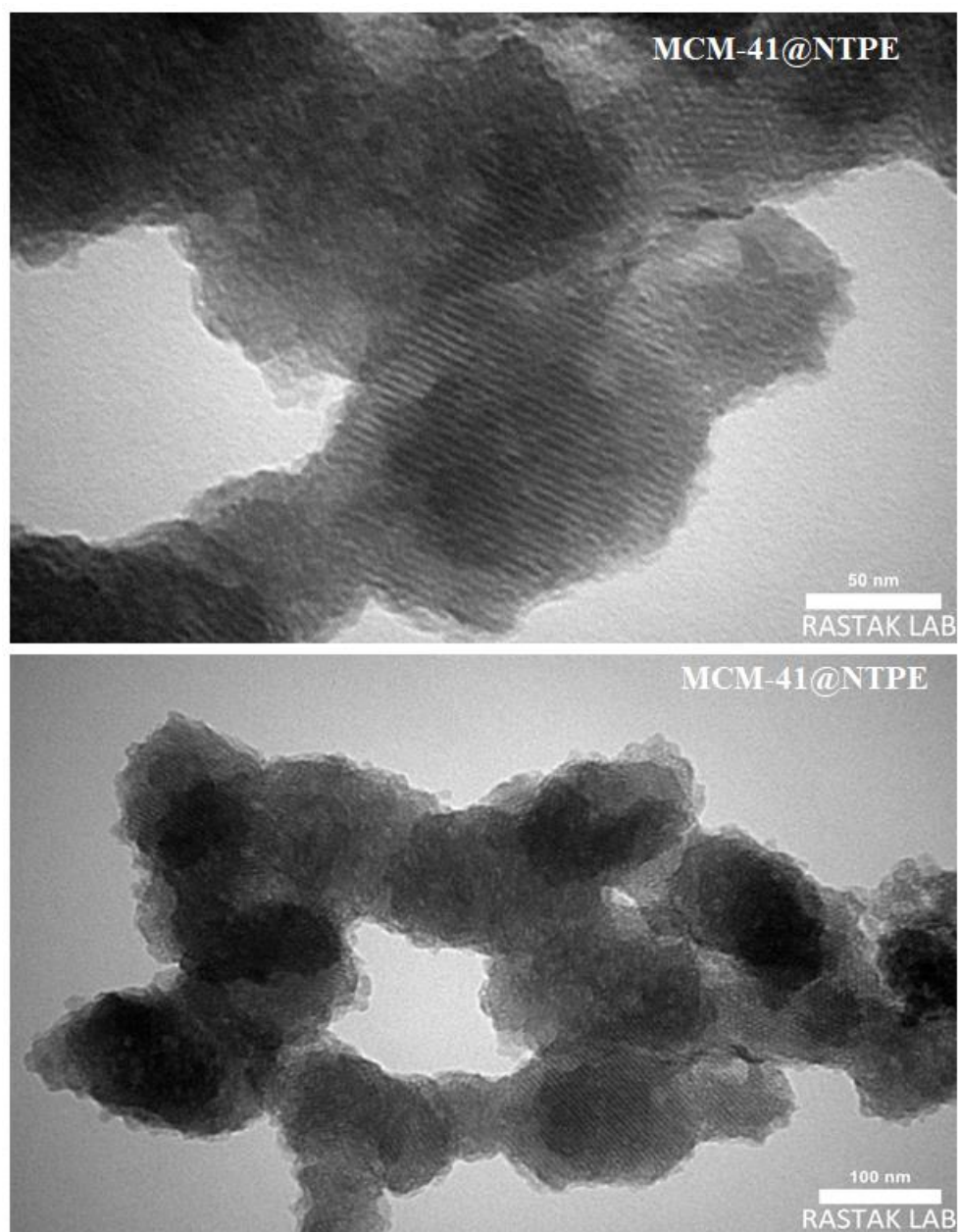


Figure (3.43): TEM images of MCM-41@NTPE at different scales.

3.5 The characterization of MCM-41@NTPE-BSAL

MCM-41@NTPE-BSAL was synthesized through heterogeneous reaction between 5-Bromosalicylaldehyde and MCM-41@NTPE in toluene as a solvent for 24 hrs.. The structures of MCM-41@NTPE-BSAL was characterized using various techniques.

3.5.1 Elemental analysis

The elemental analysis results of MCM-41@NTPE-BSAL were tabulated in Table (3.17). The carbon percentage and hydrogen in MCM-41@NTPE-BSAL were more than in MCM-41@NTPE, these findings show that the 5-Bromosalicylaldehyde was successfully incorporated onto MCM-41@NTPE.

Table (3.17): The percentage of elements present in MCM-41@NTPE-BSAL that can be found through elemental analysis.

Sample	Elemental analysis %			
	C	H	N	S
MCM-41@NTPE-BSAL	19.85	13.72	8.00	-----

3.5.2 Fourier –transform infrared spectroscopic analysis (FT-IR):

Fig.(3.44) shows the FTIR spectrum of MCM-41@NTPE-BSAL. The band related to the O-H vibration of Si-OH is shifted to $\sim 3400\text{ cm}^{-1}$. The C-H aliphatic and aromatic groups stretching vibration was responsible for low intensity bands peak at ~ 3000 and 2500 cm^{-1} [245, 287]. The presence of the azomethine C=N group was confirmed by the identification of a peak at 1640 cm^{-1} which interfere with double bond bands, indicating the successful of Schiff base ligand formation [275]. The peak at 3340 and 1655 cm^{-1} is attributed to the stretching and bending of N-H bond in the secondary amine of the same moiety. This provides substantial evidence that the reaction between MCM-41@NTPE and 5-Bromosalicylaldehyde was successful in producing the required Schiff base. The bands due to C-O vibrations usually appear in the vicinity of $1000\text{--}1300\text{ cm}^{-1}$ [271]. However, after functionalization with 5-Bromosalicylaldehyde, these bands overlapped with that of the siloxane group (Si-O-Si), although relatively small bands still appeared as exhibited from the FT-IR spectrum of MCM-41.

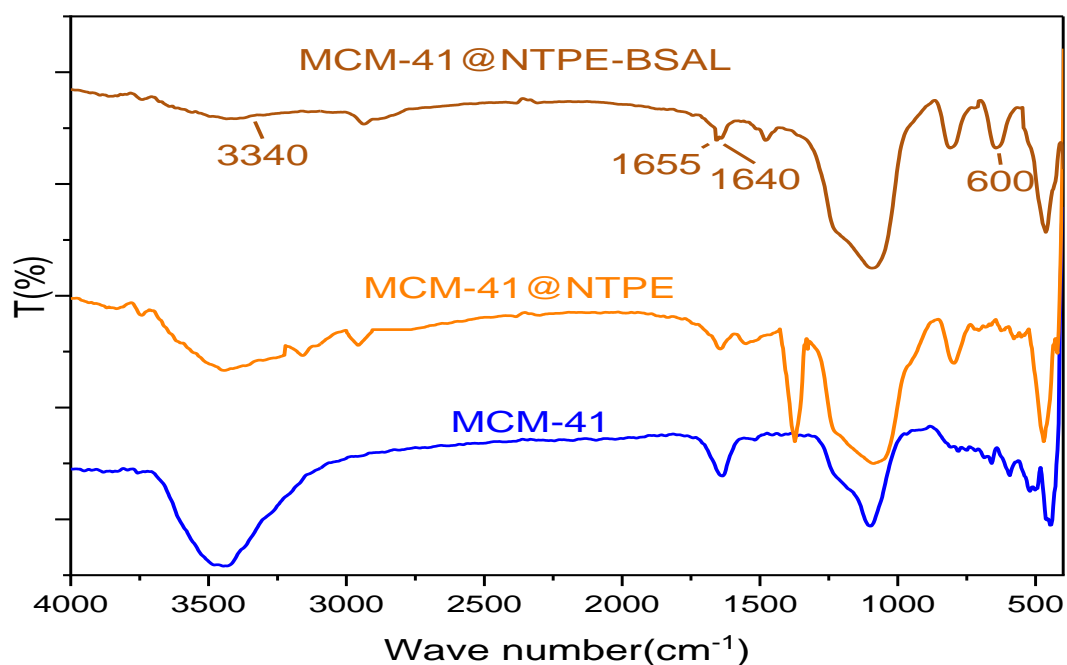


Figure (3.44): FTIR spectra for MCM-41@NTPE-BSAL and starting materials.

3.5.3 X-ray powder diffraction(XRD)

The X-ray diffraction (XRD) analysis was carried out of synthesized material MCM-41@NTPE-BSAL. The results of XRD analysis at low angle is presented in Fig.(3.45). The peak at approximately 2.17° (100) is attributed to the presence of a hexagonal mesoporous structure, which is characteristic of MCM-41@NTPE-BSAL. This can be seen in TEM images in Fig.(3.53). The intensity of the peaks for MCM-41@NTPE-BSAL however, were low compared to MCM-41@NTPE and MCM-41, which might be because of the filling of the mesoporous honeycomb structure of MCM-41@NTPE by organic molecules [271]. The high angle XRD pattern (Fig.(3.46)) showed a broad peak at 22° from 2 theta was observed due to the amorphous structure of the MCM-41@NTPE-BSAL [249].

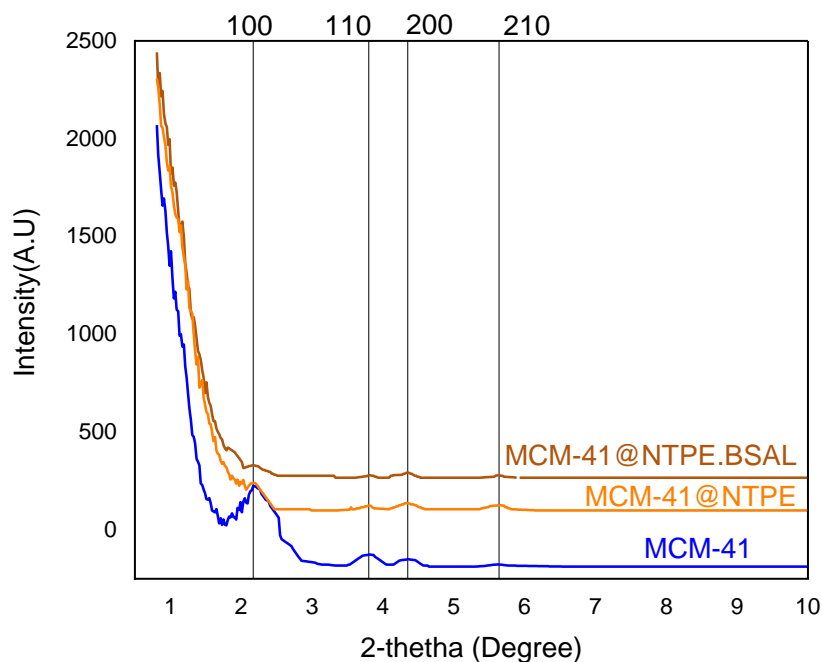


Figure (3.45): XRD spectra (low angle) MCM-41@NTPE-BSAL and starting materials.

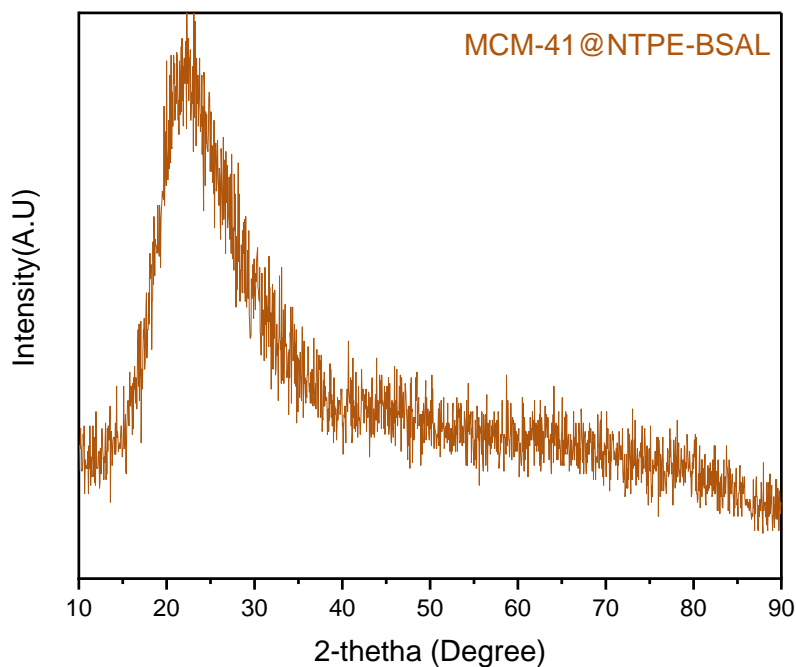


Figure (3.46): XRD spectrum (high angle) of MCM-41@NTPE-BSAL.

3.5.4 Nitrogen adsorption-desorption analysis

The specific surface area and the pore size distribution can be demonstrated via N_2 adsorption-desorption analysis. From the results represented in Fig.(3.47), specific

surface area, the average pore volume and average pore diameter according to BET plot were illustrated in Table(3.18). The samples porosity changed, but they still had a narrow pore width distribution, which is typical for MCM-41 derivative materials[273].

However, the hysteresis loop was detected in MCM-41@NTPE-BSAL within the range from $0.4 < P/P_0 < 1$, associated with capillary condensation as per in the IUPAC classification. The sample exhibited type IV isotherm with H3 hysteresis loop, which is characteristic for mesoporous solids. The pore size distribution Fig(3.48) ranging (5-10) nm is within the mesoporous materials [254].

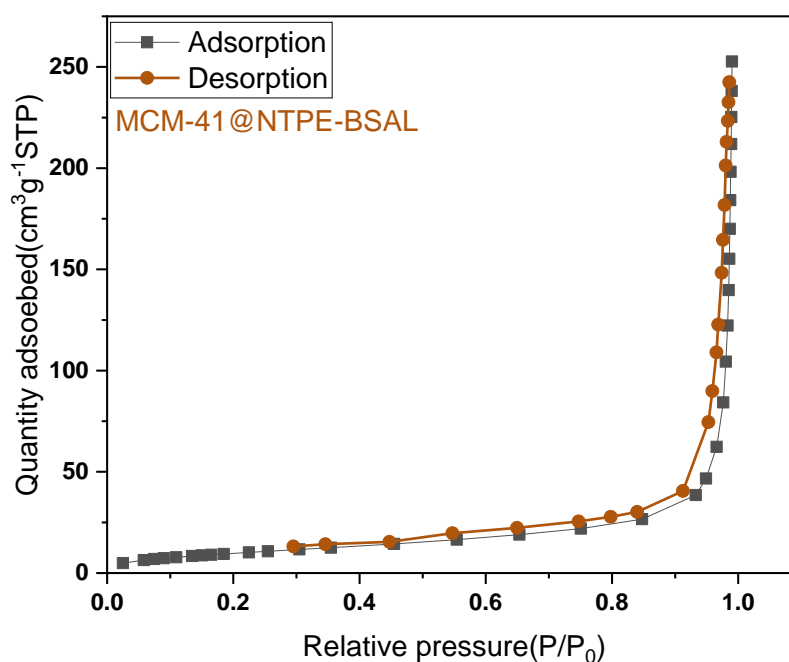


Figure (3.47): N₂ adsorption–desorption isotherms of MCM-41@NTPE-BSAL

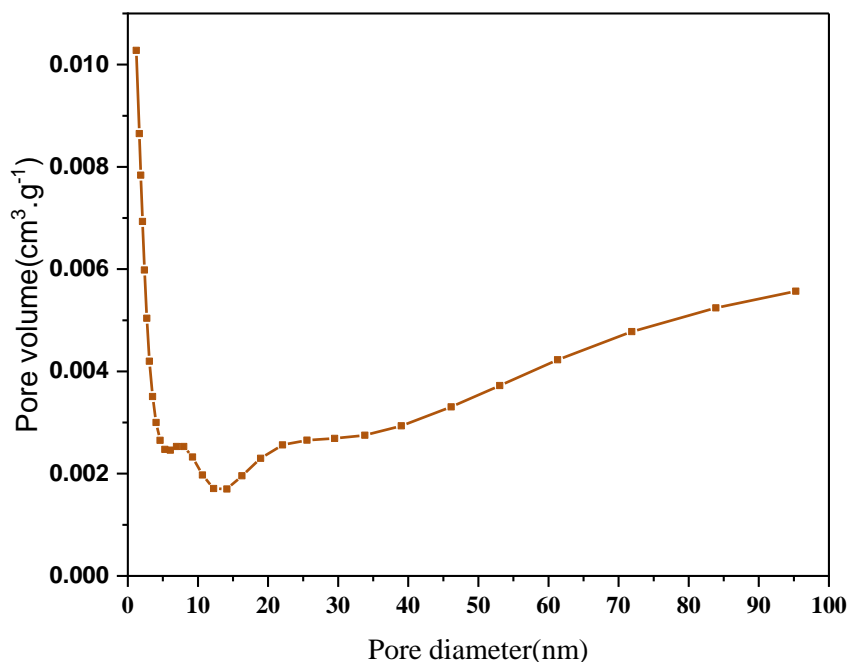


Figure (3.48): Pore size distribution of MCM-41@NTPE-BSAL.

The pore volume and surface area of MCM-41@NTPE-BSAL Table(3.18) decreased significantly compared to MCM-41 that was prepared, but increased compare MCM-41@NTPE as a result of the presence of a carbon network that increase the effective sites which makes the surface highly effective towards adsorbed nitrogen gas. This type of isotherm shows that the particles are plate-like[218].

Table (3.18): BET analysis for MCM-41@NTPE-BSAL and starting materials.

Compounds	BET surface area (m ² .g ⁻¹)	Total pore volume (cm ³ .g ⁻¹)	Average pore size (nm)
MCM-41	548.92	0.94	0.94
MCM-41@NTPE	8.873	0.094	42.468
MCM-41@NTPE-BSAL	37.802	0.3384	40.417

3.5.5 Thermogravimetric analysis (TGA/DSC):

The thermogravimetric analysis(TGA/DSC) was done in a temperature ranging from 15°C to 900 °C. The results of this technique are shown in the fig.(3.49).MCM-41@NTPE-BSAL compound undergoes decomposition in three distinct stages, as observed in the thermogravimetric analysis: The first stage (100°C)(10%)when physisorbed water is lost; The second loss(400-500°C)(10%) was related to the decomposition of organic moiety for MCM-41@NTPE-BSAL on the surface of silica. The third(500-750°C) continuous loss of weight(38%) was attributed to breakdown of Si-OH groups in the silica structure and transforming them into Si-O-Si siloxane group. The results show that the synthesis procedure was successful and that a high-stability material was produced [287].

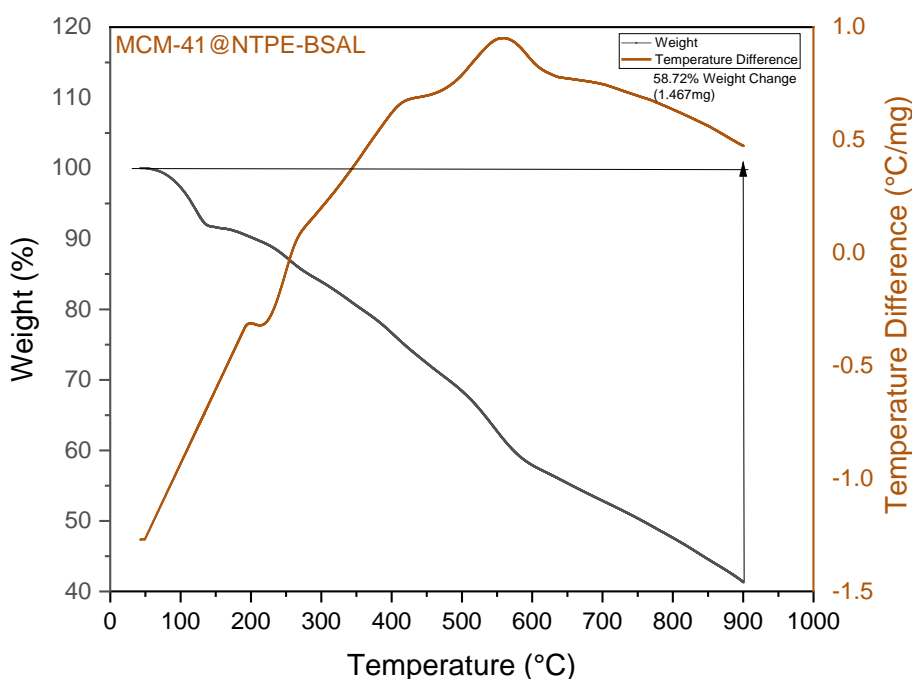


Figure (3.49): TGA/DSC plot of MCM-41@NTPE-BSAL

3.5.6 Atomic force microscopy(AFM)

Fig.(3.50)shows the atomic force microscopy(AFM) images and granularity normal distribution of the MCM-41@NTPE-BSAL. The results demonstrated that the functionalization of MCM-41@NTPE led to a decrease in the surface roughness material

upon functionalization from 1.161 nm to 0.429nm. This change may be attributed to the successful modification of the surface of the ligand between MCM-41@NTPE and 5-Bromosalicylaldehyde.

Table (3.19): AFM parameters for MCM-41@NTPE-BSALand starting materials.

Sample	Average roughness (Ra)	Root square roughness (Rms)	Average height (Sz)
MCM-41	0.702 nm	0.896 nm	7.900 nm
MCM-41@NTPE	1.161 nm	1.585 nm	12.090 nm
MCM-41@NTPE-BSAL	0.429nm	0.761nm	9.201 nm

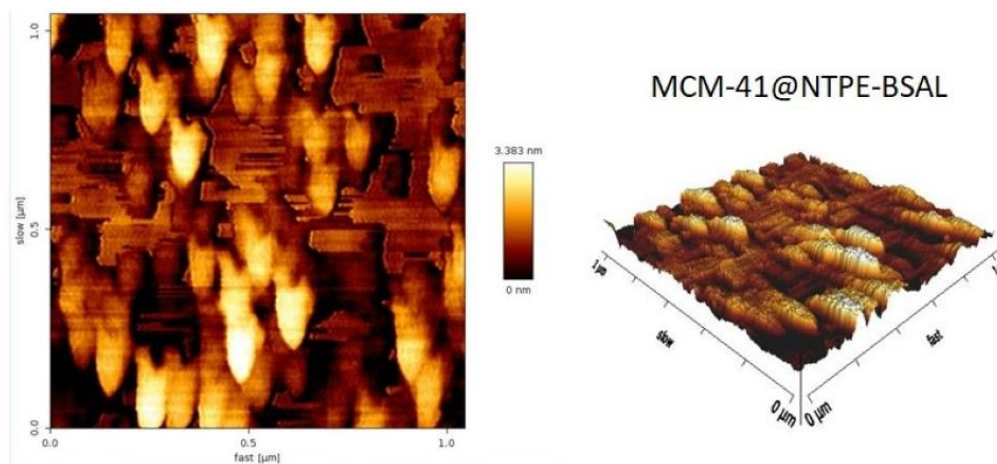


Figure (3.50): AFM 2D (on left) and 3D (on right) micrographs of MCM-41@NTPE-BSAL.

3.5.7 Field emission scanning electron microscopy-energy dispersive X-ray (FESEM and EDX)

FESEM micrographs for MCM-41@NTPE-BSAL are shown in Fig. (3.51).The material formed smooth with a spherical agglomeration, and this spherical morphology was preserved for the composite materials. The average diameter ranges between (20-100)nm, which corresponds to the average diameter of mesoporous and macroporous materials [264].

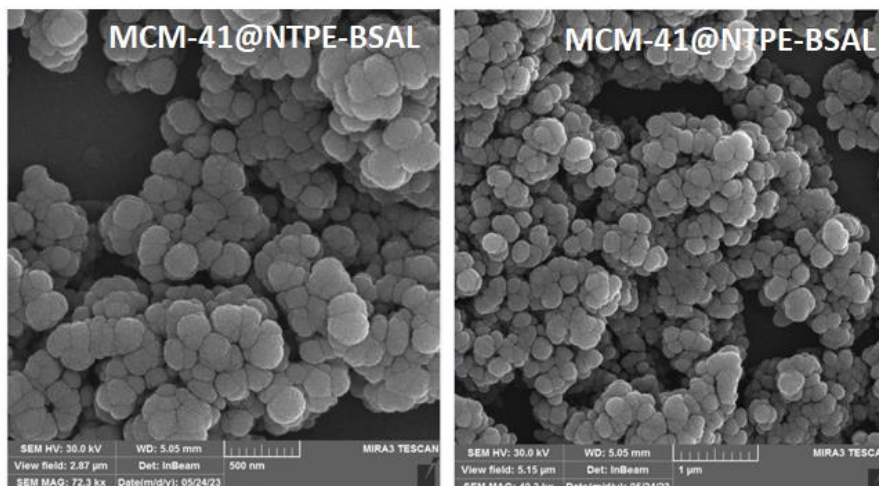


Figure (3.51): FESEM analysis of MCM-41@NTPE-BSAL at scales of 500 nm and 1000 nm.

Fig. (3.52) also shows the EDX analysis of MCM-41@NTPE-BSAL. The analysis of this spectrum revealed that the compounds contained carbon, nitrogen and bromine, in addition to oxygen and silicon in the complex, from which it can be further concluded that the 5-bromosalicylaldehyde was incorporated onto the MCM-41@NTPE, inducing modification to the textural and chemical properties. The average values of the chemical composition obtained from the EDX analysis are shown in Table(3.20).

Table(3.20) : The average values obtained from EDX analysis for MCM-41@NTPE-BSAL.

Elements	Average mass (%)
Si	24.43
O	46.09
N	8.77
C	17.68
Br	3.04

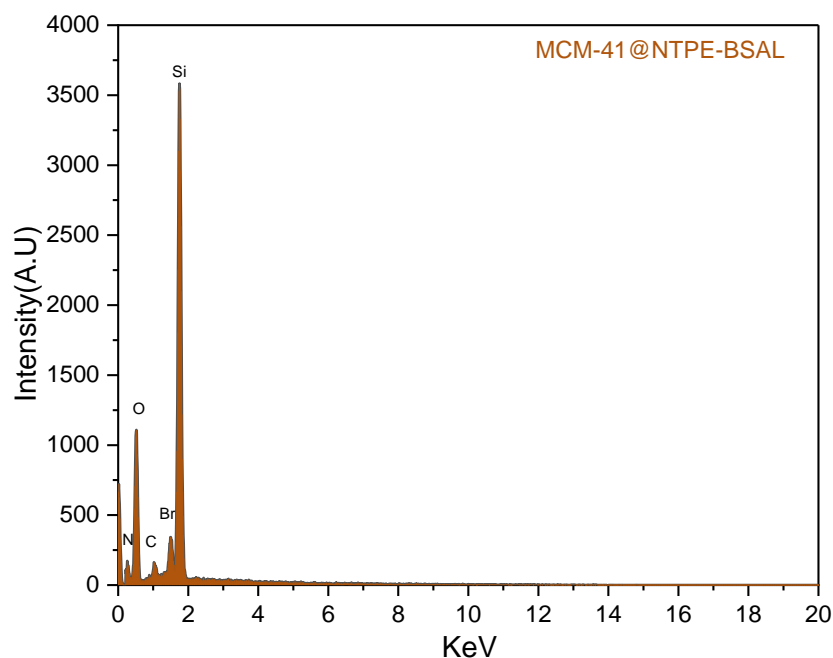


Figure (3.52): EDX analysis of MCM-41@NTPE-BSAL.

3.5.8 Transmission electron microscopy(TEM)

Fig.(3.53) shown TEM images of MCM-41@NTPE-BSAL, not clear honeycomb structures arrangement was kept after 5-Bromosalicylaldehyde was incorporated onto MCM-41@NTPE with heterogeneous spherical shapes distributed [288].Also, the samples had a ordered porous structured just like what has been found before in MCM-41 compounds[248].

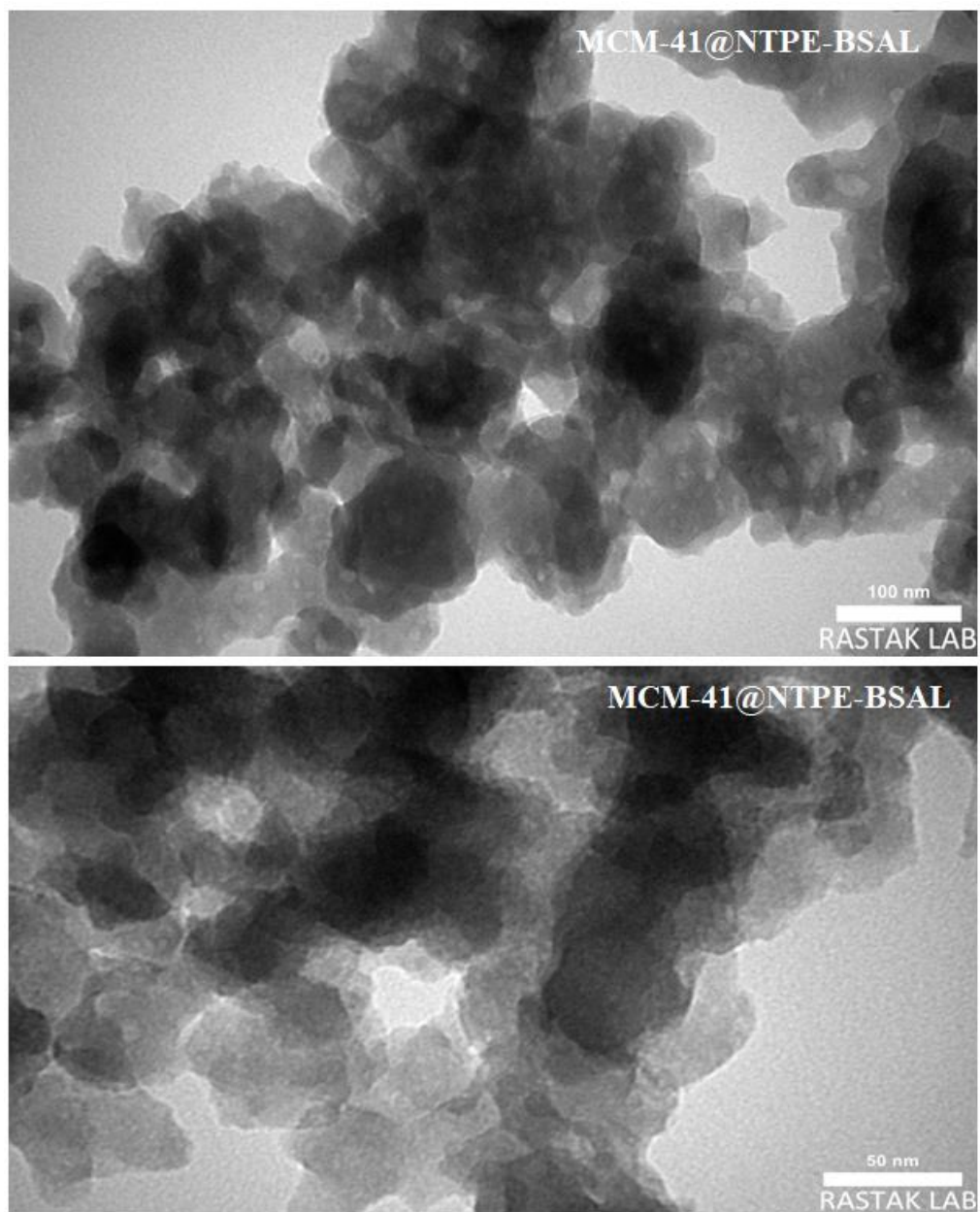


Figure (3.53): TEM images of MCM-41@NTPE-BSAL at different scales.

4. Removal of metal ions from aqueous solution.

Diverse techniques have been applied in the attempt to eliminate the impact of pollution from these sources, which include ion exchange, membrane filtration, precipitation, adsorption, coagulation, and oxidation. The process of adsorption with porous compounds can involve different mechanisms which include hydrophobic interactions, electrostatic interactions, ion-dipole interactions, coordination by surface metal cations, ion exchange, hydrogen bonding, and dispersion forces, amongst others[184].

Adsorption is the process of adhesion of solid, liquid or gaseous substances to the surface of another substance[289].The bonds that formed in this process between the atoms of the adsorbent and the adsorbed materials are ionic, covalent and metallic bonds[290].In addition, the atoms on the surface of the adsorbent are not completely surrounded by many other adsorbent atoms, but rather the adsorbed materials can accumulate.The adsorption process is easy and cost-effective compared to other separation methods, as the adsorbent can be reused without a significant change in its performance[291, 292].The process of adsorption is present in most natural, biological and chemical systems and has wide applications in the pharmaceutical industries, water treatment and dye industries[293].

4.1 Study of uv-visible spectra of divalent ions (Cobalt and Copper)

Figs.(4.1) and (4.2) shows the spectra of absorption of Co(II) and Cu(II) within the wavelength(400-1100)nm, the ions exhibits a distinct peak of absorption at(λ_{\max} .equal to 620 and 730 nm),respectively.

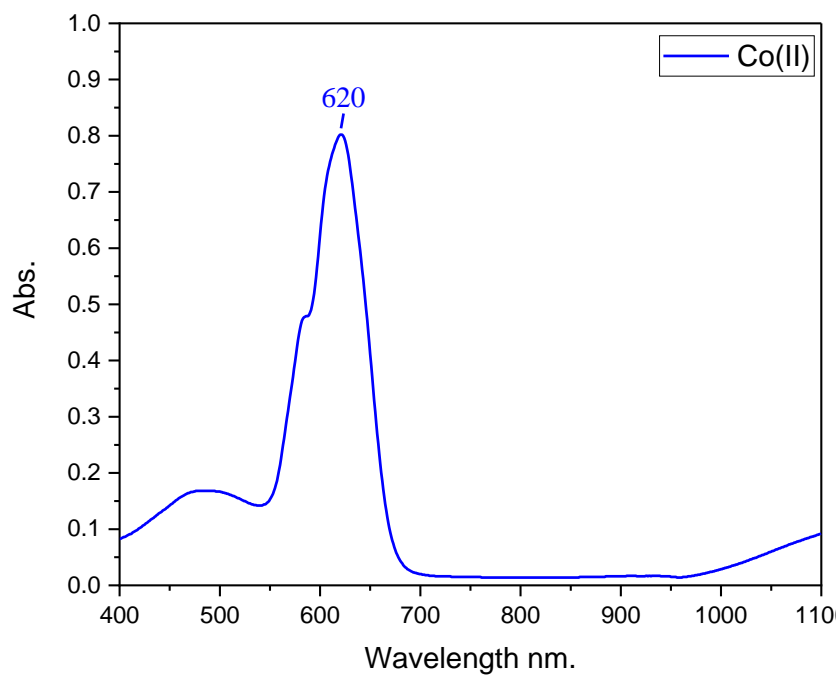


Figure (4.1): Uv-vissible of Co (II) ions

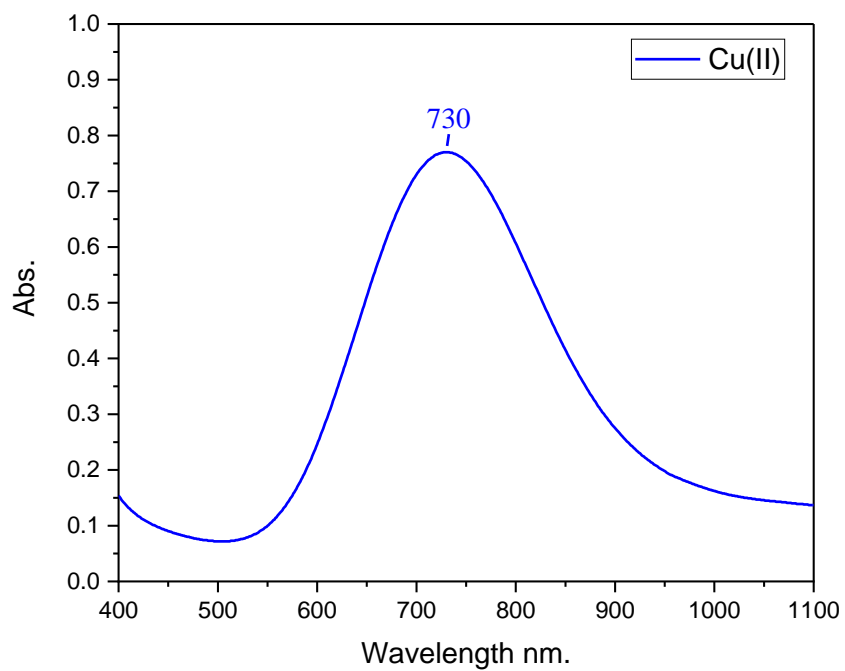


Figure (4.2):Uv-vissible of Cu(II) ions.

4.2 Calibration curve of ions (Co (II) and Cu (II))

Figs. (4.3) and (4.4) shows calibration curve of divalent ions cobalt and copper, respectively, which show that Co (II) and Cu (II) ions obey Lambert-Beer rule within the concentration range (20-600) $\mu\text{g}\cdot\text{mL}^{-1}$ for cobalt and (20-500) $\mu\text{g}\cdot\text{mL}^{-1}$ for copper.

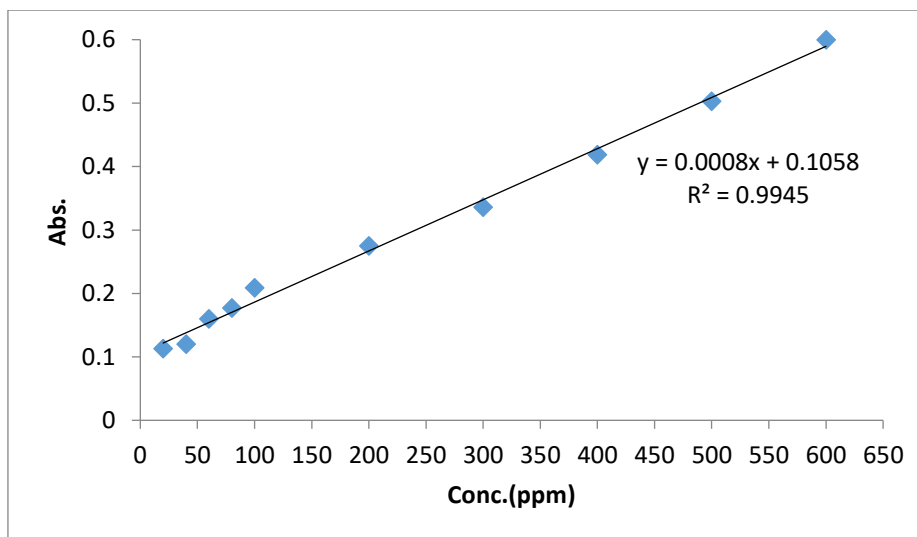


Figure (4.3): Calibration curve of Co (II) ion.

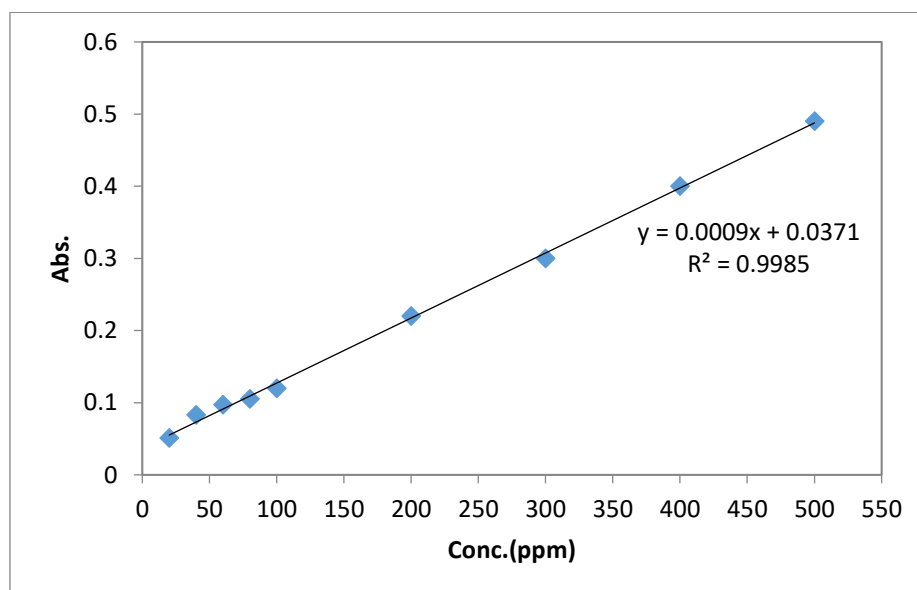


Figure (4.4): Calibration curve of Cu (II) ion.

4.3 Removal tests

4.3.1. Removal ions experiments

Calibration curves for each of the ions were constructed by preparing a series of diluted solutions for each ion. Next, an amount of each prepared ligands, was combined with 50 mL of each metal ions solution, Co (II) and Cu (II), respectively. The amount of metal ion was determined through enabling the insoluble complex to settle and by take a specific amount of the supernatant using a micropipette. The impact of different variables on the metal ions such as exposure time, pH, metal ion concentration, and effects of mass of the RH-SiO₂, MCM-41 and derivative compounds were investigated. The following equation was used to calculate the removal of cobalt and copper from aqueous solutions[235]:

$$\% \text{ Removal (E)} = (C_0 - C_e / C_0) * 100 \%$$

Where C₀ and C_e are the initial concentration at zero and the adsorbed concentration after contact time, respectively.

4.3.1.1 Removal ions by RH-SiO₂ and MCM-41

4.3.1.1.1. Effect of exposure time

It is necessary to study effect of exposure time for a substance to reach equilibrium in order to plan experiments for adsorption. The influence exposure time on adsorption of RH-SiO₂ and MCM-41 was examined, the removal of ions by adsorbent prepared were detailed to be a function of diverse contact time[294]. The metal ion removal of Co (II) (0.05 M) and Cu (II) (0.05 M) ions was determined by shaking the RH-SiO₂ or MCM-41, separately in the aqueous metal solutions for various times, as illustrated in Figs.(4.5) and (4.6). It was demonstrated that there was an increase in the removal of metal ions as a function of exposure time, though in a nonlinear manner, due to diffusion factors. This increase can be characterized as a fast initial removal followed by a period of constant removal as a result of saturation of RH-SiO₂ and blocking the pore for MCM-41 by Co(II)

and Cu(II) ions, separately occurred after time progressing. This aligns with the hypotheses of other workers [295].

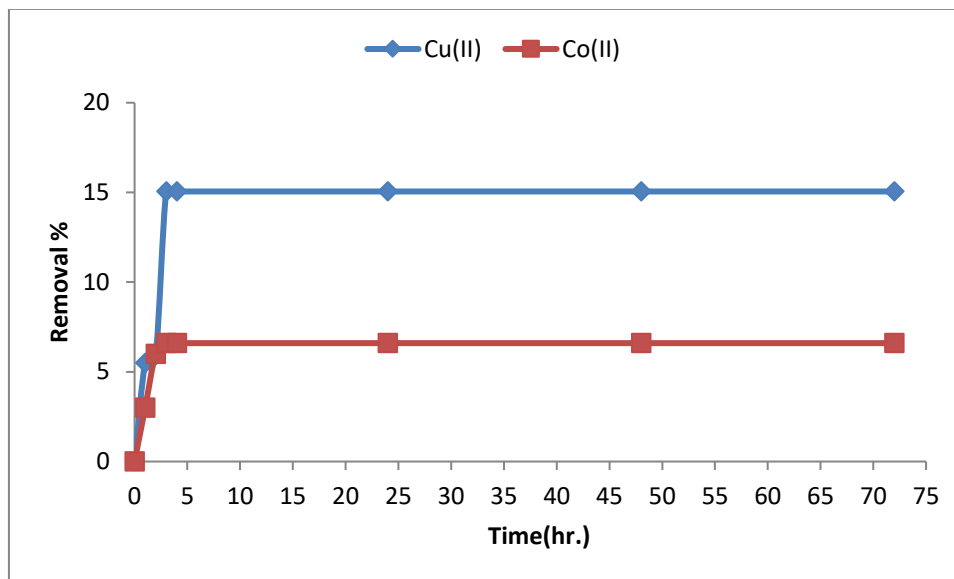


Figure (4.5): The removal of Cu (II) and Co (II) ions by the RH-SiO₂ ligand as a function of time.

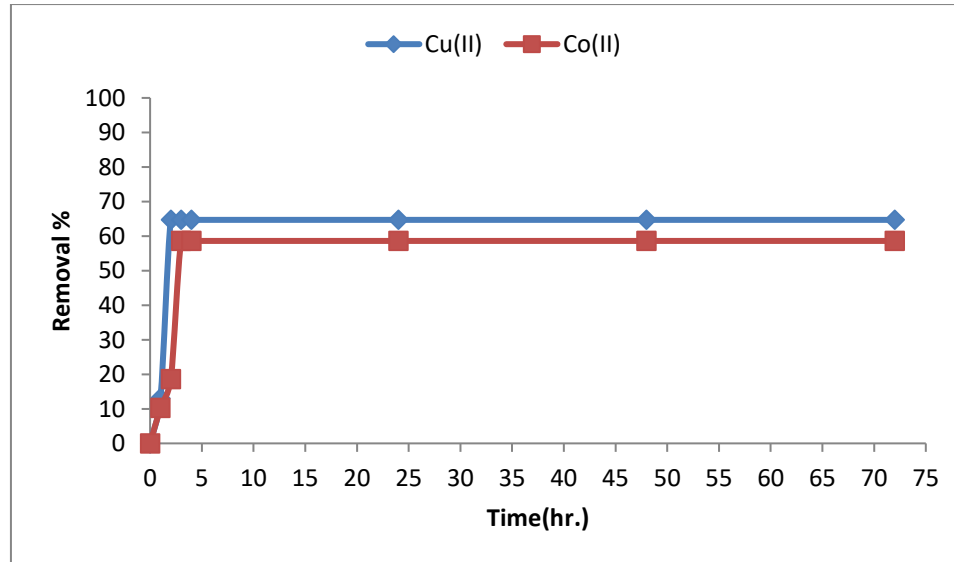


Figure (4.6): The removal of Cu (II) and Co (II) ions by the MCM-41 ligand as a function of time

4.3.1.1.2. Effect of pH

The pH of the aqueous solution is very important for the adsorption process. It changes the electric charge on the surface of the material that adsorbs, the degree of ionization of

the material present in the solution, and how the groups on the active sites of the adsorbent separate. It also changes the way the solute behaves in the solution [296].

Solutions of Co (II) (0.05 M) and Cu (II) (0.05 M) ions of various acidities, adjusted using NH_4OH (0.1M)/ HCl (0.1 M), separately, were mixed with RH-SiO₂ and MCM-41, respectively. It was observed that there was an increasing removal of metals with increasing pH. At pH 6, the highest removal was observed for Co(II) ions with RH-SiO₂, and MCM-41, as shown in Figs(4.7) and (4.8), while for the Cu(II) ion the highest removal occurred at pH 5 for both RH-SiO₂ and MCM-41, as shown in Figs(4.9) and (4.10). The pH influenced the adsorbance and the adsorbent surface, where the hydroxide and hydrogen ions compete for the adsorbent surface, where a change in the acidity of the solution can affect the adsorption process in either a negative or positive manner [297]. It is usually thought that when the pH is lower, more hydrogen will concentrate on the surfaces of the RH-SiO₂ and MCM-41, leading to strong competition between the adsorption proton and metal ions by the active site on the surface, causing more free metal ions to remain in solution [298]. After the highest value, the amount of removal doesn't change due to the production of metal oxide [299, 300]. It is clear that the removal of the divalent metal ions increases in the order Cu (II) > Co (II). The order of metal removal capacities agreed with the stability constants established by Irving William and the acid-base concept developed by Pearson [301].

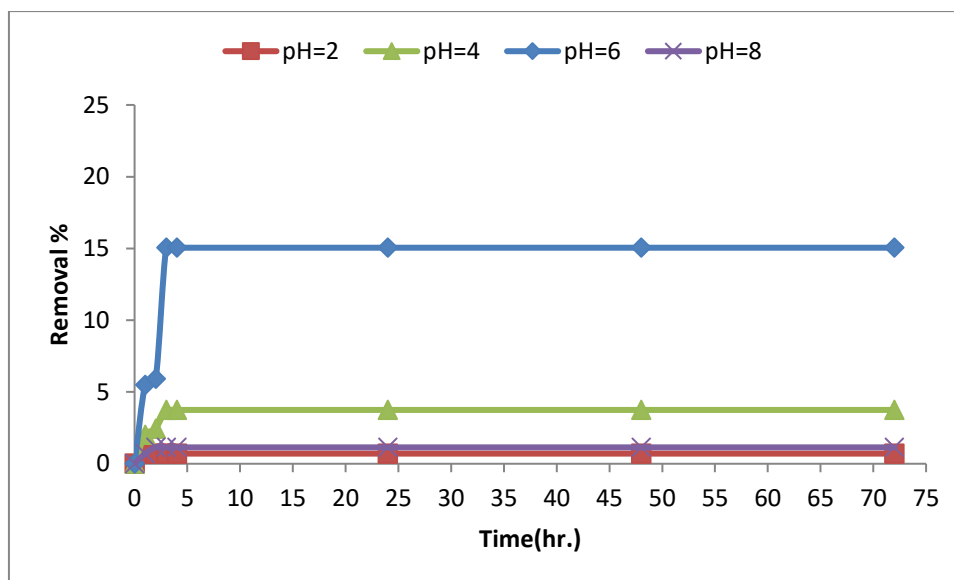


Figure (4.7): The removal of Co (II) ions by RH-SiO₂ at various pHs.

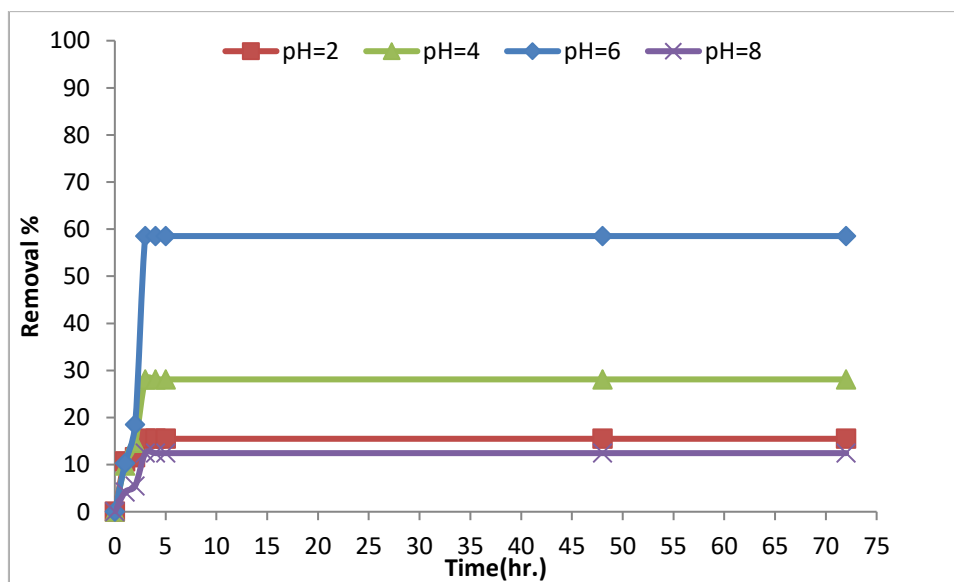


Figure (4.8): The removal of Co (II) ions by MCM-41 at various pHs.

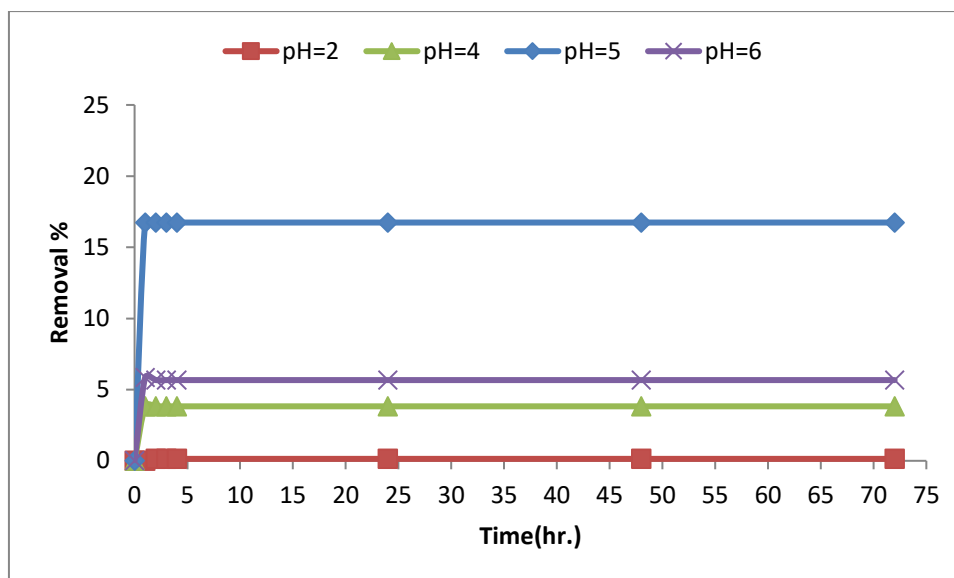


Figure (4.9): The removal of Cu (II) ions by RH-SiO₂ at various pHs.

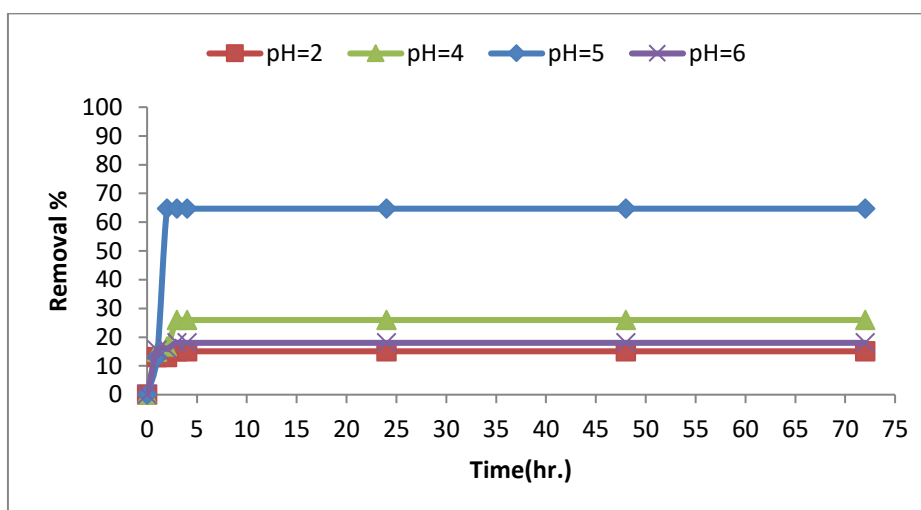


Figure (4.10): The removal of Cu (II) ions by MCM-41 at various pHs.

4.3.1.1.3. Effect of concentration of Co (II) and Cu (II) ions

The concentration of ions has a big impact on adsorption. The removal of ions increases as the initial concentration of ions increases. The initial concentration gives an important driving force to overcome all mass-transfer resistance of adsorption between the aqueous and solid phases[294]. Different concentration of cobalt and copper ions (0.02–0.1M) were used to investigate the removal of ions at optimized pH for both ions. The results are shown in Figs.(4.11),(4.12),(4.13) and(4.14) demonstrated that the

removal of ions increased with an increase in the concentration of Co(II) and Cu(II) ions at various times [295], which could possibly be because each ion forms a 1:1 complex with the ligand at high concentration; in contrast, when the concentration of the ion is low, there is minimal amount of uptake of ions due to the formation of a 1:2 complex (metal to ligand) [302]. The higher concentration of metal ions means a larger number of binding sites are occupied, which results in increased removal [303]. Over this concentration, the balance was come to likely since of the limited number of active sites available to adsorb on the compounds surfaces. As expected, the large molecule may well be adsorbed essentially on the outside surface or in wider pores. In this way, upon covering the surface, a second layer was not favorable [304].

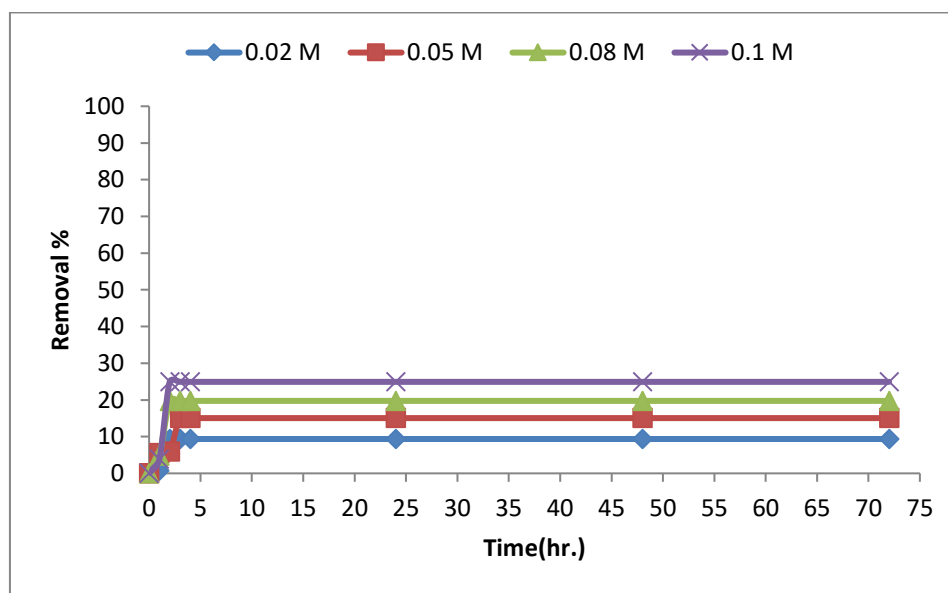


Figure (4.11): The removal of Co (II) ions by RH-SiO₂ using various initial concentration

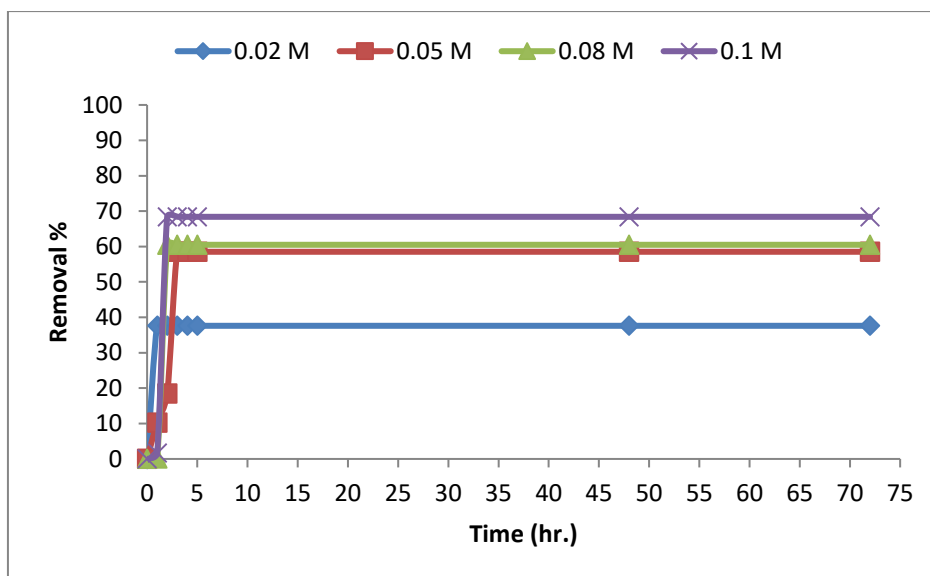


Figure (4.12): The removal of Co (II) ions by MCM-41 using various initial concentration

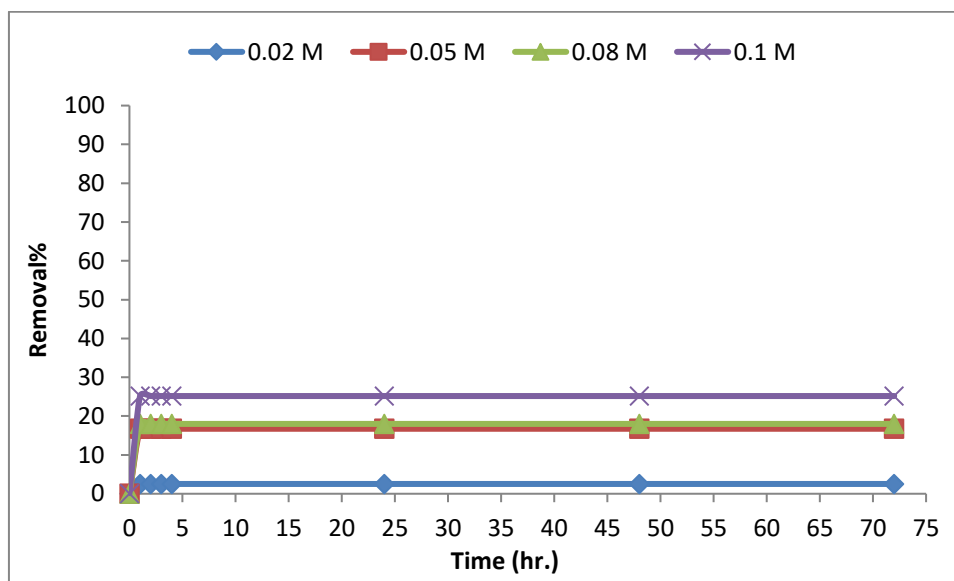


Figure (4.13): The removal of Cu (II) ions by RH-SiO₂ using various initial concentration.

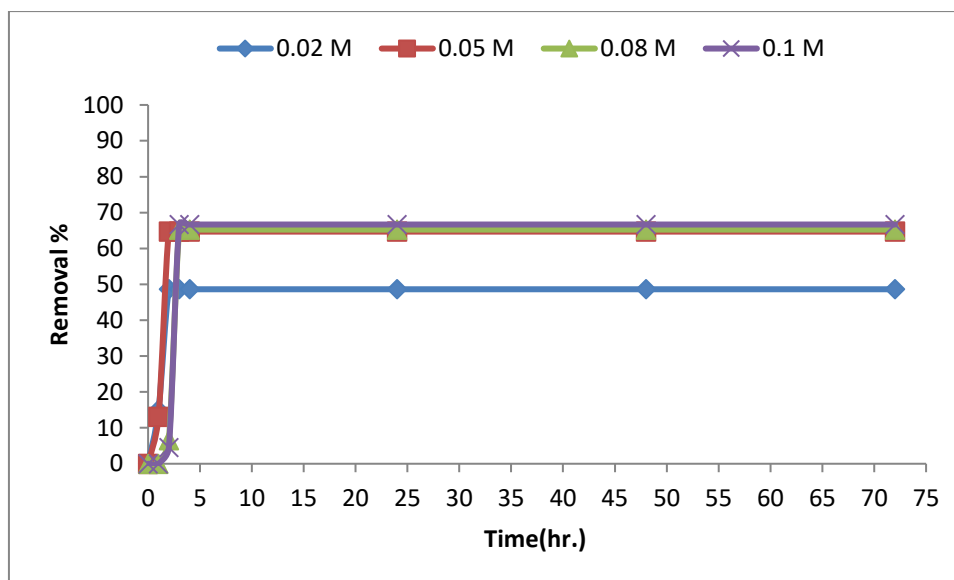


Figure (4.14): The removal of Cu (II) ions by MCM-41 using various initial concentration.

4.3.1.1.4. Effect of mass of RH-SiO₂ and MCM-41

The experiment has been performed by taking different amounts of adsorbent (0.1, 0.15 and 0.2 g per 50 mL) in the test solutions at optimized pH for both ions (cobalt at 0.05 M and copper at 0.05 M). Figs. (4.15),(4.16),(4.17)and(4.18) shows how the removal of Co(II) and Cu(II) ions varied as adsorbent amount were increased from 0.1 to 0.2 g. Maximum removal of Co(II) and Cu(II) ions were observed for 0.2 g at RH-SiO₂. Similarly, a maximum removal of Co (II) and Cu(II) ions occurred when using 0.2 g of MCM-41. The finding demonstrated a progressive increasing in the removal of metal ion as the adsorbent quantity was increased [305, 306]. However, a subsequent increase in adsorbent will not affect the removal of Cu (II) and Co (II) ions from the solution. This can be due to donor sites of the solid ligand being blocked by the ligand itself which leads to decrease the surface area of the ligands [307].The results also showed that MCM-41 shows more efficient removal of Co(II) and Cu(II) ions in solution than RH-SiO₂ with increasing adsorbent amount.

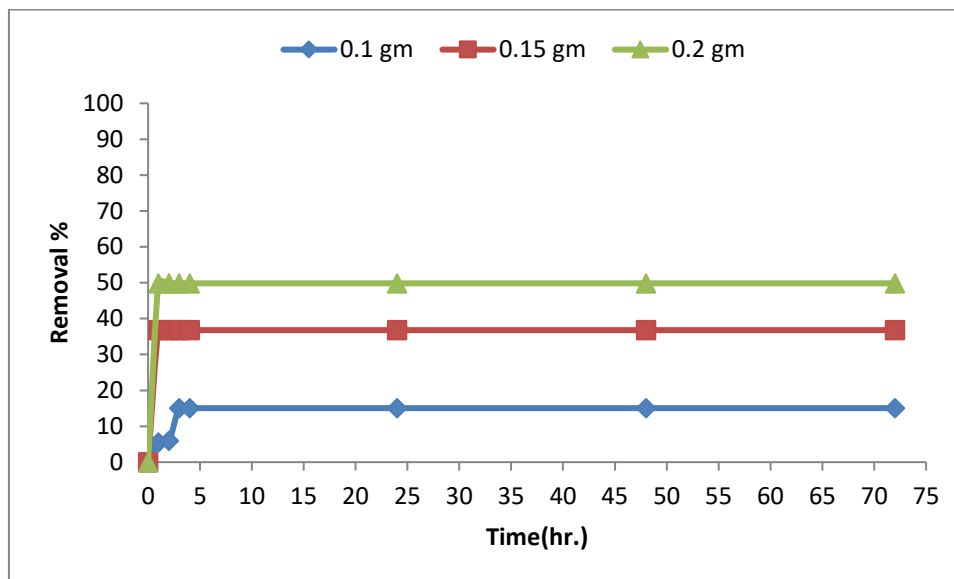


Figure (4.15): The removal of Co (II) ions by various mass of RH-SiO₂.

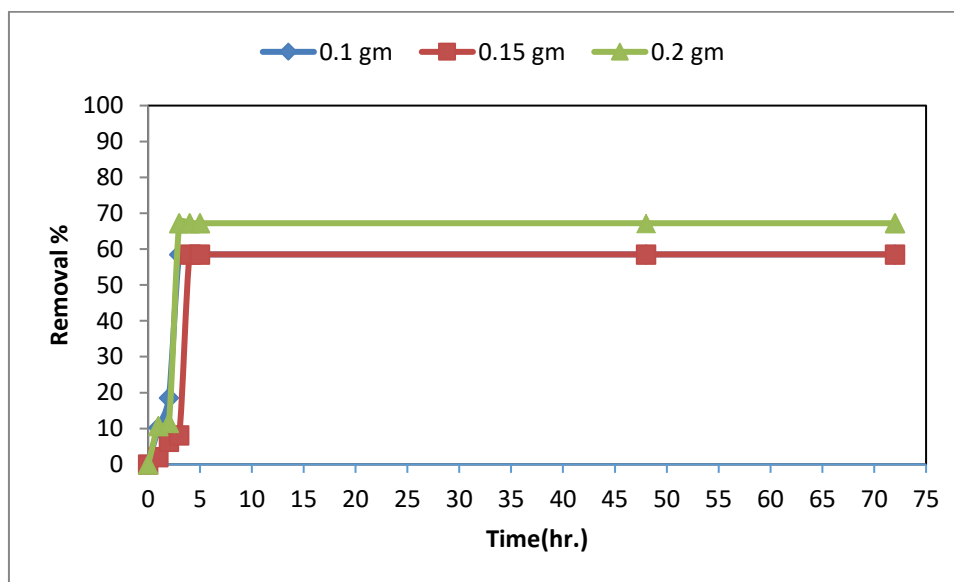


Figure (4.16): The removal of Co (II) ions by various mass of MCM-41.

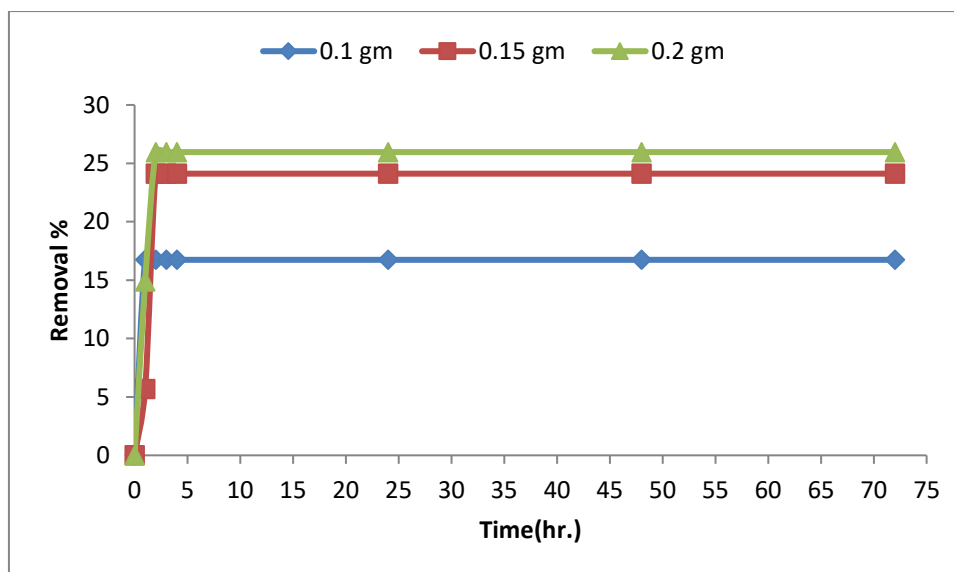


Figure (4.17): The removal of Cu (II) ion by various mass of RH-SiO₂.

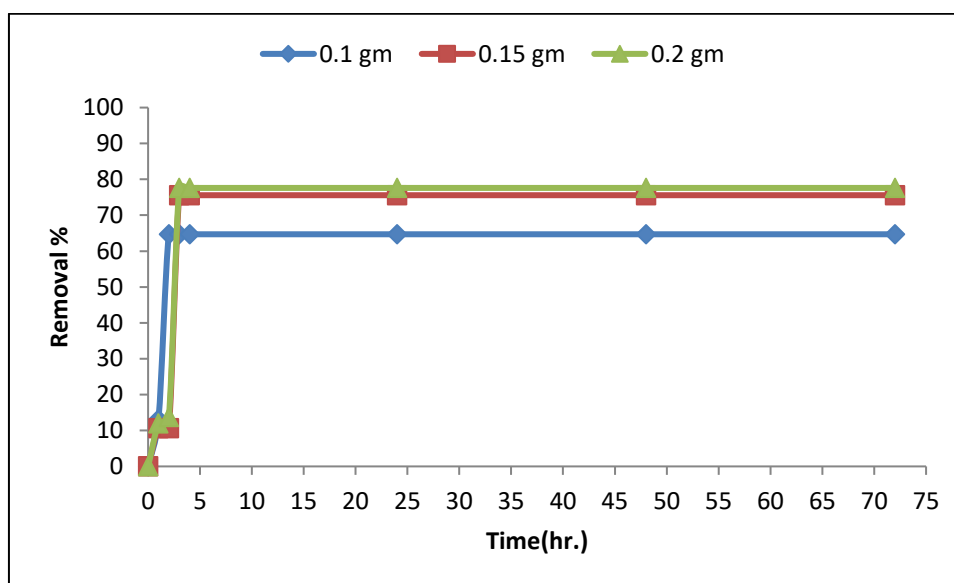


Figure (4.18): The removal of Cu (II) ion by various mass of MCM-41.

4.3.1.2 Removal of metal ions by MCM-41@APTES and MCM-41@APTES-BSAL

4.3.1.2.1. Effect of exposure time

Figs.(4.19) and (4.20) show the removal efficiency of metal ions (0.05M for Co (II) and 0.05M for Cu (II) ions), separately. The removal of ions was determined by shaking 0.1g of ligands with 50 mL aqueous divalent metal ion for 72 hrs..The removal of metal ions is adsorbed increases over time, but not in a straight line. The increase in metal ion

removal with increase the time of exposure due to diffusion factors. Initially the removal of ions increased during the first hour. Then, after 4 hours, it became very slow, probably because of blocking the pore. It was found that there was no change in the removal of ions when the stirring time was increased. Therefore, the equilibrium time of the removal process is over four hours[295].

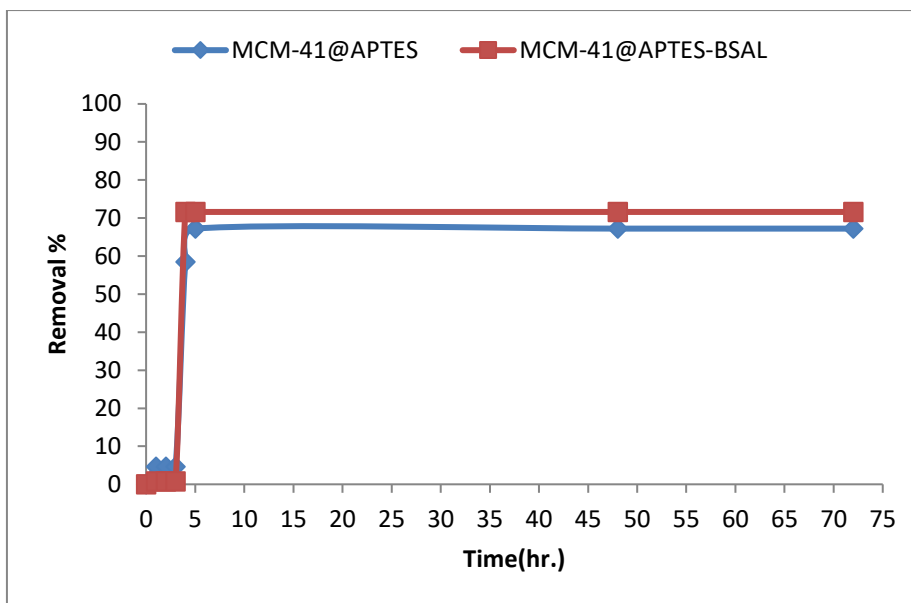


Figure (4.19): The removal of Co (II) ion by MCM-41@APTES and MCM-41@APTES-BSAL ligand versus time.

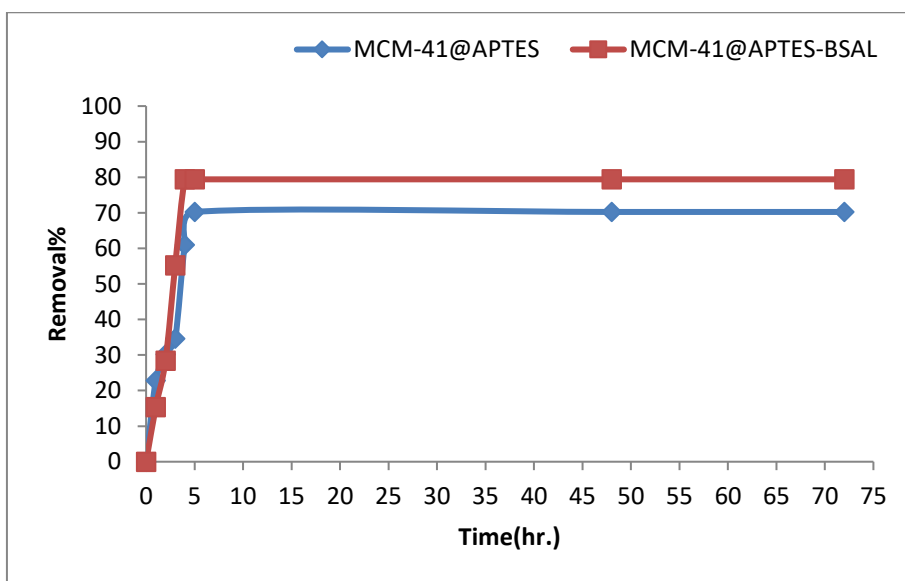


Figure (4.20): The removal of Cu (II) ions by MCM-41@APTES and MCM-41@APTES-BSAL ligand versus time.

4.3.1.2.2. Effect of pH

The effects of the acidity level (pH) on the removal of copper and cobalt ions by MCM-41@APTES and MCM-41@APTES-BSAL were investigated by mixed 50 mL(0.05)M of metal ions and 0.1g of MCM-41@APTES and MCM-41@APTES-BSAL, at different PH, respectively. The temperature was kept at 25 °C.

Figs.(4.21),(4.22),(3.23)and(4.24) show that the amount of Co(II) and Cu(II) adsorbed by MCM-41@APTES and MCM-41@APTES-BSAL, respectively increased when the pH increased, but after the highest value there is no change in the amount of removal of ions. At low pH levels, the active sites on the surface of the adsorbents were overly filled with protons, which made it difficult for ions to bond with the active sites. When the solution becomes less acidic, the functional groups on the adsorbent surface lose their protons. This causes the surface of adsorbent become more negatively charged and helps the binding of cations. The removal of ions that can be adsorbed increases when the pH is higher[308]. Removing metal ions decreased when the pH is more high(pH=6 for Co(II) and PH=5 for Cu(II) ,respectively) because their hydroxides are formed[299], causing in precipitates. So, when the pH is high, metal ions are taken out by making solid precipitates instead of adsorption[309].

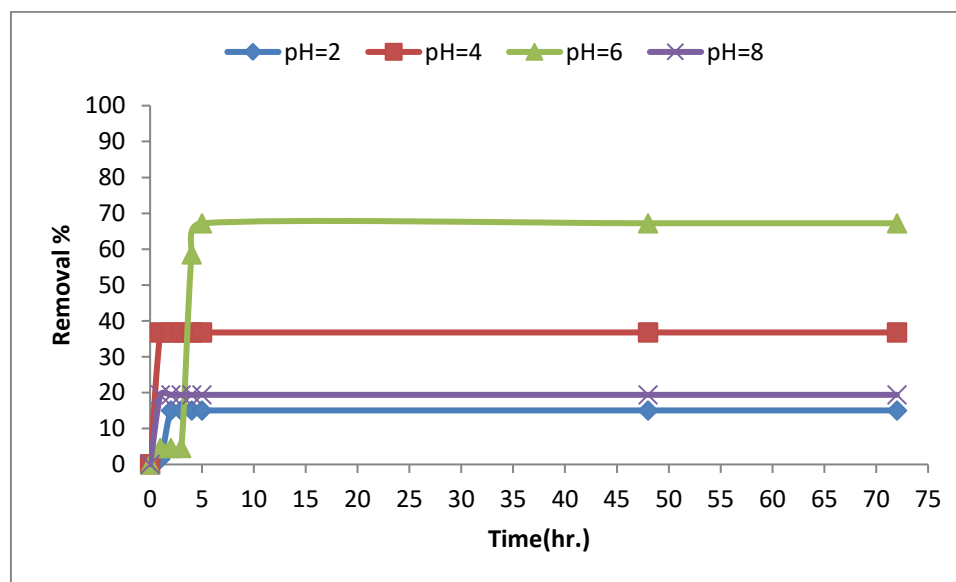


Figure (4.21): The removal of Co (II) ions by MCM-41@APTES with various pHs.

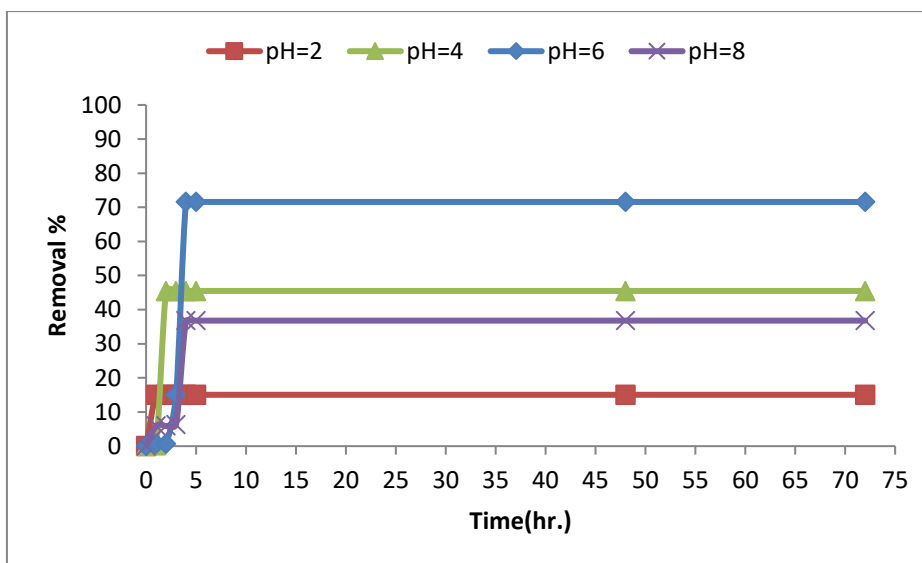


Figure (4.22): The removal of Co (II) ions by MCM-41@APTES-BSAL with various pHs.

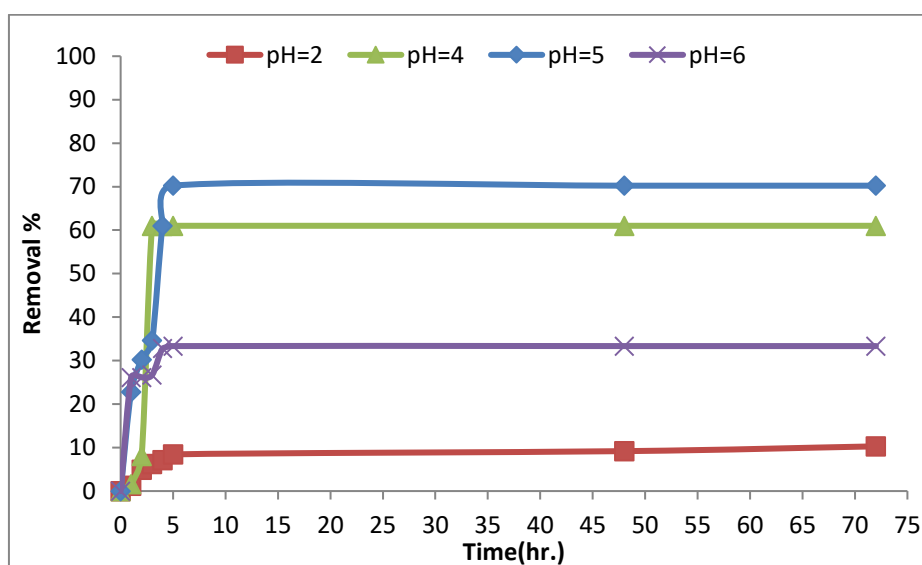


Figure (4.23): The removal of Cu (II) ions by MCM-41@APTES with various pHs.

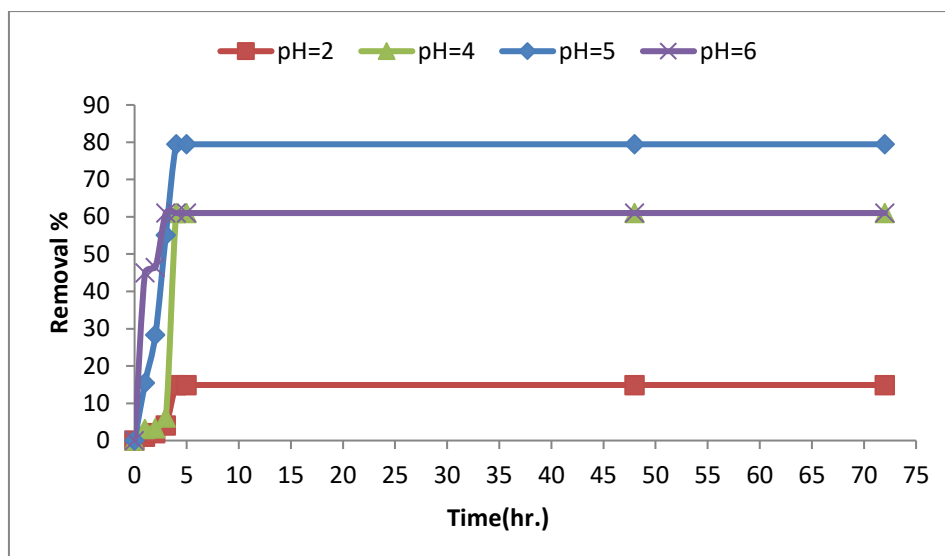


Figure (4.24): The removal of Cu (II) ions by MCM-41@APTES-BSAL with various pHs.

4.3.1.2.3. Effect of concentration of Co (II) and Cu (II) ions

Effects of the initial concentration of metal ions on the removal process were studied. 0.1 grams of MCM-41@APTES and MCM-41@APTES-BSAL, separately were shaken for 72 hours with three different initial concentration solutions of metal ions, which has ranging from (0.02– 0.10 M) at optimum pH. The findings, as seen in Figs.(4.25),(4.26),(4.27)and(4.28) indicate that the ability to adsorb increases as the initial concentration of metal ions increases, due to the formation of 1:1 complex (metal to ligand) at high concentration in contrast, when the concentration of the ion is low, there is minimal amount of uptake of ions due to the formation of a 1:2 complex(metal to ligand) [299].

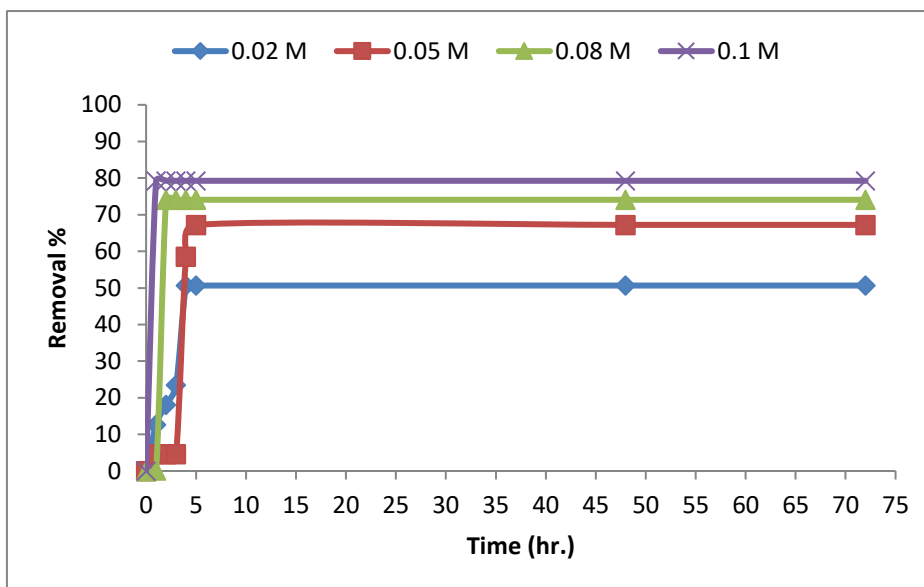
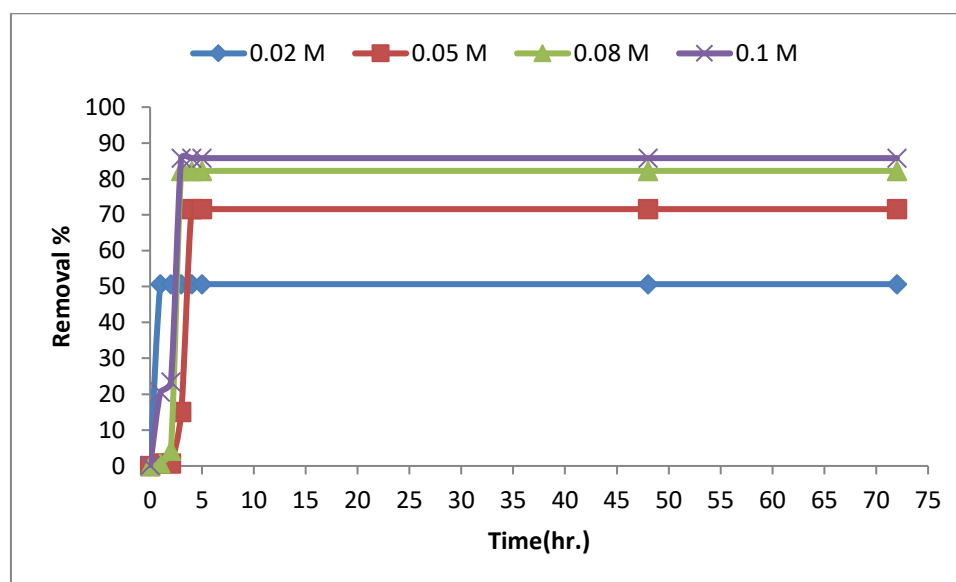


Figure (4.25): The removal of Co (II) ions by MCM-41@APTES with various initial concentration.



Figure(4.26):The removal of Co (II) ions by MCM-41@APTES-BSALwith various initial concentration

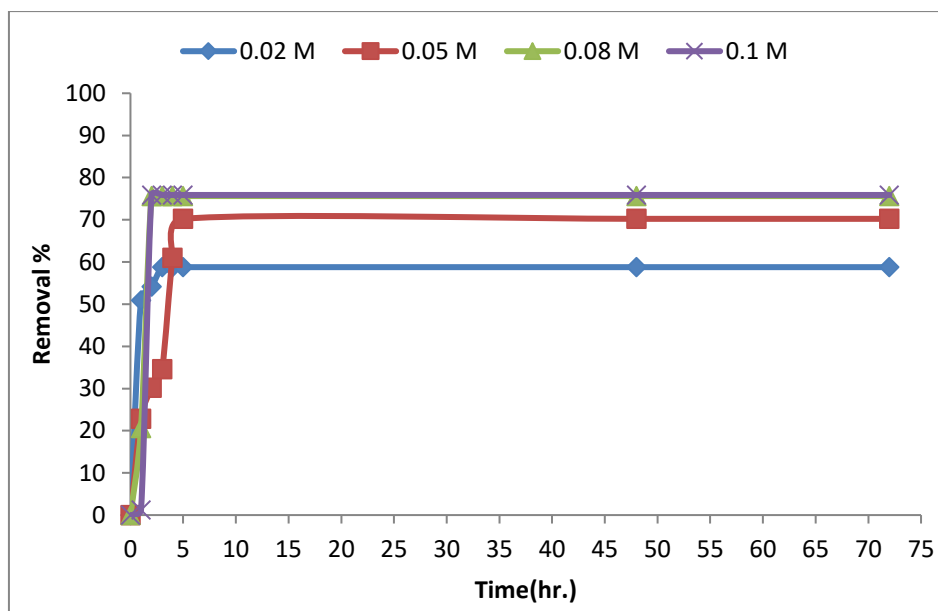


Figure (4.27): The removal of Cu (II) ions by MCM-41@APTES with various initial concentration

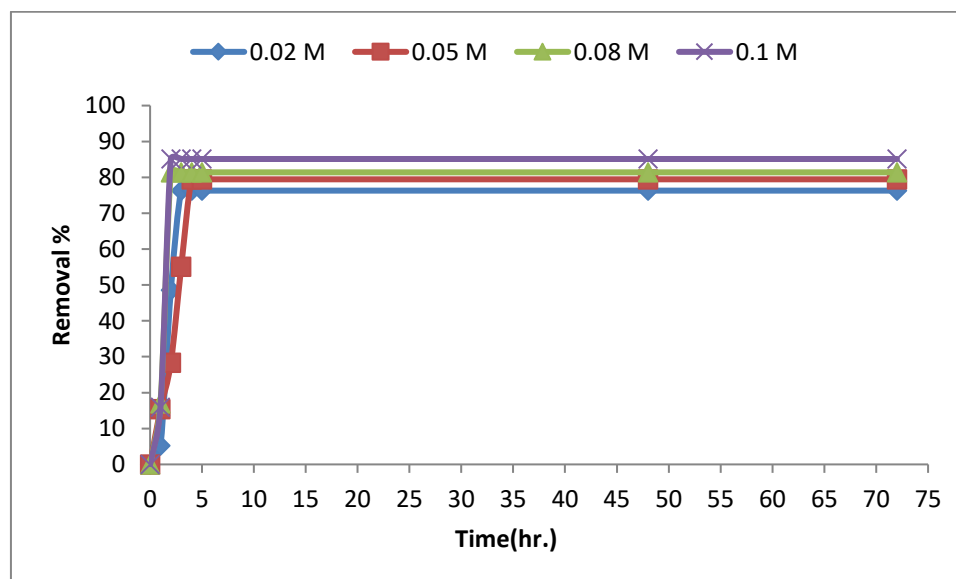


Figure (4.28): The removal of Cu (II) ions by MCM-41@APTES-BSAL with various initial concentration

4.3.1.2.4. Effect of mass of the (MCM-41@APTES and MCM-41@APTES-BSAL)

Different amounts of adsorbent were tested :(0.10, 0.15 and 0.20) g per 50 mL of aqueous solution of ions at optimized pH, starting period for 72 hrs. to study adsorbent

amount effect. Figs. (4.29), (4.30), (4.31) and (4.32) show how the removal of Co (II) and Cu (II) ions varied as adsorbent amount were increased. The findings indicated a gradual increase in removal of metal ions as the adsorbent amount was increased. More Cu (II) ions were adsorbed as the amount of an adsorbent amount increased due to the number of binding sites was increased. Similarly, a maximum removal of Co (II) ions. Using more adsorbent did not make a big difference in the removal of ions. The high amount of the adsorbent would increase the number of places where metal ions can attach. This was found by Babel and Kurniawan [310], and Najua et al. also reported the same [306]. It was also found that when more adsorbent was used than the maximum amount it could adsorb, the efficiency of removal no change because the sites where the ions adsorption are too crowded, causing a difference in the concentration of ions between the solution and the surface of the substance that adsorbs them [311]. The results also showed that MCM-41@APTES-BSAL is better at adsorbing ions from a solution compared to MCM-41@APTES when more adsorbent was added due to more active side on the surface.

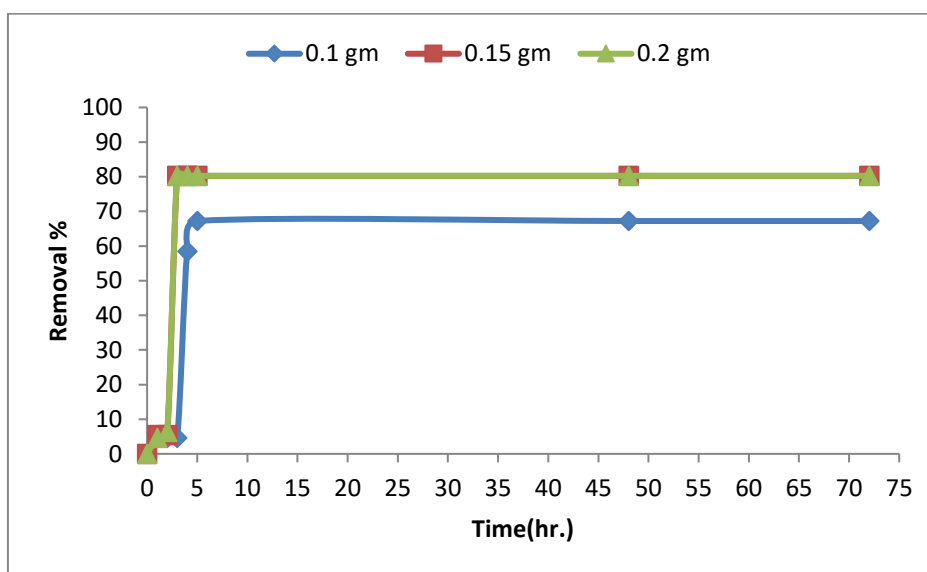


Figure (4.29): The removal of Co (II) ions by MCM-41@APTES with various mass.

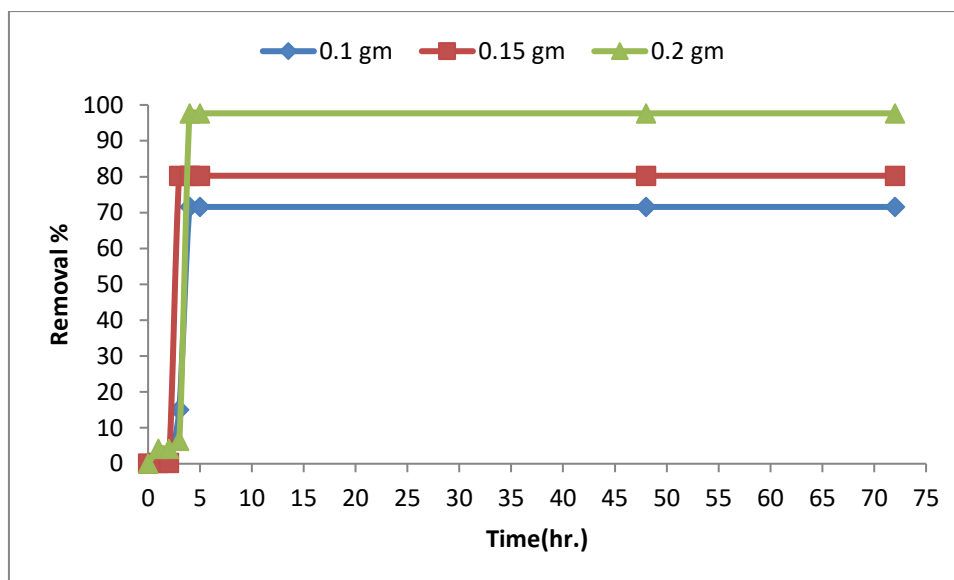


Figure (4.30): The removal of Co (II) ions by MCM-41@APTES-BSAL with various mass.

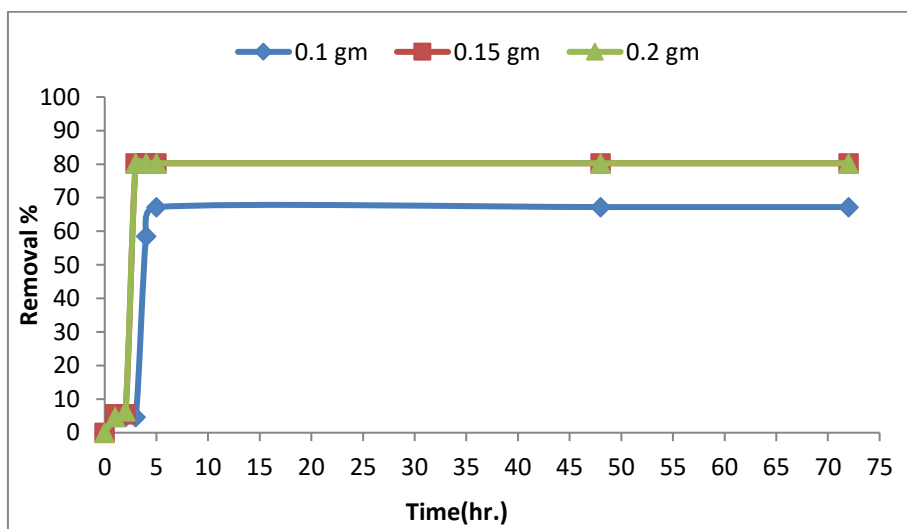


Figure (4.31): The removal of Cu (II) ion by MCM-41@APTES with various mass.

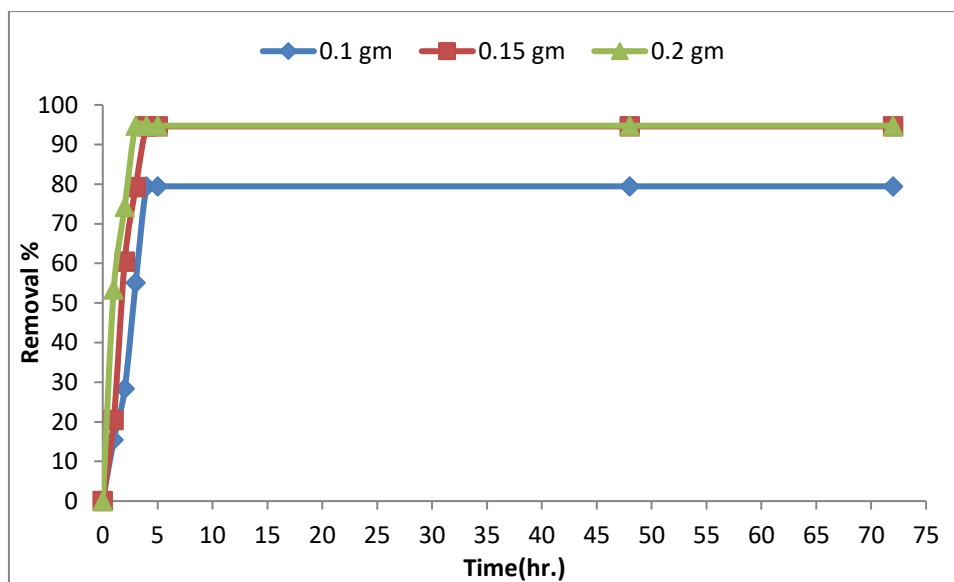


Figure (4.32): The removal of Cu (II) ion by MCM-41@APTES-BSAL with various mass.

4.3.1.3 Removal of metal ions by MCM-41@NTPE and MCM-41@NTPE-BSAL

4.3.1.3.1. Effect of exposure time

To investigate shaking time affects in the removal of metal ions from aqueous solution, 0.1g of prepared ligands (MCM-41@NTPE and MCM-41@NTPE-BSAL), respectively mixed with 50 mL aqueous solution of divalent metal ions (cobalt and copper) for 72 hrs .at optimizing pH. The results are shown in Figs. (4.33), (4.34), (4.35) and (4.36) which explain the concentration of metal ions as a function of exposure time in a non-linear fashion. The metal ion removal increased rapidly at first, then no change occurs as time increase (removal process's equilibrium), the increase in the removal of metal ions may be attributed to diffusion factors. These results are in agreement other services [299].

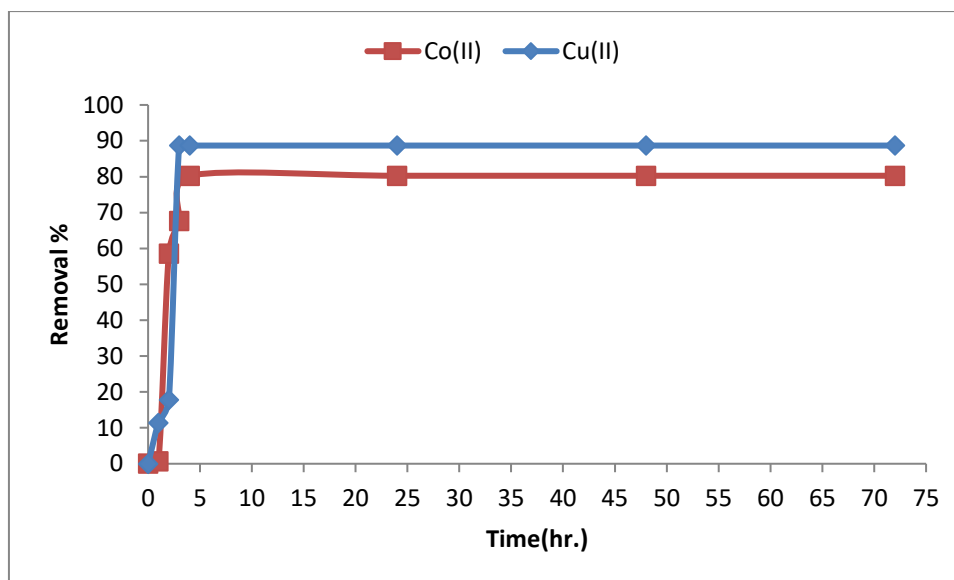


Figure (4.33): The removal of Co (II) and Cu (II) ions by MCM-41@ NTPE ligand versus time.

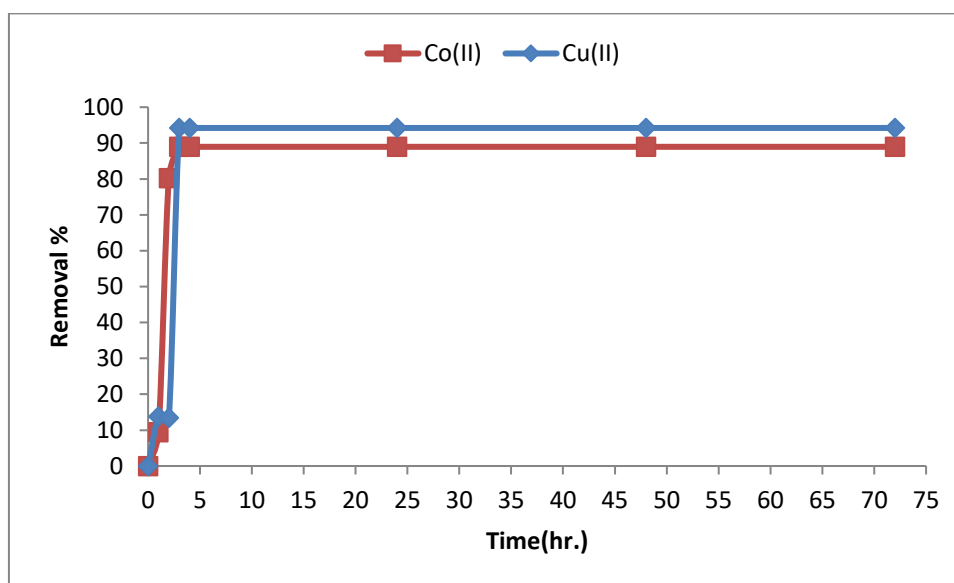
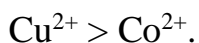


Figure (4.34): The removal of Co (II) and Cu (II) ions by MCM-41@NTPE-BSAL ligand versus time.

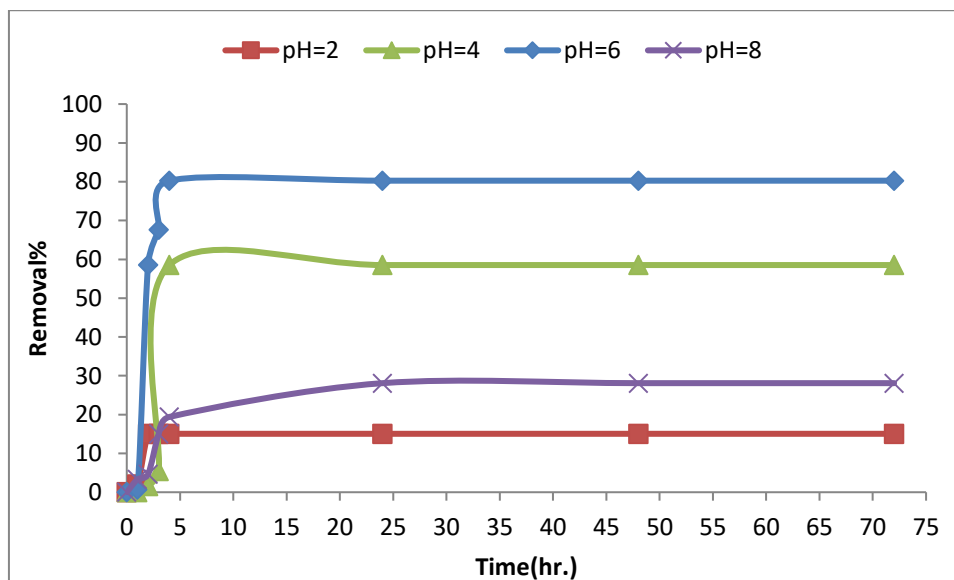
4.3.1.3.2. Effect of pH

Figs.(4.35),(4.36),(4.37)and(4.38) show the effect of the pH value(adjusted using NH_4OH (0.1 M)/ HCL (0.1 M)) on the removal of Co(II) and Cu(II) and ions from aqueous solution by MCM-41@NTPE and MCM-41@NTPE-BSAL.The findings revealed that as the pH value increased, more metal ions were adsorbed. The highest

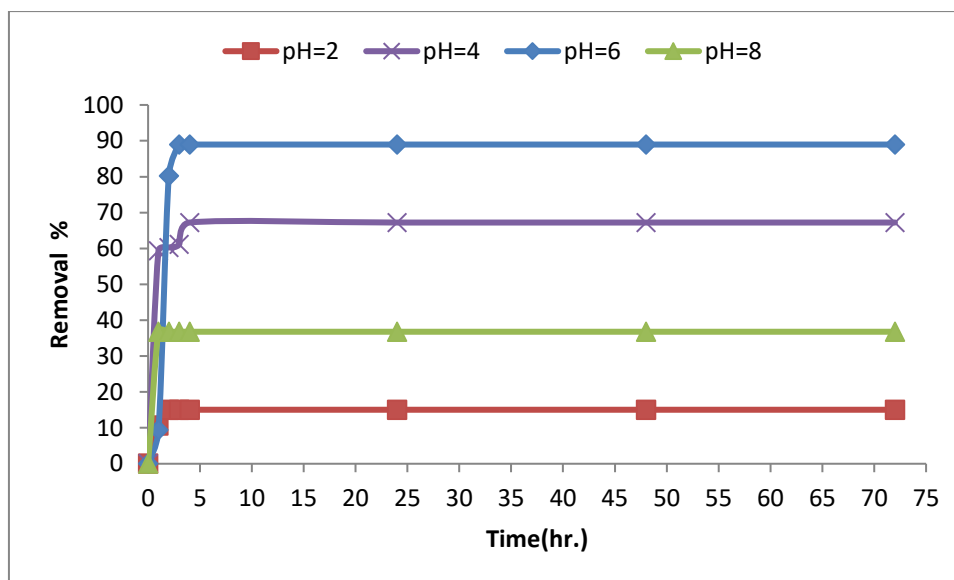
removal of metal ions occurred at a pH= 6 for cobalt and pH=5 for copper. When the pH is low, the removal capacity is low because the amine parts become protonated. This makes it harder for metal ions to adsorbed[312].At high pH values, metal ions begin to form hydroxides, which were less soluble and therefore less available to the ligand. This is why high pH values were not studied in this experiment [312]. It is obvious that the amount of divalent metal ions increase in the following order:



The order of removal for divalent metals follows the stability constants established by Irving William and the acid-base theory explained by Pearson[301].The ligands have different properties depending on the atoms they contain (N and O). Due to this characteristic, they have the ability to bind with both soft and hard metal ions. This usually happens when the number of atoms that are used for donation in a ligand system increases[301].



Figure(4.35):The removal of Co(II) ions by MCM-41@ NTPE at various pHs.



Figure(4.36):The removal of Co(II) ions by MCM-41@NTPE-BSAL at various pHs.

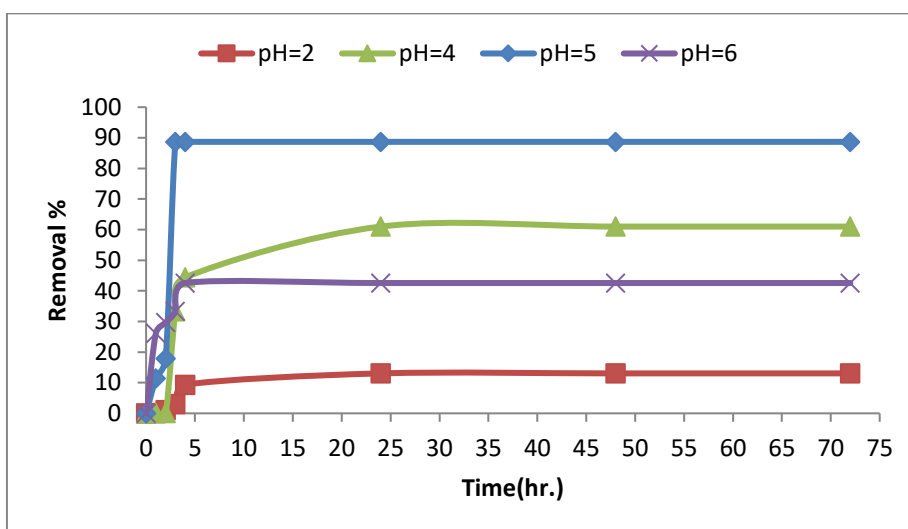


Figure (4.37): The removal of Cu (II) ions by MCM-41@ NTPE at various pHs.

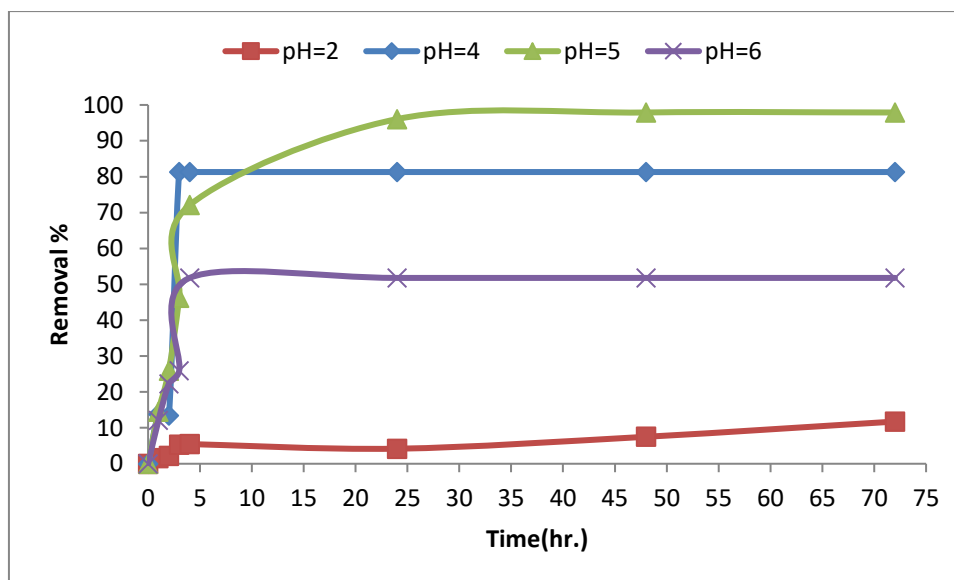


Figure (4.38): The removal of Cu (II) ions by MCM-41@NTPE-BSAL at various pHs.

4.3.1.3.3. Effect of concentration of Co (II) and Cu (II) ions

Figs.(4.39),(4.40),(4.41) and (4.42) shows how concentration of ions affects the removal of Co(II) and Cu(II) ions by MCM-41@NTPE and MCM-41@NTPE-BSAL.0.1g of MCM-41@NTPE and MCM-41@NTPE-BSAL were shaken with 50 mL of aqueous ions solution at different concentration(0.02,0.05 and 0.1M) for 72 hrs. at optimized pH for both ions. The removal increased with increasing concentration of each metal ions [295],The maximum removal concentration of ions almost happened during the 3 hrs., no change in the absorption of ions after that, this can say that the condition of saturation occurred[299].

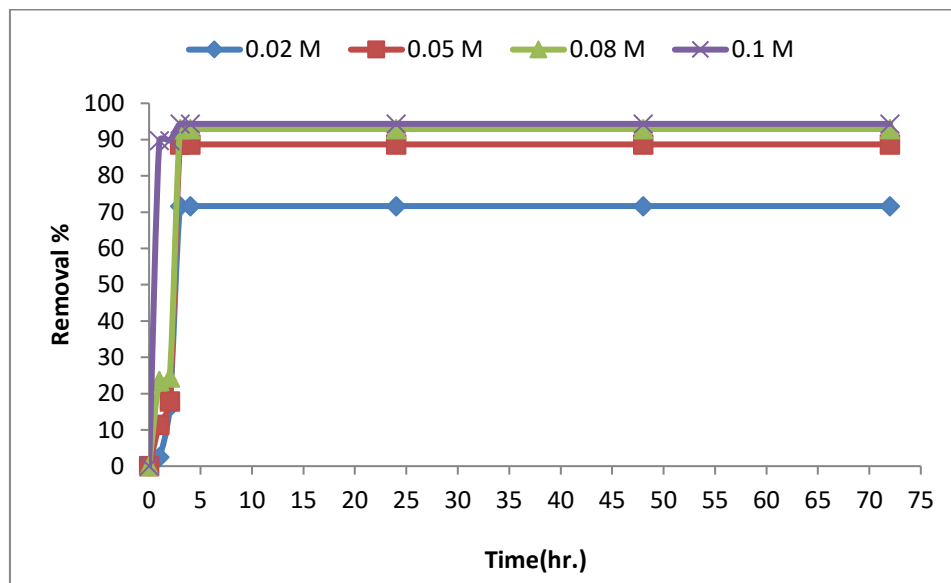


Figure (4.39): The removal of Co (II) ions by MCM-41@NTPE at various initial concentration.

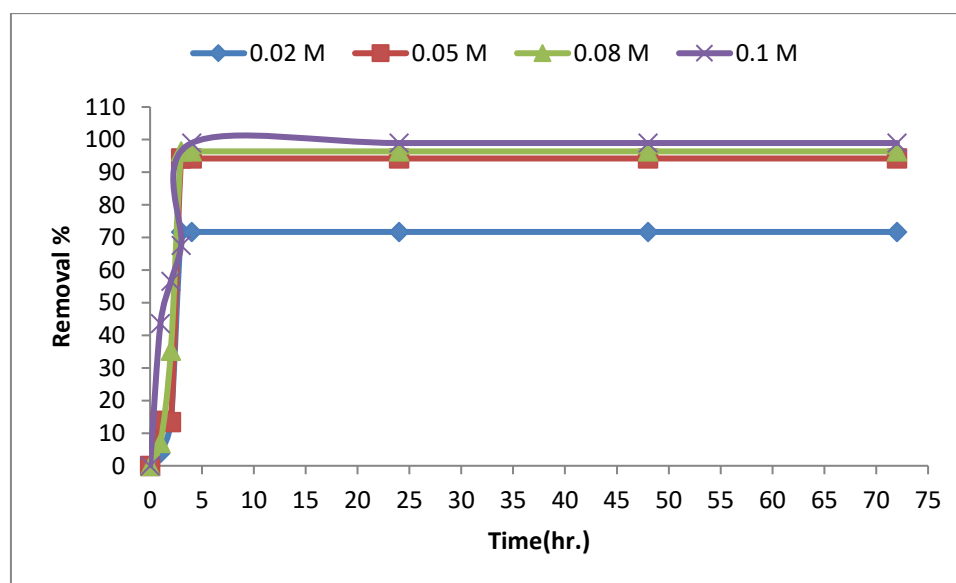


Figure (4.40): The removal of Co (II) ions by MCM-41@NTPE-BSAL at various initial concentration.

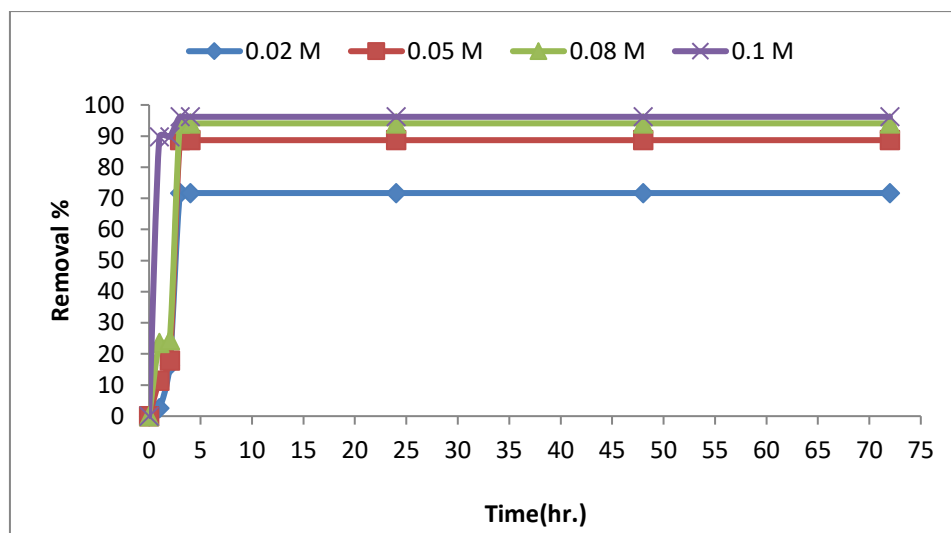


Figure (4.41): The removal of Cu (II) ions by MCM-41@NTPE at various initial concentration.

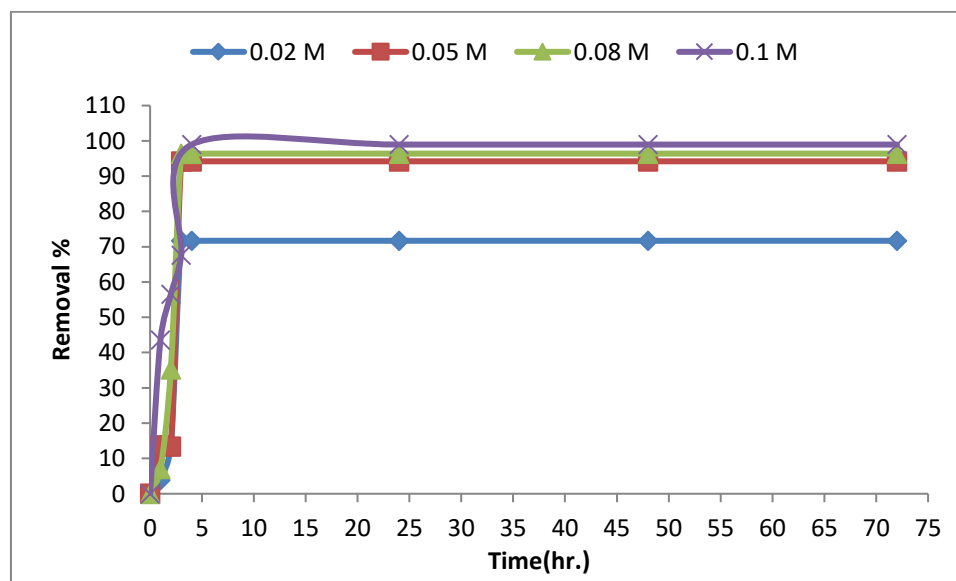


Figure (4.42): The removal of Cu (II) ions by MCM-41@NTPE-BSAL at various initial concentration.

4.3.1.3.4. Effect of mass of MCM-41@NTPE and MCM-41@NTPE-BSAL

The impact of the MCM-41@NTPE and MCM-41@NTPE-BSAL amount were examined utilizing three distinctive mass of ligand (0.1, 0.15, and 0.2 g) per 50 mL of ions at optimized pH. A Figs. (4.43), (4.44), (4.45) and (4.46) shows how much MCM-

41@NTPE and MCM-41@NTPE-BSAL could removal Co (II) and Cu (II) ions, respectively. The removal efficiencies of both ions Co(II) and Cu(II) increased gradually with increasing adsorbent amount of compounds[313].It is easy to understand that the ability of MCM-41@NTPE and MCM-41@NTPE-BSAL to removal depends on how active its surface.This means that MCM-41@NTPE and MCM-41@NTPE-BSAL needs to have a certain amount of surface area available for the ions to interact with. So, if you increase the amount of MCM-41@NTPE and MCM-41@NTPE-BSAL, it will increase the ability to removal ions. Clearly, the MCM-41@NTPE-BSAL was better at adsorbing ions from the solution compared to MCM-41@NTPE. However, a subsequent increase in adsorbent will not affect the removal of Cu (II) and Co (II) ions from the solution. This could be due to donor sites of the solid ligand being blocked by the ligand itself [307].

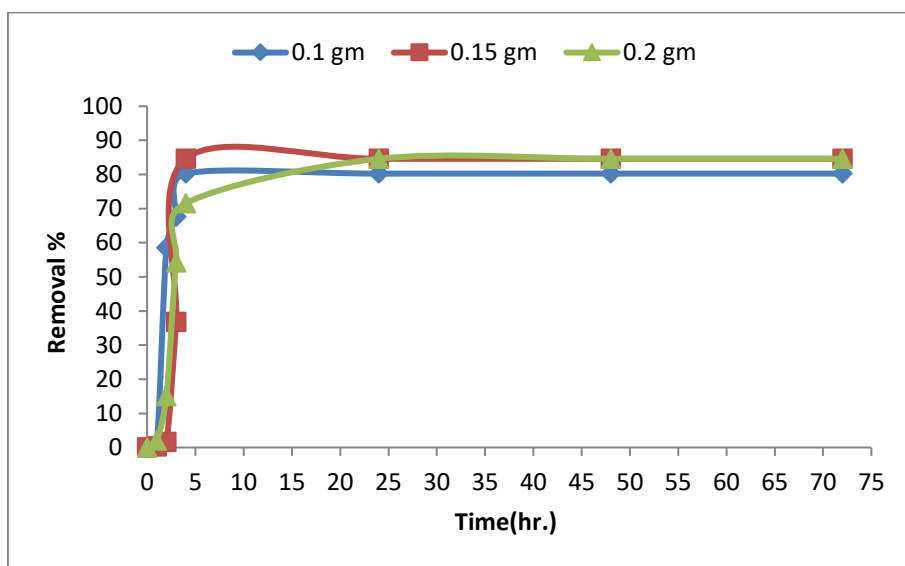


Figure (4.43): The removal of Co (II) ions by MCM-41@NTPE with various mass

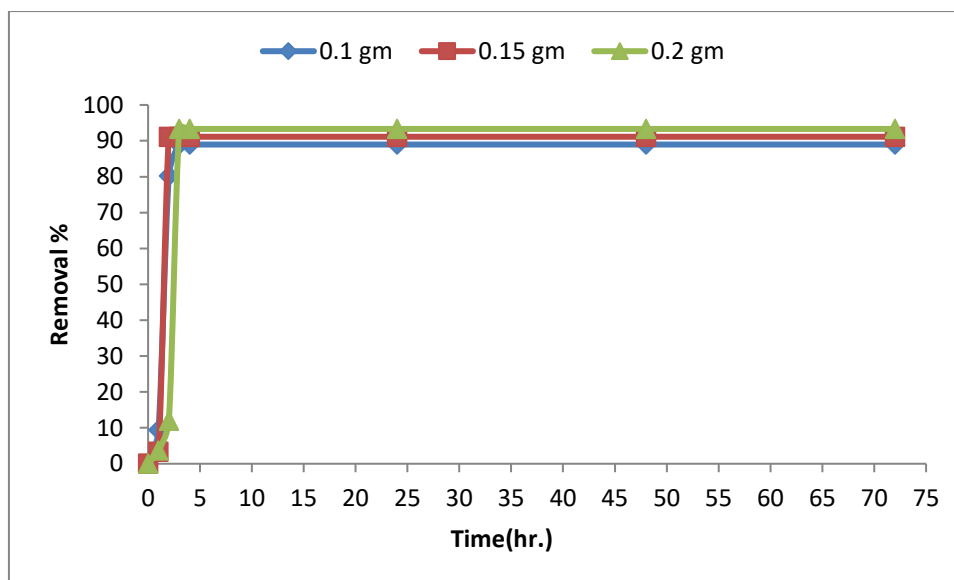


Figure (4.44): The removal of Co (II) ions by MCM-41@NTPE-BSAL with various mass

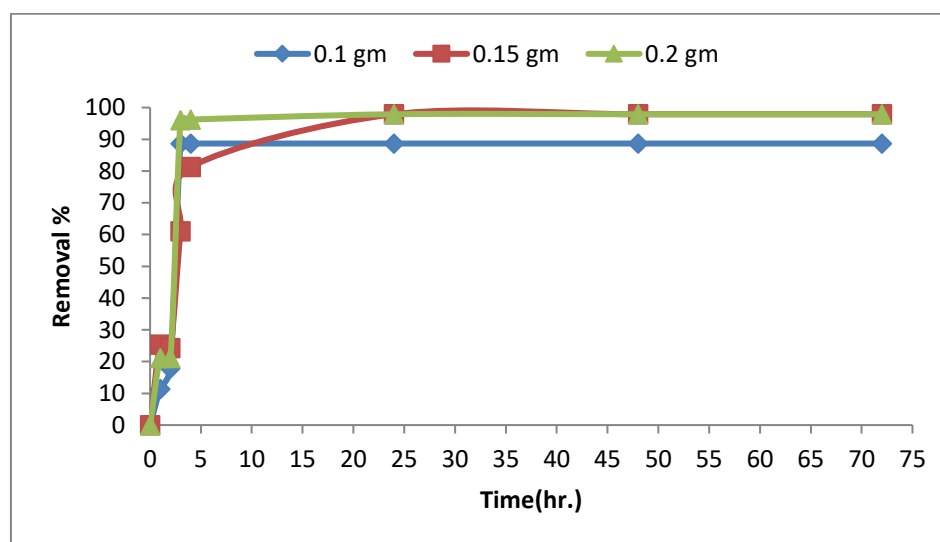


Figure (4.45): The removal of Cu (II) ions by MCM-41@NTPE with various mass

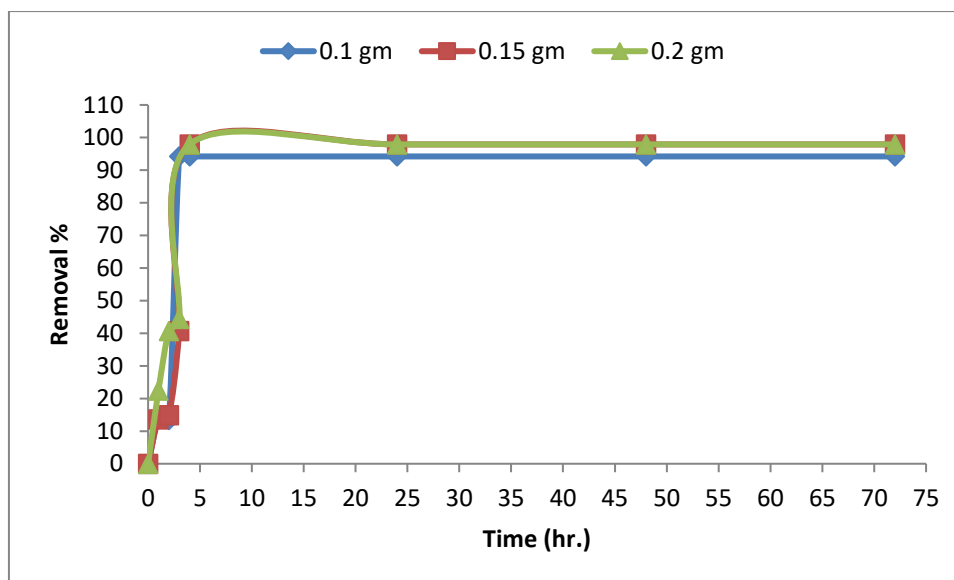


Figure (4.46): The removal of Cu (II) ions by MCM-41@NTPE-BSAL with various mass .

4.4 Column separation experiment

A glass column (500 mm long, 25 mm diameter) was washed, and then it was oven dried. A amount of the RH-SiO₂, MCM-41 and functionalized ligand was packed in the column, respectively. After each use the column was washed with deionized water. Before any sample injection, the column was conditioned by passage of 50 cm³ of the appropriate eluent at optimum pH, The pH of the eluent was controlled using NH₄OH (0.1 M)/HCL (0.1 M), and the amount of metal ion was determined using spectrophotometer. The following equation was used to calculate the removal of cobalt and copper from aqueous solutions[235]:

$$\text{Removal} = (C_0 - C_e)$$

Where C₀ and C_e are the initial concentration at zero and the adsorbed concentration after contact time, respectively. Table (4.1) shows the removal of different concentration (20,50,100,500 and1000)ppm of ions with the compounds prepared.

Table (4.1): Different concentration (20, 50,100,500 and1000) ppm

Co(II)+MCM-41											
	0.1g of ligand					0.05 g	0.15g	PH=2	pH=4	pH=6	pH=8
Time (min)	20ppm	50ppm	100ppm	500ppm	1000ppm	50ppm		50ppm			
	Removal										
0	0.000	0.000	0.000	0.000	0.000	0.000	0.000	0.000	0.000	0.000	0.000
10	18.875	48.875	98.875	485.375	980.750	12.500	49.875	18.875	31.375	48.875	2.625
20	18.875	48.875	98.875	485.375	980.750	25.125	49.875	20.125	31.375	48.875	5.125
30	18.875	48.875	98.875	485.375	980.750	48.875	49.875	20.125	31.375	48.875	6.125
Co(II)+ MCM-41@APTES											
	0.1g of ligand					0.05 g	0.15g	PH=2	pH=4	pH=6	pH=8
Time (min)	20ppm	50ppm	100ppm	500ppm	1000ppm	50ppm		50ppm			
	Removal										
0	0.000	0.000	0.000	0.000	0.000	0.000	0.000	0.000	0.000	0.000	0.000
10	18.950	48.950	98.950	491.25	982.500	7.625	47.625	41.375	46.000	48.950	47.625
20	18.950	48.950	98.950	491.25	982.500	20.125	49.500	40.125	46.000	48.950	48.125
30	18.950	48.950	98.950	491.25	982.500	21.375	49.500	40.125	46.000	48.950	48.125
Co(II)+ MCM-41@APTES-BSAL											
	0.1g of ligand					0.05 g	0.15g	PH=2	pH=4	pH=6	pH=8
Time (min)	20ppm	50ppm	100ppm	500ppm	1000ppm	50ppm		50ppm			
	Removal										
0	0.000	0.000	0.000	0.000	0.000	0.000	0.000	0.000	0.000	0.000	0.000
10	19.000	25.125	72.625	495.000	990.000	12.625	48.875	1.375	25.125	25.125	1.375
20	19.000	49.000	98.125	495.000	990.000	20.125	49.875	2.625	48.000	49.000	2.625
30	19.000	49.000	98.375	495.000	990.000	26.375	49.875	20.125	48.000	49.000	7.625
Co(II)+ MCM-41@NTPE											
	0.1g of ligand					0.05 g	0.15g	PH=2	pH=4	pH=6	pH=8
Time	20ppm	50ppm	100ppm	500ppm	1000ppm	50ppm		50ppm			

(min)	Removal										
0	0.000	0.000	0.000	0.000	0.000	0.000	0.000	0.000	0.000	0.000	0.000
10	19.875	47.625	97.625	490.000	985.000	22.625	47.625	7.625	47.625	47.625	7.625
20	19.875	48.975	98.875	490.000	988.750	32.625	49.875	23.875	47.975	48.975	13.875
30	19.875	48.975	98.875	494.375	988.750	48.875	49.875	23.875	47.975	48.975	20.125
Co(II)+ MCM-41@NTPE-BSAL											
	0.1g of ligand					0.05 g	0.15g	PH=2	pH=4	pH=6	pH=8
Time (min)	20ppm	50ppm	100ppm	500ppm	1000ppm	50ppm		50ppm			
	Removal										
0	0.000	0.000	0.000	0.000	0.000	0.000	0.000	0.000	0.000	0.000	0.000
10	19.999	49.875	97.625	997.000	999.000	20.125	48.875	12.500	48.875	49.875	7.625
20	19.999	49.875	99.875	997.000	999.000	50.000	49.900	26.375	48.875	49.875	20.125
30	19.999	49.875	99.875	997.000	999.000	50.000	49.900	26.375	48.875	49.875	26.375
Cu(II)+ MCM-41											
	0.1g of ligand			0.05 g	0.15g	PH=2	pH=4	pH=5	pH=6		
Time (min)	20ppm	50ppm	100ppm	50ppm			50ppm				
	Removal										
0	0.00	0.00	0.00	0.00	0.00	0.00	0.00	0.00	0.00	0.00	0.00
10	11.222	44.556	0.111	36.778	49.000	39.000	44.000	44.556	44.556	2.333	
20	19.000	44.556	92.333	36.778	49.000	39.000	44.556	44.556	44.556	13.444	
30	19.000	45.667	93.444	47.889	49.000	40.111	44.556	45.667	45.667	30.111	
Cu(II)+ MCM-41@APTES											
	0.1g of ligand			0.05 g	0.15g	PH=2	pH=4	pH=5	pH=6		
Time (min)	20ppm	50ppm	100ppm	50ppm			50ppm				
	Removal										
0	0.00	0.00	0.00	0.00	0.00	0.00	0.00	0.00	0.00	0.00	0.00
10	19.000	47.889	41.111	24.444	49.889	2.222	47.889	49.889	49.889	11.111	
20	19.000	49.000	97.778	40.000	49.889	11.111	49.889	49.000	49.000	24.444	

30	19.000	49.000	97.778	48.889	49.889	22.222	49.889	49.889	24.444
Cu(II)+ MCM-41@APTES-BSAL									
	0.1g of ligand			0.05 g	0.15g	PH=2	pH=4	pH=5	pH=6
Time (min)	20ppm	50ppm	100ppm	50ppm		50ppm			
	Removal								
0	0.00	0.00	0.00	0.00	0.00	0.00	0.00	0.00	0.00
10	19.000	13.444	30.000	13.333	49.889	20.000	34.444	13.444	2.222
20	19.000	47.889	96.667	24.444	49.889	28.889	49.889	47.889	7.777
30	19.000	50.000	96.667	46.667	49.889	28.889	49.889	50.000	7.777
Cu(II)+ MCM-41@NTPE									
	0.1g of ligand			0.05 g	0.15g	PH=2	pH=4	pH=5	pH=6
Time (min)	20ppm	50ppm	100ppm	50ppm		50ppm			
	Removal								
0	0.00	0.00	0.00	0.00	0.00	0.00	0.00	0.00	0.00
10	19.000	13.444	30.000	13.333	49.889	20.000	34.444	13.444	2.222
20	19.000	47.889	96.667	24.444	49.889	28.889	49.889	47.889	7.777
30	19.000	49.000	96.667	46.667	49.889	28.889	49.889	49.000	7.777
Cu(II)+ MCM-41@NTPE-BSAL									
	0.1g of ligand			0.05 g	0.15g	PH=2	pH=4	pH=5	pH=6
Time (min)	20ppm	50ppm	100ppm	50ppm		50ppm			
	Removal								
0	0.00	0.00	0.00	0.00	0.00	0.00	0.00	0.00	0.00
10	19.000	13.444	30.000	13.333	49.889	20.000	34.444	13.444	2.222
20	19.000	48.889	97.667	47.444	49.889	29.889	49.889	48.889	8.000
30	19.000	49.000	97.667	47.667	49.889	29.889	49.889	49.000	8.000

4.5 Column recovery experience

3.0 g of adsorbent were placed into a glass column to generate a bed height that varied by 3.0 cm. Ion solutions were constantly supplied to the column until it was saturated (no removal was observed while evaluating the yield), the amount of eluent was measured using a spectrophotometer. After that, attempt to activate the components first with a 15 cm³ solution of 0.5 M hydrochloric acid, then with 0.5M nitric acid, and finally with deionized water. Then put 50 ml of aqueous solution of ions respectively, determination the removal after activation s. The results show activation of compounds leads to removal of ions ~ (35-42) % may be due to the difficulty in remove the ions inside the pours by using acids as shown in Table (4.2).

Table (4.2): Removal% after activation

compounds	Removal%(Co(II)) after activation	Removal%(Cu(II)) after activation
MCM-41	40	42
MCM-41@APTES	35	36
MCM-41@APTES-BSAL	38	40
MCM-41@NTEP	34	35
MCM-41@NTEP-BSAL	37	38

4.6 Determination of Co(II) ion in Vitamin B12

The amount of Co (II) in a pharmaceuticals(Vit B12) was measured using prepared compounds .Table (4.3)shows the outcomes of Co(II)ions analysis.

Table (4.3): Results of determination of Co (II) ions in Vit.B12 .

compounds	Concentration present of Co(II) µg/mL	Concentration remain of Co(II) µg/mL after used compounds	Removal%
MCM-41	43	4	90.697
MCM-41@APTES	43	2	95.348
MCM-41@APTES-BSAL	43	1	97.674
MCM-41@NTEP	43	1	97.674
MCM-41@NTEP-BSAL	43	0.5	98.837

This compounds can be applied for quality control of pharmaceutical dosage forms that containing Co (II) ions.

4.7 Adsorption equilibrium isotherms

Isotherm models are mathematical expressions that help to understand the type of interaction between the adsorbent and the adsorbate, It is also used to determine the extent of the effect of temperature on adsorption.

4.7.1 Langmuir isotherm model

Langmuir isotherm is applied when only one layer of molecules is adsorbed on the surface of the adsorbent. Single-layer adsorption is characterized by the fact at moderate concentration the maximum amount is adsorbed. When the concentration of the adsorbent increases, the layer of adsorbent is covered with a monomolecular layer of adsorbent. The Langmuir's equation is[240]:

$$Q_e = \frac{abC_e}{1 + bC_e}$$

Q_e : the amount of adsorption at the equilibrium adsorbed concentration (mg/g).

C_e : the equilibrium concentration of the adsorbate(mg/L)

b : Langmuir constant(L/mg)

a :the maximum adsorption capacity[314]

Then the dimensionless equilibrium term R_L was developed by Hall et al. (1966), that known as the separation factor, to describe Langmuir constant. R_L give information of the nature of the adsorption isotherm[315]:

$$R_L = \frac{1}{1 + C_e b}$$

To determine the type of adsorption, the separation factor RL is used, which is used to determine the geometry of the isotherm using the data in the Table (4.4).

Table (4.4): The value of separation factor.

R_L	Details regarding the absorption
$RL > 1$	Unwanted
$RL = 1$	Linear
$0 < RL < 1$	Favorable
$RL = 0$	Irreversible

Results from plots of $1/Q_e$ versus $1/C_e$ are shown in Tables (4.5) and (4.6), a,b and RL can be determined from the slope, and intercept from the plot .

Table(4.5) :Langmuir parameters for Co(II) ion adsorption.

	a(mg/g)	b(L/mg)	RL	R^2
MCM-41	67.9348	2.2142	0.0473	0.9186
MCM-41@APTES	76.9231	1.9979	0.0527	0.9087
MCM-41@APTES-BSAL	83.3333	3.3307	0.0310	0.92479
MCM-41@NTPE	174.2160	4.5147	0.0227	0.9700
MCM-41@NTPE-BSAL	200.0000	0.5637	0.2157	0.9874

Table (4.6):Langmuir parameters for Cu(II) ion adsorption.

	a(mg/g)	b(L/mg)	RL	R^2
MCM-41	66.6667	2.9846	0.0347	0.9257
MCM-41@APTES	73.0994	2.9602	0.0350	0.91321
MCM-41@APTES-BSAL	152.9052	2.8233	0.0367	0.9708
MCM-41@NTPE	121.8027	1.2208	0.0892	0.9716
MCM-41@NTPE-BSAL	245.0980	3.4872	0.0279	0.9761

4.7.2 Freundlich isotherm model

At a restricted concentration range, it is possible to describe the experimental data using the experimental isotherm proposed by Freundlich[241]:

$$\text{Log } Q_e = \text{Log } K_f + \frac{1}{n} \text{Log } C_e$$

Q_e : the amount of adsorption at the equilibrium adsorbed concentration (mg/g).

C_e : the equilibrium concentration of the adsorbate(mg/L)

KF: adsorption capacity

n: adsorption intensity.

The results from plotted Log Q_e versus Log C_e are shown in tables below that shows compounds follow Freundlich isotherm, K_f and n were calculated from the intercept and the slope of the plot. The magnitude of the exponent n gives an indication of the favorability while KF the capacity of the adsorbent/adsorbate. Favourable adsorption when $1/n$ less than one and unfavorable adsorption when $1/n > 1$. Tables (4.7) and (4.8) show the result.

Table(4.7) : Freundlich parameters for Co(II) ion adsorption.

	1/n	K_f	R²
MCM-41	0.8676	1.5283	0.9926
MCM-41@APTES	0.6444	0.7897	0.9940
MCM-41@APTES-BSAL	0.7038	2.2161	0.9980
MCM-41@NTPE	0.7500	2.0293	0.9946
MCM-41@NTPE-BSAL	0.3574	2.2725	0.9970

Table(4.8) : Freundlich parameters for Cu(II) ion adsorption.

	1/n	K_f	R²
MCM-41	0.9514	2.4997	0.9928
MCM-41@APTES	0.8346	1.1171	0.9982
MCM-41@APTES-BSAL	0.7908	4.0978	0.9992
MCM-41@NTPE	0.7058	2.1334	0.9988
MCM-41@NTPE-BSAL	0.2637	2.0264	0.9995

The descending order of fit of the models is as follows: Freundlich > Langmuir which means the results indicate multi-layer adsorption[316].

4.8 Conclusions

1. This work involved synthesizing mesoporous hybrid solid organosilicone ligand complexes.
2. Iraqi rice husks were utilized to extract silica and prepared RH-SiO₂.
3. RH has been used to prepare a dark filtrate (sodium silicate).
4. Sodium silicate was used successively to prepare MCM-41 by mixing it with CTAB (cetyltrimethylammonium bromide) .
5. [3-(aminopropyl)triethoxysilane] was immobilized onto MCM-41 via a heterogeneous process to maintain MCM-41@APTES then with 5-Bromosalicylaldehyde to obtain MCM-41@APTES-BSAL.
6. N-[3-(Trimethoxysilyl)propyl]ethylenediamine was immobilized onto MCM-41 via a heterogeneous process to maintain MCM-41@NTPE then with 5-Bromosalicylaldehyde to obtain MCM-41@NTPE-BSAL.
7. Several techniques that improve ligands synthesis were used to characterize the newly created ligands:
 - a. The percentage of element in the prepared ligands was revealed by CHNS analysis.
 - b. FTIR spectra for MCM-41@APTES-BSAL and MCM-41@NTPE-BSAL showed the presence of a peak for C=N group at 1651 cm⁻¹ in addition to some distinguish peaks for the prepared ligands.
 - c. X-ray diffraction indicated an amorphous structure with a wide, diffused peak that peaked at 22-23° (2-theta), for high angle and distinct peak at low angle.
 - d. The specific surface area, pore size distribution, type of isotherm and the hysteresis loop were demonstrated via N₂ adsorption–desorption analysis.
 - e. Through TGA/DSC the results show that the synthesis procedure was successful and that a high-stability material was produced.

-
- f. AFM analysis showed that the average roughness was change after being functionalization.
 - g. FESEM and TEM were used to monitor the size and morphology of prepared compounds. The average diameter between (20-50) nm was corresponding to the average diameter of mesoporous materials.
 - h. The presences of elements were approved according to EDX analysis.
8. The prepared compounds were applied successfully to remove some of divalent metal ions from aqueous solutions.
9. Co(II) and Cu(II) ions were removed from aqueous solution using the RH-SiO₂, MCM-41 and functionalized materials. This application leads to the following conclusions:-
- a. It was demonstrated that the removal of metal ions increased in a nonlinear way as a function of exposure time.
 - b. The maximum removal of metal ions for Co (II) and Cu (II) ions effect by the acidity of solution.
 - c. An increase in the concentration of metal ions has been found to enhance the removal of heavy metals.
 - d. The acquired data demonstrated that as the ligand mass increased, the maximal adsorption removal also increased.
 - e. amount of divalent metal ions increase in the following order: Cu²⁺ > Co²⁺ by repared componds.
 - f. MCM-41@APTES-BSAL better than MCM-41@APTES and MCM-41@NTPE-BSAL better than MCM-41@NTPE in removals of Co (II) and Cu (II) ions from aqueous solution.
10. The R² values indicate that a multilayer adsorption of Co (II) and Cu (II) ions onto compounds prepared, and that the adsorption isotherm data were best matched to the Freundlich adsorption isotherm model.
11. Homemade column has been successively applied used to remove Co (II) and Cu (II) ion at different concentration.

12. Removal of Co (II) ions from Vit.B12 was demonstrated via using MCM-41 and ligands prepared.

4.9 Future studies:

The researcher would like to recommend the following as a possible future project in this field of study:

- 1- Examining various sources for the creation of mesoporous silica could be interesting.
- 2- Investigations into various techniques for silica preparation are possible.
- 3- It is interesting to note how different kinds of organic groups can functionalize on silica.
- 4- It would be interesting to investigate the preconcentration of various metal ions.
- 5- It is crucial to look into further uses for the produced ligands.
- 6- The application of novel methods, such as ^{29}Si MAS spectroscopy and X-ray photoelectron spectroscopy (XPS), in the characterization of these solid ligands.
- 7- Effect of additional parameters like temperature on removal of ions can be studied.
- 8- Using the prepared compounds in removal of other ions from aqueous solution to assist with minimum pollution.

References

1. Ruiz-Hitzky E, Aranda P, Darder M, Rytwo G (2010) Hybrid materials based on clays for environmental and biomedical applications. *J Mater Chem* 20:9306–9321
2. Bergaya F, Lagaly G (2013) *Handbook of clay science*. Newnes
3. Berke H (2007) The invention of blue and purple pigments in ancient times. *Chem Soc Rev* 36:15–30
4. Zhu Y-P, Yuan Z-Y (2014) *Mesoporous Organic-Inorganic Non-Siliceous Hybrid Materials: Basic Principles and Promising Multifunctionality*. Springer
5. Rouquerol F, Rouquerol J, Sing K (1999) Assessment of mesoporosity. *Adsorpt by powders porous solids* 191–217
6. Lowell S, Shields JE, Thomas MA, Thommes M (2006) *Characterization of porous solids and powders: surface area, pore size and density*. Springer Science & Business Media
7. Ha C-S, Park SS (2019) *Periodic Mesoporous Organosilicas*. Springer Singapore, Singapore 507:508
8. Beck JS, Vartuli JC, Roth WJ, et al (1992) A new family of mesoporous molecular sieves prepared with liquid crystal templates. *J Am Chem Soc* 114:10834–10843
9. Sun X, Shi Y, Zhang P, et al (2011) Container effect in nanocasting synthesis of mesoporous metal oxides. *J Am Chem Soc* 133:14542–14545
10. Yonemoto BT, Hutchings GS, Jiao F (2014) A general synthetic approach for ordered mesoporous metal sulfides. *J Am Chem Soc* 136:8895–8898
11. Park SS, Moorthy MS, Chu S-W, Dong F, Guo W, Ha C-S (2013) Controlled drug delivery of hollow mesostructured materials. *Adv Porous Mater* 1:4–33
12. Park SS, Santha Moorthy M, Ha C-S (2014) Periodic mesoporous organosilicas for advanced applications. *NPG Asia Mater* 6:e96–e96
13. Ghorbani F, Kamari S (2019) Core–shell magnetic nanocomposite of Fe₃O₄@SiO₂@NH₂ as an efficient and highly recyclable adsorbent of methyl red dye from aqueous environments. *Environ Technol Innov* 14:100333

14. Kamari S, Shahbazi A (2020) Biocompatible Fe₃O₄@SiO₂-NH₂ nanocomposite as a green nanofiller embedded in PES–nanofiltration membrane matrix for salts, heavy metal ion and dye removal: Long–term operation and reusability tests. *Chemosphere* 243:125282
15. Kheshti Z, Ghajar KA, Moreno-Atanasio R, Neville F, Ghasemi S (2020) Investigating the high gradient magnetic separator function for highly efficient adsorption of lead salt onto magnetic mesoporous silica microspheres and adsorbent recycling. *Chem Eng Process Intensif* 148:107770
16. Liu X, Min S, Wang F, Zhang Z (2020) Confining Mo-activated CoS_x active sites within MCM-41 for highly efficient dye-sensitized photocatalytic H₂ evolution. *J Colloid Interface Sci* 563:112–121
17. Alkafajy AM, Albayati TM (2020) High performance of magnetic mesoporous modification for loading and release of meloxicam in drug delivery implementation. *Mater Today Commun* 23:100890
18. Mamaeva V, Sahlgren C, Lindén M (2013) Mesoporous silica nanoparticles in medicine—Recent advances. *Adv Drug Deliv Rev* 65:689–702
19. Ngullie RC, Bhuvaneshwari K, Shanmugam P, Boonyuen S, Smith SM, Sathishkumar M (2022) Magnetically recoverable biomass-derived carbon-aerogel supported ZnO (ZnO/MNC) composites for the photodegradation of methylene blue. *Catalysts* 12:1073
20. Prabhakar UPS, Shanmugam P, Boonyuen S, Chandrasekar LP, Pothu R, Boddula R, Radwan AB, Al-Qahtani N (2024) Non-covalent functionalization of surfactant-assisted graphene oxide with silver nanocomposites for highly efficient photocatalysis and anti-biofilm applications. *Mater Sci Energy Technol* 7:205–215
21. Munusamy S, Mandlimath TR, Swetha P, et al (2023) Nitrogen-doped carbon dots: Recent developments in its fluorescent sensor applications. *Environ Res* 231:116046
22. Parasuraman B, Shanmugam P, Govindasamy P, Nangan S, Gnanasekaran L,

- Thangavelu P (2023) Photocatalytic degradation of tetracycline contaminated wastewater over Bi₂S₃/BiWO₆/rGO ternary nanocomposite under visible light irradiation. *J Taiwan Inst Chem Eng* 105:249
23. Shanmugam P, Parasuraman B, Boonyuen S, Thangavelu P, AlSalhi MS, Zheng ALT, Viji A (2024) Hydrothermal synthesis and photocatalytic application of ZnS-Ag composites based on biomass-derived carbon aerogel for the visible light degradation of methylene blue. *Environ Geochem Health* 46:92
 24. Llinàs Riera M del C (2016) New functionalization methodologies of mesoporous silica nanoparticles (MSNs) for biomedical applications
 25. Vartuli JC, Schmitt KD, Kresge CT, et al (1994) Effect of surfactant/silica molar ratios on the formation of mesoporous molecular sieves: inorganic mimicry of surfactant liquid-crystal phases and mechanistic implications. *Chem Mater* 6:2317–2326
 26. Carrott MMLR, Conceição FL, Lopes JM, Carrott PJM, Bernardes C, Rocha J, Ribeiro FR (2006) Comparative study of Al-MCM materials prepared at room temperature with different aluminium sources and by some hydrothermal methods. *Microporous mesoporous Mater* 92:270–285
 27. Fitaroni LB, Venâncio T, Tanaka FH, Gimenez JCF, Costa JAS, Cruz SA (2019) Organically modified sepiolite: thermal treatment and chemical and morphological properties. *Appl Clay Sci* 179:105149
 28. Kumar S, Malik MM, Purohit R (2017) Synthesis methods of mesoporous silica materials. *Mater Today Proc* 4:350–357
 29. Schmidt HK, Geiter E, Mennig M, Krug H, Becker C, Winkler R-P (1998) The sol-gel process for nano-technologies: new nanocomposites with interesting optical and mechanical properties. *J sol-gel Sci Technol* 13:397–404
 30. Qi K, Chen X, Liu Y, Xin JH, Mak CL, Daoud WA (2007) Facile preparation of anatase/SiO₂ spherical nanocomposites and their application in self-cleaning textiles. *J Mater Chem* 17:3504–3508

31. Niesz K, Yang P, Somorjai GA (2005) Sol-gel synthesis of ordered mesoporous alumina. *Chem Commun* 1986–1987
32. Hoffmann F, Cornelius M, Morell J, Fröba M (2006) Silica-based mesoporous organic–inorganic hybrid materials. *Angew Chemie Int Ed* 45:3216–3251
33. Yamauchi Y, Kuroda K (2008) Rational design of mesoporous metals and related nanomaterials by a soft-template approach. *Chem Asian J* 3:664–676
34. Chen C-Y, Burkett SL, Li H-X, Davis ME (1993) Studies on mesoporous materials II. Synthesis mechanism of MCM-41. *microporous Mater* 2:27–34
35. Pal N, Bhaumik A (2013) Soft templating strategies for the synthesis of mesoporous materials: Inorganic, organic–inorganic hybrid and purely organic solids. *Adv Colloid Interface Sci* 189:21–41
36. Yao Y, Zhang M, Shi J, Gong M, Zhang H, Yang Y (2001) Encapsulation of fluorescein into MCM-41 mesoporous molecular sieve by a sol–gel method. *Mater Lett* 48:44–48
37. Newalkar BL, Komarneni S, Katsuki H (2000) Rapid synthesis of mesoporous SBA-15 molecular sieve by a microwave–hydrothermal process. *Chem Commun* 2389–2390
38. Chen Y, Chen H, Guo L, He Q, Chen F, Zhou J, Feng J, Shi J (2010) Hollow/rattle-type mesoporous nanostructures by a structural difference-based selective etching strategy. *ACS Nano* 4:529–539
39. Zhao D, Feng J, Huo Q, Melosh N, Fredrickson GH, Chmelka BF, Stucky GD (1998) Triblock copolymer syntheses of mesoporous silica with periodic 50 to 300 angstrom pores. *Science* (80-) 279:548–552
40. Wan Y, Zhao (2007) On the controllable soft-templating approach to mesoporous silicates. *Chem Rev* 107:2821–2860
41. Shen S, Chow PS, Kim S, Zhu K, Tan RBH (2008) Synthesis of carboxyl-modified rod-like SBA-15 by rapid co-condensation. *J Colloid Interface Sci* 321:365–372
42. Liu X, Zhu L, Zhao T, Lan J, Yan W, Zhang H (2011) Synthesis and

- characterization of sulfonic acid-functionalized SBA-15 for adsorption of biomolecules. *Microporous mesoporous Mater* 142:614–620
43. Zhu L, Liu X, Chen T, Xu Z, Yan W, Zhang H (2012) Functionalized periodic mesoporous organosilicas for selective adsorption of proteins. *Appl Surf Sci* 258:7126–7134
 44. Nie W, Luo Y, Yang Q, Feng G, Yao Q, Lu Z-H (2020) An amine-functionalized mesoporous silica-supported PdIr catalyst: boosting room-temperature hydrogen generation from formic acid. *Inorg Chem Front* 7:709–717
 45. Gu C, Chia PA, Zhao XS (2004) Doping of europium in the pores of surface-modified SBA-15. *Appl Surf Sci* 237:387–392
 46. He Q, Zhang Z, Gao F, Li Y, Shi J (2011) In vivo biodistribution and urinary excretion of mesoporous silica nanoparticles: effects of particle size and PEGylation. *small* 7:271–280
 47. Bernardoni F, Fadeev AY (2011) Adsorption and wetting characterization of hydrophobic SBA-15 silicas. *J Colloid Interface Sci* 356:690–698
 48. Wang X, Du X, Li C, Cao X (2008) Direct synthesis and characterization of phenyl-functionalized SBA-15. *Appl Surf Sci* 254:3753–3757
 49. Luan Z, Fournier JA, Wooten JB, Miser DE (2005) Preparation and characterization of (3-aminopropyl) triethoxysilane-modified mesoporous SBA-15 silica molecular sieves. *Microporous mesoporous Mater* 83:150–158
 50. Yu H, Zhai Q-Z (2009) Mesoporous SBA-15 molecular sieve as a carrier for controlled release of nimodipine. *Microporous Mesoporous Mater* 123:298–305
 51. Mirji SA, Halligudi SB, Sawant DP, Jacob NE, Patil KR, Gaikwad AB, Pradhan SD (2006) Adsorption of octadecyltrichlorosilane on mesoporous SBA-15. *Appl Surf Sci* 252:4097–4103
 52. Chong ASM, Zhao XS, Kustedjo AT, Qiao SZ (2004) Functionalization of large-pore mesoporous silicas with organosilanes by direct synthesis. *Microporous Mesoporous Mater* 72:33–42

53. Wang M, Duan F, Mu X (2019) Effect of surface silanol groups on friction and wear between amorphous silica surfaces. *Langmuir* 35:5463–5470
54. Mureseanu M, Reiss A, Stefanescu I, David E, Parvulescu V, Renard G, Hulea V (2008) Modified SBA-15 mesoporous silica for heavy metal ions remediation. *Chemosphere* 73:1499–1504
55. Pérez-Quintanilla D, Del Hierro I, Fajardo M, Sierra I (2006) Mesoporous silica functionalized with 2-mercaptopyridine: Synthesis, characterization and employment for Hg (II) adsorption. *Microporous Mesoporous Mater* 89:58–68
56. Cauvel A, Renard G, Brunel D (1997) Monoglyceride synthesis by heterogeneous catalysis using MCM-41 type silicas functionalized with amino groups. *J Org Chem* 62:749–751
57. Li J, Qi T, Wang L, Liu C, Zhang Y (2007) Synthesis and characterization of imidazole-functionalized SBA-15 as an adsorbent of hexavalent chromium. *Mater Lett* 61:3197–3200
58. Lu J, Li Z, Zink JJ, Tamanoi F (2012) In vivo tumor suppression efficacy of mesoporous silica nanoparticles-based drug-delivery system: enhanced efficacy by folate modification. *Nanomedicine Nanotechnology, Biol Med* 8:212–220
59. Kim S, Ida J, Gulians V V, Lin YS (2005) Tailoring pore properties of MCM-48 silica for selective adsorption of CO₂. *J Phys Chem B* 109:6287–6293
60. Dragoi B, Dumitriu E, Guimon C, Auroux A (2009) Acidic and adsorptive properties of SBA-15 modified by aluminum incorporation. *Microporous Mesoporous Mater* 121:7–17
61. Hoffmann F, Fröba M (2011) Vitalising porous inorganic silica networks with organic functions—PMOs and related hybrid materials. *Chem Soc Rev* 40:608–620
62. Zhao XS, Lu GQ (1998) Modification of MCM-41 by surface silylation with trimethylchlorosilane and adsorption study. *J Phys Chem B* 102:1556–1561
63. Huh S, Wiench JW, Yoo J-C, Pruski M, Lin VS-Y (2003) Organic functionalization and morphology control of mesoporous silicas via a co-condensation synthesis

- method. *Chem Mater* 15:4247–4256
64. Chen H-T, Huh S, Wiench JW, Pruski M, Lin VS-Y (2005) Dialkylaminopyridine-functionalized mesoporous silica nanosphere as an efficient and highly stable heterogeneous nucleophilic catalyst. *J Am Chem Soc* 127:13305–13311
 65. Ozin GA (2000) Panoscopic materials: synthesis over ‘all’length scales. *Chem Commun* 419–432
 66. Bradbury J (2004) Nature’s nanotechnologists: unveiling the secrets of diatoms. *PLoS Biol* 2:e306
 67. Yang C, Chao K (2002) Functionalization of molecularly templated mesoporous silica. *J Chinese Chem Soc* 49:883–893
 68. Martins L, Cardoso D (2007) Influence of surfactant chain length on basic catalytic properties of Si-MCM-41. *Microporous mesoporous Mater* 106:8–16
 69. Carlsson N, Gustafsson H, Thörn C, Olsson L, Holmberg K, Åkerman B (2014) Enzymes immobilized in mesoporous silica: A physical–chemical perspective. *Adv Colloid Interface Sci* 205:339–360
 70. Wu Z, Zhao D (2011) Ordered mesoporous materials as adsorbents. *Chem Commun* 47:3332–3338
 71. Zhang L, Zhang W, Shi J, Hua Z, Li Y, Yan J (2003) A new thioether functionalized organic–inorganic mesoporous composite as a highly selective and capacious Hg²⁺ adsorbent. *Chem Commun* 210–211
 72. Roussel T, Pellenq R-M, Bienfait M, Vix-Guterl C, Gadiou R, Beguin F, Johnson M (2006) Thermodynamic and neutron scattering study of hydrogen adsorption in two mesoporous ordered carbons. *Langmuir* 22:4614–4619
 73. Saha D, Deng S (2009) Hydrogen adsorption on ordered mesoporous carbons doped with Pd, Pt, Ni, and Ru. *Langmuir* 25:12550–12560
 74. Deng Y, Qi D, Deng C, Zhang X, Zhao D (2008) Superparamagnetic high-magnetization microspheres with an Fe₃O₄@ SiO₂ core and perpendicularly aligned mesoporous SiO₂ shell for removal of microcystins. *J Am Chem Soc*

130:28–29

75. Yan Z, Tao S, Yin J, Li G (2006) Mesoporous silicas functionalized with a high density of carboxylate groups as efficient absorbents for the removal of basic dyestuffs. *J Mater Chem* 16:2347–2353
76. Colilla M, Manzano M, Izquierdo-Barba I, Vallet-Regí M, Boissiere C, Sanchez C (2010) Advanced drug delivery vectors with tailored surface properties made of mesoporous binary oxides submicronic spheres. *Chem Mater* 22:1821–1830
77. Hao N, Li L, Tang F (2016) Shape matters when engineering mesoporous silica-based nanomedicines. *Biomater Sci* 4:575–591
78. Laugel G, Arichi J, Moliere M, Kiennemann A, Garin F, Louis B (2008) Metal oxides nanoparticles on SBA-15: Efficient catalyst for methane combustion. *Catal Today* 138:38–42
79. Fu W, Yamaguchi A, Kaneda H, Teramae N (2008) Enzyme catalytic membrane based on a hybrid mesoporous membrane. *Chem Commun* 853–855
80. Sugino K, Oya N, Yoshie N, Ogura M (2011) A simple modification creates a great difference: new solid-base catalyst using methylated N-substituted SBA-15. *J Am Chem Soc* 133:20030–20032
81. Sun S, Wang W, Shang M, Ren J, Zhang L (2010) Efficient catalytic oxidation of tetraethylated rhodamine over ordered mesoporous manganese oxide. *J Mol Catal A Chem* 320:72–78
82. Mondal J, Sen T, Bhaumik A (2012) Fe₃O₄@ mesoporous SBA-15: a robust and magnetically recoverable catalyst for one-pot synthesis of 3, 4-dihydropyrimidin-2 (1 H)-ones via the Biginelli reaction. *Dalt Trans* 41:6173–6181
83. Chandra D, Yokoi T, Tatsumi T, Bhaumik A (2007) Highly luminescent organic–inorganic hybrid mesoporous silicas containing tunable chemosensor inside the pore wall. *Chem Mater* 19:5347–5354
84. Lee S-J, Park SS, Lee SH, Hong S-H, Ha C-S (2013) Rare-Earth Metal Oxide Doped Transparent Mesoporous Silica Plates Under Non-Aqueous Condition as a

- Potential UV Sensor. *J Nanosci Nanotechnol* 13:7459–7466
85. Sarkar K, Dhara K, Nandi M, Roy P, Bhaumik A, Banerjee P (2009) Selective zinc (II)-ion fluorescence sensing by a functionalized mesoporous material covalently grafted with a fluorescent chromophore and consequent biological applications. *Adv Funct Mater* 19:223–234
 86. El-Safty SA, Ismail AA, Matsunaga H, Nanjo H, Mizukami F (2008) Uniformly mesocaged cubic Fd 3 m monoliths as modal carriers for optical chemosensors. *J Phys Chem C* 112:4825–4835
 87. Melde BJ, Johnson BJ (2010) Mesoporous materials in sensing: morphology and functionality at the meso-interface. *Anal Bioanal Chem* 398:1565–1573
 88. Slowing II, Trewyn BG, Giri S, Lin V (2007) Mesoporous silica nanoparticles for drug delivery and biosensing applications. *Adv Funct Mater* 17:1225–1236
 89. Melde BJ, Johnson BJ, Charles PT (2008) Mesoporous silicate materials in sensing. *Sensors* 8:5202–5228
 90. Domansky K, Liu J, Wang L-Q, Engelhard MH, Baskaran S (2001) Chemical sensors based on dielectric response of functionalized mesoporous silica films. *J Mater Res* 16:2810–2816
 91. Zhang T, Wang R, Geng W, Li X, Qi Q, He Y, Wang S (2008) Study on humidity sensing properties based on composite materials of Li-doped mesoporous silica A-SBA-15. *Sensors Actuators B Chem* 128:482–487
 92. Han B-H, Manners I, Winnik MA (2005) Oxygen sensors based on mesoporous silica particles on layer-by-layer self-assembled films. *Chem Mater* 17:3160–3171
 93. Johnson-White B, Zeinali M, Shaffer KM, Patterson Jr CH, Charles PT, Markowitz MA (2007) Detection of organics using porphyrin embedded nanoporous organosilicas. *Biosens Bioelectron* 22:1154–1162
 94. Zhang F, Yan Y, Yang H, Meng Y, Yu C, Tu B, Zhao D (2005) Understanding effect of wall structure on the hydrothermal stability of mesostructured silica SBA-15. *J Phys Chem B* 109:8723–8732

95. Zhao XS, Lu GQ, Millar GJ (1996) Advances in mesoporous molecular sieve MCM-41. *Ind Eng Chem Res* 35:2075–2090
96. Steel A, Carr SW, Anderson MW (1994) ¹⁴N NMR study of surfactant mesophases in the synthesis of mesoporous silicates. *J Chem Soc Chem Commun* 1571–1572
97. McBain JW (1932) The sorption of gases and vapours by solids. (No Title)
98. Fromherz P (1981) Micelle structure: A surfactant-block model. *Chem Phys Lett* 77:460–466
99. Lawrence MJ (1994) Surfactant systems: their use in drug delivery. *Chem Soc Rev* 23:417–424
100. Lowell S, Shields JE, Thomas MA, Thommes M (2012) Characterization of porous solids and powders: surface area, pore size and density. Springer Science & Business Media
101. Abboud M, Sahlabji T, Haija MA, El-Zahhar AA, Bondock S, Ismail I, Keshk SMAS (2020) Synthesis and characterization of lignosulfonate/amino-functionalized SBA-15 nanocomposites for the adsorption of methylene blue from wastewater. *New J Chem* 44:2291–2302
102. Brunauer S, Emmett PH, Teller E (1938) Adsorption of gases in multimolecular layers. *J Am Chem Soc* 60:309–319
103. Redfern SK, Azzu N, Binamira JS (2012) Rice in Southeast Asia: facing risks and vulnerabilities to respond to climate change. *Build Resil Adapt Clim Chang Agri Sect* 23:1–14
104. Mburu BK, Ngucia CW (2022) Adoption of climate change friendly New Rice for Africa (NERICA) varieties among farmers in Mwea West Sub-county, Kenya. *African J Environ Sci Technol* 16:71–78
105. Prasad R, Pandey M (2012) Rice husk ash as a renewable source for the production of value added silica gel and its application: an overview. *Bull Chem React Eng Catal* 7:1–25

106. Tsai WT, Lee MK, Chang YM (2007) Fast pyrolysis of rice husk: Product yields and compositions. *Bioresour Technol* 98:22–28
107. Patel M, Karera A, Prasanna P (1987) Effect of thermal and chemical treatments on carbon and silica contents in rice husk. *J Mater Sci* 22:2457–2464
108. Shaheen SM, Antoniadis V, Shahid M, et al (2022) Sustainable applications of rice feedstock in agro-environmental and construction sectors: a global perspective. *Renew Sustain Energy Rev* 153:111791
109. Vlaev LT, Markovska IG, Lyubchev LA (2003) Non-isothermal kinetics of pyrolysis of rice husk. *Thermochim Acta* 406:1–7
110. Mane VS, Mall ID, Srivastava VC (2007) Kinetic and equilibrium isotherm studies for the adsorptive removal of Brilliant Green dye from aqueous solution by rice husk ash. *J Environ Manage* 84:390–400
111. Foo KY, Hameed BH (2009) Utilization of rice husk ash as novel adsorbent: a judicious recycling of the colloidal agricultural waste. *Adv Colloid Interface Sci* 152:39–47
112. Joseph K, Tolêdo Filho RD, James B, Thomas S, Carvalho LH de (1999) A review on sisal fiber reinforced polymer composites. *Rev Bras Eng Agrícola e Ambient* 3:367–379
113. Soltani N, Bahrami A, Pech-Canul MI, González LA (2015) Review on the physicochemical treatments of rice husk for production of advanced materials. *Chem Eng J* 264:899–935
114. Abo-El-Enein SA, Eissa MA, Diafullah AA, Rizk MA, Mohamed FM (2009) Removal of some heavy metals ions from wastewater by copolymer of iron and aluminum impregnated with active silica derived from rice husk ash. *J Hazard Mater* 172:574–579
115. Srivastava A, Singh SK (2020) Utilization of alternative sand for preparation of sustainable mortar: A review. *J Clean Prod* 253:119706
116. Chaudhary DS, Jollands MC (2004) Characterization of rice hull ash. *J Appl Polym*

Sci 93:1–8

117. Gupta VK, Rastogi A, Dwivedi MK, Mohan D (1997) Process development for the removal of zinc and cadmium from wastewater using slag—a blast furnace waste material. *Sep Sci Technol* 32:2883–2912
118. Srivastava A, Singh SK (2020) Utilization of alternative sand for preparation of sustainable mortar: A review. *J Clean Prod* 253:119706
119. Rajeswari A, Jackcina Stobel Christy E, Gopi S, Jayaraj K, Pius A (2020) Characterization studies of polymer-based composites related to functionalized filler-matrix interface. In: *Interfaces in Particle and Fibre Reinforced Composites*. Elsevier, pp 219–250
120. Mirmohamadsadeghi S, Karimi K (2020) Recovery of silica from rice straw and husk. In: *Current Developments in Biotechnology and Bioengineering*. Elsevier, pp 411–433
121. Jarrar B, Al-Doaiss A, Shati A, Al-Kahtani M, Jarrar Q (2021) Behavioural alterations induced by chronic exposure to 10 nm silicon dioxide nanoparticles. *IET nanobiotechnology* 15:221–235
122. Le NH, Hajjar-Garreau S, Bonne M, Megías-Sayago C, Louis B, Lebeau B, Balan L (2020) Photo-induced generation of size controlled Au nanoparticles on pure siliceous ordered mesoporous silica for catalytic applications. *Microporous Mesoporous Mater* 295:109952
123. Nuaklong P, Jongvivatsakul P, Pothisiri T, Sata V, Chindaprasirt P (2020) Influence of rice husk ash on mechanical properties and fire resistance of recycled aggregate high-calcium fly ash geopolymer concrete. *J Clean Prod* 252:119797
124. Dominic M, Joseph R, Sabura Begum PM, Kanoth BP, Chandra J, Thomas S (2020) Green tire technology: Effect of rice husk derived nanocellulose (RHNC) in replacing carbon black (CB) in natural rubber (NR) compounding. *Carbohydr. Polym.* 230
125. Al Soubaihi RM, Saoud KM, Ye F, Myint MTZ, Saeed S, Dutta J (2020) Synthesis

- of hierarchically porous silica aerogel supported Palladium catalyst for low-temperature CO oxidation under ignition/extinction conditions. *Microporous Mesoporous Mater* 292:109758
126. Başgöz Ö, Güler Ö (2020) The unusually formation of porous silica nano-stalactite structure by high temperature heat treatment of SiO₂ aerogel synthesized from rice hull. *Ceram Int* 46:370–380
 127. Badawy MEI, El-Nouby MAM, Kimani PK, Lim LW, Rabea EI (2022) A review of the modern principles and applications of solid-phase extraction techniques in chromatographic analysis. *Anal Sci* 38:1457–1487
 128. Pant P, Gupta C, Kumar S, Grewal A, Garg S, Rai A (2020) Curcumin loaded Silica Nanoparticles and their therapeutic applications: A review. *J Mater Nanosci* 7:1–18
 129. Niculescu V-C, Raboaca M (2021) Efficient Rice-Husk-Derived Silica Nanocatalysts for Organic Dye Removal from Water. *Catalysts* 11:815
 130. Kalderis D, Koutoulakis D, Paraskeva P, Diamadopoulos E, Otal E, del Valle JO, Fernández-Pereira C (2008) Adsorption of polluting substances on activated carbons prepared from rice husk and sugarcane bagasse. *Chem Eng J* 144:42–50
 131. Tarley CRT, Ferreira SLC, Arruda MAZ (2004) Use of modified rice husks as a natural solid adsorbent of trace metals: characterisation and development of an on-line preconcentration system for cadmium and lead determination by FAAS. *Microchem J* 77:163–175
 132. Ong SoonAn OS, Seng ChyeEng SC, Lim PohEng LP (2007) Kinetics of adsorption of Cu (II) and Cd (II) from aqueous solution on rice husk and modified rice husk.
 133. Krishnani KK, Meng X, Christodoulatos C, Boddu VM (2008) Biosorption mechanism of nine different heavy metals onto biomatrix from rice husk. *J Hazard Mater* 153:1222–1234
 134. Srinivasan K (1998) Studies on chromium adsorption by Rice husk carbon. *Indian J*

Environ Heal 30:376–387

135. Marshall WE, Champagne ET, Evans WJ (1993) Use of rice milling byproducts (hulls & bran) to remove metal ions from aqueous solution. *J Environ Sci Heal Part A* 28:1977–1992
136. Mishra SP, Tiwari D, Dubey RS (1997) The uptake behaviour of rice (Jaya) husk in the removal of Zn (II) ions—A radiotracer study. *Appl Radiat Isot* 48:877–882
137. Elham A, Hossein T, Mahnoosh H (2010) Removal of Zn (II) and Pb (II) ions using rice husk in food industrial wastewater. *J Appl Sci Environ Manag* 14:
138. Munaf E, Zein R (1997) The use of rice husk for removal of toxic metals from waste water. *Environ Technol* 18:359–362
139. Wong KK, Lee CK, Low KS, Haron MJ (2003) Removal of Cu and Pb by tartaric acid modified rice husk from aqueous solutions. *Chemosphere* 50:23–28
140. Ong S-A, Seng C-E, Lim P (2007) Kinetics of adsorption of Cu (II) and Cd (II) from aqueous solution on rice husk and modified rice husk. *Electron J Environ Agric Food Chem* 6:1764–1774
141. Yahaya N, Abustan I, Latiff M, Bello OS, Ahmad MA (2011) Fixed-bed column study for Cu (II) removal from aqueous solutions using rice husk based activated carbon. *Int J Eng Technol* 11:248–252
142. Tiwari DP, Singh DK, Saksena DN (1995) Hg (II) adsorption from aqueous solutions using rice-husk ash. *J Environ Eng* 121:479–481
143. Bansal M, Singh D, Garg VK, Rose P (2009) Use of agricultural waste for the removal of nickel ions from aqueous solutions: equilibrium and kinetics studies. *Int J Civ Environ Eng* 3:174–180
144. Roy D, Greenlaw PN, Shane BS (1993) Adsorption of heavy metals by green algae and ground rice hulls. *J Environ Sci Heal Part A* 28:37–50
145. Zulkali MMD, Ahmad AL, Norulakmal NH (2006) *Oryza sativa* L. husk as heavy metal adsorbent: optimization with lead as model solution. *Bioresour Technol* 97:21–25

146. Turan NG, Mesci B (2011) Adsorption of copper (II) and zinc (II) ions by various agricultural by-products. Experimental studies and modelling. *Environ Prot Eng* 37:143
147. Barquilha CER, Cossich ES, Tavares CRG, Silva EA (2019) Biosorption of nickel (II) and copper (II) ions by *Sargassum* sp. in nature and alginate extraction products. *Bioresour Technol Reports* 5:43–50
148. Motsi T (2010) Remediation of acid mine drainage using natural zeolite
149. Sağ Y, Aktay Y (2000) Mass transfer and equilibrium studies for the sorption of chromium ions onto chitin. *Process Biochem* 36:157–173
150. Kobya M, Demirbas E, Senturk E, Ince M (2005) Adsorption of heavy metal ions from aqueous solutions by activated carbon prepared from apricot stone. *Bioresour Technol* 96:1518–1521
151. Ammann L (2003) Cation exchange and adsorption on clays and clay minerals
152. Eslami H, Samaei MR, Shahsavani E, Ebrahimi AA (2017) Biodegradation and fate of linear alkylbenzene sulfonate in integrated fixed-film activated sludge using synthetic media. *Desalin Water Treat* 92:128–133
153. Tofighy MA, Mohammadi T (2011) Adsorption of divalent heavy metal ions from water using carbon nanotube sheets. *J Hazard Mater* 185:140–147
154. Badamasi H, Olusola JA, Durodola SS, Akeremale OK, Ore OT, Bayode AA (2023) Contamination Levels, Source Apportionments, and Health Risks Evaluation of Heavy Metals from the Surface Water of the Riruwai Mining Area, North-Western Nigeria. *Pollution* 9:929–949
155. Yang T, Han C, Liu H, Yang L, Liu D, Tang J, Luo Y (2019) Synthesis of Na-X zeolite from low aluminum coal fly ash: characterization and high efficient As (V) removal. *Adv Powder Technol* 30:199–206
156. Han C, Yang T, Liu H, Yang L, Luo Y (2019) Characterizations and mechanisms for synthesis of chitosan-coated Na-X zeolite from fly ash and As (V) adsorption study. *Environ Sci Pollut Res* 26:10106–10116

157. Kapur M, Mondal MK (2014) Competitive sorption of Cu (II) and Ni (II) ions from aqueous solutions: Kinetics, thermodynamics and desorption studies. *J Taiwan Inst Chem Eng* 45:1803–1813
158. Parab H, Joshi S, Shenoy N, Lali A, Sarma US, Sudersanan M (2006) Determination of kinetic and equilibrium parameters of the batch adsorption of Co (II), Cr (III) and Ni (II) onto coir pith. *Process Biochem* 41:609–615
159. Güzel F, Yakut H, Topal G (2008) Determination of kinetic and equilibrium parameters of the batch adsorption of Mn (II), Co (II), Ni (II) and Cu (II) from aqueous solution by black carrot (*Daucus carota* L.) residues. *J Hazard Mater* 153:1275–1287
160. Ali AH (2013) Comparative study on removal of cadmium (II) from simulated wastewater by adsorption onto GAC, DB, and PR. *Desalin Water Treat* 51:5547–5558
161. Mohammed AA (2015) Biosorption of lead, cadmium, and zinc onto sunflower shell: equilibrium, kinetic, and thermodynamic studies. *Iraqi J Chem Pet Eng* 16:91–105
162. Malakootian M, Almasi A, Hossaini H (2008) Pb and Co removal from paint industries effluent using wood ash. *Int J Environ Sci Technol* 5:217–222
163. Chiang YW, Ghyselbrecht K, Santos RM, Martens JA, Swennen R, Cappuyns V, Meesschaert B (2012) Adsorption of multi-heavy metals onto water treatment residuals: Sorption capacities and applications. *Chem Eng J* 200:405–415
164. Yaro AS, Al-Hassani MH, Rasheed HAK (2015) Copper biosorption using local Iraqi natural agents. *Desalin Water Treat* 54:533–539
165. Çelekli A, Bozkurt H (2011) Bio-sorption of cadmium and nickel ions using *Spirulina platensis*: kinetic and equilibrium studies. *Desalination* 275:141–147
166. Shaheen SM, Eissa FI, Ghanem KM, El-Din HMG, Al Anany FS (2013) Heavy metals removal from aqueous solutions and wastewaters by using various byproducts. *J Environ Manage* 128:514–521

167. Singha B, Das SK (2013) Adsorptive removal of Cu (II) from aqueous solution and industrial effluent using natural/agricultural wastes. *Colloids Surfaces B Biointerfaces* 107:97–106
168. Vojoudi H, Badiei A, Bahar S, Ziarani GM, Faridbod F, Ganjali MR (2017) A new nano-sorbent for fast and efficient removal of heavy metals from aqueous solutions based on modification of magnetic mesoporous silica nanospheres. *J Magn Magn Mater* 441:193–203
169. Salmani MH, Ehrampoush MH, Eslami H, Eftekhar B (2020) Synthesis, characterization and application of mesoporous silica in removal of cobalt ions from contaminated water. *Groundw Sustain Dev* 11:100425
170. Shen W, He Y, Zhang S, Li J, Fan W (2012) Yeast-based microporous carbon materials for carbon dioxide capture. *ChemSusChem* 5:1274–1279
171. Ning P, Li F, Yi H, Tang X, Peng J, Li Y, He D, Deng H (2012) Adsorption equilibrium of methane and carbon dioxide on microwave-activated carbon. *Sep Purif Technol* 98:321–326
172. Diagboya PN, Olu-Owolabi BI, Adebowale KO (2014) Microscale scavenging of pentachlorophenol in water using amine and tripolyphosphate-grafted SBA-15 silica: Batch and modeling studies. *J Environ Manage* 146:42–49
173. Korai MA, Shar GA, Soomro GA, et al (2020) A novel method for the estimation of cobalt (II) in practical samples using ammonium pyrrolidine dithiocarbamate. *Environ Prog Sustain Energy* 39:e13348
174. Al-Jubouri SM, Holmes SM (2020) Immobilization of cobalt ions using hierarchically porous 4A zeolite-based carbon composites: Ion-exchange and solidification. *J Water Process Eng* 33:101059
175. Conry RR (2006) Copper: inorganic & coordination chemistry. *Encycl Inorg Chem*
176. Institute EC (2019) Copper as electrical conductive material with above-standard performance properties
177. Huitorel B, El Moll H, Utrera-Melero R, et al (2018) Evaluation of ligands effect on

- the photophysical properties of copper iodide clusters. *Inorg Chem* 57:4328–4339
178. Yin Y, Gu J, Wang X, Zhang K, Hu T, Ma J, Wang Q (2018) Impact of copper on the diazotroph abundance and community composition during swine manure composting. *Bioresour Technol* 255:257–265
 179. Nazeer F, Ma Z, Gao L, Wang F, Khan MA, Malik A (2019) Thermal and mechanical properties of copper-graphite and copper-reduced graphene oxide composites. *Compos Part B Eng* 163:77–85
 180. Snigur D, Chebotarev A, Dubovyi V, Barbalat D, Klochkova A (2020) Room temperature cloud point extraction: An application to preconcentration and spectrophotometric determination of copper (II). *J Serbian Chem Soc* 85:89–96
 181. Ghanei-Motlagh M, Taher MA, Saheb V, Fayazi M, Sheikhshoaie I (2011) Theoretical and practical investigations of copper ion selective electrode with polymeric membrane based on N, N'-(2, 2-dimethylpropane-1, 3-diyl)-bis (dihydroxyacetophenone). *Electrochim Acta* 56:5376–5385
 182. Bradl H (2005) Heavy metals in the environment: origin, interaction and remediation. Elsevier
 183. Chu Z, Fan X, Wang W, Huang W (2019) Quantitative evaluation of heavy metals' pollution hazards and estimation of heavy metals' environmental costs in leachate during food waste composting. *Waste Manag* 84:119–128
 184. Wu H, Xiao Y, Guo Y, Miao S, Chen Q, Chen Z (2020) Functionalization of SBA-15 mesoporous materials with 2-acetylthiophene for adsorption of Cr(III) ions. *Microporous Mesoporous Mater* 292:109754
 185. Fu F, Wang Q (2011) Removal of heavy metal ions from wastewaters: a review. *J Environ Manage* 92:407–418
 186. Zaini MAA, Amano Y, Machida M (2010) Adsorption of heavy metals onto activated carbons derived from polyacrylonitrile fiber. *J Hazard Mater* 180:552–560
 187. Sud D, Mahajan G, Kaur MP (2008) Agricultural waste material as potential adsorbent for sequestering heavy metal ions from aqueous solutions—A review.

Bioresour Technol 99:6017–6027

188. Bishnoi NR (2005) Fungus-an alternative for bioremediation of heavy metal containing wastewater: a review
189. Nadaroglu H, Kalkan E, Demir N (2010) Removal of copper from aqueous solution using red mud. *Desalination* 251:90–95
190. Wang S, Wu H (2006) Environmental-benign utilisation of fly ash as low-cost adsorbents. *J Hazard Mater* 136:482–501
191. Ibrahim HS, Jamil TS, Hegazy EZ (2010) Application of zeolite prepared from Egyptian kaolin for the removal of heavy metals: II. Isotherm models. *J Hazard Mater* 182:842–847
192. Olu-Owolabi BI, Popoola DB, Unuabonah EI (2010) Removal of Cu²⁺ and Cd²⁺ from aqueous solution by bentonite clay modified with binary mixture of goethite and humic acid. *Water, Air, Soil Pollut* 211:459–474
193. Kannamba B, Reddy KL, AppaRao B V (2010) Removal of Cu (II) from aqueous solutions using chemically modified chitosan. *J Hazard Mater* 175:939–948
194. Kruk M, Jaroniec M, Sayari A (2000) New insights into pore-size expansion of mesoporous silicates using long-chain amines. *Microporous mesoporous Mater* 35:545–553
195. Yoshitake H (2005) Highly-controlled synthesis of organic layers on mesoporous silica: their structure and application to toxic ion adsorptions. *New J Chem* 29:1107–1117
196. Öztürk Er E, Dalgıç Bozyiğit G, Büyükpınar Ç, Bakırdere S (2022) Magnetic nanoparticles based solid phase extraction methods for the determination of trace elements. *Crit Rev Anal Chem* 52:231–249
197. Patel K, Panchal N, Ingle P (2019) Review of extraction techniques. *Int J Adv Res Chem Sci* 6:6–21
198. Cãmara JS, Perestrelo R, Berenguer C V, et al (2022) Green extraction techniques as advanced sample preparation approaches in biological, food, and environmental

- matrices: a review. *Molecules* 27:2953
199. Dugheri S, Marrubini G, Mucci N, Cappelli G, Bonari A, Pompilio I, Trevisani L, Arcangeli G (2021) A review of micro-solid-phase extraction techniques and devices applied in sample pretreatment coupled with chromatographic analysis. *Acta Chromatogr* 33:99–111
 200. Wu A, Zhao X, Wang J, et al (2021) Application of solid-phase extraction based on magnetic nanoparticle adsorbents for the analysis of selected persistent organic pollutants in environmental water: a review of recent advances. *Crit Rev Environ Sci Technol* 51:44–112
 201. Fontanals N, Pocurull E, Borrull F, Marcé RM (2019) Role of solid-phase extraction in wastewater-based epidemiology. *Curr Opin Environ Sci Heal* 9:26–33
 202. Ayyıldız MF, Fındıkoğlu MS, Chormey DS, Bakırdere S (2020) A simple and efficient preconcentration method based on vortex assisted reduced graphene oxide magnetic nanoparticles for the sensitive determination of endocrine disrupting compounds in different water and baby food samples by GC-FID. *J Food Compos Anal* 88:103431
 203. Xu Y, Shi Y, Lei F, Dai L (2020) A novel and green cellulose-based Schiff base-Cu (II) complex and its excellent antibacterial activity. *Carbohydr Polym* 230:115671
 204. Nafia RA, Faraj FL (2019) Synthesis and characterization of new indole schiff bases and study effect of the compounds on lymphatic cell in metaphase in human blood. *J Pharm Sci Res* 11:1319–1326
 205. Turan B, Şendil K, Şengül E, Gültekin MS, Taslimi P, Gulçin İ, Supuran CT (2016) The synthesis of some β -lactams and investigation of their metal-chelating activity, carbonic anhydrase and acetylcholinesterase inhibition profiles. *J Enzyme Inhib Med Chem* 31:79–88
 206. BERBER N (2020) Preparation and characterization of some Schiff base compounds. *Adıyaman Univ J Sci* 10:179–188
 207. Abu-Dief AM, El-Khatib RM, Aljohani FS, Alzahrani SO, Mahran A, Khalifa ME,

- El-Metwaly NM (2021) Synthesis and intensive characterization for novel Zn (II), Pd (II), Cr (III) and VO (II)-Schiff base complexes; DNA-interaction, DFT, drug-likeness and molecular docking studies. *J Mol Struct* 1242:130693
208. Rauf A, Shah A, Munawar KS, Ali S, Tahir MN, Javed M, Khan AM (2020) Synthesis, physicochemical elucidation, biological screening and molecular docking studies of a Schiff base and its metal (II) complexes. *Arab J Chem* 13:1130–1141
209. Patil SK, Vibhute BT (2021) Synthesis, characterization, anticancer and DNA photocleavage study of novel quinoline Schiff base and its metal complexes. *Arab J Chem* 14:103285
210. Turan N, Adigüzel R, Buldurun K, Bursal E (2016) Spectroscopic, thermal and antioxidant properties of novel mixed ligand-metal complexes obtained from saccharinate complexes and azo dye ligand (mnppa)
211. Buldurun K, Turan N, Aras A, Mantarcı A, Turkan F, Bursal E (2019) Spectroscopic and structural characterization, enzyme inhibitions, and antioxidant effects of new Ru (II) and Ni (II) complexes of Schiff base. *Chem Biodivers* 16:e1900243
212. Hameed A, Al-Rashida M, Uroos M, Abid Ali S, Khan KM (2017) Schiff bases in medicinal chemistry: a patent review (2010-2015). *Expert Opin Ther Pat* 27:63–79
213. Kursunlu AN, Guler E, Dumrul H, Kocyigit O, Gubbuk IH (2009) Chemical modification of silica gel with synthesized new Schiff base derivatives and sorption studies of cobalt (II) and nickel (II). *Appl Surf Sci* 255:8798–8803
214. Zhao L, Wang S, Wu Y, Hou Q, Wang Y, Jiang S (2007) Salicylidene Schiff base assembled with mesoporous silica SBA-15 as hybrid materials for molecular logic function. *J Phys Chem C* 111:18387–18391
215. Ghorbanloo M, Monfared HH, Janiak C (2011) The catalytic function of a silica gel-immobilized Mn (II)-hydrazide complex for alkene epoxidation with H₂O₂. *J Mol Catal A Chem* 345:12–20

216. Fekri LZ, Zeinali S (2020) Copper/Schiff-base complex immobilized on amine functionalized silica mesoporous magnetic nanoparticles under solvent-free condition: A facile and new avenue for the synthesis of thiazolidin-4-ones. *Appl Organomet Chem* 34:e5629
217. Rather RA, Siddiqui ZN (2018) Synthesis, characterization and application of Nd-Salen schiff base complex Immobilized Mesoporous Silica in solvent free synthesis of pyranopyrazoles. *J Organomet Chem* 868:164–174
218. Tahmasbi L, Sedaghat T, Motamedi H, Kooti M (2018) Mesoporous silica nanoparticles supported copper (II) and nickel (II) Schiff base complexes: Synthesis, characterization, antibacterial activity and enzyme immobilization. *J Solid State Chem* 258:517–525
219. Xu Z, Wang K, Liu Q, Guo F, Xiong Z, Li Y, Wang Q (2018) A bifunctional adsorbent of silica gel-immobilized Schiff base derivative for simultaneous and selective adsorption of Cu (II) and SO₄²⁻. *Sep Purif Technol* 191:61–74
220. Mureseanu M, Filip M, Bleotu I, Spinu CI, Marin AH, Matei I, Parvulescu V (2023) Cu (II) and Mn (II) Anchored on Functionalized Mesoporous Silica with Schiff Bases: Effects of Supports and Metal–Ligand Interactions on Catalytic Activity. *Nanomaterials* 13:1884
221. Muthusami R, Ramachandran V, Palaniappan M, Arumugam S, Palanisamy K, Irena K, Rangappan R (2021) Cu (II) Schiff base complex functionalized mesoporous silica nanoparticles as an efficient catalyst for the synthesis of questiomycin A and photo-Fenton-like rhodamine B degradation. *J Solid State Chem* 302:122429
222. Vareda JP, Matos PD, Valente AJM, Durães L (2022) A new Schiff base organically modified silica aerogel-like material for metal ion adsorption with Ni selectivity. *Adsorpt Sci Technol* 2022:8237403
223. Ali HH, Hussein KA, Mihsen HH (2023) Antimicrobial Applications of Nanosilica Derived from Rice Grain Husks. *Silicon*. <https://doi.org/10.1007/s12633-023->

02467-7

224. Ali HH, Mihsen HH, Hussain KA (2023) Synthesis, Characterization and Antimicrobial Studies of Modified Silica Materials Derived from Rice Husks. *Bionanoscience* 13:1163–1176
225. Shojaeepour F, Kazemzad M, Rahimpour MR, Khanlarkhani A, Hafizi A (2018) Physico-chemical characterization of shaped mesoporous silica prepared by pseudomorphic transformation as catalyst support in methane steam reforming. *React Kinet Mech Catal* 124:229–245
226. Stuart BH (2004) *Infrared spectroscopy: fundamentals and applications*. John Wiley & Sons
227. Sharma R, Bisen DP, Shukla U, Sharma BG (2012) X-ray diffraction: a powerful method of characterizing nanomaterials. *Recent Res Sci Technol* 4:77–79
228. Dias A, Ciminelli VST (2000) Analysis of nitrogen adsorption-desorption isotherms for the estimation of pore-network dimensions and structure of ferroelectric powders. *Ferroelectrics* 241:9–16
229. Cheng SZD, Li CY, Calhoun BH, Zhu L, Zhou WW (2000) Thermal analysis: the next two decades. *Thermochim Acta* 355:59–68
230. Zhong Q, Inniss D, Kjoller K, Elings VB (1993) Fractured polymer/silica fiber surface studied by tapping mode atomic force microscopy. *Surf Sci Lett* 290:L688–L692
231. Goldstein JI, Newbury DE, Michael JR, Ritchie NWM, Scott JHJ, Joy DC (2017) *Scanning electron microscopy and X-ray microanalysis*. Springer
232. Nasrollahzadeh M, Atarod M, Sajjadi M, Sajadi SM, Issaabadi Z (2019) Plant-mediated green synthesis of nanostructures: mechanisms, characterization, and applications. In: *Interface science and technology*. Elsevier, pp 199–322
233. Scimeca M, Bischetti S, Lamsira HK, Bonfiglio R, Bonanno E (2018) Energy Dispersive X-ray (EDX) microanalysis: A powerful tool in biomedical research and diagnosis. *Eur J Histochem* EJH 62:

234. Marczenko Z, Balcerzak M (2000) Separation, preconcentration and spectrophotometry in inorganic analysis. Elsevier
235. Nguyen TT, Ma HT, Avti P, et al (2019) Adsorptive removal of iron using SiO₂ nanoparticles extracted from rice husk ash. *J Anal Methods Chem* 2019:
236. Zhang G, Feng S, Cheng D (1996) Catalytic fluorimetric determination of trace cobalt in vitamin B12. *Microchem J* 53:308–315
237. Giles CH (1960) Studies in adsorption: Part X1. A system of classification of solution adsorption isotherms, and its use in diagnosis of adsorption mechanisms and in measurement of specific surface areas of solids. *J chem Soc* 111:3973–3993
238. Karaj I (2016) Raw and modified rice husk performance in removal of Basic Blue 41 from aqueous solutions. *J Occup Environ Heal* 1:41–49
239. Samarghandi MR, Zarrabi M, NOORI SM, Panahi R, Foroghi M (2012) Removal of Acid Red 14 by pumice stone as a low cost adsorbent: kinetic and equilibrium study
240. Langmuir I (1918) The adsorption of gases on plane surfaces of glass, mica and platinum. *J Am Chem Soc* 40:1361–1403
241. Freundlich H (1907) Über die adsorption in lösungen. *Zeitschrift für Phys Chemie* 57:385–470
242. Nayak J, Bera J (2009) A simple method for production of humidity indicating silica gel from rice husk ash. *J Met Mater Miner* 19:
243. Timofeeva MN, Kalashnikova GO, Shefer KI, Mel'gunova EA, Panchenko VN, Nikolaev AI, Gil A (2020) Effect of the acid activation on a layered titanosilicate AM-4: The fine-tuning of structural and physicochemical properties. *Appl Clay Sci* 186:105445
244. Sobh HS, Mihsen HH (2019) Synthesis of functionalized silica from rice husks containing C-I end group. *Baghdad Sci J* 16:886–891
245. Adam F, Batagarawa MS (2013) Tetramethylguanidine–silica nanoparticles as an efficient and reusable catalyst for the synthesis of cyclic propylene carbonate from

- carbon dioxide and propylene oxide. *Appl Catal A Gen* 454:164–171
246. Mohamed AS, AbuKhadra MR, Abdallah EA, El-Sherbeeney AM, Mahmoud RK (2020) The photocatalytic performance of silica fume based Co₃O₄/MCM-41 green nanocomposite for instantaneous degradation of Omethoate pesticide under visible light. *J Photochem Photobiol A Chem* 392:112434
247. Mohsin AD, Mihsen HH (2022) Preparation of novel absorbent derived from rice husk ash and its application for removing metal ions (Co(II) and Ni(II)) from aqueous solutions. In: *AIP Conference Proceedings*. p 030027
248. Appaturi JN, Adam F (2013) A facile and efficient synthesis of styrene carbonate via cycloaddition of CO₂ to styrene oxide over ordered mesoporous MCM-41-Imi/Br catalyst. *Appl Catal B Environ* 136–137:150–159
249. Mohsin AD, Mihsen HH (2020) Uptake of metal ions (Co (II) and Ni (II)) by silica-salicylaldehyde derived from rice husks. *J Inorg Organomet Polym Mater* 30:2172–2181
250. Nabieh KA, Mortada WI, Helmy TE, Kenawy IMM, Abou El-Reash YG (2021) Chemically modified rice husk as an effective adsorbent for removal of palladium ions. *Heliyon* 7:
251. Langmuir I (1916) The constitution and fundamental properties of solids and liquids. Part I. Solids. *J Am Chem Soc* 38:2221–2295
252. Mihsen HH, Rfaish SY, Abass SK, Sobh HS (2018) Synthesis and characterization of silica-thioamide hybrid compounds derived from rice husk ash with expected biological and catalytic activity. *J Glob Pharma Technol* 10:590–598
253. Ghadermazi M, Moradi S, Mozafari R (2020) Rice husk-SiO₂ supported bimetallic Fe–Ni nanoparticles: As a new, powerful magnetic nanocomposite for the aqueous reduction of nitro compounds to amines. *RSC Adv* 10:33389–33400
254. Attol DH, Mihsen HH, Jaber SA, Alwazni WS, Eesa MT (2023) Synthesis of Organic Functionalized Silica from Rice Husk as an Antibacterial Agents. *Silicon* 15:2349–2357

255. Puri A (2013) Phototriggerable liposomes: current research and future perspectives. *Pharmaceutics* 6:1–25
256. Rout L, Mohan A, Thomas AM, Ha C-S (2020) Rational design of thermoresponsive functionalized MCM-41 and their decoration with bimetallic Ag–Pd nanoparticles for catalytic application. *Microporous Mesoporous Mater* 291:109711
257. Vaysipour S, Rafiee Z, Nasr-Esfahani M (2020) Synthesis and characterization of copper (II)-poly (acrylic acid)/M-MCM-41 nanocomposite as a novel mesoporous solid acid catalyst for the one-pot synthesis of polyhydroquinoline derivatives. *Polyhedron* 176:114294
258. Rugar D, Hansma P (1990) Atomic force microscopy. *Phys Today* 43:23–30
259. Alhadhrami A, Mohamed GG, Sadek AH, Ismail SH, Ebnalwaled AA, Almalki ASA (2022) Behavior of silica nanoparticles synthesized from rice husk ash by the sol–gel method as a photocatalytic and antibacterial agent. *Materials (Basel)* 15:8211
260. Visakh PM, Morlanes MJM (2016) *Nanomaterials and nanocomposites: zero-to three-dimensional materials and their composites*. John Wiley & Sons
261. Hoyt M (2008) *5 Analyses of. Nanotechnol Environ* 99
262. Fleck RA, Humbel BM (2019) *Biological Field Emission Scanning Electron Microscopy, 2 Volume Set*. John Wiley & Sons
263. Inkson BJ (2016) Scanning electron microscopy (SEM) and transmission electron microscopy (TEM) for materials characterization. In: *Materials characterization using nondestructive evaluation (NDE) methods*. Elsevier, pp 17–43
264. Lee CK, Chiang AST, Tsay CS (1995) The Characterization of Porous Solids from Gas Adsorption Measurements. *Key Eng Mater* 115:21–44
265. Huseynov E, Garibov A, Mehdiyeva R (2016) TEM and SEM study of nano SiO₂ particles exposed to influence of neutron flux. *J Mater Res Technol* 5:213–218
266. Kamari S, Ghorbani F (2021) Extraction of highly pure silica from rice husk as an

- agricultural by-product and its application in the production of magnetic mesoporous silica MCM-41. *Biomass Convers. Biorefinery* 11:3001–3009
267. Abbas SK, Hassan ZM, Mihsen HH, Eesa MT, Attol DH (2020) Uptake of Nickel(II) Ion by Silica-o-Phenylenediamine Derived from Rice Husk Ash. *Silicon* 12:1103–1110
268. Antonakou E, Lappas A, Nilsen MH, Bouzga A, Stöcker M (2006) Evaluation of various types of Al-MCM-41 materials as catalysts in biomass pyrolysis for the production of bio-fuels and chemicals. *Fuel* 85:2202–2212
269. Rath D, Rana S, Parida KM (2014) Organic amine-functionalized silica-based mesoporous materials: an update of syntheses and catalytic applications. *RSC Adv* 4:57111–57124
270. MIHSEN HH, SOBH HS (2018) Preparation and Characterization of Thiourea-Silica Hybrid as Heterogeneous Catalyst. *Asian J Chem* 30:
271. Abbas SH, Adam F, Muniandy L (2020) Green synthesis of MCM-41 from rice husk and its functionalization with nickel(II) salen complex for the rapid catalytic oxidation of benzyl alcohol. *Microporous Mesoporous Mater* 305:
272. Davarpanah J, Sayahi MH, Ghahremani M, Karkhoei S (2019) Synthesis and characterization of nano acid catalyst derived from rice husk silica and its application for the synthesis of 3, 4-dihydropyrimidinones/thiones compounds. *J Mol Struct* 1181:546–555
273. Muniandy L, Adam F, Rahman NRA, Ng EP (2019) Highly selective synthesis of cyclic carbonates via solvent free cycloaddition of CO₂ and epoxides using ionic liquid grafted on rice husk derived MCM-41. *Inorg Chem Commun* 104:1–7
274. Vaysipour S, Rafiee Z, Nasr-Esfahani M (2020) Synthesis and characterization of copper (II)-poly(acrylic acid)/M-MCM-41 nanocomposite as a novel mesoporous solid acid catalyst for the one-pot synthesis of polyhydroquinoline derivatives. *Polyhedron* 176
275. Pervaiz M, Ahmad I, Yousaf M, et al (2019) Synthesis, spectral and antimicrobial

- studies of amino acid derivative Schiff base metal (Co, Mn, Cu, and Cd) complexes. *Spectrochim Acta Part A Mol Biomol Spectrosc* 206:642–649
276. Hello KM, Mihsen HH, Mosa MJ, Magtoof MS (2015) Hydrolysis of cellulose over silica-salicylaldehyde phenylhydrazone catalyst. *J Taiwan Inst Chem Eng* 46:74–81
277. Liu Q, Wang H, Liu J, Huang H (2011) AFM image processing for estimating the number and volume of nanoparticles on a rough surface. *Surf interface Anal* 43:1354–1359
278. Si Z, Wang Z, Cai D, Li G, Li S, Qin P (2020) A high-permeance organic solvent nanofiltration membrane via covalently bonding mesoporous MCM-41 with polyimide. *Sep Purif Technol* 241:116545
279. Adam F, Andas J, Rahman IA (2010) A study on the oxidation of phenol by heterogeneous iron silica catalyst. *Chem Eng J* 165:658–667
280. Sutra P, Brunel D (1996) Preparation of MCM-41 type silica-bound manganese(III) Schiff-base complexes. *Chem Commun* 2485
281. Carmona VB, Oliveira RM, Silva WTL, Mattoso LHC, Marconcini JM (2013) Nanosilica from rice husk: extraction and characterization. *Ind Crops Prod* 43:291–296
282. Kamari S, Ghorbani F (2021) Extraction of highly pure silica from rice husk as an agricultural by-product and its application in the production of magnetic mesoporous silica MCM-41. *Biomass Convers Biorefinery* 11:3001–3009
283. Thuadaj N, Nuntiya A (2008) Synthesis and characterization of nanosilica from rice husk ash prepared by precipitation method. *J Nat Sci Spec Issue Nanotechnol* 7:59–65
284. Sing KSW (1985) Reporting physisorption data for gas/solid systems with special reference to the determination of surface area and porosity (Recommendations 1984). *Pure Appl Chem* 57:603–619
285. Allen T, Allen T (1981) Sampling and sizing from the atmosphere. Part Size Meas 64–102

286. Hao S, Zhong Y, Pepe F, Zhu W (2012) Adsorption of Pb^{2+} and Cu^{2+} on anionic surfactant-templated amino-functionalized mesoporous silicas. *Chem Eng J* 189:160–167
287. Al-Hasani TJ, Mihsen HH, Hello KM, Adam F (2017) Catalytic esterification via silica immobilized p-phenylenediamine and dithiooxamide solid catalysts. *Arab J Chem* 10:S1492–S1500
288. Cai Q, Lin W-Y, Xiao F-S, Pang W-Q, Chen X-H, Zou B-S (1999) The preparation of highly ordered MCM-41 with extremely low surfactant concentration. *Microporous Mesoporous Mater* 32:1–15
289. Ray SS, Gusain R, Kumar N (2020) Carbon nanomaterial-based adsorbents for water purification: Fundamentals and applications. Elsevier
290. Saravanan A, Kumar PS, Govarathanan M, et al (2021) Adsorption characteristics of magnetic nanoparticles coated mixed fungal biomass for toxic Cr (VI) ions in aquatic environment. *Chemosphere* 267:129226
291. Tanti KK, Singh P, Roy S, et al (2020) Water Contamination Removing copper ions
292. Kumar N, Reddy L, Parashar V, Ngila JC (2017) Controlled synthesis of microsheets of ZnAl layered double hydroxides hexagonal nanoplates for efficient removal of Cr (VI) ions and anionic dye from water. *J Environ Chem Eng* 5:1718–1731
293. Amin NK (2009) Removal of direct blue-106 dye from aqueous solution using new activated carbons developed from pomegranate peel: adsorption equilibrium and kinetics. *J Hazard Mater* 165:52–62
294. Chowdhury S, Mishra R, Saha P, Kushwaha P (2011) Adsorption thermodynamics, kinetics and isosteric heat of adsorption of malachite green onto chemically modified rice husk. *Desalination* 265:159–168
295. Yang JJ, El-Nahhal IM, Chuang I-S, Maciel GE (1997) Synthesis and solid-state NMR structural characterization of polysiloxane-immobilized amine ligands and

- their metal complexes. *J Non Cryst Solids* 209:19–39
296. Shamik Chowdhury SC, Rahul Mishra RM, Papita Saha PS, Praveen Kushwaha PK (2011) Adsorption thermodynamics, kinetics and isosteric heat of adsorption of malachite green onto chemically modified rice husk.
297. Ouyang D, Zhuo Y, Hu L, Zeng Q, Hu Y, He Z (2019) Research on the Adsorption Behavior of Heavy Metal Ions by Porous Material Prepared with Silicate Tailings. *Minerals* 9:291
298. Witek-Krowiak A, Szafran RG, Modelski S (2011) Biosorption of heavy metals from aqueous solutions onto peanut shell as a low-cost biosorbent. *Desalination* 265:126–134
299. El-Nahhal IM, Zaggout FR, El-Ashgar NM (2000) Uptake of divalent metal ions (Cu^{2+} , Zn^{2+} and Cd^{2+}) by polysiloxane immobilized monoamine ligand system
300. Cotton FA, Wilkinson G, Murillo CA, Bochmann M (1999) *Advanced inorganic chemistry*. John Wiley and Sons, Inc.
301. El-Ashgar NM, El-Nahhal IM, Ahmed MA, Abu Shaweesh AA, Chehimi MM (2018) Synthesis, characterization, and metal uptake of multiple functionalized immobilized-polysiloxane diamine-thiol chelating ligand derivatives. *J Iran Chem Soc* 15:2325–2338
302. Zaggout FR, El-Nahhal IM, El-Ashgar NM (2001) Uptake of divalent metal ions (Cu^{2+} , Zn^{2+} , and Cd^{2+}) by polysiloxane immobilized diamine ligand system. *Anal Lett* 34:247–266
303. Georgin J, Dotto GL, Mazutti MA, Foletto EL (2016) Preparation of activated carbon from peanut shell by conventional pyrolysis and microwave irradiation-pyrolysis to remove organic dyes from aqueous solutions. *J Environ Chem Eng* 4:266–275
304. Imyim A, Prapalimrungsi E (2010) Humic acids removal from water by aminopropyl functionalized rice husk ash. *J Hazard Mater* 184:775–781
305. Garg D, Kumar S, Sharma K, Majumder CB (2019) Application of waste peanut

- shells to form activated carbon and its utilization for the removal of Acid Yellow 36 from wastewater. *Groundw Sustain Dev* 8:512–519
306. Onundi YB, Mamun AA, Khatib MF Al, Ahmed YM (2010) Adsorption of copper, nickel and lead ions from synthetic semiconductor industrial wastewater by palm shell activated carbon. *Int J Environ Sci Technol* 7:751–758
307. Attol DH, Mihsen HH (2020) Synthesis of Silica-Salen Derivative from Rice Husk Ash and its Use for Extraction of Divalent Metal Ions Co(II), Ni(II) and Cu(II). *Indones J Chem* 20:16–28
308. Olayinka OK, Oyedeji OA, Oyeyiola A (2009) Removal of chromium and nickel ions from aqueous solution by adsorption on modified coconut husk. *African J Environ Sci Technol* 3:
309. Zou W, Li K, Bai H, Shi X, Han R (2011) Enhanced cationic dyes removal from aqueous solution by oxalic acid modified rice husk. *J Chem Eng Data* 56:1882–1891
310. Babel S, Kurniawan TA (2004) Cr (VI) removal from synthetic wastewater using coconut shell charcoal and commercial activated carbon modified with oxidizing agents and/or chitosan. *Chemosphere* 54:951–967
311. Ali RM, Hamad HA, Hussein MM, Malash GF (2016) Potential of using green adsorbent of heavy metal removal from aqueous solutions: adsorption kinetics, isotherm, thermodynamic, mechanism and economic analysis. *Ecol Eng* 91:317–332
312. Mahmoud ME (1996) Comparison of metal uptake properties of silica gel-bound ion exchangers and some amine derivatives. *Anal Lett* 29:1791–1804
313. Al-Abbasy DHA (2019) Synthesis and Characterization of Organosilicon Ligands and Used It in Removal of Some Divalent Metal Ions from Their Aqueous Solutions. Univ Kerbala
314. Atkins PW, De Paula J, Keeler J (2023) *Atkins' physical chemistry*. Oxford university press

315. López A, Lázaro N, Morales S, Marqués AM (2002) Nickel biosorption by free and immobilized cells of *Pseudomonas fluorescens* 4F39: a comparative study. *Water Air Soil Pollut* 135:157–172
316. Anbalagan K, Senthil Kumar P, Sangita Gayatri K, Shahul Hameed S, Sindhuja M, Prabhakaran C, Karthikeyan R (2015) Removal and recovery of Ni (II) ions from synthetic wastewater using surface modified *Strychnos potatorum* seeds: experimental optimization and mechanism. *Desalin Water Treat* 53:171–182

الخلاصة

تعتبر قشور الارز (RH) واحدة من المخلفات الزراعية الاكثر شيوعا في جميع انحاء العالم. يمكن تحويل قشور الارز نفسها الى سليكات الصوديوم. يتم تحضير MCM-41 من سيليكات الصوديوم. تتضمن هذه الاطروحة ثلاث خطوات, اولها استخلاص السيليكا من قشور الارز, تخليق RH-SiO₂ و MCM-41 والمركبات الوظيفية من السيليكا المستخلصة. تتضمن الخطوتان الثانية والثالثة تشخيص المركبات المصنعه بنجاح من خلال استخدام تقنيات مختلفة واستخدامها في تطبيقات تحليليه.

تم توظيف السيليكا المسامية MCM-41 مع 3-aminopropyltriethoxysilane (APTES) للحصول على MCM-41@APTES. في الخطوة التاليه 5-bromosalicylaldehyde (BSAL) تم تصعيده مع MCM-41@APTES في التلوين للحصول على مادة متوسطة المساميه تحتوي قاعدة شيف MCM-41@APTES-BSAL. بلاضافه الى ذلك تم توظيف السيليكا متوسطة المسام MCM-41 باستخدام N-[3-(trimethoxysilyl)propyl]ethylenediamine للحصول على MCM-41@NTPE. في الخطوة التاليه تم اضافة 5-bromosalicylaldehyde (BSAL) بالتصعيد مع MCM-41@NTPE باستخدام التلوين للحصول على مادة سيليكامسامة ذات قاعدة شيف MCM-41@NTPE-BSAL.

تم تشخيص كمية الكربون, والهيدروجين, والنروجين الموجوده في المركبات المحضره من خلال التحليل العنصري. اظهرت اطياف تحت الحمراء للمركبات المحضره عدة قمم مميزه تعود للمركبات. اظهر تحليل حيود الاشعه السينيه والمجهر الالكتروني النافذ انه تم تكوين MCM-41 والمركبات الوظيفيه بترتيب سداسي مرتب للغاية. كشف تحليل الامتزاز والامتصاص متوسط قطر المسام وحجم المسام الاجمالي ومساحة السطح المحدد. كشف تحليل قياس الوزن الحراري لـ RH-SiO₂ و MCM-41 عن خطوتين لتحليل الكتله بينما للمركبات الموظفه عن ثلاث خطوات لفقدان الوزن. تم توضيح التصميمات السطحيه لـ RH-SiO₂ و MCM-41 من خلال تحليل مجهر القوة الذريه الذي يوضح وجود كتل ذات اشكال مختلفه في RH-SiO₂. بالنسبه لـ MCM-41 يتضح من النتيجة ان معامل خشونه منخفض. الزيادة في عوامل تحليل مجهر القوة الذرية لـ MCM-41@APTES مقارنة MCM-41 ثم تقليل متوسط خشونة MCM-41@APTES-BSAL عند توظيف MCM-41@APTES مع (BSAL) ادى الى انخفاض خشونة السطح مقلنة مع MCM-41. بينما MCM-41@NTPE-BSAL اظهرت النتائج ان توظيف MCM-41@NTPE ادى الى نقصان خشونة السطح للمواد الموظفه. تظهر صور FESEM ان RH-SiO₂ يتكون من سليكا غير متبلوره بينما بالنسبه لـ MCM-41 والمركبات الموظفه يتضح من

الصور ان الجزيئات ناعمه ذات تكتلات كروية. وبحسب تحليل EDX فان وجود العناصر في المركب الصلب قد اثبت.

المواد المساميه(المواد العضويه وغير العضويه)المشتقة من قشور الارز كمواد ممتازة منخفضة الكلفه وتطبيقها في امتزاز ايونات الكوبلت والنحاس الثنائي من محاليلها المائيه بعد تحضير عمود زجاجي, ومحاولة اعاده تنشيط العمود.تم اجراء تجارب الازاله بعد تضبيب الظروف الفضلى من تركيز ايونات الكوبلت والنحاس الثنائي ودرجة الحموضة و وقت التعرض وكمية ماده. كمية ايون الكوبلت في المركبات الصيدلانيه(فيتامين B12) تم تقديره باستخدام المركبات المحضره.اظهرت نماذج لانكميور وفريندلج ان بيانات فرليندلج اكثر تفضيلا للامتزاز بطريقه متعددة الطبقات.



جمهورية العراق
وزارة التعليم العالي والبحث العلمي
جامعة كربلاء
كلية العلوم
قسم الكيمياء

تخليق مركبات السليكا المسامية المعتمدة والمشتقة من قشور الارز وتطبيقاتها التحليلية

اطروحة مقدمة الى كلية العلوم - جامعة كربلاء وهي جزء من متطلبات نيل درجة الدكتوراه
فلسفة العلوم في الكيمياء
من قبل

رغد سعد حاتم البستان

بكلوريوس علوم - جامعة كربلاء (2005)
ماجستير علوم - جامعة كربلاء (2012)

بأشراف

أ.د. حيدر حميد محسن

أ.د. علاء فراك حسين

2024 ميلادي

1446 هجري